Vector Mesons in Medium
in a Transport Approach

Janus Weil

Dissertation

Institut für Theoretische Physik
Fachbereich 07 (Mathematik und Informatik, Physik, Geographie)
Justus-Liebig-Universität Gießen

2013

Contents

1 Introduction

1.1 In-medium physics

While the vacuum properties of most hadrons are known to reasonable accuracy nowadays, it is a heavily debated question how these properties change inside nuclear matter. In particular, various theoretical predictions regarding the in-medium properties of the light vector mesons have been suggested. For recent reviews see [1–3].

In general, those in-medium modifications can be subdivided into two classes:

1. The first class of effects predicts a so-called "collisional broadening" of the meson spectral function, due to collisions with the hadronic medium.

2. A second class of predictions claims that the vector-meson masses are shifted in the medium due to the partial restoration of chiral symmetry [4].

The first one is a standard many-body effect: In vacuum, a hadronic resonance can only go out of existence by making a decay into (typically two or three) other particles. Its total width is therefore given by its decay width (which can be a sum of several partial widths for decaying into different channels):

$$\Gamma_{\text{tot,vac}} = \Gamma_{\text{dec}} = \sum_i \Gamma_i \qquad (1)$$

When the hadronic resonance is embedded in some sort of hadronic medium, which can for example be given by a 'cold' nucleus or the ('hot') fireball of a heavy-ion collision, this situation is changed. Now the particle cannot only decay, but it can also scatter (elastically or inelastically). While an elastic scattering will only alter the particle's momentum, an inelastic collision will result in an absorption of the particle and the creation of other particles. Therefore the total width of the particle will gain an extra term, which is given by the 'collisional' width, due to collisions in the medium:

$$\Gamma_{\text{tot,med}} = \Gamma_{\text{dec}} + \Gamma_{\text{coll}} \qquad (2)$$

The collisional width can be related to the collision cross section in low-density approximation via

$$\Gamma_{\text{coll}} = \rho \left\langle v_{rel} \sigma_{\text{inel}} \right\rangle, \qquad (3)$$

where σ_{inel} is the inelastic collision cross-section in the medium, v_{rel} is the relative velocity of the ω with respect to the hadronic medium and the brackets indicate an integration over the Fermi momentum of the nucleons.

The expectation of an in-medium mass shift is usually motivated through the (partial) restoration of chiral symmetry in the medium: At sufficiently large temperatures and/or densities, the chiral symmetry of QCD, which is spontaneously broken in vacuum, is restored. This has the effect that chiral partners, i.e. states with equal spin but opposite parity, should become degenerate. Examples of mesonic chiral-partner pairs are the π and σ ($J = 0$), or the ρ and a_1 ($J = 1$).

Another related effect is that the chiral condensate $|\langle q\bar{q} \rangle|$ is expected to drop with increasing density and temperature [6], as shown in fig. 1. Unfortunately the chiral condensate
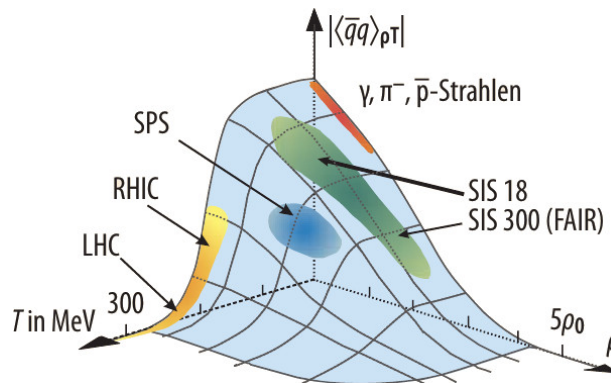
Figure 1: Chiral condensate as a function of density and temperature. Figure taken from [5], as adapted from [6].

is not a directly observable quantity. However, QCD sum rules can provide a connection between the chiral condensate the spectral functions of hadrons, which can be accessed experimentally e.g. via dilepton spectra.

While QCD sum rules can provide constraints on in-medium modifications, they do not provide definitive predictions. The first sum-rule calculations, which assumed sharp δ-like spectral functions and neglected the width, indeed predicted a mass shift [4]. However, it was shown later that an extended calculation, using a finite width, does not support this prediction [7]. Instead of strictly requiring a mass shift, it yields a certain band of allowed values in the space of in-medium masses and widths, cf. fig. 2. This means that the sum rules can be fulfilled either by a dropping mass or by an increased width, or even by different combinations of the two effects. In this sense, the predictive power of QCD sum rules is limited, and one needs to rely on models, in order to make any statements about in-medium properties.
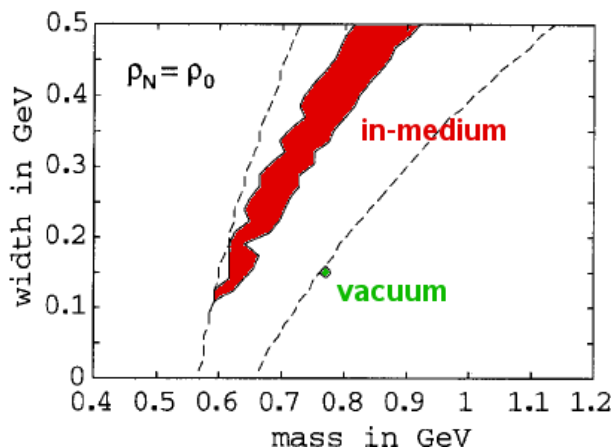
Figure 2: QCD sum-rule constraints on in-medium mass and width of the ρ meson. Figure taken from [7].

One can use effective hadronic models to describe the interaction of a particle with the surrounding medium. The composition of the medium itself depends on the experimental

setup, of course. In cold nuclear matter, accessible e.g.·by photon-induced reactions on nuclei, the medium is exclusively given by nucleons. In heavy-ion collisions at low energies, one has a hadron-resonance-gas, which in the low-energy regime is dominated by baryons, i.e. mostly nucleons and nucleon resonances. Increasing the energy in such a system will increase the temperature, and thereby the amount of pions. Further increasing the energy beyond the critical temperature (which is believed to be of the order of 160-170 MeV, see e.g. [8]), the hadron gas will dissolve into a plasma of quarks and gluons (the quark-gluon plasma, QGP).

In the context of this thesis, however, we will mostly focus on the low-energy region, where the medium is either cold nuclear matter or a baryon-dominated hadron-resonance gas. In this regime, the in-medium properties of vector mesons are determined dominantly by their coupling to baryonic resonances.

The primary absorption mechanism for the ρ meson is $\rho N \to R$, which results in a collisional broadening of the spectral function. R here denotes a N^* or Δ^* resonance, which has a coupling to the ρ. However, the spectral function does not simply become broader. Due to the coupling to the resonances, structures and secondary peaks can appear in the spectral function, which deviate from a simple Breit-Wigner form. Fig. 3 shows an example of a hadronic-model calculation of the (transversal) ρ spectral function at normal nuclear matter density, as a function of absolute momentum q and mass m [9].
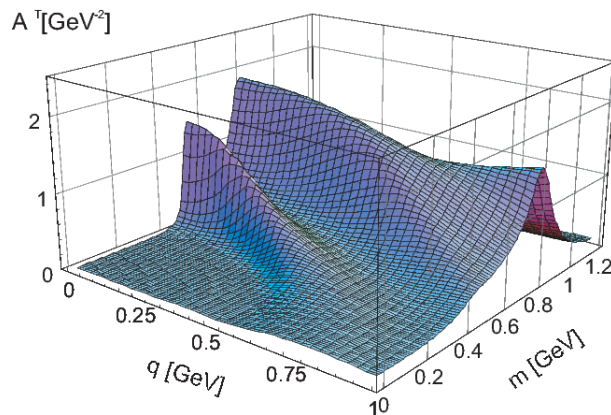
Figure 3: In-medium spectral function of the ρ meson from [10].

Besides the main peak at the nominal ρ mass, which broadens with growing momentum, a second peak appears at smaller masses. This structure is generated by the coupling to the $D_{13}(1520)$ resonance, which plays a dominant role for the ρ's in-medium spectral function. Similar hadronic models have been developed in [3, 11].

One of the main results of this work will be to show that the coupling to the $D_{13}(1520)$ (and other resonances) does not only affect strongly the in-medium self-energy, but it can already play a role in elementary nucleon-nucleon collisions, where the dominant production mechanism of the ρ is via the production and decay of exactly these baryonic resonances, which also dominate the in-medium dynamics.

In both cases, the $D_{13}(1520)$ plays a special role, for two reasons: Firstly, it couples quite strongly to the ρ, and secondly it is very light. In fact it is so light, that an $N^*(1520)$ resonance on its mass shell cannot decay into an on-shell ρ. Instead a decaying $N^*(1520)$ will mostly populate the low-mass tail of the ρ meson, so that a ρ meson produced in this

way will, already in the vacuum, deviate from the standard ρ shape, as e.g. observed in the reaction $e^+e^- \to \pi^+\pi^-$.

This 'modification' of the ρ meson due to its production mechanism is clearly not an 'in-medium' effect, since it can already appear in elementary collisions like $pp \to NN^*(1520) \to \rho NN$, where no proper hadronic medium is present, except for the two nucleons involved in the collision. However, it is still related to the in-medium modification of the spectral function, since it is generated by the same physical phenomenon: The coupling of the ρ meson to baryonic resonances through a ρNR vertex.

1.2 Possible probes of in-medium effects

The most direct method of measuring the in-medium properties of a vector meson, is to actually observe it decaying in the medium. However, the prominent hadronic decay modes of the vector mesons are unfavorable for studying in-medium effects, since they are affected by strong final-state interactions with the hadronic medium. If a decay like $\rho \to \pi\pi$ happens inside the medium, the decay pions have little chance of propagating outside without rescattering. Once they scatter inelastically, they are absorbed and cannot be detected at all. But also an elastic scattering already changes their momentum, and distorts the reconstructed invariant mass, so that the original in-medium information is lost.

In contrast to the hadronic modes, the rare dilepton decay modes are much better suited for in-medium studies. Since the leptons only interact electromagnetically, they are ideally suited to carry the in-medium information outside to the detector, nearly undisturbed by the hadronic medium. The only expected distortion is a minor correction due to the Coulomb force, which can usually be neglected. All light vector mesons (ρ, ω, ϕ) have a direct decay mode into e^+e^-. However, the branching ratio of these is far below the dominant hadronic decays, usually of the order of 10^{-5}, therefore one limiting factor is to collect sufficient statistics from these rare decays. Another experimental problem is the large background from uncorrelated lepton pairs, which do not originate from the same physical decay.

Dilepton spectra from nuclear reactions with elementary projectiles have been studied for example with the CLAS detector at JLAB, where photons with energies of a few GeV interact with nuclei [12–14], or by the E325 experiment at KEK, where 12 GeV protons were used as projectiles [15].

Early measurements of dilepton spectra from heavy-ion collisions in the low-energy regime were conducted by the DLS collaboration [16, 17], showing an excess over the expected yield. A similar excess was also observed in experiments at higher energies [18, 19], where it could be attributed to an in-medium broadening of spectral functions [20–22]. For the DLS data such in-medium effects never provided a convincing explanation - a problem that was soon known as the "DLS puzzle" [23–26].

More recently, the HADES collaboration at GSI has set up an ambitious program for measuring dilepton spectra from p+p, p+A and A+A reactions [27–33], in order to systematically check the old DLS data with improved statistics and to finally resolve the DLS puzzle. Up to now this endeavor has fully confirmed the validity of the DLS data and shifted the puzzle into the theory sector. It is clear that a detailed understanding of the elementary reactions is the most important prerequisite for explaining the heavy-ion

data.

On the side of the hadronic decays, most notably $\omega \to \pi^0 \gamma$ has been investigated by the CBELSA/TAPS group in photon-induced reactions [34–37]. Here, the direct observation of the $\omega \to \pi^0 \gamma$ decay in the medium is more difficult than e.g. for $\rho \to e^+ e^-$. First, the ω has a larger lifetime than the ρ and therefore a smaller probability to decay in the medium. And while the photon can escape the medium without interacting strongly, this is not the case for the π^0 which is expected to undergo strong final-state interactions. Various methods have been developed for overcoming this problem. However, we will show later that final-state interactions are still a severe limitation of the $\pi^0 \gamma$ decay, at least for the direct observation of in-medium decays.

However, there are other, more indirect, methods of using the $\pi^0 \gamma$ decay for the determination of the ω's in-medium properties. In so-called 'transparency ratio' measurements, nuclei of different sizes are used to determine the absorption of ω mesons in nuclear matter, and thereby its in-medium width. This method does not suffer from the FSI problem, but does not allow to make any statements about possible in-medium mass shifts.

Apart from the two methods already mentioned, there are further possibilities of investigating ω mesons in medium: For example one can study the ω excitation function on nuclei by measuring the ω photoproduction cross section as a function of the incoming photon energy (again via the $\pi^0 \gamma$ decay). If the ω mass is shifted in the medium, this should be observable as a shift of the production threshold on nuclei.

And finally also the mometum spectrum of produced ω mesons might give hints about in-medium properties: If the ω is modified in the medium, then this can change the kinematics at the production vertex, which in turn influences the momentum spectrum.

1.3 Motivation

Since this thesis presents results for two different areas (dileptons at SIS energies and ω photoproduction), also the motivation is twofold. For the dilepton part, the basic motivation is given by the fact that dilepton production in the few-GeV regime has been a puzzle for a long time (usually called the 'DLS puzzle') and in fact still is at present. The new data obtained by the HADES collaboration has provided new experimental insights and, by fully confirming the old DLS data, shifted the puzzle into the theory sector. Although a large number of theoretical investigations have been carried out over time [23–26, 38–53], dilepton production in the few-GeV is still not fully understood and this thesis tries to make a contribution to finally solving this riddle.

Since previous dilepton studies with the GiBUU model have rather focused on photon- and pion-induced reactions [54–56], this work presents the first GiBUU investigation of dilepton production from pp, pA and AA collisions (apart from the early heavy-ion studies [38], which were done with a predecessor model).

For the ω photoproduction, which was previously studied in [57–60], our investigations were mostly motivated by the availability of new data [36, 37], which could not confirm earlier results on an in-medium mass shift of the ω meson [34]. Furthermore, improvements in the treatment of in-medium spectral functions provided additional incentive to re-investigate this topic.

1.4 Overview

In this thesis, we use the Giessen Boltzmann-Uehling-Uhlenbeck transport model (GiBUU) [61,62] to study and constrain possible in-medium modifications of vector mesons in nuclear matter. We start by introducing the model in chapter 2, describing the basic functionality and building blocks, such as the elementary collision cross sections and decays relevant for our investigations, as well as the propagation through mean fields, including the "off-shell" propagation of particles with density-dependent spectral functions.

After laying out the general features of the model, chapter 3 presents the results we have obtained for dilepton production at SIS energies, compared to the data measured by the HADES and DLS collaborations. This includes dilepton production from pp, pA and AA collisions.

After that we discuss in chapter 4 the different possibilites of determining the in-medium properties of the ω meson from photoproduction experiments via the $\pi^0\gamma$ decay, as carried out by the CBELSA/TAPS group.

Finally, we close this thesis with a summary of the obtained results, some concluding remarks and an outlook to possible follow-up investigations.

2   The GiBUU transport model

Our tool for the numerical simulation of nuclear reactions is the hadronic transport model GiBUU (i.e. the 'Giessen BUU project'), which provides a unified framework for various types of elementary reactions on nuclei as well as heavy-ion collisions in a broad energy range [61, 62]. This model takes care of the correct transport-theoretical description of the hadronic degrees of freedom in nuclear reactions, including the propagation, collisions and decays of particles.

While many other transport models are primarily focused on high-energy heavy-ion collisions, one of the strengths of the GiBUU model is that it is not only capable of treating 'hadronic' collisions like AA [63–66], pA [67] and πA [56, 66, 68], but also electroweak reactions on nuclei, like γA [56, 66–69], eA [67–69] and νA [70] (the A in our notation stands for a nucleus of mass number A). For the latter three, only the primary electroweak reaction on a nucleon is treated in a special way, while the rest of the reaction (i.e. the 'hadronic afterburner') with all secondary collisions and decays is basically treated on the same footing for all types of reactions. This is one of the big advantages of this approach: By treating all the different types of reactions under the umbrella of one single model, this allows to make cross links and to transfer (theoretical and experimental) constraints from one part of the model to another. In particular it leads to a thorough testing of the central components of the model, such as the hadronic collision term and the mean-field potentials, in various situations and setups. In this thesis we apply the model mostly to hadronic reactions (pA, AA and πA), but also to photon-induced reactions.

As it is a hadronic model, the basic degrees of freedom are baryons and mesons. The model currently includes 61 baryons and 22 mesons in total. The list of baryons includes 31 non-strange particles (N, Δ and resonances), 24 strange particle (Λ, Σ, Ξ, Ω and resonances) and 6 charmed particles (single-charmed only: Λ_c, etc). The list of mesons includes the full SU(4) multiplets of pseudoscalar and vector mesons (which are actually 16-plets, but in our scheme count ten particles only, since isospin multiplets are collected into one particle ID) as well as the scalar sigma meson. Multi-charmed baryons and particles including bottom quarks are currently not treated. For the complete list of particles, see [61].

The numerical implementation of the model is realized in Fortran. While the major part of the code has been updated to the reasonably modern Fortran 95 dialect, with even a few features from Fortran 2003, certain legacy parts of the code are still written in FORTRAN 77. The development of the code is managed through a Subversion repository, which facilities a collaborative development, with several people working simultaneously on the same code base with minimal interference. The GiBUU website and wiki hosts additional facilities for documentation and collaborative development [62]. It also provides public releases of the source code, which are available after registration.

2.1   The BUU equation

In GiBUU the spectral one-particle phase-space distributions, $F(x, p)$, of all particles are obtained by solving the coupled Boltzmann-Uehling-Uhlenbeck (BUU) equations for each particle species [71]

$$\{p_0 - H, F(x,p)\}_{\mathrm{pb}} - \mathrm{tr}\left\{\Gamma(x,p)f(x,p), \mathrm{Re}\, S^{\mathrm{ret}}(x,p)\right\}_{\mathrm{pb}} = C(x,p), \qquad (4)$$

which can be derived from the Kadanoff-Baym equations via gradient expansion [72]. The leftmost term is usually referred to as the 'Vlasov' or 'drift' term, which by itself basically describes stable, non-interacting particles propagating through a mean field. The second term on the left-hand side is called 'off-shell' or 'back-flow' term. It is essential for off-shell transport, becomes important only when treating density-dependent spectral functions and leads to the correct asymptotic spectral functions of particles when they leave the nucleus. $\{\ldots\}_{\mathrm{pb}}$ denotes the Poisson bracket, defined as

$$\{A, B\}_{\mathrm{pb}} = \frac{\partial A}{\partial p_\mu}\frac{\partial B}{\partial x^\mu} - \frac{\partial A}{\partial x_\mu}\frac{\partial B}{\partial p^\mu}. \qquad (5)$$

In the back-flow term, the quantity $S^{\mathrm{ret}}(x,p)$ term denotes the retarded Green's function and $f(x,p)$ is the phase-space density related to F by

$$F(x,p) = 2\pi g f(x,p)\mathcal{A}(x,p) , \qquad (6)$$

where $\mathcal{A}(x,p)$ is the spectral function of the particle and g is the spin-degeneracy factor. The spectral function usually has the form

$$\mathcal{A}(x,p) = \frac{1}{\pi}\frac{p^2\Gamma}{(p^2 - M^2)^2 + p^2\Gamma^2}, \qquad (7)$$

where M is the pole mass and Γ is the width, which in vacuum only depends on the invariant mass p^2, but in medium can depend on the full x and p four-vectors (where the x dependence is typically connected to a density or temperature dependence). The spectral function is normalized as

$$\int_0^\infty \mathcal{A}(x,p)\mathrm{d}p_0 = 1.$$

The single-particle Hamiltonian H in eq. (4) is given in the most general relativistic form by

$$H = \sqrt{(m + U)^2 + (\vec{p} - \vec{A})^2} + A_0 \qquad (8)$$

with a scalar potential U and a vector potential $A = (A_0, \vec{A})$. The potentials implemented in GiBUU include hadronic mean-field potentials, the Coulomb potential as well as the so-called 'off-shell' potential, which will be discussed in more detail in section 2.4.

The non-relativistic mean-field potential typically enters the Hamiltonian as the zeroth component of a vector potential, and is given by a isospin-averaged Skyrme-type nucleon potential supplemented by a momentum-dependent term [73]:

$$V_N(x, \vec{p}) = A\frac{\rho(\vec{x})}{\rho_0} + \left(\frac{\rho(\vec{x})}{\rho_0}\right)^\gamma + \frac{2C}{\rho_0}\sum_{i=n,p}\int\frac{\mathrm{d}p'}{(2\pi)^3}\frac{g f_i(x, \vec{p'})}{1 + (\vec{p} - \vec{p'})^2/\Lambda^2} \qquad (9)$$

The default values for the five free parameters are $A = -29.3\,\mathrm{MeV}$, $B = 57.2\,\mathrm{MeV}$, $\gamma = 1.76$, $C = -63.6\,\mathrm{MeV}$ and $\Lambda = 2.13\,\mathrm{fm}^{-1}$, but also alternative parameter sets are available, which result in a softer or stiffer equation of state. The potential as shown is

used for the nucleon and all spin-$^1/_2$ resonances, while the potential for the Δ and all spin-$^3/_2$ resonances is assumed to be $\frac{2}{3}V_N$.

The expression $C(x,p)$ on the right-hand side of (4) denotes the collision term, which includes all sorts of scattering and decay processes and couples all particle species. The processes relevant for our investigations will be described in detail in the following two sections. The collision term consists of a one-, two- and three-body part in the GiBUU implementation, each of which contains both a gain and a loss term:

$$C(x,p) = C^{(1)}(x,p) + C^{(2)}(x,p) + C^{(3)}(x,p) + ... \tag{10}$$

$$= C^{(1)}_{\text{gain}}(x,p) - C^{(1)}_{\text{loss}}(x,p) \tag{11}$$

$$+ C^{(2)}_{\text{gain}}(x,p) - C^{(2)}_{\text{loss}}(x,p) \tag{12}$$

$$+ C^{(3)}_{\text{gain}}(x,p) - C^{(3)}_{\text{loss}}(x,p) + ... \tag{13}$$

The one-body part represents particle decays (including $1 \to 2$ and $1 \to 3$ processes), while the two- and three-body parts represent collisions of 2 or 3 particles, respectively. In principle there would be also higher terms, but those are neglected, since they only become important at very high densities. For a short derivation of the complete transport equation and further details we refer the reader to [61].

In order to solve the BUU equation numerically, we rely on the test-particle ansatz. Here the phase-space densities are approximated by a large number N of test particles, each represented by a δ-distribution in coordinate and momentum space:

$$F(x,p) = \lim_{N \to \infty} \frac{(2\pi)^4}{N} \sum_{j=1}^{N} \delta(\vec{r} - \vec{r_j}(t))\delta(\vec{p} - \vec{p_j}(t))\delta(p^0 - p_j^0(t)) \tag{14}$$

Further aspects of the numerical implementation are discussed in full detail in [61].

2.2 Particle Decays

In this section, we will give an overview over the decay modes implemented in the GiBUU collision term. We start with the hadronic decays, which are limited to two-body decays for the baryons and two- and three-body decays for the mesons. Higher multiplicity decays are only indirectly taken into account by multi-step decay chains (like e.g. $N^* \to \rho N \to 2\pi N$ or $N^* \to \pi\Delta \to 2\pi N$). After the hadronic decays, we also discuss the dilepton decays, which are incorporated through a perturbative treatment and represent a basic and important ingredient for the various dilepton spectra presented in section 3.

2.2.1 Hadronic decays

All the resonances parameters and branching ratios in the GiBUU model are taken from the Manley/Saleski partial-wave analysis [74]. Though being roughly twenty years old by now, it is still one of the most complete and extensive analyses available. It incorporates large amounts of data from $\pi N \to \pi N$, $\pi N \to \eta N$ and $\pi N \to 2\pi N$ reactions. Therefore it is able to fix the $R \to \pi N, \eta N, 2\pi N$ decay channels. The $R \to 2\pi N$ decay is not included directly, but proceeds via one of four possibilities: $R \to \pi\Delta, \rho N, \sigma N, \pi N^*(1440)$. All of those finally end up in a $2\pi N$ final state (the last one only partially, the others completely).

Reaction channels with more than 2 pions in the final state are not directly supported by data, but can be constrained by the missing inelasticity when subtracting the known channels. The Manley analysis includes a $\rho\Delta$ decay channel (corresponding to a three-pion final state), which is only used to absorb the strength from the unknown channels. In that sense, Manley has no real evidence for the $\rho\Delta$ final state in particular, but just uses this decay channel to account for the left-over strength. Therefore we take the freedom to replace the $\rho\Delta$ decays by $\sigma\Delta$, in order to avoid an overestimation of the ρ-meson production (which is important for dilepton spectra). The influence of Manley's $\rho\Delta$ decay channels on dilepton spectra was already discussed in [55] for the case of pion-induced reactions. The dilepton spectra actually give a hint that the needed 3π inelasticity might not be in the $\rho\Delta$, but instead in some other channel, as e.g. $\sigma\Delta$ (or a 'direct', i.e. non-resonant, $3\pi N$ decay).

We note already here that some of the branching ratios which are important for the present study, in particular those for decays into ρN and ωN are not very well known and still under experimental investigation [75,76]. Especially the decay $D_{13}(1520) \to \rho N$, which is of particular importance for the dilepton results, has recently been claimed to have a branching ratio of only 8 - 17% [77], which is slightly smaller than the value of 21% from the Manley analysis and the PDG value of 15 - 25% [78].

Also for the width parametrizations of the hadronic decays we follow the treatment of Manley [74], which assumes that the partial width of a resonance R decaying into two particles a and b is given by:

$$\Gamma_{R\to ab}(m) = \Gamma^0_{R\to ab} \frac{\rho_{ab}(m)}{\rho_{ab}(M_0)}. \tag{15}$$

Here m is the actual (off-shell) mass of the resonance R, M_0 is its pole mass, $\Gamma^0_{R\to ab} = \Gamma_{R\to ab}(M_0)$ is the partial width at the pole mass and the function ρ_{ab} is defined as:

	rating	M_0 [MeV]	Γ_0 [MeV]	branching ratio in %						
				πN	ηN	$\pi\Delta$	ρN	σN	$\pi N^*(1440)$	$\sigma\Delta$
$P_{11}(1440)$	****	1462	391	69	—	22_P	—	9	—	—
$S_{11}(1535)$	***	1534	151	51	43	—	2_S+1_D	1	2	—
$S_{11}(1650)$	****	1659	173	89	3	2_D	3_D	2	1	—
$D_{13}(1520)$	****	1524	124	59	—	5_S+15_D	21_S	—	—	—
$D_{15}(1675)$	****	1676	159	47	—	53_D	—	—	—	—
$P_{13}(1720)$	*	1717	383	13	—	—	87_P	—	—	—
$F_{15}(1680)$	****	1684	139	70	—	10_P+1_F	5_P+2_F	12	—	—
$P_{33}(1232)$	****	1232	118	100	—	—	—	—	—	—
$S_{31}(1620)$	**	1672	154	9	—	62_D	25_S+4_D	—	—	—
$D_{33}(1700)$	*	1762	599	14	—	74_S+4_D	8_S	—	—	—
$P_{31}(1910)$	****	1882	239	23	—	—	—	—	67	10_P
$P_{33}(1600)$	***	1706	430	12	—	68_P	—	—	20	—
$F_{35}(1905)$	***	1881	327	12	—	1_P	87_P	—	—	—
$F_{37}(1950)$	****	1945	300	38	—	18_F	—	—	—	44_F

Table 1: Resonance parameters according to Manley [74] (columns 2-4), together with branching ratios of the resonance decay modes (columns 7-13). Subscripts indicate the relative angular momentum of the outgoing particles in the respective decay channel.

$$\rho_{ab}(m) = \int dm_a^2 dm_b^2 \mathcal{A}_a(m_a^2)\mathcal{A}_b(m_b^2)\frac{p_f}{m}B_L^2(p_f R)\mathcal{F}_{ab}^2(m). \tag{16}$$

In this formula m_a and m_b denote the masses of the particles a and b (which are integrated over), $\mathcal{A}_a$ and $\mathcal{A}_b$ are their spectral functions and p_f is the final state momentum of a and b in the CM frame. Finally, L is the orbital angular momentum of a and b in the final state and B_L are the so-called "Blatt-Weisskopf functions". The parameter R is usually called the "interaction radius", which is assumed to be 1 fm. The form factor $\mathcal{F}_{ab}$ is only relevant for unstable decay products and will be discussed later.

For the πN decay, the angular momentum in the decays is directly fixed by the PWA. For other decays, like e.g. $\pi\Delta$ and ρN, multiple partial waves with different L can contribute (constrained by angular momentum and parity conservation). The explicit expressions of the first few B_L are the following:

$$
\begin{aligned}
B_0(x) &= 1 \\
B_1(x) &= \frac{x}{\sqrt{1+x^2}}, \\
B_2(x) &= \frac{x^2}{\sqrt{9+3x^2+x^4}}, \\
B_3(x) &= \frac{x^3}{\sqrt{225+45x^2+6x^4+x^6}},
\end{aligned}
$$

For P-wave decays (i.e. L=1), such as $\Delta \to \pi N$ and $\rho \to \pi\pi$, the width becomes:

$$\Gamma(m) = \Gamma_0 \frac{m_0}{m}\left(\frac{q}{q_0}\right)^3 \frac{q_0^2+\Lambda^2}{q^2+\Lambda^2}. \tag{17}$$

Here m_0 is the mother particle's pole mass, m is its off-shell mass, Γ_0 is the on-shell width (at $m = m_0$); q denotes the final-state center-of-mass momentum for mass m, while q_0 is the same quantity for mass m_0, and $\Lambda = 1/R = 1\,\mathrm{fm}^{-1}$ can be viewed as a
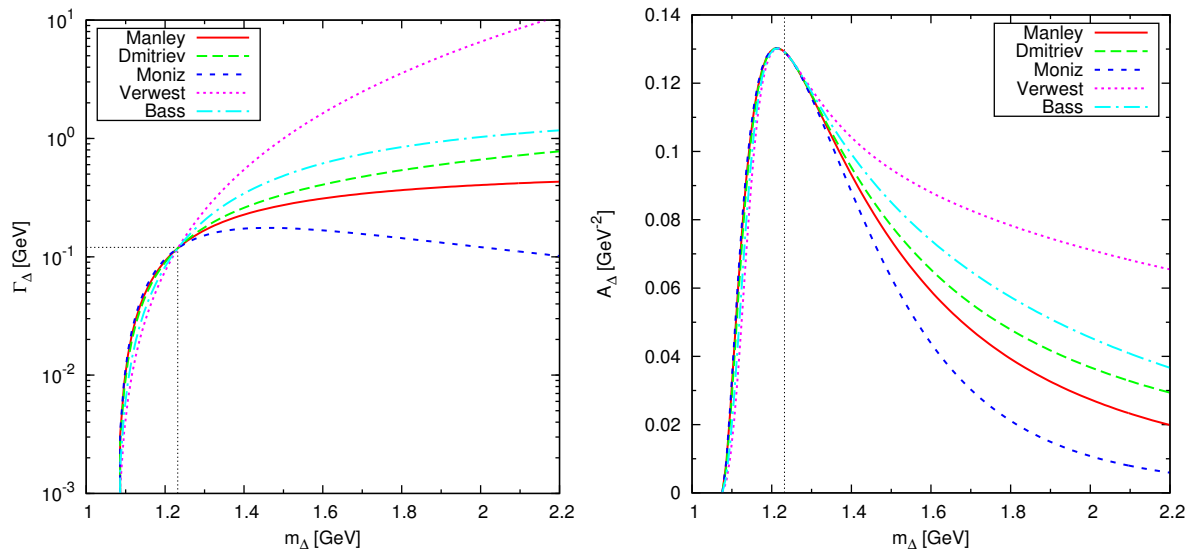
Figure 4: Vacuum width and spectral function of the Δ resonance in various parametrizations [74, 79–82].

cutoff parameter. It has been shown in [66], that eq. (17) gives a good description of the experimental phase shifts in $\pi\pi$ and πN scattering.

Since there has been a significant amount of discussion about the role of the Δ resonance in dilepton spectra, we compare here the Δ width parametrization in our model (according to Manley) to several other parametrizations [79–82]:

$$\Gamma_{\text{Dmitriev}} = \Gamma_0 \left(\frac{q}{q_0}\right)^3 \frac{q_0^2 + \kappa^2}{q^2 + \kappa^2}, \qquad\qquad \kappa = 0.2\,\text{GeV}, \qquad (18)$$

$$\Gamma_{\text{Moniz}} = \Gamma_0 \frac{m_0}{m} \left(\frac{q}{q_0}\right)^3 \left(\frac{q_0^2 + \beta^2}{q^2 + \beta^2}\right)^2, \qquad\qquad \beta = 0.3\,\text{GeV}, \qquad (19)$$

$$\Gamma_{\text{Verwest}} = \Gamma_0 \left(\frac{q}{q_0}\right)^3 \frac{\sqrt{q^2 + m_\pi^2} + m_N}{\sqrt{q_0^2 + m_\pi^2} + m_N}, \qquad\qquad (20)$$

$$\Gamma_{\text{Bass}} = \Gamma_0 \frac{m_0}{m} \left(\frac{q}{q_0}\right)^3 \frac{1.2}{1 + 0.2\left(\frac{q}{q_0}\right)^2}. \qquad\qquad (21)$$

Figure 4 shows a comparison of the mass-dependent width $\Gamma_\Delta^{tot}(m) = \Gamma_{\pi N}(m)$ as well as the Δ spectral function, given by

$$\mathcal{A}(m) = \frac{1}{\pi} \frac{m\Gamma(m)}{(m^2 - m_0^2)^2 + (m\Gamma(m))^2} . \qquad\qquad (22)$$

While all width parametrizations by construction agree at the Δ pole mass of $m_0 = 1232\,\text{MeV}$, where they are constrained by the on-shell value of $\Gamma_\Delta(m_0) \approx 0.118\,\text{MeV}$ [78], they deviate strongly in the far-offshell region of $m \gg m_0$. The same applies to the spectral function. This is one of several factors, which contribute to the large uncertainty of the dilepton yield from offshell Δ decays, as we will discuss later. We normally use the

Manley width of equ. (17) for the $\Delta \to \pi N$ decay, but we will also discuss the influence of the hadronic width parametrization of the Δ on the dilepton spectrum (e.g. in section 3.1.8).

For decays with unstable daughter particles, an additional form factor $\mathcal{F}_{ab}$ is involved (for stable daughter particles, it is defined to be unity) [9]:

$$\mathcal{F}_{ab}(m) = \frac{\lambda_{ab}^4 + \frac{1}{4}(s_0 - M_0^2)^2}{\lambda_{ab}^4 + (m^2 - \frac{1}{2}(s_0 + M_0^2))^2}, \tag{23}$$

where s_0 is the Mandelstam s for the threshold of the regarded process, and the parameter λ is chosen to be [68]:

$$\lambda = \begin{cases} 1.6\,\text{GeV} & \text{for unstable meson, e.g. } \rho N, \eta N, \sigma N \\ 2.0\,\text{GeV} & \text{for unstable baryon, e.g. } \pi\Delta, \pi N^*(14440) \\ 0.85\,\text{GeV} & \text{if both are unstable, e.g. } \rho\Delta/\sigma\Delta \end{cases} \tag{24}$$

Already in [68] it was shown that this additional form factor has only minor influence on the spectral functions of most resonances. We have further verified that it has no significant influence on the dilepton spectra of ρ mesons from resonance decays.

In principle the decays of mesons are treated on the same footing as the baryon decays, i.e. using the Manley parametrization of eq. (15) and (16). In particular this is done for all the 2-body decays of the vector mesons, like $\rho \to 2\pi$, $\omega \to 2\pi$, $\phi \to 2K$, $\omega \to \pi^0\gamma$ and $\phi \to \rho\pi$.

However, for the mesons also three-body decays are implemented, such as $\omega \to 3\pi$ and $\phi \to 3\pi$. Since the Manley analysis only treats two-body final states, we cannot apply it to three-body decays. Instead we use the three-body decay formula found in [78]:

$$d\Gamma = \frac{1}{(2\pi)^5}\frac{1}{16M^2}|\mathcal{M}|^2|\vec{p}_1^*||\vec{p}_3|dm_{12}d\Omega_1^*d\Omega_3. \tag{25}$$

For simplicity we assume the matrix element $\mathcal{M}$ to be constant, and the distribution of the angles Ω_1^* and Ω_3 to be isotropic. If we then forget about overall constant factors, we get the following dependency:

$$\Gamma_{V\to 3\pi} \propto \frac{\mathcal{F}_{3\pi}(M)}{M^2}\int|\vec{p}_1^*||\vec{p}_3|dm_{12}. \tag{26}$$

Here $m_{12} = (p_1 + p_2)^2$ is the invariant mass of particle 1 and 2, $|\vec{p}_1^*|$ is the absolute momentum in their CM frame and $|\vec{p}_3|$ is the absolute momentum of particle 3 in the rest frame of the decaying particle. After integrating out m_{12} numerically, this formula gives us the mass dependence of the width, which we normalize to the value at the pole mass. Further we use an additional dipole form factor $\mathcal{F}_{3\pi}(m) = (\Lambda^2 + M_0^2)/(\Lambda^2 + m^2)$ in order to regulate the high-mass behavior, with M_0 being the pole mass of the decaying particle (ω or ϕ) and a constant $\Lambda = 0.5\,\text{GeV}$. This is done in order to avoid problems with the off-shell propagation (see chapter 2.4.2), which puts certain restrictions on the behavior of $\partial\Gamma/\partial m$ (i.e. it does not work if $\partial\Gamma/\partial m$ is too large). These off-shell issues are also the reason for not using the $\omega \to 3\pi$ width from [56].

2.2.2   Dilepton decays

In the GiBUU model the following dilepton decay modes are taken into account:

- direct decays:

  - $V \to e^+ e^-$ with $V = \rho^0, \omega, \phi$,
  - $\eta \to e^+ e^-$,

- Dalitz decays:

  - $P \to e^+ e^- \gamma$ with $P = \pi^0, \eta$,
  - $\omega \to \pi^0 e^+ e^-$,
  - $\Delta \to N e^+ e^-$,
  - $R \to N e^+ e^-$, with R=N^*, Δ^* (via $R \to \rho N$).

Since the dilepton decays are extremely rare (with typical branching ratios in the order of 10^{-5}), it would be very inefficient to treat them on the same footing as the hadronic decays: Only about one in 10^5 ρ mesons would actually decay into a dilepton pair (and the rest into pions), resulting in poor statistics and long running times.

Therefore we apply here the so-called 'shining' technique [66, 83, 84], which is in fact used by most current transport models (e.g. [47, 49]). The shining approach is a time-integration technique, which assumes that each test particle continuously radiates off lepton pairs during it complete lifetime (until it decays hadronically or is absorbed). In this procedure, each radiated dilepton acquires a weight factor according to the actual probability for the decay to happen in this timestep, which is $P = \Gamma_{ee}/\gamma \cdot \mathrm{d}t$, with the dilepton width Γ_{ee}, a Lorentz factor γ and the time-step size $\mathrm{d}t$. In this way one obtains a sufficient number of dilepton events, although each of them carries only a small weight P (due to the smallness of Γ_{ee}).

Since the simulation can only run for a finite number N of timesteps (thus covering a finite time interval of $N\mathrm{d}t$), all unstable particles are forced to decay at the end of the simulation. Assuming free vacuum decays (and neglecting any further rescattering or absorption), the probability for a particle to make a dilepton decay after the last timestep is simply given by the branching ratio $P = \Gamma_{ee}/\Gamma_{tot}$. This represents a final contribution to the shining procedure, accounting for all decays that would have happened only after the last timestep (which is particularly important for long-lived dilepton sources like π and η).

In the following, we start by describing the direct and Dalitz decays of the mesons (both vector and pseudoscalar), then move to the Dalitz decays of the Δ and the resonances R and finally lay out our treatment of bremsstrahlung.

2.2.2.1   Direct meson decays

The leptonic decay widths of the vector mesons are taken under the assumption of strict vector-meson dominance (VMD),

$$\Gamma_{V \to e^+ e^-}(\mu) = C_V \frac{m_V^4}{\mu^3}, \tag{27}$$

where μ is the meson's off-shell mass, m_V is the pole mass, and the constants C_V are listed in table 2 (taken from [78]).

V	$m_V(\mathrm{MeV})$	$\Gamma_{ee}(\mathrm{keV})$	$C_V = \Gamma_{ee}/m_V$
ρ	775.49	7.04	$9.078 \cdot 10^{-6}$
ω	782.65	0.60	$7.666 \cdot 10^{-7}$
ϕ	1019.455	1.26	$1.234 \cdot 10^{-6}$

Table 2: Dilepton-decay constants for $V \to e^+ e^-$.

Although the physical threshold of the dileptonic decay channels of course lies at $2m_e$, contributions of ρ mesons below $m = 2m_\pi$ are frequently neglected in transport simulations. The reason for this artificial threshold is purely numerical: The ρ spectral function has a sharp drop at the 2π threshold, and it is numerically very difficult to populate the spectral function below this threshold, where it is almost vanishing. Here we make additional numerical efforts to include the contribution of ρ mesons below the 2π threshold, since it can give significant contributions to the total dilepton spectrum for certain reactions.

Below the 2π threshold, the ρ meson width becomes very small because here only the electromagnetic decay width is active. This smallness of the width, however, is counteracted to some degree by the propagator of the virtual photon that enhances small dilepton masses, see eq. (27).

It is clear that the physical threshold of the dilepton mass in such a Dalitz decay must be at $2m_e$, and not $2m_\pi$. In order to get contributions below $2m_\pi$, it is important to take into account the dilepton width in the spectral function of the ρ meson (where it is typically neglected in transport simulations). Thus the total vacuum decay width of the ρ meson, which is shown in fig. 5a, becomes:

$$\Gamma^\rho_{\mathrm{tot,vac}}(m) = \Gamma_{\pi\pi}(m) + \Gamma_{ee}(m) \tag{28}$$

While the hadronic width $\Gamma_{\pi\pi}$, as given by eq. (17), vanishes below $m = 2m_\pi$, the leptonic width Γ_{ee}, given by eq. (27), extends down to $m = 2m_e$. From a conceptual point is it easy to incorporate such contributions, by simply adding the leptonic width term. The only problem is of a numerical nature: Since the dilepton width is so much smaller than the hadronic width, the spectral function of the ρ only has tiny contributions below $2m_\pi$, see fig. 5c, and it is numerically very hard to properly populate this tail in a test-particle treatment. This is the reason why the contributions below $2m_\pi$ in our spectra often suffer from poor Monte-Carlo sampling statistics.

Further it should be noted that the total width in the medium contains an collisional width term in addition, which adds further strength, also below the 2π threshold.

Fig. 5d shows the ρ spectral function multiplied with the branching ratio into dileptons,

$$\mathcal{A}(m) \cdot \frac{\Gamma_{ee}}{\Gamma_{tot}} = \frac{1}{\pi} \frac{m\Gamma_{ee}(m)}{(m^2 - m_0^2)^2 + (m\Gamma_{tot}(m))^2}. \tag{29}$$

The dilepton yield from ρ decays is proportional to this quantity. As the figure shows, the negligence of the dilepton contribution to the total width is well justified above the 2π
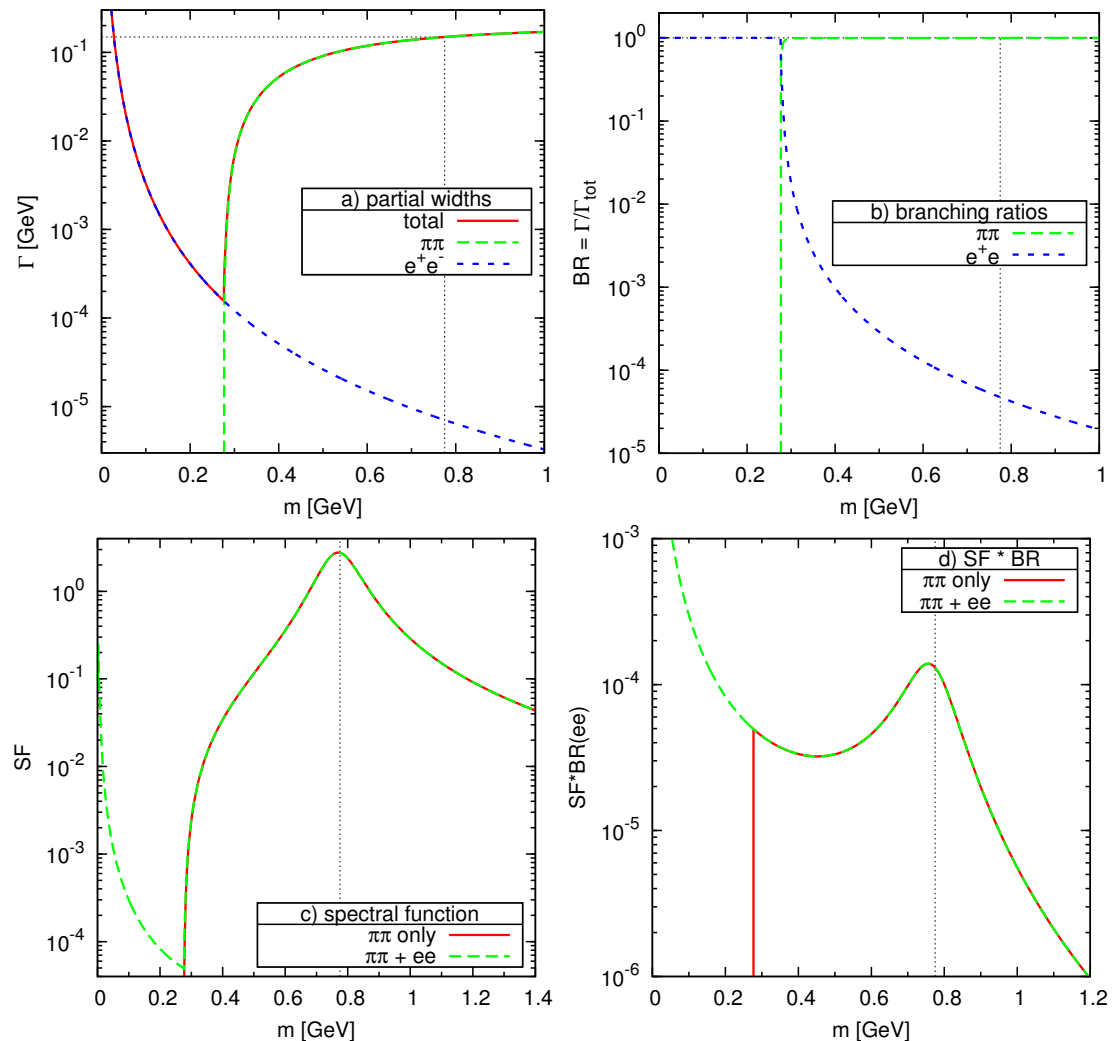
Figure 5: Top: Partial widths (left) and branching ratios (right) of the ρ meson as a function of mass. Bottom: Bare spectral function of the ρ meson (left) and spectral function multiplied with dilepton branching ratio (right).

threshold. Contributions below this threshold, however, are only achieved by using the dilepton width already in the population of the spectral function. Note in particular the smooth behavior at the 2π threshold, which does not show any discontinuity. However, the population of the low-mass tail of the ρ meson (below $2m_\pi$) certainly depends on the production process: If the ρ meson originates from a pion-pion collision, invariant masses below the 2π threshold are of course forbidden kinematically, but if the ρ meson is produced via a baryonic resonance (which is the dominant production mechanism in low-energy pp and AA reactions), then there is no threshold at $2m_\pi$ and the ρ spectral function can be populated down to $2m_e$.

In principle such dilepton contributions below the hadronic decay thresholds are also present for the ω and ϕ meson. However, for these we can safely neglect them: The ω and ϕ are much more narrow than the ρ, and therefore their spectral function has already dropped so strongly at the hadronic threshold that the dilepton contributions are

negligible so far off the mass shell. This is different for the ρ due to its large mass (and the effects of resonance couplings which come on top of that, as we will discuss later).

Apart from the vector mesons, also the pseudoscalar η meson is known to have a direct leptonic decay mode. However, only the direct decay into a $\mu^+\mu^-$ pair has been observed so far, while for the e^+e^- decay only an upper limit of $\mathrm{BR}(\eta \to e^+e^-) < 2.7 \cdot 10^{-5}$ is known [85]. In fact this limit has been pushed down to $4.9 \cdot 10^{-6}$ lately using HADES dilepton data [31]. However, the theoretical expectation from helicity suppression is still four orders of magnitude lower [86]. The absence of any η peak in the measured spectra allows us to conclude that the true branching ratio must be significantly lower than the upper limit just mentioned [56]. Therefore we do not include the $\eta \to e^+e^-$ decay in our analysis.

2.2.2.2   Meson Dalitz decays

The Dalitz decays of the pseudoscalar mesons, $P = \pi^0, \eta$, are treated via the parametrization [87],

$$\frac{\mathrm{d}\Gamma_{P\to\gamma e^+e^-}}{\mathrm{d}\mu} = \frac{4\alpha}{3\pi} \frac{\Gamma_{P\to\gamma\gamma}}{\mu} \left(1 - \frac{\mu^2}{m_P^2}\right)^3 |F_P(\mu)|^2, \tag{30}$$

with $\Gamma_{\pi^0\to\gamma\gamma} = 7.8 \cdot 10^{-6}\,\mathrm{MeV}$, $\Gamma_{\eta\to\gamma\gamma} = 4.6 \cdot 10^{-4}\,\mathrm{MeV}$ and the form factors,

$$F_{\pi^0}(\mu) = 1 + b_{\pi^0}\mu^2, \qquad b_{\pi^0} = 5.5\,\mathrm{GeV}^{-2}, \tag{31}$$

$$F_\eta(\mu) = \left(1 - \frac{\mu^2}{\Lambda_\eta^2}\right)^{-1}, \quad \Lambda_\eta = 0.676\,\mathrm{GeV}. \tag{32}$$

While the pion form factor and the value of b_π have been adopted from [87], the value of Λ_η has been recently determined from the HADES data at 2.2 GeV beam energy [88] and agrees reasonably well with the values found by NA60 [89] and CB/TAPS [90]. As shown in [91], the dilepton decays of the pseudoscalar mesons is expected to follow an anisotropic angular distribution,

$$\frac{\mathrm{d}\Gamma_{P\to\gamma e^+e^-}}{\mathrm{d}\cos\theta} \propto 1 + \cos^2(\theta), \tag{33}$$

where θ is the angle of the electron momentum with respect to the dilepton momentum. This has been confirmed recently by HADES data [92]. All other decays are treated isotropically in our model.

The parametrization of the ω Dalitz decay,

$$\frac{\mathrm{d}\Gamma_{\omega\to\pi^0 e^+e^-}}{\mathrm{d}\mu} = \frac{2\alpha}{3\pi} \frac{\Gamma_{\omega\to\pi^0\gamma}}{\mu} \left[\left(1 + \frac{\mu^2}{\mu_\omega^2 - m_\pi^2}\right)^2 - \frac{4\mu_\omega^2\mu^2}{(\mu_\omega^2 - m_\pi^2)^2}\right]^{3/2} |F_\omega(\mu)|^2,$$

$$|F_\omega(\mu)|^2 = \frac{\Lambda_\omega^4}{(\Lambda_\omega^2 - \mu^2)^2 + \Lambda_\omega^2\Gamma_\omega^2}, \tag{34}$$

is adopted from [66,93] with $\Gamma_{\omega\to\pi^0\gamma} = 0.703\,\mathrm{MeV}$, $\Lambda_\omega = 0.65\,\mathrm{GeV}$ and $\Gamma_\omega = 75\,\mathrm{MeV}$. Here we note that the form factor of the ω Dalitz decay is also well-constrained by data [89].

2.2.2.3   Delta Dalitz decay

For the Δ-Dalitz decay, i.e. $\Delta^+ \to p e^+ e^-$ and $\Delta^0 \to n e^+ e^-$, we use the parametrization of Krivoruchenko et al. [94],

$$\frac{\mathrm{d}\Gamma_{\Delta \to N e^+ e^-}}{\mathrm{d}\mu} = \frac{2\alpha}{3\pi\mu}\Gamma_{\Delta \to N\gamma^*}(\mu), \tag{35}$$

$$\Gamma_{\Delta \to N\gamma^*}(\mu) = \frac{\alpha}{16}\frac{(m_\Delta + m_N)^2}{m_\Delta^3 m_N^2}\left[(m_\Delta + m_N)^2 - \mu^2\right]^{1/2}$$

$$\times \left[(m_\Delta - m_N)^2 - \mu^2\right]^{3/2}|F_\Delta(\mu)|^2, \tag{36}$$

where μ is the invariant mass of the dilepton pair and we neglect the electron mass. In the literature, other parametrizations of this Dalitz decay exist [24, 38], and e.g. the one from [38] has been used in earlier versions of the Giessen BUU Model [66] (where also the factor-of-two error in the coupling constant of [38] was fixed). However, it was claimed in [94] that all previous calculations of this Dalitz width were erroneous. We note that the parametrization of [24] at least has a normalization error and overestimates the real-photon width by about a factor of 1.6, but otherwise seems to agree roughly with [38].
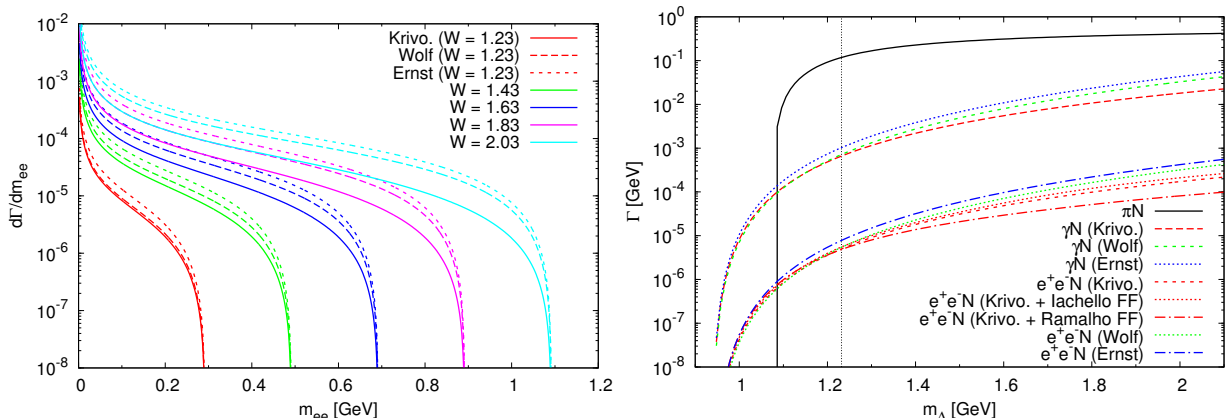

Figure 6: Left: Mass-differential width of the Δ Dalitz decay for different off-shell masses W of the Δ, in various parametrizations [24, 38, 94]. Right: Integrated dilepton width of the Δ in various parametrizations, compared to the πN and γN widths.

We compare in fig. 6 the three parametrizations cited above. While those of Krivoruchenko [94] and Wolf [38] at least agree for on-shell Deltas, all three disagree strongly for far-off-shell masses W. Unfortunately, these off-shell contributions dominate over the on-shell contribution, as the plot shows: The Dalitz width grows strongly with W, and large dilepton masses m_{ee} are only populated by large Δ masses W. This means that the dilepton yield from Δ Dalitz decays is highly sensitive to uncertainties in the off-shell behavior of the leptonic and hadronic widths (cf. section 2.2.1, in particular fig. 4).

In fig. 6, we also show the integrated dilepton width, defined as

$$\Gamma_{\Delta \to N e^+ e^-}(m_\Delta) = \int_{2m_e}^{m_\Delta - m_N} \mathrm{d}\mu \frac{\mathrm{d}\Gamma_{\Delta \to N e^+ e^-}}{\mathrm{d}\mu}, \tag{37}$$

compared to the real-photon width $\Gamma_{\Delta \to N\gamma^*}(\mu = 0)$ and the hadronic width for $\Delta \to \pi N$. This shows again the rather large differences one gets from different width parametrizations (and form factors), but it also shows that the integrated dilepton width is so small that it can be neglected in the total width. Even below the πN threshold there is only a small tail, which we neglect in our simulations (this situation is different from the $\rho \to e^+e^-$ width, which rises below the hadronic threshold and can become quite important there).

On top of the variations of the hadronic and leptonic widths of the Δ comes yet another uncertainty: The electromagnetic N-Δ transition form factor $F_\Delta(\mu)$, which appears in eq. (36), is an issue of ongoing debate. Unlike the other semileptonic Dalitz decays, it is poorly constrained by data. At least at the real-photon point ($\mu = 0$) it is fixed by the decay width $\Gamma_{\Delta \to N\gamma} \approx 0.118 \, \text{MeV} \cdot 0.0056 = 0.66 \, \text{MeV}$ [95] to $|F_\Delta(0)| = 3.03$, and also in the space-like region this form factor is well-constrained by electron-scattering data on the nucleon. However, it is basically unknown in the time-like regime, which is being probed by the Δ Dalitz decay.

Theoretical models for the N-Δ transition form factor usually assume one or more VMD-inspired poles in the time-like region [96–99]. However, the data in the space-like region does not provide sufficient constraints to fix the behavior in the time-like region.

Moreover, a VMD-like Δ form factor would imply a coupling of the Δ to the ρ meson, which has never been observed directly and could only play a role far off the Δ pole, where its strength is completely unknown [100].

In general the Δ form factor can be decomposed into a magnetic, electric and Coulomb component [96] as

$$|F_\Delta(\mu)|^2 = G_M^2 + 3G_E^2 + \frac{\mu^2}{2m_\Delta^2}G_C^2. \tag{38}$$

However, most models neglect the latter two and and only treat the magnetic dipole form factor G_M, which is expected to dominate [96, 98, 99].
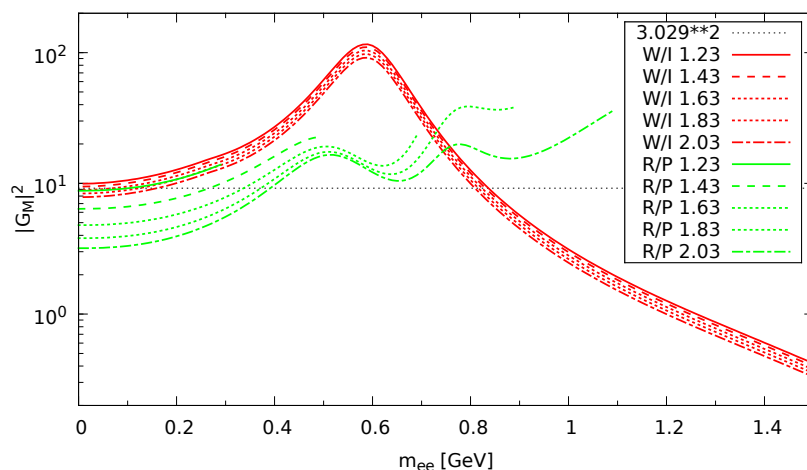

Figure 7: Delta Dalitz transition form factor, according to the models of Wan/Iachello [98] and Ramalho/Pena [99], for different off-shell Delta masses.

In fig. 7, we compare the models of Wan/Iachello [98] and Ramalho/Pena [99] as a function of the dilepton mass m_{ee} and for selected values of the off-shell Δ mass W.

The Wan/Iachello model exhibits only a very weak W dependence and shows a strong single peak at $m_{ee} \approx 0.6\,\text{GeV}$, which is enhanced over the real-photon point ($m_{ee} = 0$) by an order of magnitude.

The model of Ramalho and Pena shows a similar slowly-rising behavior at small dilepton masses, but then deviates from the former model in several features: Firstly, it does not only have a single peak, but emerges into a pronounced double-peak structure at higher W (for this model, we only plot the form factor only in the kinematical limit of $m_{ee} < W - m_N$; for the first model, this limit was ignored). This feature is due to the two-component nature of the model: It involves a coupling of the virtual photon to the valence quarks as well as the pion cloud. While the bare-quark coupling generates a peak at the nominal ρ mass of 775 MeV, the peak from the pion cloud is shifted towards smaller masses.
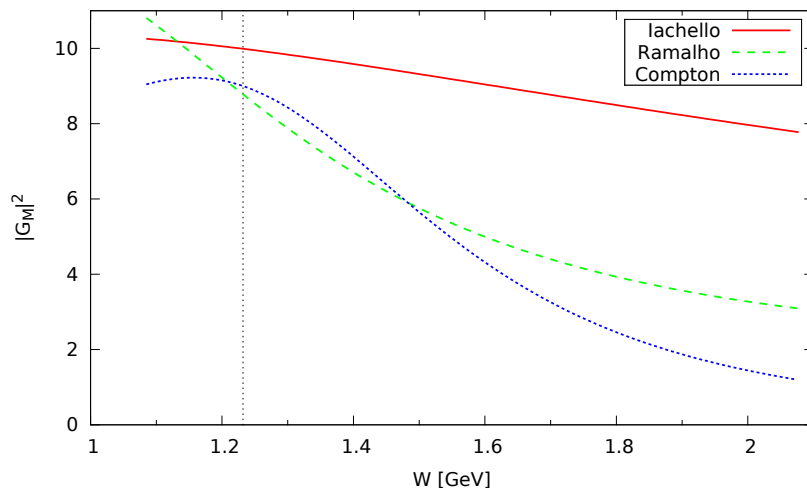

Figure 8: W dependence (at $q^2 = 0$) of the Delta Dalitz transition form factor models of Wan/Iachello [98] and Ramalho/Pena [99], compared to the one obtained from Compton scattering [101].

A second difference is given by the fact that the Ramalho model shows a much stronger W dependence. This W dependence comes almost exclusively from the valence-quark coupling, while the pion-cloud contribution is basically independent of W. In the Iachello model, the valence-quark contribution is much smaller, which also results in a less pronounced W dependence. The stronger W dependence in the Ramalho model has the effect of lowering the peak structures, so that the form factor in total deviates much less from the scenario of a constant form factor than in the Iachello model. At the real photon point of $q^2 = 0$, it is possible to fix the W dependence of the form factor via Compton scattering data on the nucleon, i.e. $\gamma N \to \gamma N$, which has been done in [101]. In fig. 8, we compare the W dependence of the Iachello and Ramalho models at $q^2 = 0$ to that obtained from Compton scattering. First of all, one can see that the different models are only approximately equal at the on-shell value of $W = 1.232\,\text{GeV}$, since the $\Delta \to N\gamma$ coupling is only fixed experimentally to a precision of around 10% [78]. Furthermore it

is apparent that the steeper W dependence of the Ramalho form factor fits better the constraint from Compton scattering, while the Iachello model exhibits a rather flat behavior, with the consequence that it probably overestimates the dilepton contributions of the high-mass tail of the Δ spectral function (which are quite important, as has been shown in fig. 6).

In the presentation of our results in the following sections, we will mostly use the form-factor model of Ramalho/Pena, since it appears to us to be the best model which is presently available. However, we also use the Wan/Iachello model in a few spots to illustrate the influence of this form factor and to demonstrate the uncertainty which is connected to it.

2.2.2.4   Resonance Dalitz decays

For the other baryonic resonances $R = N^*, \Delta^*$ we don't explicitly include a Dalitz decay, but evaluate their contributions to the dilepton spectrum through the two-step process $R \to N\rho \to Ne^+e^-$, relying on the branching ratios determined by Manley et al. [74]. In the transport-typical manner we cut the corresponding diagrams, separating the production and decay vertices of the resonance and neglecting any phases and interferences.
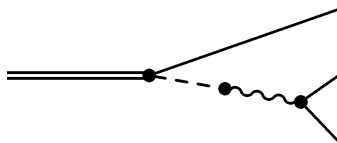
In this approach we get dilepton contributions from every baryonic resonance which has a ρN decay mode, cf. table 1. When determining the partial width for the ρN channel according to eq. (15) and (16), it is important to include the dilepton width in the ρ spectral function $\mathcal{A}_\rho$:

$$\rho_{\rho N}(m) = \int_{2m_e}^{\sqrt{s}-m_N} dm_\rho^2 \mathcal{A}_\rho(m_\rho^2) \frac{p_f}{m} B_L^2(p_f R) \mathcal{F}_{\rho N}^2(m). \tag{39}$$

In fig. 9 we show all partial width parametrizations and the corresponding branching ratios for the example of the $D_{13}(1520)$ resonance, which will later turn out to be particularly important for the dilepton production.

When neglecting the dilepton width (solid lines), the πN channel dominates the total width at the peak mass (marked by a dotted line) and below. Since it's the lightest decay channel, it also defines the minimum mass the resonance can have to be $m_{min} = m_N + m_\pi$. Above the peak mass, the ρN width starts to rise strongly and soon dominates over the πN channel. At very large masses, however, it drops again, so that πN becomes the strongest channel again. The $\pi \Delta$ channels only give minor contributions. Without the dilepton width, the integration in eq. (39) starts at $2m_\pi$, and the ρ spectral function only has contributions from the $\rho \to 2\pi$ decay. But when including the dilepton width, the integration has to start already at $2m_e$ and the spectral function contains additional contributions from the dilepton decay. These additional contributions also cause a slight modification of the ρN width, as shown by the dashed lines in fig. 9. As expected, these
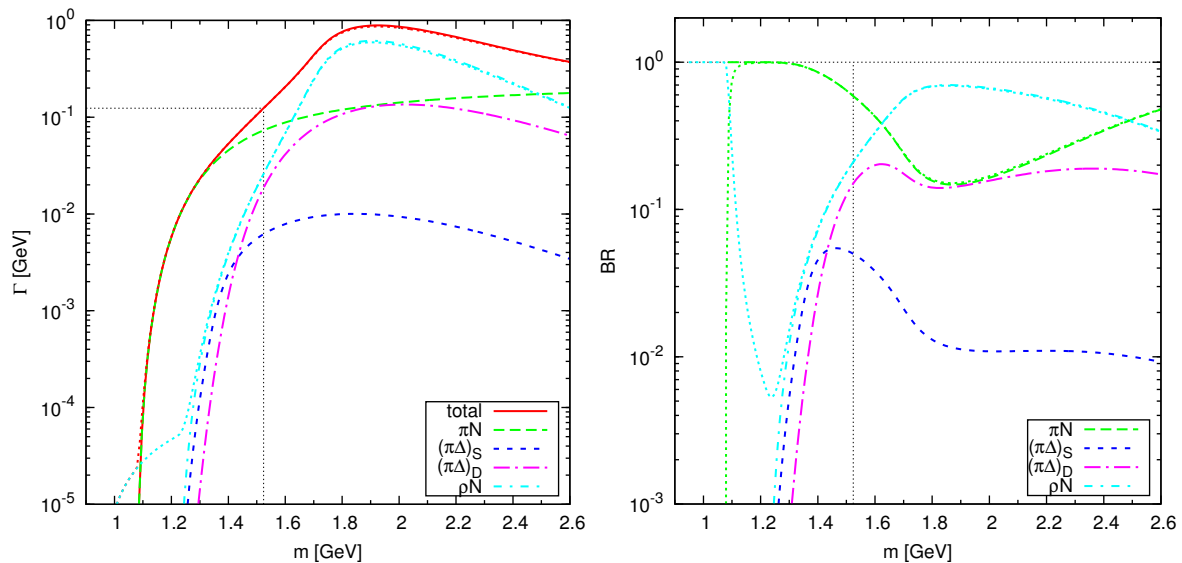
Figure 9: Partial width parametrizations and corresponding branching ratios for all decay channels of the $D_{13}(1520)$ resonance (dotted: including dilepton width).

modifications are limited to small masses ($m \lesssim m_N + 2m_\pi$), and in particular the dilepton width introduces contributions below $m_N + m_\pi$.

In an alternative treatment, used e.g. in [41, 42], the resonance decays are treated like (one-step) Dalitz decays, analogous to the case of the Δ described in the previous section. They are fixed at the photon point ($q^2 = 0$) to the known branching ratios of the radiative decays $R \to \gamma N$. The extension to finite virtualities ($q^2 > 0$) proceeds via electromagnetic transition form factors at the $RN\gamma^*$ vertex, which parametrize the internal structure of this coupling (usually via vector-meson dominance, cf. the earlier discussion for the Δ). These two methods should be fully equivalent if the phase relations between the decaying resonance and the dileptons can be neglected and a corresponding form factor is used (our model relies on the assumption of strict VMD). Any interaction of the ρ meson between its production and decay, leading to a broadening of the ρ spectral function, could be absorbed into a medium dependence of the form factor.

One advantage of our two-step approach is that, unlike the radiative Dalitz approach, it is not fixed at the photon point (at small masses the dilepton spectrum is anyway dominated strongly by the π^0 Dalitz decay), but instead relies on 'hadronic' information (e.g. partial-wave analyses of $\pi N \to 2\pi N$ data). This means that it is 'anchored' prisely in that region of q^2, where it is expected to be most relevant, i.e. in the vector-meson mass region. The Dalitz description is worthless in that region without a proper form factor, and these form factors are often highly speculative and poorly constrained by data. Making the connection from the radiative decays $R \to \gamma N$ to the hadronic decays $R \to \rho N$ is a known problem, and has never been solved satisfactorily. We avoid this problem by fixing the resonance contributions in the relevant mass region. However, this also means that our resonance contributions are not expected to be reliable in the very low-mass region.

2.2.2.5   NN bremsstrahlung

In addition to the dilepton decay modes discussed in the previous sections, we include bremsstrahlung contributions from NN processes in phase-space corrected soft-photon approximation (SPA) [38, 102], which can be written as

$$\frac{\mathrm{d}\sigma_{pn \to pne^+e^-}}{\mathrm{d}M\mathrm{d}E\mathrm{d}\Omega} = \frac{\alpha^2}{6\pi^3}\frac{q}{ME^2}\bar{\sigma}(s)\frac{R_2(s_2)}{R_2(s)} \ , \tag{40}$$

$$\bar{\sigma}(s) = \frac{s - (m_1 + m_2)^2}{2m_1^2}\sigma_{el}(s) \ , \tag{41}$$

$$R_2(s) = \sqrt{1 - (m_1 + m_2)^2/s} \ , \tag{42}$$

$$s_2 = s + M^2 - 2E\sqrt{s} \ . \tag{43}$$

Here M is the mass of the dilepton pair, q, E and Ω are its momentum, energy and solid angle in the pn center-of-mass frame and s is the Mandelstam-s variable. Further, m_1 is the mass of the charged particle (proton), m_2 is the nucleon mass and σ_{el} is the elastic NN cross section.

pp bremsstrahlung cannot be treated in this simple approximation, since it involves a destructive interference between the graphs involved. Due to this interference it is much smaller than the pn bremsstrahlung and therefore is being neglected here. (Strictly speaking this is only true for low energies. At higher energies, however, bremsstrahlung is anyway outshined by other dilepton sources.)

Further we note that also the bremsstrahlung contribution involves a form factor, i.e. the time-like electromagnetic nucleon form factor. Just as the Δ transition form factor, it is not well-constrained in the time-like region and is often neglected in theoretical calculations. Event the recent effective-Lagrangian models, which describe the NN interaction by one-boson exchange (OBE), do not include a proper electromagnetic form factor for the nucleon [43, 44, 51].

Of course it is clear that the soft-photon approximation represents a simplifying assumption, and can only give an approximation to the full bremsstrahlung amplitude. One possible way to improve upon this treatment in the future, would be to use the OBE-model results from [44] or [51] as an input to our transport simulations. However, there are several things to take care of in such an approach. Most importantly, one has to be careful about double counting: The OBE model results usually contain resonance contributions, which are in principle already included in our model, however, in a different way. While in our approach the resonances only contribute to the dilepton spectrum through a ρN decay (which amounts to the assumption of strict VMD, cf. the discussion in the previous section), the OBE models assume that the resonances radiate off dilepton pairs without any form factor at the electromagnetic vertex. Due to this lack of an electromagnetic transition form factor for the resonances, the resonance contributions in the OBE models (see e.g. [43]) are expected to significantly underestimate the dilepton yield in the vector meson mass region.

If one wants to include NN bremsstrahlung results from an OBE model, one should not use those terms which include the excitation of an intermediate resonance (in order to avoid double counting), but only those with intermediate nucleon lines (which we will here

refer to as 'pure bremsstrahlung'). Also one loses interference terms in this procedure, which anyway are usually neglected in the transport approach.

Going even one step further, it should be possible to fully rely on an effective Lagrangian model for the complete description of dilepton production from NN collisions. Strictly speaking, this has never been accomplished yet. In the treatment of [43, 51], 'mesonic' contributions of π^0, η, ρ and ω have only been included in an inconsistent way by relying on input from transport models for their production cross sections etc.

However, in our resonance-model approach (which will be described in section 2.3.1), basically all π, η and ρ mesons are assumed to be produced via the production of baryonic resonances. Since such resonances are anyway included in the OBE models, it should in principle be possible to obtain the mesonic contributions consistently in the effective Lagrangian approach, instead of treating them as 'external' inputs to the model, which are added incoherently to the OBE results. An additional challenge would be the inclusion of the ω and ϕ mesons, for which the resonance couplings are not as clear.

If one had such a fully consistent OBE-model treatment for all processes, which contribute to dilepton production, it could in turn be fed back as input for the treatment of NN collisions in transport models. In this way one might even be able to include interference effects in the elementary reactions.

2.2.2.6 πN bremsstrahlung

Apart from NN bremsstrahlung, we also apply the soft-photon approximation of eq. (40) to πN bremsstrahlung, with $m_1 = m_\pi$ and $\sigma_{el} = \sigma_{el}^{\pi N}$.

While SPA is already a somewhat crude approximation for the NN case, there are additional issues with πN processes. In particular, the SPA ansatz uses the elastic cross section, which in the πN case is strongly dominated by resonance contributions ($\pi N \rightarrow R \rightarrow \pi N$). Since we already include such resonance contributions through the corresponding Dalitz decays, severe double-counting issues are expected.

Moreover, the 'lowest' dilepton contributions from πN collisions are not of elastic nature (as in $\pi N \rightarrow \pi N e^+ e^-$ in analogy to $NN \rightarrow NN e^+ e^-$), but instead of the form $\pi N \rightarrow N e^+ e^-$. While our model covers some of these via resonance production with a subsequent Dalitz decay, we miss others, e.g. those with an intermediate nucleon instead of a resonance, or t-channel type diagrams (for a more complete list see [103]). However, these missing diagrams are not well-represented by the SPA ansatz, since they do not have a lot in common with elastic πN scattering.

Moreover, it should be noted that our treatment of bremsstrahlung, just like the dilepton decays, is 'perturbative', in the sense that bremsstrahlung pairs are created at every elastic collision (with a corresponding perturbative weighting factors) and the collision kinematics is not altered by radiating off the lepton pair.

We will occasionally show πN bremsstrahlung contributions in the heavy-ion results (just for comparison), but we advise against taking them too serious (due to the problems mentioned). Further we note that currently the only effective-Lagrangian calculation of the process $\pi N \rightarrow e^+ e^- N$ available is the one from [103].

2.3 2-body collisions

The two-body part of the collision term is separated into two different regimes in terms of the available energy, $\sqrt{s}$: a resonance model description at low energies and the PYTHIA string model at high energies.

For baryon-baryon collisions, the transition between the two is usually performed at $\sqrt{s} = 2.6\,\text{GeV}$. There is a small window around this border ($\pm 0.2\,\text{GeV}$), where both models are merged linearly into each other in order to ensure a smooth transition. For meson-baryon collisions, the transition region lies at $\sqrt{s} = 2.2 \pm 0.2\,\text{GeV}$.

Unfortunately, the transition region in this default GiBUU prescription lies right inside the range of energies used for the HADES experiment. However, we think that it is important to describe all HADES spectra with one consistent model. In this thesis we therefore explore the possibility of pushing the transition region up to higher energies and using an extended resonance model for all reactions measured by HADES.

In the high-energy regime the GiBUU collision term relies on the Monte Carlo event generator PYTHIA (v6.4) [104, 105], which is based on the Lund string model. Although PYTHIA clearly has its strengths at higher energies (tens to hundreds of GeV), it is used in GiBUU down to energies of a few GeV. This works surprisingly well, as has recently been demonstrated for example by GiBUU's successful description of pion data measured by the HARP collaboration [106].

Despite this good description of pion observables in the few-GeV energy regime, it turned out that the HADES dilepton data for p+p collisions at 3.5 GeV pose a somewhat greater challenge for PYTHIA [107]. Most prominently, the vector-meson production is strongly overestimated by the default PYTHIA parameters, and also the intrinsic p_T distribution needs to be adjusted slightly to reproduce the HADES p_T spectra. In [107], a set of parameters has been proposed, which improve the PYTHIA-based simulations at 3.5 GeV (which we will also discuss later on in section 3.1.4). Unfortunately, such a tuning is expected to be energy-dependent, and the need for tuning shows that the string-model description starts to fail at low energies.

On the other hand, a resonance description should in principle be applicable in the whole energy regime probed by the HADES experiment ($\sqrt{s} \lesssim 3.2\,\text{GeV}$), we try in the following to set up such a description as an alternative to the string-model approach.

2.3.1 NN

The low-energy part of the nucleon-nucleon collision term is given by a resonance model based on the Teis analysis [108], in which all collision cross sections are assumed to be dominated by the excitation of baryon resonances. The GiBUU model currently contains around 30 nucleon resonances, for a complete list see [61]. However, only the subset used in the Teis analysis is actually being populated in NN collisions, see table 3. The properties (masses, widths and branching ratios) of all the resonances are taken from the partial-wave analysis of Manley [74]. All of these states, except for the $P_{33}(1600)$, are not only found in the Manley analysis, but have been confirmed, e.g., by the more recent analysis of Arndt et al. [109] and received a four-star rating from the PDG [78].

The resonance model used in this work is based on the Teis model, but modifies and extends it in several aspects [110]. We take into account the following nucleon-nucleon scattering channels:

	M_0 [MeV]	Γ_0 [MeV]	$\|\mathcal{M}^2\|/16\pi\ [\mathrm{mb\,GeV^2}]$	
			NR	ΔR
$P_{11}(1440)$	1462	391	70	—
$S_{11}(1535)$	1534	151	8	60
$S_{11}(1650)$	1659	173	4	12
$D_{13}(1520)$	1524	124	4	12
$D_{15}(1675)$	1676	159	17	—
$P_{13}(1720)$	1717	383	4	12
$F_{15}(1680)$	1684	139	4	12
$P_{33}(1232)$	1232	118	OBE	210
$S_{31}(1620)$	1672	154	7	21
$D_{33}(1700)$	1762	599	7	21
$P_{31}(1910)$	1882	239	14	—
$P_{33}(1600)$	1706	430	14	—
$F_{35}(1905)$	1881	327	7	21
$F_{37}(1950)$	1945	300	14	—

Table 3: Resonance parameters according to Manley [74] (columns 2 and 3), together with matrix elements for production in pp collisions (columns 4 and 5).

1. $NN \to NN$

2. $NN \to N\Delta$,

3. $NN \to NN^*,\ N\Delta^*$,

4. $NN \to \Delta\Delta$,

5. $NN \to \Delta N^*,\ \Delta\Delta^*$,

6. $NN \to NN\pi$ (non-res. BG)

7. $NN \to NN\omega,\ NN\pi\omega,\ NN\phi$ (non-res.),

8. $NN \to BYK$ (with $B = N, \Delta;\ Y = \Lambda, \Sigma$).

For the elastic cross sections (first item), we rely on the parametrizations by Cugnon et al. [111] (for beam momenta below $p_\mathrm{lab} \approx 2.776\,\mathrm{GeV}$) and the PDG [112] (above):

$$\sigma_\mathrm{el}^{pp} = \begin{cases} 5.12 m_N/(s - 4m_N^2) + 1.67 & \text{for } p_\mathrm{lab} < 0.435 \\ 23.5 + 1000(p_\mathrm{lab} - 0.7)^4 & \text{for } 0.435 < p_\mathrm{lab} < 0.8 \\ 1250/(p_\mathrm{lab} + 50) - 4(p_\mathrm{lab} - 1.3)^2 & \text{for } 0.8 < p_\mathrm{lab} < 2 \\ 77/(p_\mathrm{lab} + 1.5) & \text{for } 2 < p_\mathrm{lab} < 2.776 \\ 11.9 + 26.9 p_\mathrm{lab}^{-1.21} + 0.169 \log(p_\mathrm{lab})^2 - 1.85 \log(p_\mathrm{lab}) & \text{for } 2.776 < p_\mathrm{lab} \end{cases} \quad (44)$$

$$
\sigma_{\mathrm{el}}^{pn} = \begin{cases} 17.05 m_N/(s - 4m_N^2) - 6.83 & \text{for } p_{\mathrm{lab}} < 0.525 \\ 33 + 196|p_{\mathrm{lab}} - 0.95|^{2.5} & \text{for } 0.525 < p_{\mathrm{lab}} < 0.8 \\ 31/\sqrt{p_{\mathrm{lab}}} & \text{for } 0.8 < p_{\mathrm{lab}} < 2 \\ 77/(p_{\mathrm{lab}} + 1.5) & \text{for } 2 < p_{\mathrm{lab}} < 2.776 \\ 11.9 + 26.9 p_{\mathrm{lab}}^{-1.21} + 0.169 \log(p_{\mathrm{lab}})^2 - 1.85 \log(p_{\mathrm{lab}}) & \text{for } 2.776 < p_{\mathrm{lab}} \end{cases} \tag{45}
$$

Here, the beam momentum p_{lab} is given in GeV, just as the nucleon mass m_N and the invariant energy $\sqrt{s}$, with $s = 2m_N^2 + 2m_N\sqrt{m_N^2 + p_{\mathrm{lab}}^2}$. The cross sections are given in mb.

The single-resonance excitation channels (items 2 and 3) were already included in the Teis analysis. While the $N\Delta$ channel is treated by an OBE model according to Dmitriev et al. [79], the higher resonances are produced in a pure phase-space approach with constant matrix elements,

$$
\sigma_{NN \to NR} = \frac{C_I}{p_i s} \frac{|\mathcal{M}_{NR}|^2}{16\pi} \int \mathrm{d}\mu \mathcal{A}_R(\mu) p_F(\mu). \tag{46}
$$

Here, p_i and p_F denote the center-of-mass momenta in the initial and final state, respectively. The matrix elements, $\mathcal{M}_{NR}$, have previously been fitted by Teis to exclusive meson production (π, 2π, η and ρ). Our values are listed in tab. 3. $\mathcal{A}_R$ denotes the resonance spectral function,

$$
\mathcal{A}_R(\mu) = \frac{2}{\pi} \frac{\mu^2 \Gamma_R(\mu)}{(\mu^2 - M_R^2)^2 + \mu^2 \Gamma_R^2(\mu)} . \tag{47}
$$

In principle all production channels are assumed to be isospin-symmetric, with the Clebsch-Gordan factors, C_I, resulting from this symmetry. The only exception from this isospin symmetry is the $S_{11}(1535)$ resonance: The exclusive η production, which is assumed to proceed exclusively via this resonance, is known to be significantly larger for pn than for pp [113], therefore we use

$$
|\mathcal{M}_{pn \to NN^*(1535)}|^2 = 6.5 \cdot |\mathcal{M}_{pp \to NN^*(1535)}|^2. \tag{48}
$$

Note that while the $S_{11}(1535)$ is known to dominate the η production in pp at low energies, there may of course be other contributions [114].

The single-pion production cross section cannot be described satisfactorily by resonance contributions alone, and one has to add a non-resonant background term [61,108] (slightly refitted here), whose largest contributions appear on the left-hand shoulder of the $N\Delta$ peak.

Most of the resonance-production matrix elements are adopted from Teis. However, me make a few modifications. In particular we reduce the contributions of the $D_{15}(1675)$, $P_{31}(1910)$ and $P_{33}(1600)$, which were extremely large in the Teis analysis, in favor of the $P_{11}(1440)$ and double-Δ contributions. This gives an improved threshold behavior of the 2π production channels (in line with the analysis of Cao et al. [115]), as well as a better agreement with the inelastic nucleon-nucleon cross sections, cf. fig. 10.

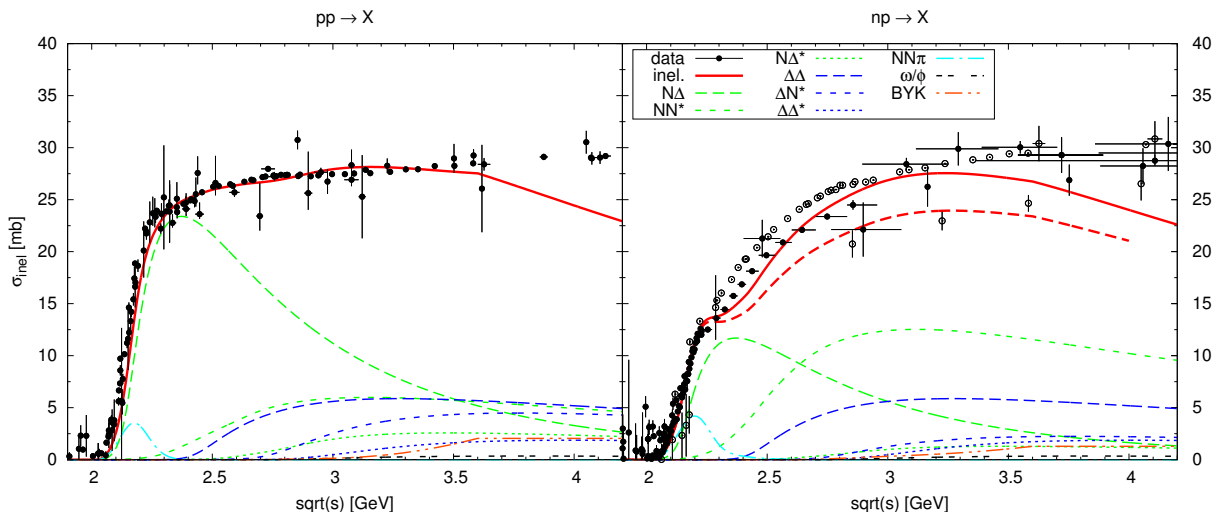Furthermore, we add another isospin-asymmetry factor for the $P_{11}(1440)$ state:

Figure 10: Inelastic pp and pn cross sections in the resonance model. The data points shown here have been obtained by subtracting the parametrized elastic cross section from the total cross section data [95]. The red dashed line denotes the inelastic np cross section without the isospin factor of eq. (49).

$$|\mathcal{M}_{pn \to NN^*(1440)}|^2 = 2 \cdot |\mathcal{M}_{pp \to NN^*(1440)}|^2. \tag{49}$$

This is done in order to improve the agreement with the np inelastic cross section data, which would otherwise be underestimated significantly (the dashed red line in fig. 10 shows the inelastic np cross section without this factor).

In order to go beyond the simple phase-space approximation, we have also introduced angular distributions for the resonance production according to

$$\frac{\mathrm{d}\sigma}{\mathrm{d}t} = \frac{b}{t^a}, \tag{50}$$

where we assume $a = 1$, motivated by t-channel exchange. Recently an effort has been started to experimentally determine the angular distribution of resonance production from HADES data, which has confirmed the validity of the t^{-a} form, with values of a close to one [116].

Also the double-resonance production (items 4 and 5), which in the Teis model was limited to $\Delta\Delta$, is performed in a phase-space approach, analogous to the single-resonance excitation:

$$\sigma_{NN \to \Delta R} = \frac{C_I}{p_i s} \frac{|\mathcal{M}_{\Delta R}|^2}{16\pi} \int \mathrm{d}\mu_1 \mathrm{d}\mu_2 \mathcal{A}_\Delta(\mu_1) \mathcal{A}_R(\mu_2) p_F(\mu_1, \mu_2). \tag{51}$$

Here one integrates over the spectral functions of both resonances ($\mu_{1,2}$ being their masses). In the Teis analysis, the production mechanisms were restricted to $NN \to NR$ and $NN \to \Delta\Delta$, so the obvious extension candidate would be general double-resonance excitation channels ($NN \to R_1 R_2$). The channels taken into account by Teis were fitted to single- and double-pion production data. Therefore his model is only guaranteed to work in the low-energy region. At higher energies, the model starts to fail, since the more inclusive

multi-meson final states are not included. If we want to describe NN collisions in the HADES energy regime of $\sqrt{s} \approx 2.4 - 3.2\,\text{GeV}$ with a resonance model, we clearly need to extend the Teis approach. We do this by restricting ourselves to the same set of resonances (cf. tab. 3), but extending the production mechanisms.

Since Teis already describes the exclusive π, 2π, ρ and η production, what is missing are channels like e.g. $\pi\eta$, $\pi\rho$, 3π, 2η, 2ρ, etc. Unfortunately there are almost no experimental data available for these channels. We thus have to rely on the cross sections obtained from Pythia as an estimate to fix these channels. According to Pythia, the inclusive ρ and η production is in fact dominated by the channels $\pi\rho$ and $\pi\eta$, respectively, at the highest HADES energy of $\sqrt{s} \approx 3.2\,\text{GeV}$. Therefore we concentrate on these two for now, and neglect all others. Our strategy to satisfy these channels relies on double-resonance excitation, $NN \to \Delta R$, where the Δ decays into πN, while the other resonance R will be one with an ηN or ρN decay channel, so that we end up with a $\pi\eta$ or $\pi\rho$ final state (note that we do not include cascade decays of single resonances into $\pi\eta N$, as treated for example in [117], since our model misses the corresponding decays modes, such as $\eta\Delta$). We add three new classes of production channels:

i) $NN \to \Delta S_{11}(1535)\ (\to NN\pi\eta)$,

ii) $NN \to \Delta N^*\ (\to NN\pi\rho)$,
    $N^* = D_{13}(1520), S_{11}(1650), F_{15}(1680), P_{13}(1720)$,

iii) $NN \to \Delta\Delta^*\ (\to NN\pi\rho)$,
    $\Delta^* = S_{31}(1620), D_{33}(1700), F_{35}(1905)$.

For each of these we need one new parameter, namely the matrix elements, $|\mathcal{M}_1|^2/16\pi = 60\,\text{mb}\,\text{GeV}^2$, $|\mathcal{M}_2|^2/16\pi = 12\,\text{mb}\,\text{GeV}^2$ and $|\mathcal{M}_3|^2/16\pi = 21\,\text{mb}\,\text{GeV}^2$, as listed in tab. 3. As mentioned before, we fix the matrix elements to roughly fit the Pythia cross sections for $\pi\eta$ and $\pi\rho$ production (with further constraints from the total pp cross section as well as the HADES dilepton data). As for the exclusive production, we assume that the η meson is produced exclusively via the $S_{11}(1535)$, while the ρ production proceeds via a number of N^* and Δ^* resonances. It should be noted that the new channels will not affect the exclusive meson production fitted by Teis, except for the 2π channel, which gets minor contributions from these channels.

The production of ω and ϕ mesons is not carried out via baryonic resonances in our model (although a coupling of the ω to nucleon resonances has been reported for example in [75, 118–120]). Instead, their production cross sections are parametrized in a phenomenological manner [121]:

$$\sigma(pp \to ppV) = a(1-x)^b x^c, \quad \text{with } x = s_0/s. \tag{52}$$

Here $s_0 = (2m_N + m_V)^2$ is the threshold energy, and the parameters a, b and c are listed in table 4. We use this parametrization not only for exclusive ω and ϕ production, but also for $NN \to NN\pi\omega$. Since there are no data available for this channel, we fitted its parameters to the Pythia results.

As seen in fig. 10, we achieve a good agreement with data for the inelastic pp cross section up to about $\sqrt{s} = 3.5\,\text{GeV}$. At higher energies, 3π and 4π production becomes important (which is underestimated by our model), as well as other channels which we

	$\sqrt{s_0}$ [GeV]	a [mb]	b	c	Ref.
ω	2.658	5.3	2.3	2.4	[122]
$\pi\omega$	2.796	1.0	1.5	1.1	-
ϕ	2.895	0.01	1.26	1.66	[123]

Table 4: Parameters for vector-meson production.

miss completely. In the np cross section there are minor deviations, and unfortunately also the quality of the data is not quite as good as for pp.

The extended resonance model presented here allows to increase the string threshold for baryon-baryon collisions from the old value of $\sqrt{s} = 2.6 \pm 0.2$ GeV to $\sqrt{s} = 3.4 \pm 0.1$ GeV, which has been adopted as a new default value in the GiBUU model by now.

Some improvements of the NN resonance model, which might be implemented in the future, could involve things like

- an improved s-dependence of the cross sections (beyond the simple phase-space approximation) or even a full OBE-model calculation of the elementary production processes and

- more non-resonant background channels. For example it is known that the η production in pp collisions does not purely proceed via the $N^*(1535)$, as assumed in our simulation, but up to 50% come from other contributions (like non-resonant terms or higher resonances) [114, 124]. However, we note that the coupling of the $NN\eta$ vertex itself is known to be small [125–128]. Furthermore, non-resonant contributions could also play a role for the ρ meson, in particular in pn collisions, as suggested by recent OBE calculations [51].

2.3.1.1   Pion production

As a further benchmark to evaluate the performance of the resonance model, we compare the single- and double-pion production cross sections to experimental data. Fig. 11 shows the exclusive pion production cross section as a function of energy for the different isospin channels. The pp channels show a reasonable agreement with the data. For $pn \to pn\pi^0$, unfortunately only data at threshold energies are available, which, however, are also well described. For all four channels it is necessary to introduce a non-resonant background contribution, which is given by the difference of the experimental data and the resonance contributions. This background contribution is restricted to the threshold region and only gives a minor correction to the resonance contributions. We use the same parametrization for the background as in [108],

$$\sigma_{NN \to NN\pi}(x) = A x^{n_1} e^{-(a x^{n_2} + b x)},$$

with $x = (\sqrt{s} - \sqrt{s_0}) \cdot 5/GeV$ and $\sqrt{s_0} = m_N + m_\pi$, but with refitted parameters (see table 5).

For the last channel, $pn \to pp\pi^-$, the agreement in the treshold region is good, but some deviations appear at higher energies. However, we note that the cross sections in
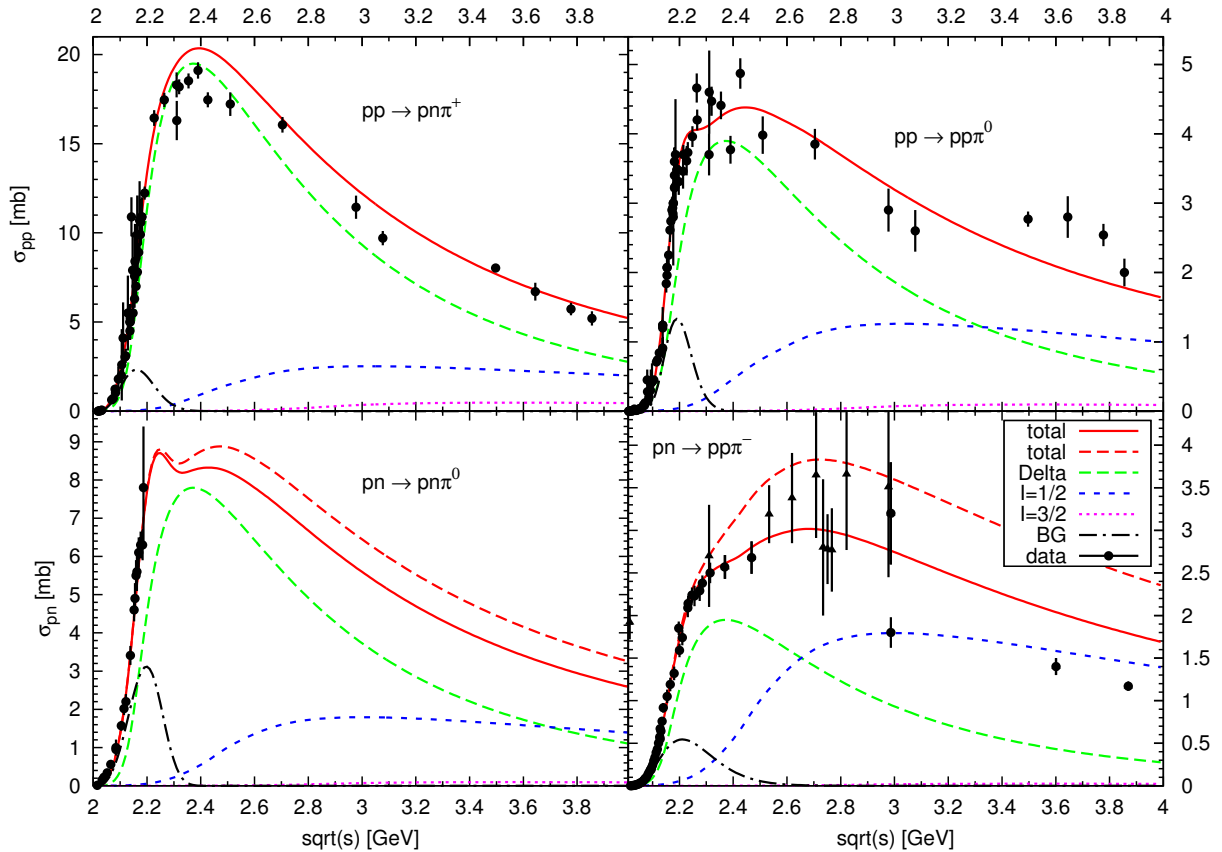
Figure 11: Single pion production cross sections. Data from [129].

this channel are smaller than in the other three, therefore the deviation here is not very large in absolute terms. Also the data which is available for this channel is only of good quality at threshold, while at higher energies the error bars are large and some data points even seem to be in conflict with each other. Therefore it's not really clear whether the agreement gets better or worse when using the isospin factor for the Roper resonance (shown by the dashed red line), which was introduced to get a good description of the total cross section.

channel	A [mb]	n_1	a	n_2	b
$pp \to pp\pi^0$	14.4301	6.32665	19.8245	1.28221	-17.3336
$pn \to pp\pi^-$	36.8751	4.08966	16.8907	0.997063	-12.6746
$pn \to pn\pi^0$	7.25069	2.306925	0.883237	3.641924	$6.6390312 \cdot 10^{-5}$
$pp \to pn\pi^+$	6.17963	2.22284	4.96358	1.66218	-3.65066

Table 5: Parameters of the 1π background parametrization.

The two- and three-pion production cross sections from pp and pn are shown in Fig. 12. Here the data situation is even worse than in the single-pi case. For several channels, no data is available at all, while for others it is rather scarce. The only channel which allows for a proper evaluation of the $\sqrt{s}$ dependence is the $\pi^+\pi^-$ final state. Here the model's overall agreement with the data is roughly ok, although at threshold the data tend to be
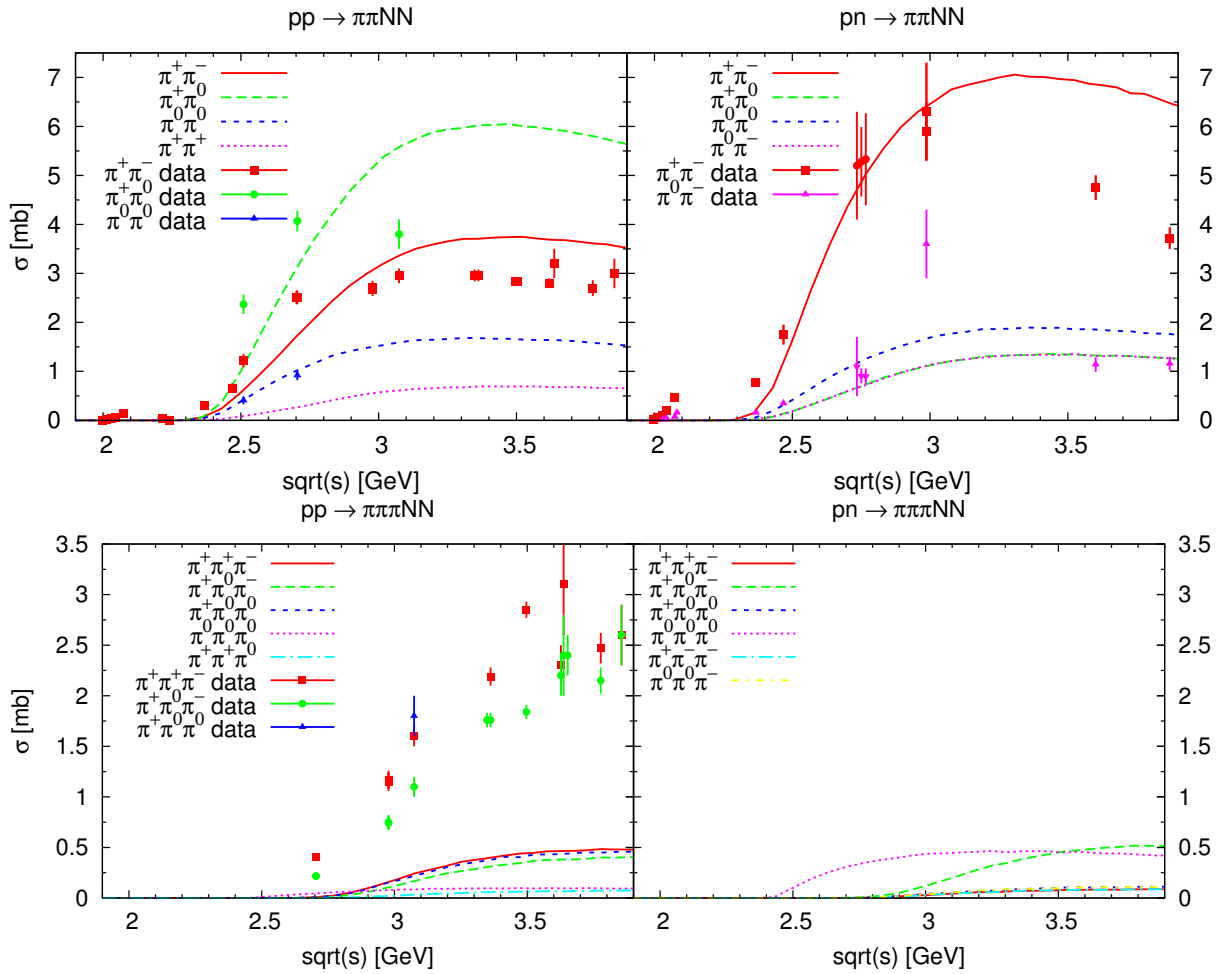
Figure 12: Double and triple pion production cross sections. Data from [129].

underestimated, while at higher energies it is slightly overestimated.

In the three-pi case, data is only available for pp collisions, but not for pn. As expected, our model underestimates the data quite strongly (by factors of 4 to 5). We remind of the fact that the Manley PWA did not include any 3π production data, and the few 3π decay channels included in the model were merely used as background parametrizations.

2.3.1.2   Delta production

Since the Δ Dalitz contribution to the dilepton spectra is a much-debated issue, we investigate here more closely the Δ production cross sections in NN collisions in different models.

Although the inclusive Δ production cross section is not that well known experimentally, one can get constraints from data for the exclusive cross section $pp \to \Delta^+ p$, cf. fig. 13, as well as the inclusive one at lower energies (where it is fixed via pion production).

Fig. 13 shows the exclusive and inclusive production cross sections for all Δ charge states in pp and pn collisions as a function of energy. We compare three models: 1) The GiBUU resonance model, as described in the preceding sections, 2) the PYTHIA string fragmentation model (Version 6.4, as included in GiBUU) and 3) the FRITIOF model
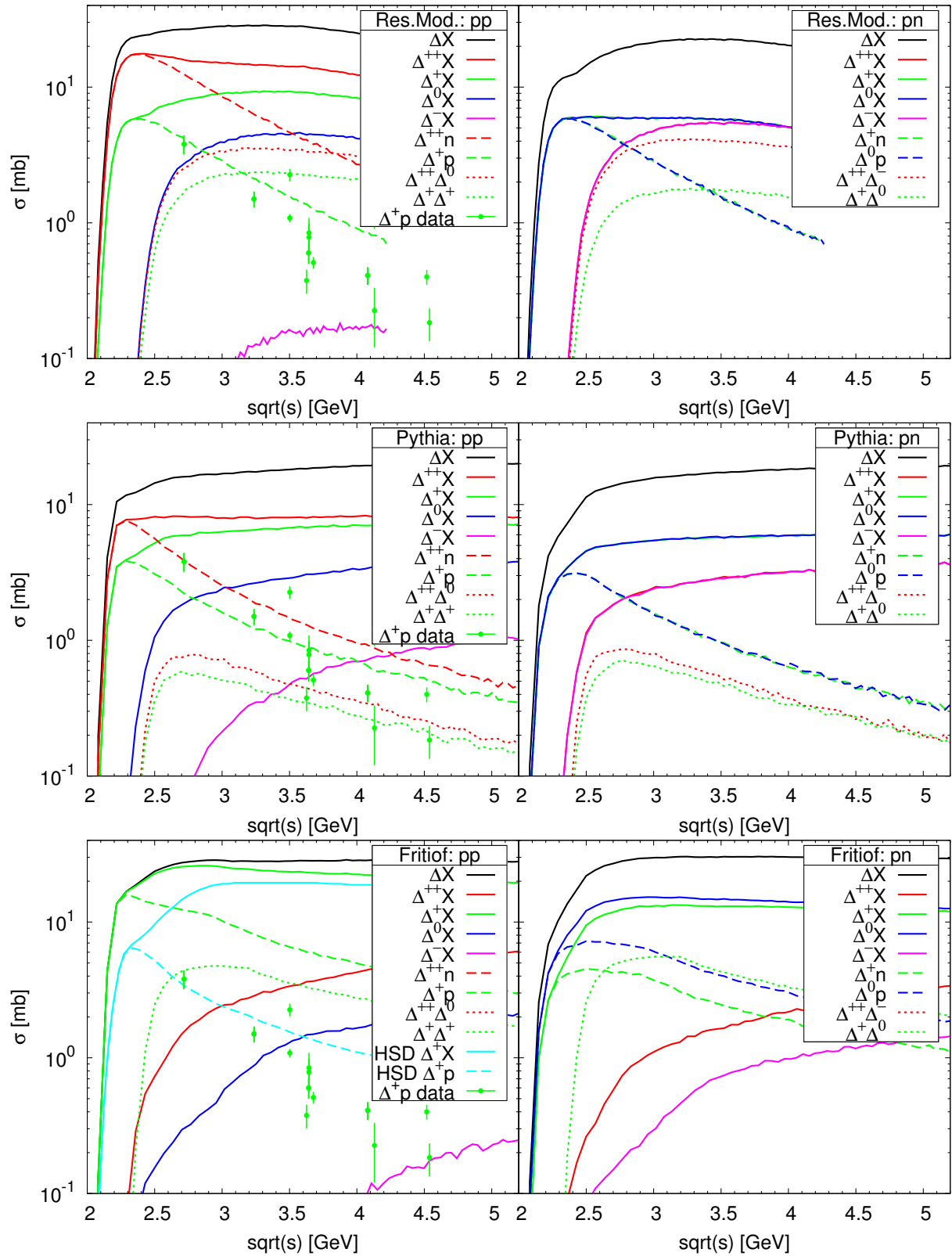
Figure 13: Inclusive and exclusive Δ production cross sections from *pp* and *pn* collisions in different models (GiBUU resonance model, PYTHIA 6.4 and FRITIOF 7.02), compared to data from [129].

(version 7.02, based on PYTHIA 5.5 and JETSET 7.1). For the Δ^+ production, we also show the HSD results as published in [53].

While the total inclusive Δ production cross section (for all charge states), is at least roughly similar in all three models, it is apparent that some of the models deviate quite strongly from each other in the decomposition into different channels and charge states. In particular, FRITIOF is completely missing exclusive Δ^{++} production, which at threshold is known to dominate the total pp cross section. On the other hand, the Δ^+ production is strongly overestimated by FRITIOF.

This shows that FRITIOF does not at all respect the proper isospin relations. Isospin symmetry demands for exclusive Δ production that

$$\sigma(pp \to \Delta^{++}n)/\sigma(pp \to \Delta^+ p) = 3,$$

cf. also section 2.3.1.4. This relation is fulfilled by construction in our resonance model. However, for FRITIOF this ratio is exactly zero, while PYTHIA does somewhat better and yields values between 1 and 2. But after all, both PYTHIA and FRITIOF are certainly not suited for exclusive particle production at threshold energies. They are high-energy models, which show their full strengths only in high-multiplicity events, and loose their validity in the threshold region.

However, the low-energy misbehavior of FRITIOF can supposedly explain (at least partially) the overestimation of Δ production in the HSD transport model, which relies on FRITIOF for all baryon-baryon collisions above $\sqrt{s} = 2.6\,\text{GeV}$ [53]. Since only the Δ^+ contributes to dilepton production, but not the Δ^{++}, the violation of the isospin relations is particularly severe. According to [53], the isospin decomposition of the FRITIOF model has been improved in HSD. But apparently this a-posterieri fix solves the problem only partially: While the exclusive production indeed seems to be improved over the original FRITIOF result, the inclusive Δ production is still significantly larger than in both PYTHIA and the GiBUU resonance model. In [53] only the correction of the exclusive $NN \to N\Delta$ channel is mentioned, but apparently no correction of $NN \to \Delta\Delta$ is done, which, as fig. 13 shows, gives major contributions in Fritiof and seems to be the main source for the discrepancy in the inclusive Δ^+ production cross section.

2.3.1.3   Strangeness production

As mentioned before, strangeness production in NN collisions proceeds through the channels $NN \to BYK$ with $B = N, \Delta$, $Y = \Lambda, \Sigma$ and $K = K^+, K^0$. In the present implementation the cross sections for all of these channels are taken from Tsushima et al. [130]. As seen in fig. 10, they only account for a small part of the total NN cross section, and are somewhat decoupled from the 'non-strange' part of the resonance model, in the sense that they are given by independent parametrizations.

These parametrizations, however, are at least inspired by the resonance-model idea: They are based on an effective-Lagrangian model, where the Kaon production is assumed to proceed via resonance formation, $NN \to NR$, with the resonance $R = N^*, \Delta^*$ subsequently making a decay $R \to YK$. The cross sections resulting from this model are then parametrized by functions $\sigma(s) = a(s/s_0 - 1)^b (s_0/s)^c$ for easier implementation in transport models, where s_0 is the threshold for the particular reaction and the parameters a, b, c are fitted separately for each channel.

Tsushima et al. use four intermediate resonances: $N^*(1650)$, $N^*(1710)$, $N^*(1720)$ and $\Delta^*(1920)$. The branching ratios for the YK decays are taken from the PDG. All of those resonances are also included in GiBUU with parameters from the Manley PWA. However, the Manley analysis did not include any $K\Sigma$ channels, and only the $N^*(1710)$ has a non-vanishing branching ratio into $K\Lambda$.
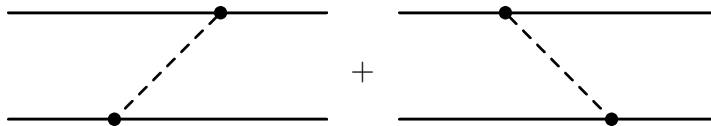
2.3.1.4   Isospin factors

The default isospin factors for baryon-baryon scattering ($B_1 B_2 \to B_3 B_4$) in the GiBUU model are based on a simple "s-channel" picture, where the incoming baryons with isospins (i_1, m_1) and (i_2, m_2) couple to a ("di-baryon") state of total isopin (I, M), where $M = m_1 + m_2$, which then in turn couples to the outgoing baryons with isospin (i_3, m_3) and (i_4, m_4). The corresponding isospin factors can be calculated via Clebsch-Gordan coefficients as (cf. equ. (A.5) in [66]):

$$C = \sum_I |\langle i_1, m_1; i_2, m_2 | I, M \rangle|^2 \cdot |\langle i_3, m_3; i_4, m_4 | I, M \rangle|^2 \tag{53}$$
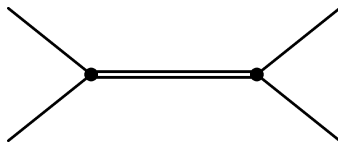
This is certainly the most straightforward approach for determining isospin factors for baryon-baryon scattering. However, it does not correspond well to the underlying physical model of how the scattering process proceeds: This is typically given by one-boson-exchange (OBE) models, which involve t- and u-channel-type graphs. With such a model, one gets a different set of isospin factors, based on the exchange of an intermediate pion with isospin $(1, m_\pi)$, with $m_\pi = m_2 - m_4 = m_3 - m_1$:

$$
\begin{aligned}
C =& |\langle i_1, m_1; 1, m_\pi | i_3, m_3 \rangle|^2 \cdot |\langle i_4, m_4; 1, m_\pi | i_2, m_2 \rangle|^2 \\
&+ |\langle i_3, m_3; 1, -m_\pi | i_1, m_3 \rangle|^2 \cdot |\langle i_2, m_2; 1, -m_\pi | i_4, m_4 \rangle|^2 + (1 \leftrightarrow 2)
\end{aligned} \tag{54}
$$

A similar approach has been taken in ref. [66] with equ. (A.16) in the context of strangeness production.

Table 6 summarizes the isospin factors for $NN \to X$ in both models. The OBE factors have been normalized such that they match the s-channel ones for the pp cases. It is apparent that the factors from both models are completely identical for $NN \to N\Delta$

		s-channel		OBE	
$NN \to NN$	$pp \to N^+N^+$	1		1	
	$pn \to N^+N^0$	1		$5/2$	
$NN \to N\Delta$	$pp \to \Delta^{++}N^0$	$3/4$	$\left.\right\}1$	$3/4$	$\left.\right\}1$
	$\to \Delta^+N^+$	$1/4$		$1/4$	
	$pn \to \Delta^+N^0$	$1/4$	$\left.\right\}1/2$	$1/4$	$\left.\right\}1/2$
	$\to \Delta^0N^+$	$1/4$		$1/4$	
$NN \to \Delta\Delta$	$pp \to \Delta^{++}\Delta^0$	$6/10$	$\left.\right\}1$	$6/14$	$\left.\right\}1$
	$\to \Delta^+\Delta^+$	$4/10$		$8/14$	
	$pn \to \Delta^{++}\Delta^-$	$7/10$	$\left.\right\}1$	$9/14$	$\left.\right\}1$
	$\to \Delta^+\Delta^0$	$3/10$		$5/14$	

Table 6: Isospin factors for $NN \to X$ in a s-channel and OBE approach. Here, N indicates any $I = 1/2$ state, while Δ indicates any $I = 3/2$ state.

reactions. For $NN \to \Delta\Delta$, the pn/pp ratios are also equal (i.e. unity), but the factors for charge assignment in the final state differ.

The only channel where the pn/pp ratio actually differs is $NN \to NN$. Here, the OBE model strongly enhances the cross section in pn (by a factor 2.5). This directly leads to a stronger production of N^* resonances in pn collisions (via $NN \to NN^*$) and can provide a justification for the enhancement factor we had to introduce for $pn \to NN^*(14440)$, as well as the enhanced η production in pn collisions (due to enhanced $N^*(1535)$ production). It can also help to explain the large isospin enhancement factors that were seen e.g. in DLS dilepton data at low energies [17]. In particular it will enhance the ρ production on the neutron through $pn \to NN^* \to NN\rho$, which will improve the agreement with the HADES data for dp at 1.25 GeV (but can probably not explain all of the underestimation seen there).

All results presented in this thesis are based on the s-channel factors for now, but the use of OBE-type factors should be investigated more closely in the future.

2.3.2   Meson-baryon collisions

In this section we discuss a few selected meson-baryon cross sections, concentrating on those that are most relevant for our work, namely πN, ωN and ρN.

2.3.2.1 πN

The πN cross section at low energies is dominated by resonance production. The production cross section for $a\, b \to R$ is given by the Breit-Wigner formula,

$$\sigma_{a\,b\to R}(s) = F_I \frac{2J_R+1}{(2J_a+1)\,(2J_b+1)} \frac{1}{\mathcal{S}_{ab}} \frac{4\pi}{p_{ab}^2(s)} \sum_f \frac{s\,\Gamma_{ab\to R}(s)\,\Gamma_{R\to f}(s)}{(s-m_R^2-\mathrm{Re}\,\Pi(s))^2 + s\Gamma_{\mathrm{tot}}^2(s)}$$

$$= F_I \frac{2J_R+1}{(2J_a+1)\,(2J_b+1)} \frac{1}{\mathcal{S}_{ab}} \frac{4\pi}{p_{ab}^2(s)} \frac{s\,\Gamma_{ab\to R}(s)\,\Gamma_{tot}(s)}{(s-m_R^2-\mathrm{Re}\,\Pi(s))^2 + s\Gamma_{tot}^2(s)} \tag{55}$$

with

$$\mathcal{S}_{ab} = \begin{cases} 1 & \text{if a,b not identical} \\ \frac{1}{2} & \text{if a,b identical} \end{cases} \tag{56}$$

denoting the symmetry factor of a and b. The term p_{ab} denotes the c.m. momentum of particles a and b, the J_i's define the total spin of the particles and

$$F_I = \left\langle I^a\,I_z^a; I^b\,I_z^b | I^R\,I_z^a + I_z^b \right\rangle^2 \tag{57}$$
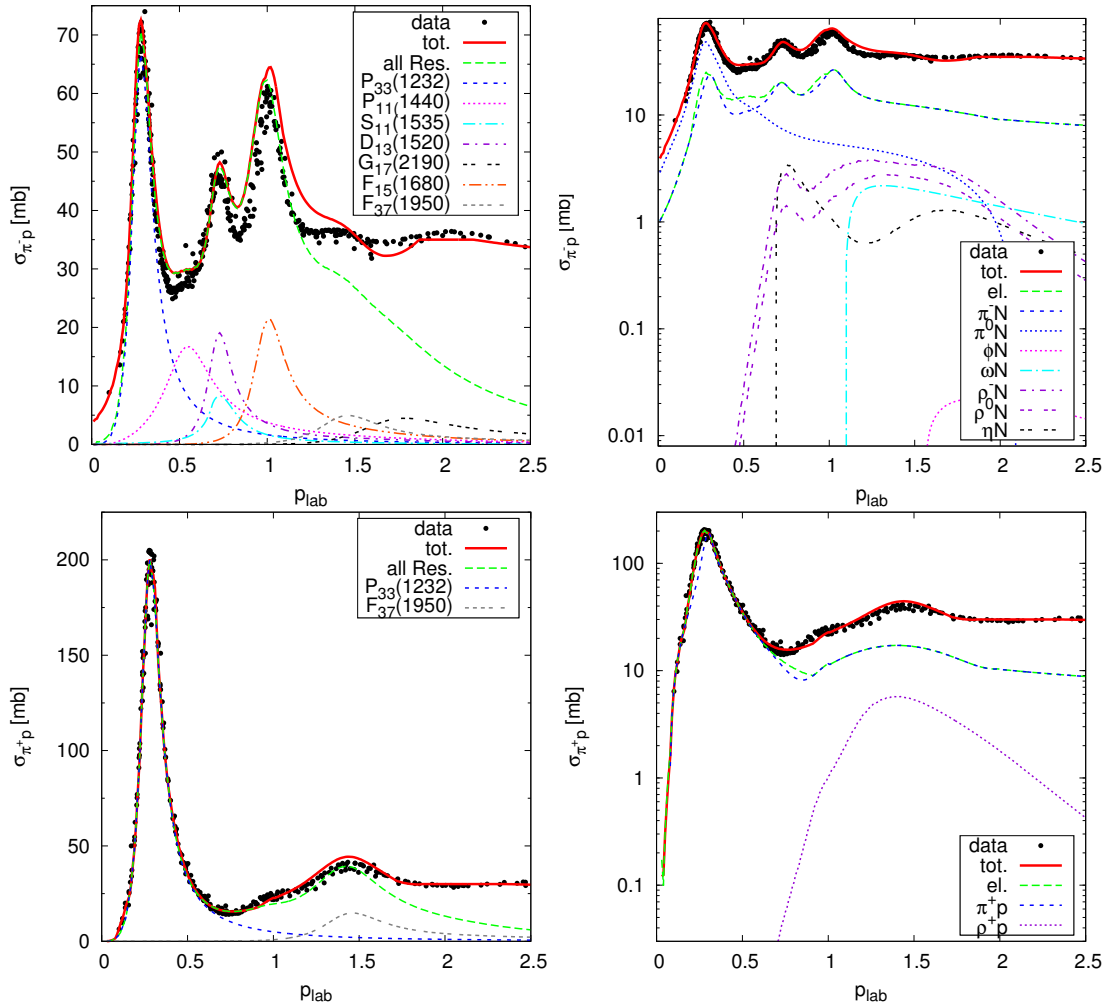
Figure 14: Total π^-p (top) and π^+p (bottom) collision cross section. Data from [78].

are the isospin Clebsch-Gordan coefficients squared. The term, $\Gamma_{ab \to R}$, denotes the so-called in-width. For stable particles a and b it is identical to the out-width $\Gamma_{R \to ab}$; for unstable particles the final result is given in [66] (Eq. (2.77)).

Fig. 14 shows the total $\pi^- p$ and $\pi^+ p$ cross sections in comparison to the data from [78]. While the left-hand side shows the cross section on a linear scale with the contributions of the most important resonances, the right-hand side uses a logarithmic scale and shows several different meson production channels (most of which are dominated by intermediate baryon-resonance production). As the figures show, the agreement with the data points is not perfect everywhere, but the deviations do not exceed the 10% level.

The pion-induced ρ production exclusively proceeds via resonance formation ($\pi N \to R \to \rho N$) and can be evaluated with the Breit-Wigner formula given above as a sum of all individual resonance contributions. The parametrizations for pion-induced ω production, $\pi N \to \omega X$, are adopted from Effenberger [66].

2.3.2.2 ωN

The absorption and rescattering of ω mesons in nuclear matter proceeds via the channels

$$
\begin{aligned}
\omega N &\to \omega N, \\
&\to \pi N, \\
&\to 2\pi N, \\
&\to R
\end{aligned}
$$

(where R is a nucleon resonance). The parametrizations of the elastic and inelastic collisions are taken from [131]:

$$\sigma_{\omega N}^{inel} = 20 + 4.0/p_\omega \, [\,\text{mb}\,] \, , \tag{58}$$

$$\sigma_{\omega N}^{el} = 5.4 + 10 exp(-0.6 p_\omega) \, [\,\text{mb}\,] \, . \tag{59}$$

Here, p_ω is the ω momentum in the lab frame (in GeV). For the elastic process, there can be contributions from resonance excitations, which we subtract from the parametrization, in order to get the elastic cross section from the non-resonant background.

The $\omega N \to \pi N$ cross section is obtained from the inverse reaction via detailed balance,

$$\sigma_{\omega N \to \pi N} = \frac{1}{3} \frac{p_f^2}{p_i^2} \sigma_{\pi N \to \omega N}, \tag{60}$$

where p_i and p_f are the center-of-mass momenta in the initial and final state, and $\frac{1}{3}$ is a spin factor. As in the elastic case, $\omega N \to \pi N$ can also have resonance contributions, which need to be subtracted to avoid double counting. However, these resonance contributions are not very large for ωN scattering, since the Manley analysis contains only two resonances which have an ωN decay mode: $P_{13}(1900)$ and $G_{17}(2190)$.

The missing inelasticity, which is not covered by the πN channel, is put in the $2\pi N$ channel by assuming
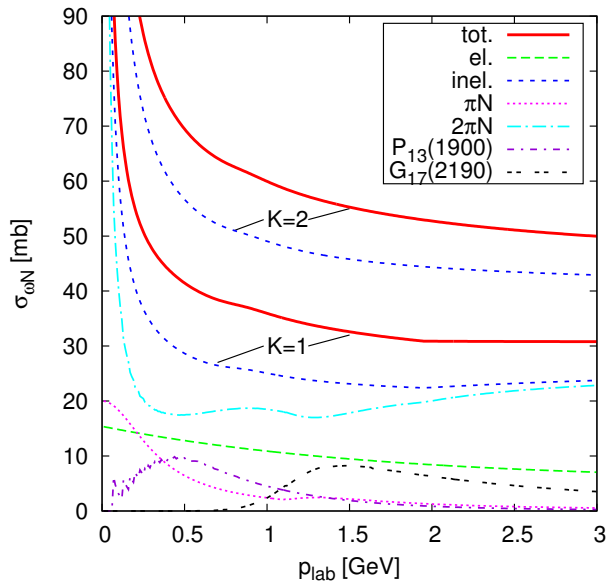
Figure 15: Total ωN collision cross section for K=1 and K=2.

$$\sigma_{\omega N \to 2\pi N} = \sigma_{\omega N}^{inel} - \sigma_{\omega N \to \pi N}. \tag{61}$$

Following ref. [60] we introduce an extra modification factor K for the inelastic ωN scattering:

$$\tilde{\sigma}_{\omega N}^{inel} = \sigma_{\omega N}^{inel} \cdot K \ .$$

For $K > 1$, the additional contributions to the cross sections are put into the channel $\omega N \to 2\pi N$.

Fig. 15 shows the total ωN cross section for $K = 1$ and $K = 2$, as well as the contributions from different channels (for $K = 1$ only).

We have chosen to put the additional absorption strength connected to the K factor into the $2\pi N$ channel, since the πN channel is constrained by the inverse reaction $\pi N \to \omega N$ via detailed balance. This strength could also be due to higher multiplicity channels like $\omega N \to 3\pi N$, or could even mimic many-body absorption processes such as $\omega N N \to X$. Another origin of the underestimated absorption strength could be the not-very-well-established coupling of the ω meson to baryon resonances and the connected uncertainties: As mentioned the GiBUU model assumes an ω coupling only for two specific resonances, but there could potentially be several more, which might carry at least part of the missing absorption strength.

2.3.2.3 ρN

For the ρ meson, the total cross section on the nucleon (including elastic and absorptive parts) is strongly dominated by the excitation of baryonic resonances, which is described by the Breit-Wigner formula of eq. (55). Fig. 16 shows the two-dimensional dependence of the ρN cross section on mass m and momentum p_{lab} of the ρ meson (colliding with a

nucleon at rest). A few ridges are visible, running along lines of constant $s = m_N^2 + m^2 + 2m_N\sqrt{m^2 + p_{lab}^2}$, which represent the contributions of various resonances, most notably the $D_{13}(1520)$, $S_{31}(1620)$ and $D_{33}(1700)$.

For low masses and momenta, the available scattering phase space gets small, and therefore the cross section drops rapidly. At large masses and momenta, i.e. above the resonance region, on the other hand, a Regge-inspired parametrization is used [132], which is basically constant in the plotted region.

It is also visible in the figure that the cross section increases strongly for $p_{\text{lab}} \to 0$ (and fixed m). The reason for this is that with the laboratory momentum p_{lab} also the center-of-mass momentum p_{ab} in the initial state goes to zero, which enters the Breit-Wigner formula as p_{ab}^{-2}. A similar behavior was already observed in the ωN cross section, which also rises strongly for $p_{\text{lab}} \to 0$.
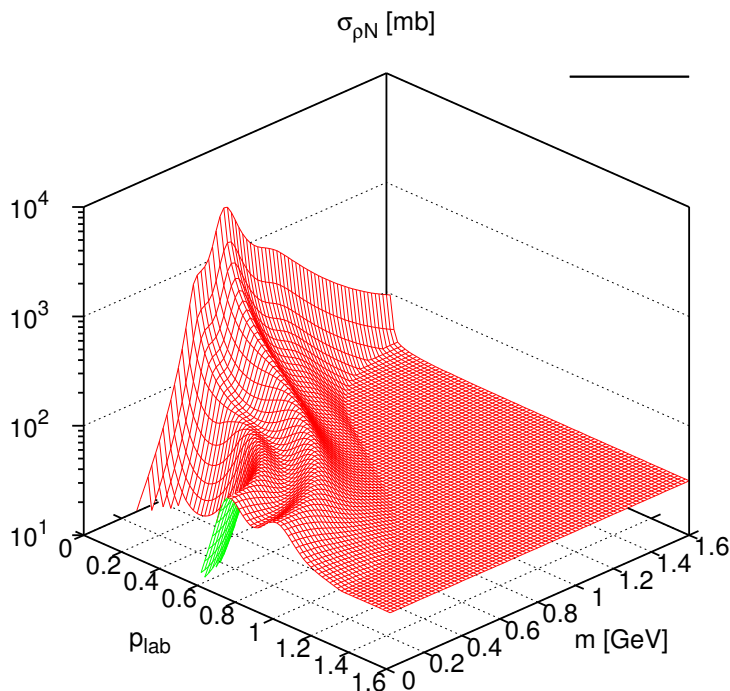
Figure 16: Total ρN collision cross section as a function of mass m and momentum p_{lab}.

2.3.3 γN collisions

The interaction of real photons with nucleons at low energies is dominated by resonance excitations (most prominently the Δ isobar, supplemented by a number of N^* and Δ^* states), leading predominantly to single- and double-pion production, as shown in fig. 17. In the GiBUU model, single- and double-pion production is performed by a mixture of resonance and background contributions, both described in detail in [68]. Note that the single-pi background can even become negative in order to compensate for negative interferences among the resonance contributions. The corresponding test particles will be propagated with negative weights, and contribute negatively to all observables [68]. In contrast to the 1π and 2π case, we do not include an explicit background contribution
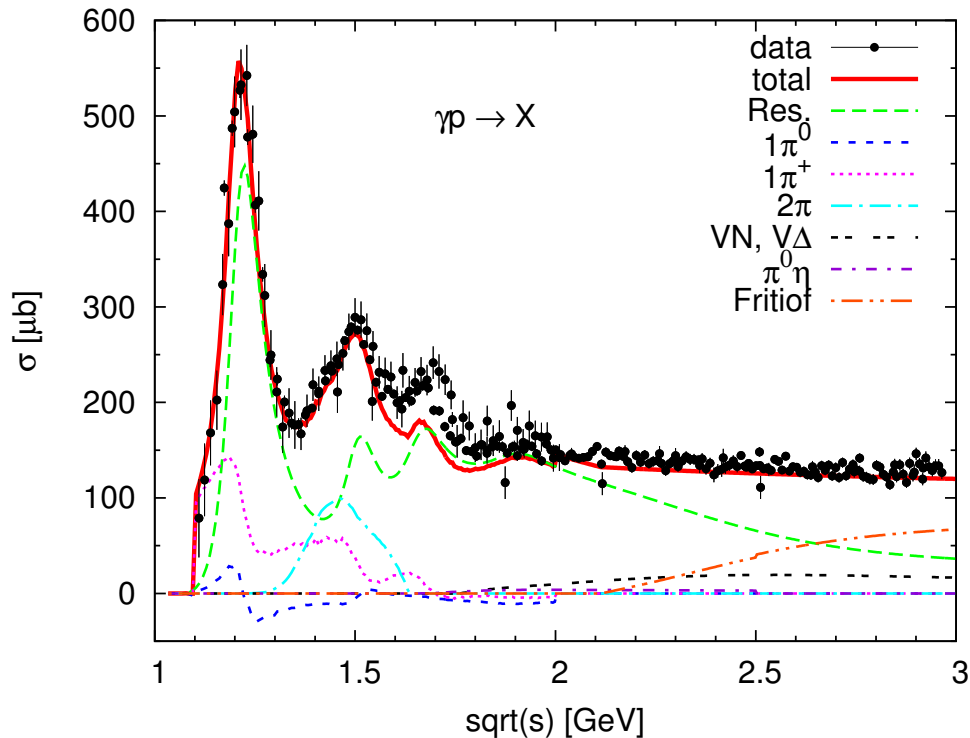
Figure 17: Total γp cross section as implemented in GiBUU. Data from [78].

for 3π production, which might be the reason for the slight underestimation of the data around $\sqrt{s} = 1.7\,\text{GeV}$.

Apart from the exclusive pion production, also other channels are treated explicitly in the GiBUU model, in particular $\pi^0\eta$ and vector meson production.

The $\pi^0\eta$ cross section is simply given by a splined parametrization of the data from [133]. The exclusive cross sections for the photo production of vector mesons on a nucleon, i.e., $\gamma N \to VN$ (with $V = \rho^0, \omega, \phi$), are adjusted to experimental data with the ansatz [66]

$$\sigma_{\gamma N \to VN} = \frac{1}{p_i s} \int_0^{\mu_{max}} \mathrm{d}(\mu^2) \left| \mathcal{M}_V(\sqrt{s}) \right|^2 p_f \mathcal{A}_V(\mu), \tag{62}$$

where we integrate over the mass, μ, of the vector meson, V, up to a maximum $\mu_{\max} = \sqrt{s} - m_N$. Here $\sqrt{s}$ is the total energy available for the reaction. The center-of-mass momenta of the initial and final state are denoted by p_i and p_f, respectively:

$$p_i = \frac{1}{2\sqrt{s}} \left(s - m_N^2 \right) \ , \tag{63}$$

$$p_f = \frac{1}{2\sqrt{s}} \sqrt{\left(s - (m_N + \mu)^2 \right) \left(s - (m_N - \mu)^2 \right)} \ . \tag{64}$$

The spectral function of the vector meson is given by

$$\mathcal{A}_V(\mu) = \frac{1}{\pi} \frac{\mu \Gamma_V(\mu)}{(\mu^2 - M_V^2)^2 + (\mu \Gamma_V(\mu))^2} \ .$$

Here, M_V is the pole mass of the vector meson, and Γ_V its total width, which for an elementary reaction is just the vacuum decay width. However, it will include contributions from collisional broadening, when we describe vector meson production in the medium.
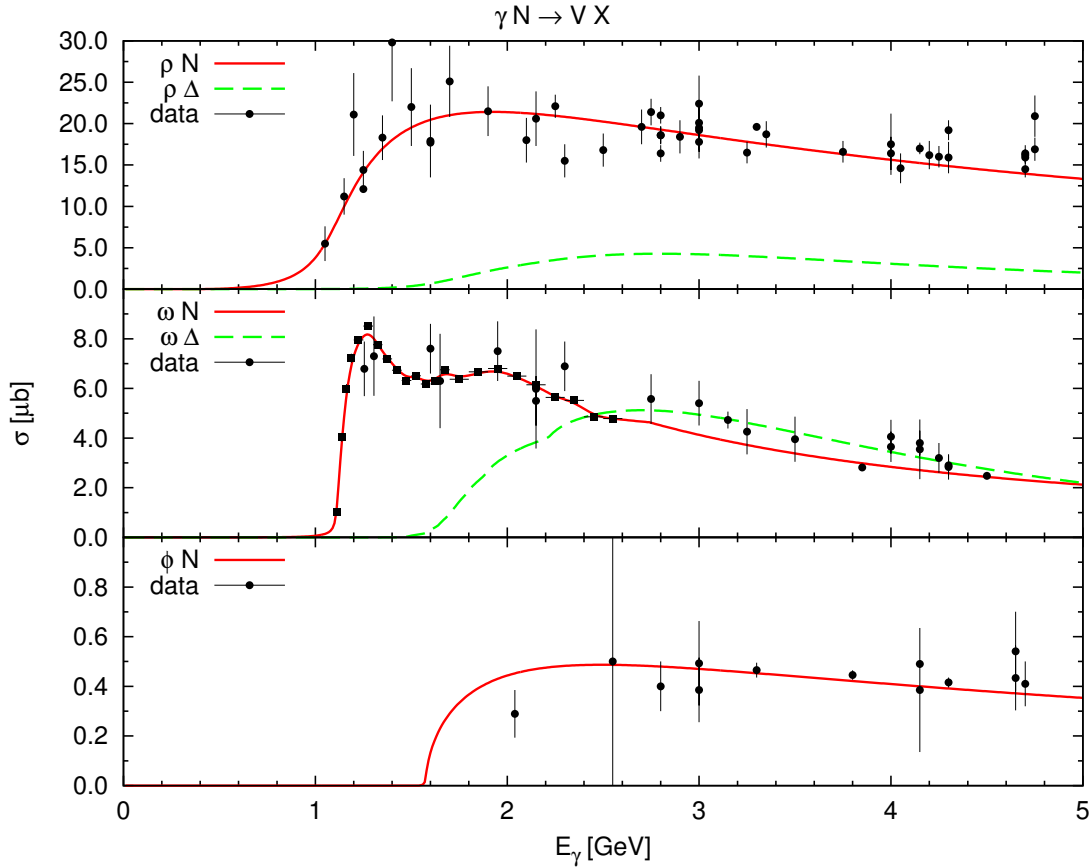
Figure 18: Photoproduction cross sections of vector mesons. Data from [78, 134].

For the ρ^0 and ϕ mesons, constant matrix elements

$$|\mathcal{M}_\rho|^2 = 160\,\mu\text{b}\cdot\text{GeV}^2\,,\tag{65}$$

$$|\mathcal{M}_\phi|^2 = 4\,\mu\text{b}\cdot\text{GeV}^2\tag{66}$$

are sufficient to obtain a good fit of the data, cf. fig. 18.

For the ω meson we use an $\sqrt{s}$-dependent matrix element. It can be directly obtained from a spline-fit to the SAPHIR data [135] for ω photoproduction on a proton. Using the fact, that in the vacuum the ω spectral function is very narrow [56] and can be approximated by the Delta-function in eq. (62), we get

$$\left|\mathcal{M}_\omega(\sqrt{s})\right|^2 = \frac{p_i\,s\,\sigma^{exp}_{\gamma N\to\omega N}(s)}{\phi_2(s)},$$

where ϕ_2 stands for the two-body phase-space integral (in the vacuum). This matrix element is then used in eq. (62) together with the in-medium spectral function.

In order to describe the photoproduction of mesons with masses below the pole mass, we follow the idea of [136] and extend the matrix element to sub-threshold energies by defining a new invariant

$$Q(\mu) = \sqrt{s_0(M_V)} - \sqrt{s_0(\mu)} + \sqrt{s} \equiv \sqrt{s} + M_V - \mu.\tag{67}$$
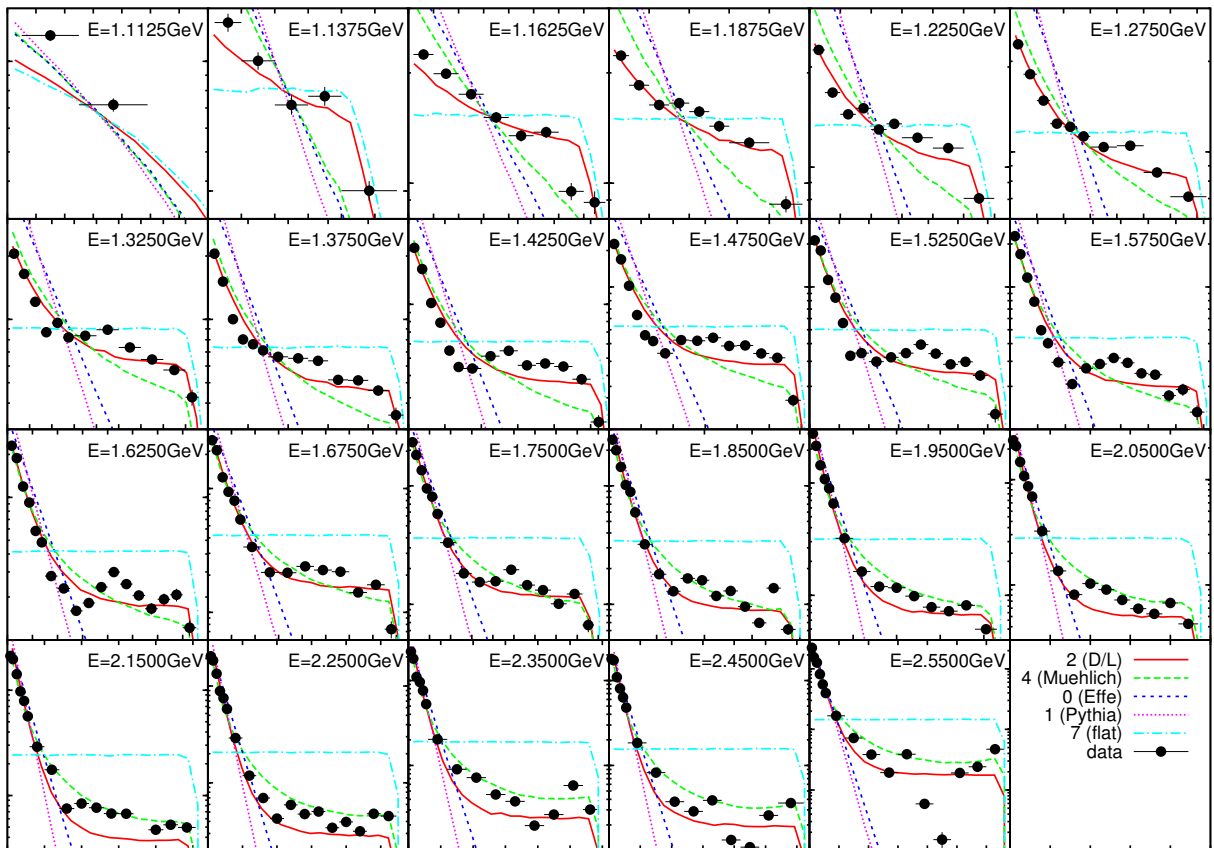
Figure 19: Angular distributions $d\sigma/dt$ for ω photoproduction as a function of $|t - t_{\min}|$ in different models, compared to data from [134].

Here $\sqrt{s_0(\mu)}$ is the threshold energy for the production of ω mesons of mass μ. With this definition one substitutes

$$\mathcal{M}(\sqrt{s}) \to \mathcal{M}[Q(\mu)] \quad .$$

In the vacuum $Q(\mu)$ is only nonzero in the vicinity of $Q(\mu) \approx \sqrt{s}$, since the ω is a very narrow state. At the same time, eq. (67) provides a reasonable prescription for the in-medium case (see [61] for more details).

For the process $\gamma N \to V\Delta$ we use the following parametrization of the total cross section [58],

$$\sigma_{\gamma N \to V\Delta} = \frac{1}{p_i s} \int d(\mu_\Delta^2) p_f(\mu_\Delta) \mathcal{A}_\Delta(\mu_\Delta) \frac{A}{(\sqrt{s} - M)^2 + \Gamma^2/4}, \tag{68}$$

where the constants, A, M, and Γ, are fitted to the experimental cross section of Ref. [137], yielding $A = 47.3\,\mu\text{b}\,\text{GeV}^4$, $M = 2.3\,\text{GeV}$ and $\Gamma = 1.8\,\text{GeV}$ for the ω meson.

For both $\gamma N \to \omega N$ and $\gamma N \to \omega\Delta$, the angular dependence is usually modeled as an exponential [66],

$$\frac{d\sigma}{dt} \propto \exp(Bt). \tag{69}$$

While such a very forward peaked distribution gives a good description of the data at large photon energies, the experimental distributions turn out to be flatter at lower photon energies [134]. In [56] a more complicated tree-level model has been developed, which includes s-, t-, and u-channel nucleon diagrams and leads to a good description of ω-photoproduction data at low energies, as seen in fig. 19. Furthermore, a very good fit of the data can be achieved by a Regge fit [138] supplemented with a constant term [58], which is used by default in the GiBUU code (while the other prescriptions can be selected optionally).

The more inclusive vector-meson-production channels (beyond $\gamma N \to \omega N$ and $\gamma N \to \omega \Delta$) and other high-multiplicity events at higher energies are described via FRITIOF [139], by assuming strict vector meson dominance (VMD) and converting the incoming photon into a ρ^0.

The total γN cross section at high energies is given by VMD [140]. FRITIOF is used to model the remaining yield, which is not covered by the resonances and exclusive channels (and opens up slightly above 2 GeV, as fig. 17 shows). For this purpose the exclusive events (e.g. exclusive pion and vector meson production) have to be removed from the FRITIOF output, in order to avoid double counting of these contributions. In the future, the old FRITIOF model should be replaced by the more recent PYTHIA, which already used for the high-energy baryon-baryon and meson-baryon collisions in GiBUU.

2.3.4   Meson-meson collisions

Meson-meson scattering is mostly relevant for heavy-ion collisions. In elementary collisions on nuclei it can in principle give some contributions, but those can usually be neglected. In fig. 20 we show the total collision cross section of $\pi^+\pi^-$, which is certainly the most important meson-meson process. The elastic cross section at low energies is clearly dominated by the formation of a ρ meson, but also the σ meson yields significant contributions at the threshold. Both are calculated with the usual Breit-Wigner formula, eq. (55).

The σ contribution, however, is somewhat uncertain, since the σ meson, or $f_0(600)$, is not very well established experimentally. The PDG currently lists it with a mass of 400 – 550 MeV and a width of 400 – 700 MeV [78]. In the GiBUU implementation, a mass of 800 MeV is used together with a width of 500 MeV. While the width fits the PDG interval, the mass is obviously not fully compatible with the current PDG values (but was compatible with previous PDG editions). We note that it was not updated, since the value of 800 MeV gives a much better agreement with the $\pi^+\pi^-$ cross section (shown in fig. 20).

With the contributions of the ρ and $f_2(1270)$ mesons, the data is well reproduced up to roughly 1.4 GeV. At higher energies no data is available, but it is expected that our model underestimates the $\pi^+\pi^-$ cross section there, since no heavier meson states (f', ρ', etc) are included. Furthermore we currently miss a high-energy treatment of the meson-meson collisions via PYTHIA (in principle this can be implemented quite easily in analogy to the BB and mB case; one just needs a proper parametrization of the total cross section, which can be found e.g. in [143]).

For dilepton production from heavy-ion collisions at low energies, in particular the process $\pi\pi \to \rho$ can give significant contributions. This is properly constrained by data and well
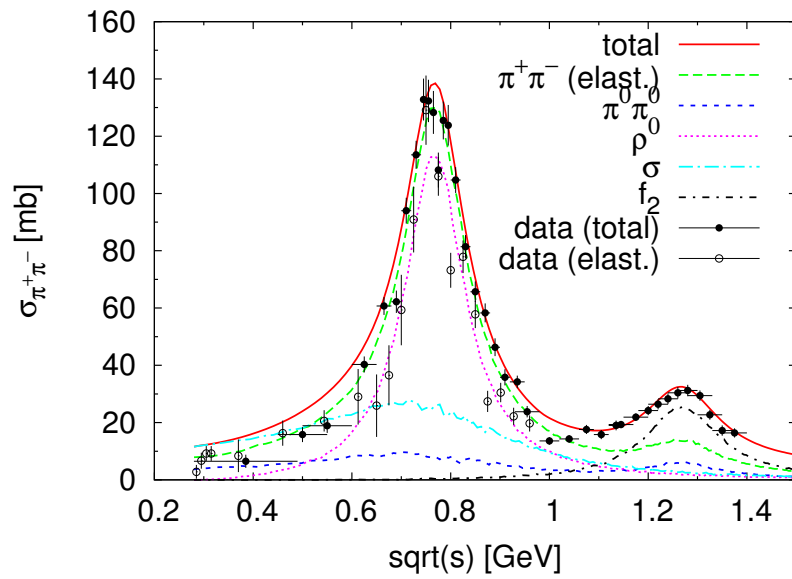
Figure 20: $\pi^+\pi^-$ scattering cross section. Data from [141, 142].

under control in our model, as shown above. At the low energies discussed in this work, pion-pion collisions above 1 GeV will not play a role.

2.4 Off-shell Propagation

The kinetic transport equation (4) presented earlier holds for stable as well as broad unstable states and in principle allows to describe the kinetics of resonances with density-dependent spectral functions [144, 145].

Often, however, dynamic changes of the spectral functions are neglected by relying on the 'on-shell' version of the BUU equation, where the off-shell term is removed:

$$\{p_0 - H(x,p), F(x,p)\}_{\mathrm{pb}} = C(x,p). \tag{70}$$

In this approximation it is still possible to describe broad resonances (by sampling their spectral function with a sufficient number of test particles), however each of the test particles propagates with a fixed mass (apart from possible changes of the effective mass due to the mean-field potentials), and therefore dynamic modifications of the spectral functions cannot be accommodated.

The propagation of particles with density-dependent spectral functions (usually referred to as "off-shell propagation") poses a particular challenge: If a particle is created in the medium, the test-particle mass should be sampled according to the full spectral function, which should take into account the in-medium self energy of the particle, and can potentially depend on quantities like the local density, temperature and chemical potential. As the particle propagates through regions of varying density and temperature, the spectral function changes accordingly, which means that also the mass distribution of test particles should be modified to reflect the changing spectral function. In particular, one needs to make sure that particles which propagate into the vacuum properly return to their vacuum spectral function (i.e. stable particles need to come back to their mass shell, even though they had a broad mass distribution in the medium. For a test-particle based transport approach, this means that one needs to accommodate for dynamically changing masses of the test particles.

Our approach to this problem is based on the off-shell equations of motion for test particles, as given in [144] and [145]. These are implemented in GiBUU through the so-called off-shell potential (OSP) ansatz. Within this ansatz the effects of the off-shell term, i.e. the second Poisson bracket on the l.h.s. of eq. (4), are absorbed into an additional potential term, which causes a dynamic modification of the effective mass.

In order to outline this method we start our discussion with the on-shell transport equation, i.e. eq. (70). The l.h.s. can be explicitly rewritten as

$$\{p_0 - H, F\}_{\mathrm{pb}} = \left[\left(1 - \frac{\partial H}{\partial p_0}\right) \frac{\partial}{\partial t} + \frac{\partial H}{\partial \vec{p}} \frac{\partial}{\partial \vec{r}} - \frac{\partial H}{\partial \vec{r}} \frac{\partial}{\partial \vec{p}} + \frac{\partial H}{\partial t} \frac{\partial}{\partial p^0} \right] F(x,p) \tag{71}$$

with the single-particle Hamilton function,

$$H(x,p) = \sqrt{m^2 + \mathrm{Re}\,\Pi(x, p_0, \vec{p}) + \vec{p}^2}\,, \tag{72}$$

where m is the pole mass of the particle species under consideration. The self-energy, Π, contains the effects of the potential; in the general off-shell case it can be explicitly dependent on p_0.

We note here that while eq. (70) is the transport equation for fermions, the analogous one

for bosons

$$\left\{p^2 - m^2 - \operatorname{Re}\tilde{\Pi}(x,p), F(x,p)/(2p^0)\right\}_{\mathrm{pb}} = \left\{p_0^2 - H^2(x,p), F(x,p)/(2p^0)\right\}_{\mathrm{pb}} = C(x,p) \tag{73}$$

reduces to the one for fermions for $|p^0 - H| \ll H$ with formally the same Hamiltonian H, provided H is not explicitly time-dependent. Thus the following considerations are also directly applicable to bosonic transport.

The generalized BUU eq. (70) can be solved numerically by using the test-particle technique, i.e., the continuous Wigner function is replaced by an ensemble of test particles represented by δ-functions,

$$F(x,p) = \lim_{n(t)\to\infty} \frac{(2\pi)^4}{N} \sum_{j=1}^{n(t)} \delta[\vec{r} - \vec{r}_j(t)]\delta[\vec{p} - \vec{p}_j(t)]\delta[p^0 - p_j^0(t)] , \tag{74}$$

where $n(t)$ denotes the number of test particles at time, t, and $\vec{r}_j(t)$ and $p_j(t)$ are the coordinates and the four-momenta of test particle, j, at time, t. As the phase-space density changes in time due to both, collisions and the Vlasov dynamics, also the number of test particles changes throughout the simulation: in the collision term, test particles are destroyed and new ones are created. At $t = 0$ we start with $n(0) = N \cdot A$ test particles, where A is the number of physical particles and N is the number of ensembles (test particles per physical particle).

Combining the time derivatives of eq. (74) and eq. (71), we find the equations of motion,

$$\frac{\mathrm{d}\vec{r}_j}{\mathrm{d}t} = \left(1 - \frac{\partial H}{\partial p_0}\right)^{-1} \frac{\partial H}{\partial \vec{p}} , \tag{75}$$

$$\frac{\mathrm{d}\vec{p}_j}{\mathrm{d}t} = -\left(1 - \frac{\partial H}{\partial p_0}\right)^{-1} \frac{\partial H}{\partial \vec{r}} , \tag{76}$$

$$\frac{\mathrm{d}p_j^0}{\mathrm{d}t} = \left(1 - \frac{\partial H}{\partial p_0}\right)^{-1} \frac{\partial H}{\partial t} . \tag{77}$$

If $\partial H/\partial p_0 = 0$, eqs. (75) and (76) become the usual Hamilton equations of motion for stable particles. Energy conservation is enforced by eq. (77), if $\partial H/\partial t = 0$. Numerically, the generalized Hamilton equations of motion (75)-(77), are solved with a predictor-corrector algorithm.

Since the Poisson-bracket term in eq. (4) has been dropped, there is, so far, nothing in eqs. (75) to (77) that restores the proper vacuum properties of a collision-broadened particle when it propagates out of the nucleus. The OSP ansatz approximately restores the proper off-shell propagation. This idea was originally introduced in [66, 146] in the spirit of an educated guess, only taking into account the density dependence of the self-energy. An improved version has been developed in Ref. [68] with the intent to solve the non-relativistic test-particle equations of motion of [145].

To introduce the (relativistic) OSP method we start by defining the offshellness (or off-shell potential), $\Delta\mu_j^2$, of the jth test particle by

$$p_j^2 = m^2 + \operatorname{Re}\Pi + \Delta\mu_j^2 . \tag{78}$$

Thus, $\sqrt{m^2 + \operatorname{Re}\Pi}$ corresponds to the in-medium pole mass and, consequently, $\Delta\mu_j^2$ is a measure of how far the test-particle invariant mass, $\mu_j = \sqrt{p_j^2}$, is off the pole [1]. Rewriting eq. (78) yields for the energy of the test particle

$$p_j^0 = \sqrt{m^2 + \operatorname{Re}\Pi + \Delta\mu_j^2 + \vec{p}^2}\ . \tag{79}$$

The effects of the off-shell propagation, contained in the Poisson-bracket term in eq. (4), are thus absorbed into the off-shell potential, $\Delta\mu_j^2$.

The OSP ansatz now consists in regulating the offshellness, $\Delta\mu_j^2$, such that the vacuum behavior is restored when the particles leave the nucleus. To achieve this, the offshellness can be written as

$$\Delta\mu_j^2(\vec{r}, p) = \chi_j \, \tilde{\Gamma}_j(\vec{r}, p), \tag{80}$$

where the off-shell parameter, χ_j, is a constant of motion for each test particle and therefore can be calculated at the time of creation, t_0, as

$$\chi_j = \frac{\Delta\mu_j^2(\vec{r}_j(t_0), p_j(t_0))}{\tilde{\Gamma}_j(\vec{r}_j(t_0), p_j(t_0))}. \tag{81}$$

Here, $\tilde{\Gamma}_j$ is related to the total width of a particle: $\tilde{\Gamma}_j(\vec{r}, p) = \mu_j \Gamma_{\text{tot}}(\vec{r}, p)$.

As each test particle is defined with its own off-shell parameter, we require a separate Hamilton function, H_j, for each test particle and replace

$$H = \sqrt{m^2 + \operatorname{Re}\Pi + \vec{p}^2} \rightarrow H_j = \sqrt{m^2 + \operatorname{Re}\Pi + \Delta\mu_j^2 + \vec{p}^2}. \tag{82}$$

Each test particle is thus propagated also under the influence of the off-shell potential, $\Delta\mu_j^2$. Note that this potential, just like χ_j, is positive for particles above the pole mass $(\mu_j > \sqrt{m^2 + \operatorname{Re}\Pi})$ and negative for those below. By inserting this Hamiltonian into the generalized Hamilton equations of motion (75)-(77), one directly obtains the relativistic test-particle equations of motion given in [144]. Using the off-shell parameter, these equations of motion simplify to

$$\dot{\vec{r}}_j = \frac{1}{1 - C_j} \frac{1}{2E_j} \left(2\vec{p}_j + \frac{\partial}{\partial\vec{p}_j} [\operatorname{Re}\Pi_j + \chi_j \tilde{\Gamma}_j] \right), \tag{83}$$

$$\dot{\vec{p}}_j = -\frac{1}{1 - C_j} \frac{1}{2E_j} \frac{\partial}{\partial\vec{r}_j} \left[\operatorname{Re}\Pi_j + \chi_j \tilde{\Gamma}_j \right], \tag{84}$$

$$\dot{\chi}_j = 0 \tag{85}$$

$$\text{with} \quad C_j = \frac{1}{2E_j} \frac{\partial}{\partial E_j} \left[\operatorname{Re}\Pi_j + \chi_j \tilde{\Gamma}_j \right], \tag{86}$$

The earlier OSP ansatz, as applied by Effenberger [66] and later by Lehr [69] and Mühlich [56], was much simpler; assuming $\Gamma_{\text{med}} \approx \gamma\Gamma_{\text{coll}}$ and $\Gamma_{\text{coll}} \propto \rho$ they chose a linear dependence in density instead of the full in-medium width in eq. (81), which is a considerable simplification from a numerical point of view.

---

[1]Remember that we suppress the particle-species index i while we keep the index j which denotes the jth test particle. For brevity, the Coulomb potential is dropped in the derivation of the OSP method.

However, this ansatz also suffered from particular problems with particles close to their production threshold, which we will discuss in more detail in section 4.1 in the context of ω photoproduction.

At first sight the implementation of the off-shell equations of motion, as given above, seems straightforward. In reality, however, a number of problems appear, which make the implementation of a fully consistent off-shell transport scheme difficult. We try to illuminate in the following the most severe obstacles.

2.4.1   Momentum-dependent in-medium self energies

One such problem concerns the momentum dependence of the total widths. To describe off-shell transport in a consistent manner, one should use collisional widths in the medium which are compatible with the collision term used in the transport model. In general such a collisional width depends on the particle's momentum (relative to the medium). Also, the equations of motion shown earlier are sensitive to such momentum dependences, as they contain terms of the form $\partial \tilde{\Gamma}_j / \partial \vec{p}_j$. However, these terms can cause test particles to become superluminous. To show this, we express the width in terms of variables $(\mu_j = \sqrt{E_j^2 - \vec{p}_j^2}, \vec{p}_j)$ instead of $(E_j, \vec{p}_j)$. Then, by combining eqs. (83) and (86) and neglecting $\operatorname{Re}\Pi_j$ we obtain the following expression for the test-particle velocity:

$$\vec{v}_j = \dot{\vec{r}}_j = \frac{\vec{p}_j}{E_j} + \left(1 - \frac{\chi_j}{2\mu_j} \frac{\partial \tilde{\Gamma}_j(\vec{r}_j, \mu_j, \vec{p}_j)}{\partial \mu_j} \right)^{-1} \frac{\chi_j}{2E_j} \frac{\partial \tilde{\Gamma}_j(\vec{r}_j, \mu_j, \vec{p}_j)}{\partial \vec{p}_j} \tag{87}$$

If the width depends on invariant mass only and not on three-momentum the velocity simplifies to the classical expression $\vec{v}_j = \vec{p}_j / E_j$. The same always holds true for on-shell particles, which have $\chi_j = 0$. This is expected, since $\operatorname{Re}\Pi_j$ is neglected. However, there is a correction term $\propto \partial \tilde{\Gamma}_j / \partial \vec{p}_j$ to the classical limit for off-shell particles if the width depends on three-momentum. In addition, the velocity is not guaranteed to be smaller than the speed of light any more. This can become a problem for particles which are already highly relativistic. For them, even a small contribution from the extra term can violate the constraint, $v \leq 1$. This problem of superluminous particles has been noted already, e.g., in [147] for pion propagation. Following [56,66,69] we circumvent this problem by keeping only the density dependence of the width and use a momentum-independent Γ_0 value which fits the full one, obtained from the collision term, on average:

$$\Gamma_{\mathrm{coll}}(\rho) = \Gamma_0 \cdot \frac{\rho}{\rho_0} . \tag{88}$$

We typically use values of $\Gamma_0 = 150\,\mathrm{MeV}$ for the ρ and ω mesons, and $\Gamma_0 = 30\,\mathrm{MeV}$ for the ϕ. The value for the ω is compatible with the transparency-ratio data of CBELSA/TAPS [35].

2.4.2   Mass dependence of vacuum widths

But even when neglecting the momentum dependence and using a total width which only depends on the invariant mass, $\Gamma_{i,tot}(\mu_i)$, one can run into trouble. The reason for this are the C-factors which enter the off-shell equations of motion. Those always appear in the form $\frac{1}{1-C_i}$, which means that the off-shell equations have a pole at $C_i = 1$, i.e. they will

only be well-behaved for $C_i < 1$. When neglecting the momentum dependence, the value of C_i only depends on $\partial \tilde{\Gamma}_i / \partial \mu_i$ (with the transformation $\frac{\partial}{\partial E} = \frac{E}{\mu} \frac{\partial}{\partial \mu}$ and $\chi = \text{const.}$):

$$C_{vac}(\mu_i) = \frac{\chi}{2\mu_i} \frac{\partial}{\partial \mu_i} [\mu_i \Gamma_{vac}(\mu_i)] = \frac{\mu_i^2 - m^2}{2\mu_i} \frac{\partial \tilde{\Gamma}/\partial \mu_i}{\tilde{\Gamma}} \tag{89}$$

However, $C_i = 1$ can already happen in vacuum if the vacuum width has a very steep mass dependence. In that sense, the condition $C_i < 1$ directly translates into a restriction of the mass-dependence of the vacuum width, which can be easily violated for realistic width parametrizations. As a possible solution to this problem, it has been proposed in [47] to simply neglect the C-factors, i.e. set $C_i = 0$. This superficially solves the problem, but considerably modifies the equations, and will affect the propagation of particles already in vacuum. In particular it means that the velocity in vacuum will be different from the expected value of $v = p/E$. One can show that it becomes:

$$\dot{\vec{r}} = \frac{\vec{p}}{p_0} \left(1 - \frac{\chi}{2\mu_i} \frac{\partial}{\partial \mu_i} \tilde{\Gamma} \right) = \frac{\vec{p}}{p_0} (1 - C_{vac}(\mu_i)) \tag{90}$$

This is only correct for $\chi = 0$ (i.e. $C = 0$), that is: at the pole. For this reason the full equations are used (including the C-factors) in the current GiBUU implementation.

Fig. 21 shows the vacuum widths and the corresponding C factors for the vector mesons (ρ, ω and ϕ) as used in the GiBUU model (for a description of the widths, see section 2.2.1). The lower part of the figure shows that the C factors are well behaved for all three mesons, i.e. $C < 1$ for the pure vacuum width, but also for in the in-medium width (when adding a constant collisional width, as discussed in the preceding section).
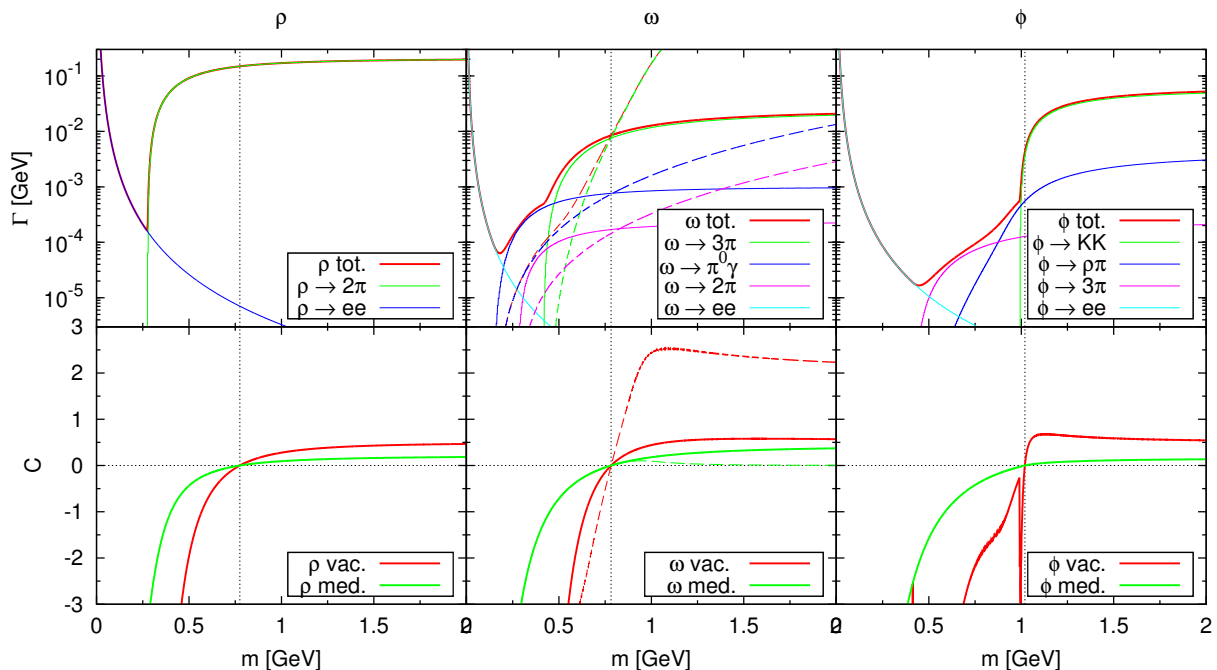
Figure 21: Vacuum decay widths and C factors for the ρ, ω and ϕ mesons. For the ω meson, the solid lines represent the width parametrizations as shown in section 2.2.1, while the dashed lines use the widths from [56].

As a side node, one should mention that $C < 1$ is not guaranteed any more in the very low mass regime when adding the dilepton widths. However, the dilepton widths are usually neglected in the spectral function for the ω and ϕ meson, and are only used for the ρ meson, where the low-mass part of the spectral function can become important through the coupling to resonances, as we will discuss in section 3.

For the ω meson, fig. 21 also shows the width parametrizations from [56] (and the corresponding C factors) as dashed lines. It has a much steeper mass dependence and the C factors easily get larger than 1. For this reason, these width parametrizations are unusable with the current off-shell potential implementation in GiBUU. We also failed to force $C < 1$ by multiplying them with a simple form factor. Note: We have verified that the same problem appears not only with the width from [56], but also for the $\omega \to 3\pi$ width from [148].

Choosing a simple analytic form for the vacuum width, e.g. $\Gamma_{vac}(\mu) = \Gamma_0 \cdot \mu^n$, one obtains $C(\mu) = \frac{n+1}{2} \cdot \frac{\mu^2 - m^2}{\mu^2}$, which is guaranteed to obey $C < 1$ for $-1 < n < 1$. This means that any vacuum width growing faster than linear with μ will be problematic for off-shell transport (leading to $C > 1$ in the high-mass tail of the spectral function). Also any width falling faster than $\frac{1}{\mu}$ will lead to $C > 1$ in the very low-mass tail of the spectral function (e.g. the dilepton widths fall with μ^{-3}). This certainly puts tight constraints on the mass dependence of the vacuum widths (as well as the in-medium width) and represents one of the limitations of the current off-shell transport treatment.

We have shown in fig. 21, that our width parametrizations of the ρ and ϕ mesons are unproblematic in this respect. For the ω, however, we had to refrain from using a more realistic width (e.g. the one used in [56]) to prevent problems with the C-factors, which occur due to the very steep mass dependence of the ω width. Therefore we use the $\omega \to 3\pi$ width of eq. (26), which is not as realistic, but compatible with the restrictions posed by off-shell transport.

2.4.3 Space-like test particles

A third area of problems is given by the fact that it is not clear from first principles that, starting from an in-medium distribution of test particles, the correct vacuum distribution will be reached when propagating out of the medium. In numerical simulations one can usually observe that this works pretty well in the area around the pole mass, where the offshellness of the particles is small. However, further away from the pole mass, in the far-off-shell regions, larger discrepancies can be observed (see fig. 22). Moreover, if the there are large medium modifications, parts of the vacuum spectral function can be pushed to masses below zero (the space-like region).

Figure 22 shows the results of an idealized 'Gedankenexperiment', in which a beam of ρ or ω mesons with a momentum of 1.5 GeV (and a mass distribution according to their vacuum spectral function) is being shot at a Ca nucleus. Since this experiment is meant to be a benchmark for the off-shell propagation of particles with density-dependent spectral functions, we assume the mesons to be stable and non-interacting (i.e. no decays or collisions are taking place, and the particles just propagate through the static density profile of the nucleus). Regarding the in-medium spectral function, we assume a pure collisional-broadening scenario (with a constant collisional width of 150 MeV for both ρ and ω).
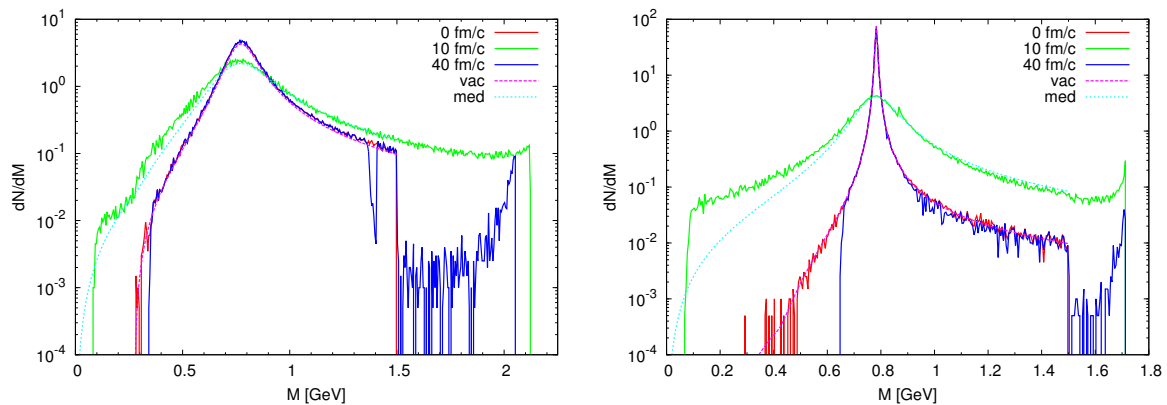
Figure 22: Spectral evolution of ρ (left) and ω (right) mesons propagating through a Ca nucleus (under the assumption of collisional broadening).

The figure shows the mass distribution of the mesons for three points in time in this virtual experiment:

- At $t = 0$ (red line) the mesons are initialized outside of the nucleus (i.e. in the vacuum). For practical reasons, we choose to populate the spectral function only up to a maximum mass of 1.5 GeV (in a realistic setup the accessible phase space would be bounded by the maximum energy available in the production process of the meson). It is apparent that the actual distribution of test particle masses closely follows the analytic vacuum spectral function (pink dashed line).

- At $t = 10 \, \mathrm{fm}$ (green line) essentially all mesons have propagated to the inside of the nucleus and reside at densities close to ρ_0. The spectral distribution has broadened significantly and roughly agrees with the analytic in-medium spectral function (cyan dashed line) at least around the pole, although further away from the pole larger deviations can be seen (in particular in the low-mass tail of the ω). Due to the broadening, also masses below the vacuum threshold mass and above our arbitrary upper mass cut of 1.5 GeV are populated now.

- At $t = 40 \, \mathrm{fm}$ the mesons have fully propagated through the nucleus and are back in vacuum again. For the most part, in particular around the pole, the mass distribution agrees well with the initial distribution (as expected). However, there are deviations, which reveal some of the limitations of our off-shell propagation scheme. Most severely, a sharp cut-off emerges in the low-mass part of the spectral function. For the ρ this cut-off is quite close to the natural vacuum threshold, but for the ω it cuts away a significant part of the low-mass tail. Furthermore, there are minor deviations in the high-mass tail.

The reason for the lower mass cut-off at the end is that the corresponding test particles have changed their mass so strongly in the medium that they have become space-like (i.e. $m^2 < 0$). These particles are simply deleted from the simulation, so that their contribution is then missing in the spectral function. Such a drift into the space-like region can happen for particles in the very low mass tail: Since they have a large negative

off-shell parameter $\chi \ll 0$, they feel a strongly negative off-shell potential and nothing prevents their (squared) mass from becoming negative if the width $\tilde{\Gamma}$ grows with density:

$$\mu^2 = m^2 + \chi \tilde{\Gamma} \tag{91}$$

For the ω, which is quite sharp in vacuum but very broad in the medium, the off-shell potential is stronger than for the ρ (which is already quite broad in the vacuum), and consequently the cut-off effect is more severe.

We note that it is conceptually not clear how to treat space-like test particles (or even whether one can still speak of a 'particle'). Therefore such test particles are just deleted in the current GiBUU implementation. The only way to overcome the cut-off problem would probably be to keep propagating such space-like test particles (after all they should become time-like again at some point). However, it is unclear what the collision cross sections or decay widths for such a 'particle' should look like. Therefore one option would be to assume that they do not scatter or decay at all.

Despite these problems in the low-mass tail, the distribution in the pole area is very well reproduced, and also above the pole mass, there are only minor deviations. However, our test setup only involves densities up to ρ_0 and in situations with larger densities (e.g. heavy-ion collisions) more severe issues can be expected.

We should also note here that the off-shell potential is technically treated just like any other potential and can assume quite large negative values below the mass pole and large positive values above. This can lead to effects like repulsion and binding. For example a very low-mass ω meson feels a strongly attractive off-shell potential and can even be bound in the nucleus due to this potential. On the other hand, a very high-mass ω feels a strongly repulsive potential. A priori it is not clear whether such effects actually have any physical meaning, or whether they are just 'artifacts' of the imperfect off-shell treatment.

2.5   In-Medium Effects

In light of the various problems encountered in the off-shell treatment, it seems hopeless to try and use a full-featured hadronic model for the in-medium spectral functions, since any nontrivial energy or momentum dependence is very likely to trigger at least some of the mentioned problems (such as superluminous or space-like test particles or poles in the EOM).
Instead, we restrict ourselves to the following simple and schematic in-medium scenarios:

1. An in-medium mass shift according to

$$m^*(\rho) = m_0 \left(1 - \alpha \frac{\rho}{\rho_0} \right), \qquad (92)$$

   with a scaling parameter parameter, $\alpha = 0.16$, as suggested in [4], corresponding to a 16% mass shift at $\rho = \rho_0$. Here, m_0 is the vacuum mass of the meson and $\rho_0 = 0.168\,\mathrm{fm}^{-3}$ is the nuclear saturation density.

2. An increase of the in-medium width due to collisions in the medium, $\Gamma_{tot} = \Gamma_{vac} + \Gamma_{coll}$, where Γ_{vac} is the vacuum decay width of the meson and the collisional width is assumed to be of the form

$$\Gamma_{coll}(\rho) = \Gamma_0 \frac{\rho}{\rho_0}. \qquad (93)$$

   The value of Γ_0 is chosen to match the GiBUU collision term. For both the ρ and ω meson we typically use values of $\Gamma_0 = 150\,\mathrm{MeV}$. For the ω meson this corresponds to $K = 2$ (cf. section 2.3.2.2), and is compatible with the CBELSA-TAPS transparency-ratio data [35].

In the following sections we will show most of our results for these two cases separately and also for a combination of both.
For photoproduction experiments, it seems sufficient to assume a linear density dependence for both mass and width, since one is anyway limited to small densities $\rho \leq \rho_0$ there, and pion FSI further reduces the sensitivity to large densitites, as we will show in the following. Therefore, nonlinearities which can appear at higher densities can be neglected. In heavy-ion collisions at SIS energies, higher densities of up to $3\rho_0$ and temperatures around 80 MeV are being probed. For this application it seems that our assumptions of a linear density dependence and a neglected temperature dependence are actually not realistic enough. However, they still provide a rough estimate of any possible in-medium modifications at least.
Apart from the density dependence, the collisional width is expected to have also a momentum dependence, since it is related to the collision cross section σ_{NX} (in low-density approximation) via

$$\Gamma_{coll} = \rho \left\langle v_{rel} \sigma_{NX} \right\rangle, \qquad (94)$$

where v_{rel} is the relative velocity of the ω with respect to the hadronic medium and the brackets indicate an integration over the momentum distribution of the nucleons. The

momentum dependence of the cross section is taken into account in the collision term (cf. section 2.3). However, the momentum dependence of Γ_{coll} is neglected in the spectral function, since it can lead to problems in the off-shell propagation, as discussed in the previous section.

Since the considered scenarios basically rely on the spectral function to still have a simple Breit-Wigner-like shape (whose peak is merely shifted and/or broadened with respect to the vacuum spectral function), they miss any other structures, which can be introduced in the in-medium spectral functions e.g. by couplings to resonances etc. Such effects were previously claimed to be particularly important for the ρ [9], but possibly also for the ω meson [56].

It would certainly be desirable to use a more involved calculation of the in-medium spectral function, like e.g. the ones from [3, 9, 11]. However, this would require either a significant improvement of the off-shell-propagation methods, or alternatively a completely different approach like e.g. a coarse-graining ansatz, where one first determines collective quantities like temperature and chemical potential from the test-particle distribution in the transport simulation on a grid, and then uses these to calculate thermal dilepton rates with a realistic in-medium spectral function.

Apart from the vector mesons, also the baryon spectral functions can be modified in the medium, which could yield additional effects on observables like dilepton spectra. For example the self-energy of the Δ isobar in nuclear matter has been discussed in [149], and also the disappearance of higher resonances in γA reactions is a well-known phenomenon [150]. However, as we will discuss in chapter 3, already the baryonic vacuum contributions to the dilepton spectra are heavily debated and connected with large uncertainties. We will show in section 3.1.8 that e.g. an in-medium modification of the Δ represents only a small additional contribution to these uncertainties.

3 Dilepton spectra at SIS energies

After describing the basic ingredients of the model, we will present in this chapter various results of dilepton spectra in the Bevalac/SIS energy regime (corresponding to beam energies of roughly 1-5 AGeV). The are two sets of data available:

1. The data measured by the DLS collaboration at LBNL in the 80s and 90s of the last century [16, 17].

2. The data measured by the HADES collaboration at GSI after the millenium [27–33].

Both data sets include different collision systems, from elementary nucleon-nucleon collisions, over proton-nucleus to nucleus-nucleus collisions. The overall quality of the HADES data is much better, both in terms of statistic and systematic errors, but also with regards to the detector acceptance and efficiency.

3.1 HADES at SIS18

The HADES collaboration has performed measurements of dilepton spectra from p+p, p+A and A+A reactions at the beam energies listed in table 7.

system	E_{kin}	$\sqrt{s}$	p_{lab}	$p_{\mathrm{lep}}^{\min}$	$p_{\mathrm{lep}}^{\max}$	$b_{\max}$	N_{π^0}	$(N_{\pi^+} + N_{\pi^-})/2$
p + p	1.25	2.42	1.98	0.05	1.8			
d + p	1.25	"	"	"	"			
p + p	2.2	2.76	2.99	0.10	2.0			
p + p	3.5	3.17	4.34	0.08	2.0			
p + Nb	3.5	"	"	0.10	2.0			
C + C	1.0	2.32	1.70	0.05	1.8	5.0	0.381	0.368
C + C	2.0	2.70	2.78	"	"	"	1.014	0.971
Ar + KCl	1.756	2.61	2.53	0.10	1.1	6.5	3.32	3.36
Au + Au	1.25	2.42	1.98	0.05	1.8	9.0	11.7	13.3

Table 7: Kinematic conditions of the collision systems measured by HADES and corresponding cuts on the single lepton momenta (all in GeV). For the nucleus-nucleus collisions also the maximum impact parameters (in fm) and the average pion numbers per event are given.

All simulated spectra which will be shown in the following have been filtered with the HADES acceptance filter (HAFT, version 2.0) [151, 152] using single-lepton acceptance matrices, in order to take care of the geometrical acceptance and resolution of the detector (the HADES geometry roughly covers the polar angle range of $15° < \theta < 85°$, and almost full 2π in azimuth). In addition, a dilepton opening angle cut of $\theta_{ee} > 9°$ is applied in all cases, as well as a cut $p_{\mathrm{lep}}^{\min} < p_{\mathrm{lep}} < p_{\mathrm{lep}}^{\max}$ on the single-lepton momenta, with the values listed in table 7 (columns 5 and 6), matching the experimental analysis procedure.
The kinematic variables E_{kin}, $\sqrt{s}$ and p_{lab} (columns 2 – 4) are related by $s = 2m_N E_{kin} + 4m_N^2$ and $p_{lab}^2 = (E_{kin} + m_N)^2 - m_N^2$ for free NN collisions.

The nucleus-nucleus collisions were simulated in a simple minimum-bias setup, with an impact parameter distribution $\mathrm{d}N/\mathrm{d}b \propto 2\pi b\,\mathrm{d}b$, only restricted by $b < b_{\max}$ (cf. column 7). The average pion numbers per event for this setup are listed in column 8 and 9, but are not directly comparable to the experimental values published in [153], since the experimental trigger bias on the centrality selection was not taken into account (which has a significant impact on absolute pion yields, but should not influence strongly the pion-normalized dilepton spectra). For this reason our pion numbers are up to 20% lower than those published in [153, 154].

Fig. 23 shows the energy distribution of inelastic baryon-baryon collisions ($\sqrt{s_{BB}}$) in the A+A and p+A reactions measured by HADES. For each of them, only a moderate tail reaches beyond the 'nominal' energy (i.e. the primary collision energy without Fermi smearing, marked with an arrow in the figure), but the majority of collisions occurs at significantly lower energies, due to the contributions of secondary collisions. To a certain extent, the distributions follow the behavior of the inelastic NN cross section, since a higher cross section leads to more collisions at a particular energy. This is the reason why the distribution only starts around $2.1\,\mathrm{GeV}$ (which corresponds to the threshold of inelastic NN collisions). We have normalized the distributions to coincide in this region and left out the elastic contributions, since they diverge at low $\sqrt{s}$.
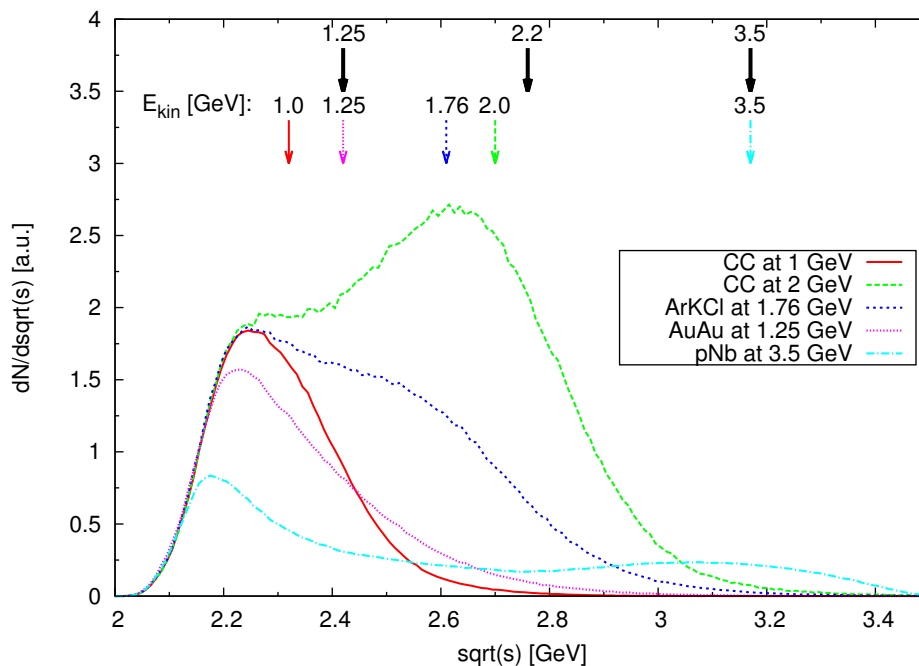
Figure 23: $\sqrt{s}$ distribution of inelastic baryon-baryon collisions in different nuclear reactions measured by HADES. The black arrows indicate the energies of the elementary HADES reactions, while the colored arrows indicate the 'nominal' energies of the A+A collisions (cf. table 7).

The peak of the distribution is quite close to the nominal energy for the C+C reactions (since this is a small system dominated by primaries), and a bit further away for Ar+KCl and Au+Au (which are significantly larger systems, and therefore more dominated by secondaries). The Au+Au distribution is qualitatively similar to the C+C system at 1

GeV, however with an enhanced high-energy tail (due to the slightly higher energy). Also the p+Nb reaction, which contains the highest energies available to the HADES detector, shows a very broad primary peak at the nominal energy and a low-energy peak to due secondary collisions.

We discuss in the following all the systems measured by HADES, in the order as listed in table 7, starting with the elementary p+p (and d+p) systems, follwed by p+Nb and ending with the nucleus-nucleus collisions.

While the description of the elementary reactions does not actually require a full-blown transport model, those reactions provide a well-controlled testing ground of both the hadronic cross sections for the production of different particles and resonances, and also of the dilepton decays and form factors involved. Only with the help of such 'baseline' investigations one has a chance to identify effects of the hadronic medium in the larger systems (which is the ultimate goal of these investigations).

3.1.1   p + p at 1.25 GeV

The lowest HADES energy, $E_{\text{kin}} = 1.25\,\text{GeV}$, corresponding to $\sqrt{s} \approx 2.4\,\text{GeV}$, is just below the η production threshold, and also for ρ mesons there is only a small sub-threshold contribution from the low-mass tail of the ρ spectral function (which is mostly due to production via the $D_{13}(1520)$ resonance).

This means that the dilepton spectrum is dominated by the π^0 and Δ Dalitz decays. One should note that at this energy, almost all pions are produced via excitation and decay of the Δ resonance.

Both of the mentioned Dalitz decays involve a transition form factor. But while the form factor of the π^0 Dalitz channel has been determined experimentally to a reasonable precision [87], the electromagnetic transition form factor of the Δ Dalitz decay is basically unknown in the time-like region (cf. section 2.2.2.3).

However, the dilepton spectrum at $E_{\text{kin}} = 1.25\,\text{GeV}$ is only mildly sensitive to this form factor, since the energy is not large enough to reach the VM pole-mass region. As fig. 24 shows, the simulation profits from including a form factor (shaded band) which exhibits a moderate rise in the time-like region of small q^2, but it is not sensitive to the actual VMD peak of such a form factor. The shown results have been obtained with the form factors of [98] and [99], as well as a constant form factor. They do not differ very strongly at this energy.

It is interesting to note that other calculations achieve a good agreement with the HADES data for pp collisions at 1.25 GeV without including any form factor for the Δ Dalitz channel [51] (which might be partly due to the different width parametrization used).

Furthermore we note that the slight overshooting in the pion channel is apparently due to the higher resonances, which are produced only in phase-space approximation. The missing treatment of proper angular momentum distributions seems to interfere with the HADES acceptance here, however it does not seem to be a problem at higher energies. We have verified that the discrepancy disappears if all pions are produced exclusively via Δ excitation, neglecting contributions from higher resonances. Furthermore, the introduction of angular distributions for the resonance production slightly mitigates the problem, but does not fully solve it.

It should also be mentioned that all our simulations are based on the usual transport approximations. In particular we assume a factorization of all amplitudes, separating
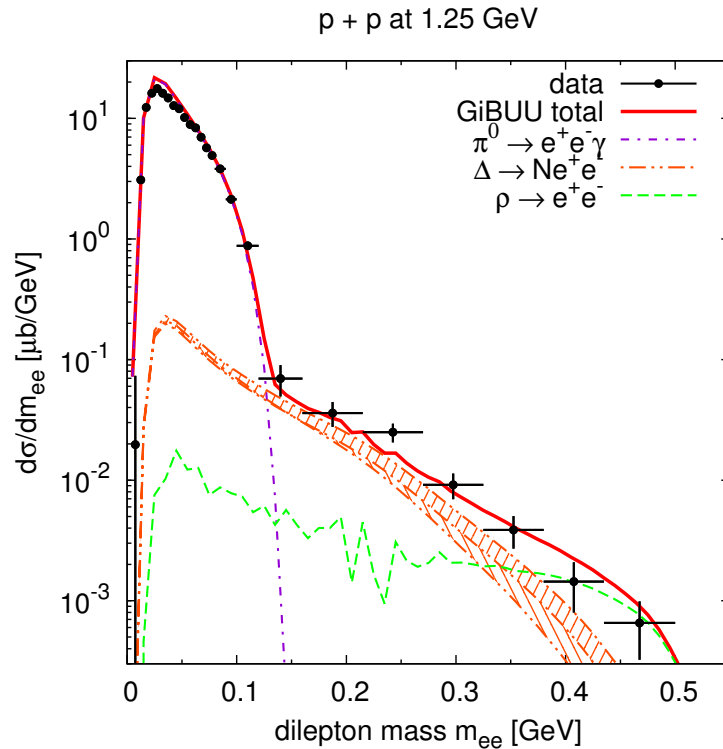
Figure 24: Dilepton mass spectrum for pp at $1.25\,\mathrm{GeV}$, in comparison to the data from [29]. The different contributions are indicated in the figure. The hatched area indicates the effect of the Δ form factor.

the production and decay vertices of a resonance and neglecting all appearing phases. Further we only add up different contributions to the dilepton spectrum incoherently, even if they could interfere quantum-mechanically. This negligence of the interference terms is probably a good approximation at higher energies, but might not be quite as good at lower energies, where interference effects could become important.

3.1.2   d + p at 1.25 GeV

In addition to the proton beam, also a deuteron beam with a kinetic energy of $1.25\,\mathrm{AGeV}$ has been used by HADES. Here, a trigger on forward-going protons has been set up in order to select the (quasi-free) np collisions, which are only accessible in this way: Detecting a forward proton means that it only acted as a spectator and the actual reaction happened on the neutron.

Due to the motion of the bound nucleons in the deuteron, the energy of the NN collisions is smeared out here, compared to the proton-beam case, with a tail reaching above the η-production threshold. The momentum distribution of the nucleons is determined by the deuteron potential, which in our simulations is given by the Argonne V18 potential [155]. Fig. 25 shows the dilepton invariant mass spectrum for this reaction. While the π^0-Dalitz channel in the low-mass region shows a similarly good agreement as in the pp case, the data points at larger invariant masses are underestimated by a factor of two or more. A stronger Δ channel can apparently not explain the shoulder in the data around $500\,\mathrm{MeV}$,
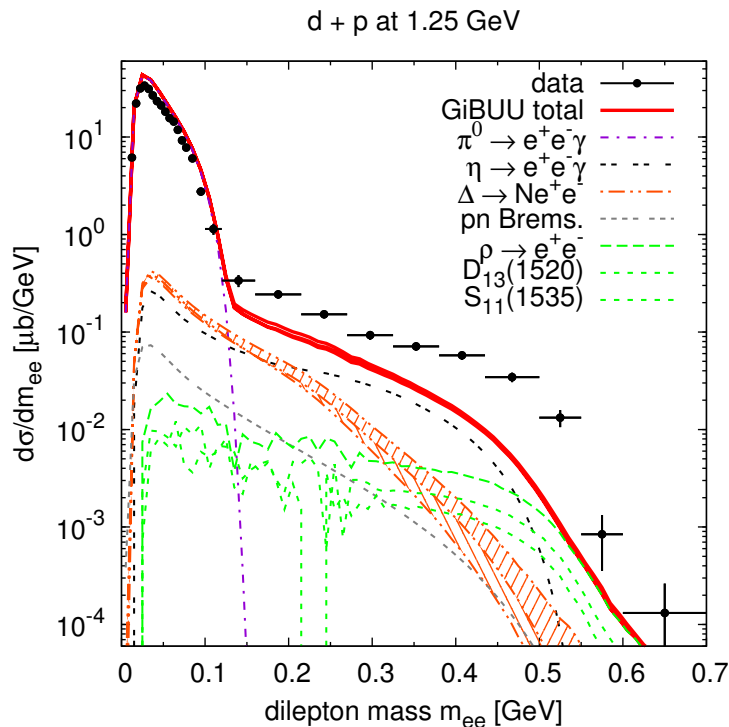
Figure 25: Dilepton mass spectrum for d+p at 1.25 GeV, in comparison to the data from [29].

since it falls off too steeply, even when including a form factor. In addition to the enhanced η production in np $\to$ npη, as described earlier, we have included a np $\to$ dη channel, which dominates the η production from np at threshold [113].

Unfortunately, the strong pn $\to$ pnρ^0 channel is experimentally not so well known. In our model, the ρ^0 production in d+p at 1.25 GeV is dominated by the $D_{13}(1520)$ and $S_{11}(1535)$ resonances. The latter is enhanced in np (since we boost its matrix element to mediate the enhanced η production on the neutron). The former is assumed to be isospin-symmetric, which may not be the case. In particular the isospin factors discussed in chapter 2.3.1.4, would increase the rho production on the neutron via the N^* resonances by a factor of 2.5.

Further isospin differences can come from non-resonant ρ production. In an OBE-model study [51] it has been found that the radiation from internal pion lines (with the appropriate VMD form factor) gives a sizable contribution at large invariant masses. Such a diagram implicitly contains a ρ^0 propagator (through the form factor), and gives additional ρ-like contributions on top of the resonance contributions included in our model.

Moreover, we might underestimate the 'pure' bremsstrahlung contributions, which do not involve resonance excitations, due to the soft-photon approximation. However, it is not expected that these terms would yield any dominant contributions [51, 156, 157].

As recently argued in [52], the inclusion of a "radiative capture" channel np $\to$ de$^+$e$^-$, fixed via deuteron photo-disintegration, might give further contributions in the high-mass region.

According to our analysis, the most probable candidate to fill the missing yield are indeed

ρ-like contributions. The radiation from internal pion lines is one such graph which we miss; this channel mainly contributes at large masses [51]. Furthermore, the subthreshold ρ production on the neutron (via baryon resonances) could be underestimated by our model. Analogous to the η case, it might be enhanced over pp $\rightarrow \rho^0 X$. And finally, channels like np $\rightarrow$ dρ^0 (related to the radiative capture) could contribute, which are completely unknown.

An additional source of dilepton strength in this reaction could be a $I(J^P) = 0(3^+)$ dibaryon resonance (also known as the 'ABC effect'), which was recently observed by WASA-at-COSY right in the relevant energy region [158], as pointed out already in [52]. It is conceivable that such a resonance could yield additional contributions to the dilepton spectrum (although this is pure speculation at this point).

The discrepancy between data and theory seen here is specific for this reaction at this particular energy; the results for nuclear collisions to be discussed later do not show such a large disagreement. We note that the observed cross section represents only about 15 - 20% of the actual cross section; the rest is being cut away by the acceptance filter. Thus, any deficiencies, for example, in the angular distribution of our dileptons could show up in rather large errors of the spectra after the acceptance cuts have been performed.

3.1.3   p + p at 2.2 GeV

Elementary pp collisions have been measured at a second beam energy of 2.2 GeV by the HADES collaboration. This energy is well above the η production threshold and is just high enough to reach the pole mass of the light vector mesons, ρ and ω, which dominate the high-mass part of the dilepton spectrum (as seen in fig. 26). The Δ channel plays a less important role here, since it is buried underneath the strong η and ρ channels. The ω only gives a small contribution, since the energy is only just at the threshold of ω production.

The ρ channel exhibits slightly more structure here than at 1.25 GeV (due to the contributions of different baryonic resonances to its production), showing a moderate step around 550 MeV. This step marks the border between a low-mass part, which is dominated by the $D_{13}(1520)$ resonance, and a high-mass part dominated by the $P_{13}(1720)$. In fig. 26 we show the contributions of these two resonances to the ρ channel, but omit the subdominant contributions of other resonances (for the sake of readability). The resonance contributions indeed improve the agreement with the data, compared to the PLUTO cocktail, which only includes phase-space population of the ρ [32]. However, there are still minor deviations, which seem to suggest an underestimation of the $D_{13}(1520)$ and an overestimation of the $P_{13}(1720)$ in our resonance cocktail at this energy.

At the bottom of fig. 26 we show the p_T spectra for three different mass bins in comparison to the data from [32]. Our simulations give a better agreement with the data than the PLUTO cocktail shown in [32] in all three mass bins. Most notably, we get an improvement from the larger ρ contribution in the highest mass bin. Compared to HSD [53], our agreement with the data at this energy is at a similar level, although the cocktail composition differs significantly: While HSD has a much bigger Δ Dalitz contribution, we have additional contributions from the higher resonances. Here the data does not have the sensitivity to properly discriminate both solutions, but the same discrepancy will show up again at higher energies.
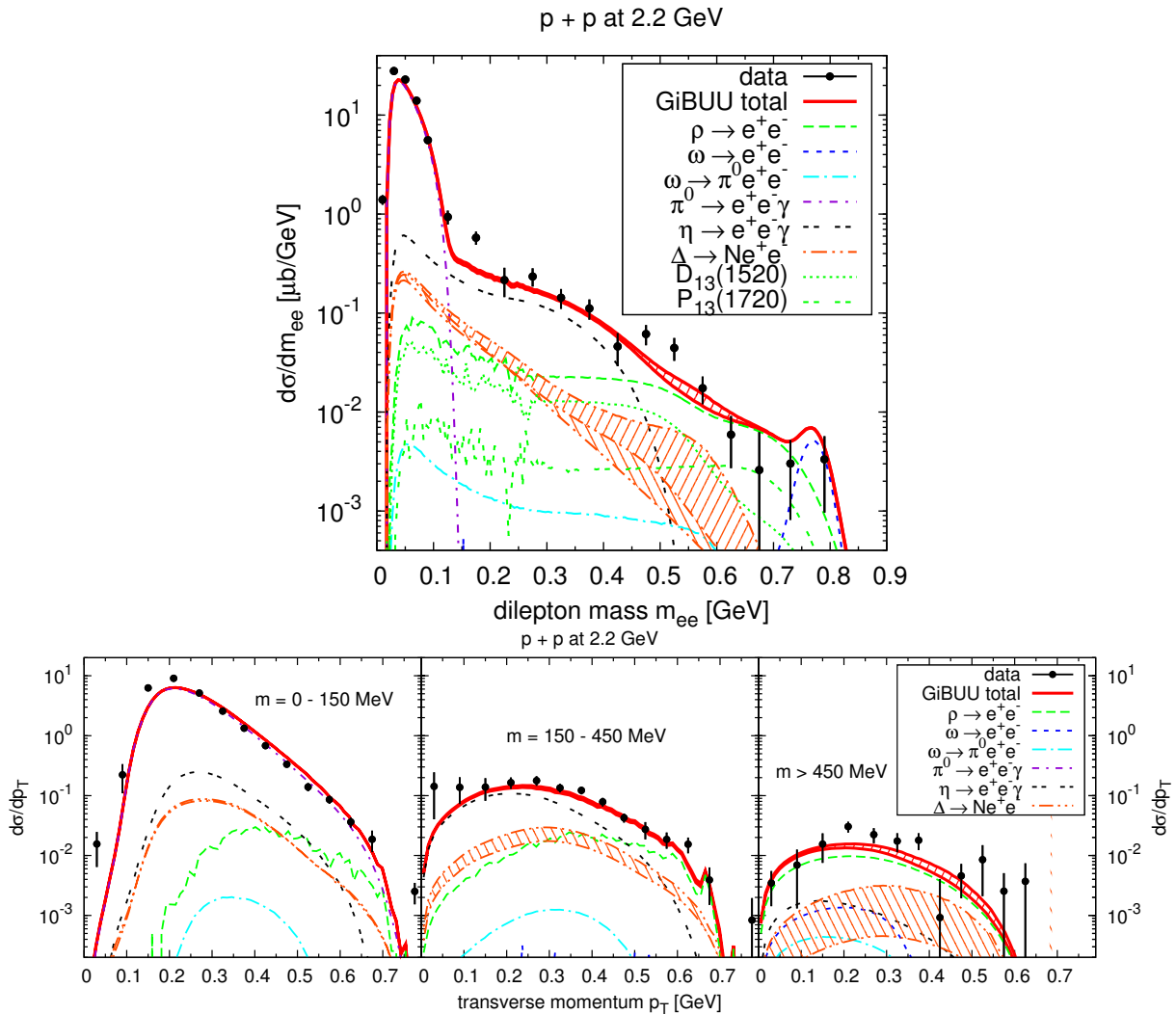
Figure 26: Top: Dilepton mass spectrum for pp at 2.2 GeV. Bottom: Transverse momentum spectra of dilepton pairs from pp at 2.2 GeV in three mass bins. The hatched area indicates the effect of the Δ form factor. Data from [32].

3.1.4   p + p at 3.5 GeV

The third and highest energy at which elementary pp reactions were measured by HADES is 3.5 GeV. Fig. 27 shows a comparison plot of a GiBUU simulation to HADES data [31] for this reaction, i.e. a proton beam of 3.5 GeV kinetic energy impinging on a fixed proton target, which corresponds to a center-of-mass energy of $\sqrt{s} = 3.18\,\text{GeV}$.

At this energy, the η, ω and ρ production channels are fully open, and even the ϕ production becomes energetically possible. The data only show a hint of a ϕ peak with very poor statistics, but it seems to be slightly underestimated by our simulation.

The η and ρ production is dominated by the channels $NN \to NN\pi\eta$ and $NN \to NN\pi\rho$, respectively. In our model these are saturated by double-resonance excitation, cf. sec. 2.3.1. The ω meson is presently produced in a non-resonant phase-space prescription through the exclusive and the $\pi\omega$ channel. Under these assumptions, we get a very good agreement with the data over the whole mass range, as shown in fig. 27(b).
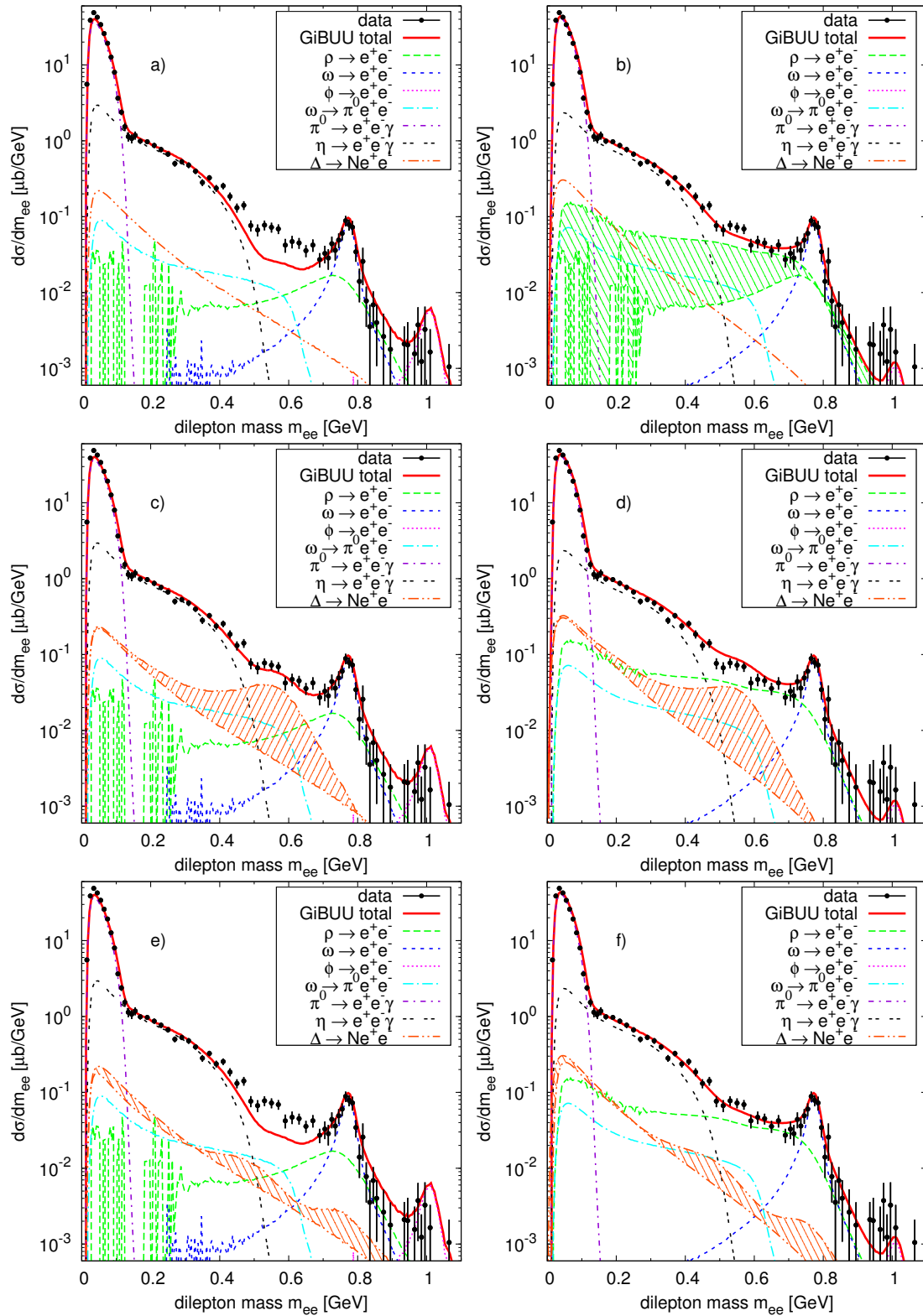
Figure 27: Dilepton mass spectrum for pp collisions at 3.5 GeV in comparison to data from [31]. Left: results obtained with PYTHIA [107], right: results obtained with the resonance model. Top: no form factor for the Delta Dalitz decay, middle: Wan/Iachello form factor [98], bottom: Ramalho/Pena form factor [99] (the effect of the form factor is indicated by a hatched band).

It is interesting to note that the resonance-model shape of the ρ channel differs significantly from the one obtained in our previous string-model investigations via PYTHIA [107], shown in fig. 27(a), which has also been adopted for the PLUTO simulations in [31]. It should be noted that we tuned a few of PYTHIA's internal parameters, cf. table 8, as discussed in [107]. The difference between the ρ in both models is illustrated in fig. 27(b), where the PYTHIA result given by the lower dashed (green) line in Fig. 27, whereas the new resonance-model based treatment yields the upper dashed line. The ρ-shape effect is due to the production of ρ mesons via nucleon resonances, i.e. $NN \to NR \to NN\rho$ and $NN \to \Delta R \to NN\pi\rho$, where the lighter resonances like e.g. $D_{13}(1520)$ will preferentially contribute to the low-mass part of the ρ spectral function. Together with the $1/m^3$ factor of the dilepton decay width, this results in a very flat distribution, which lacks a clear peak at the nominal mass, and dominates the dilepton spectrum in the intermediate mass region around 500 - 700 MeV.

Parameter	Default value	Professor tune [159]	Our value
PARJ(11)	0.5	0.31	0.15
PARJ(12)	0.6	0.4	0.2
PARJ(21)	0.36	0.313	0.25
PARJ(25)	1.0	0.63	0.63
PARJ(26)	0.4	0.12	0.12
PARP(91)	2.0		0.25

Table 8: PYTHIA parameters tuned to HADES energies [107].

The ρ spectral function is thus 'modified' already in the vacuum, simply due to the production mechanism via nucleon resonances. As seen in fig. 28, the ρ mass distribution in pp at 3.5 GeV peaks around 730 MeV, with an additional shoulder around 500 MeV (due to low-mass resonances, mainly the $D_{13}(1520)$). This spectral shape is due to phase-space limitations and specific resonance properties. It differs significantly from the mass distribution resulting from a PYTHIA simulation [107], which lacks any resonance contributions. Similar effects were already observed earlier with other models, e.g., in C+C reactions [45], and have in fact already been mentioned by early transport studies in the DLS era [160]. Unfortunately these effects have not received much attention in later years. We stress here that this 'modification' of the ρ shape is not an 'in-medium' effect at all: It is solely caused by the production mechanism via baryon resonances (which is basically a phase-space effect) and occurs already in elementary p+p collisions in the vacuum. This effect is crucial for understanding the intermediate mass region of the dilepton spectrum in pp collisions at 3.5 GeV (as seen in fig. 27) and already plays a role at 2.2 GeV (as seen in the previous section).
The particular influence of the $N^*(1520)$ resonance on dilepton spectra from NN collisions have already been investigated in [40], where it was concluded that the $N^*(1520)$ can indeed give sizable contributions to the DLS and HADES spectra, but is subject to moderate uncertainties.
It should be noted that the exact composition of the resonance contributions to the ρ channel, and therefore also its exact shape, are not fixed by data so far, but rather
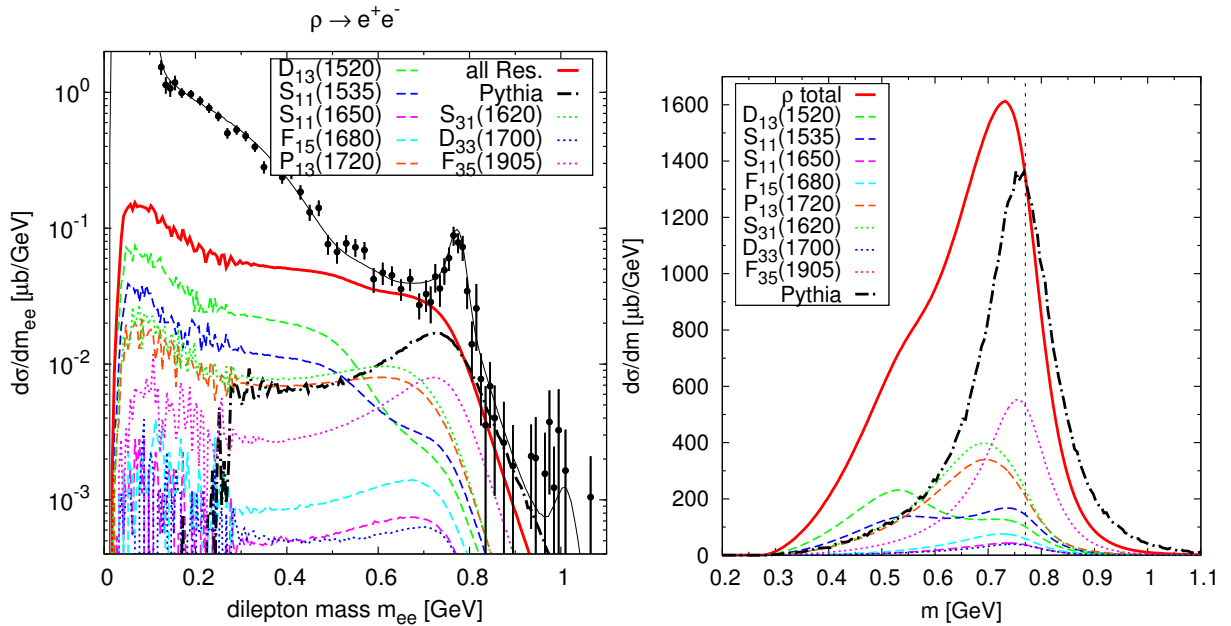
Figure 28: Top: Resonance contributions to the ρ channel in the dilepton mass spectrum. Bottom: Resonance contributions to the ρ mass distribution. The dashed line indicates the vacuum pole mass of the ρ meson. For comparison we also show the ρ meson contribution from our earlier PYTHIA simulations [107].

represent an 'educated guess'. The resonance composition can be checked via πN invariant mass spectra. Moreover, possible $\rho\Delta$ decay modes of certain resonances could give further contributions to the dilepton cocktail, as mentioned earlier.

Comparing our cocktail to other transport models like HSD [47] or UrQMD [49], one of the most significant discrepancies shows up in the size of the Δ channel. While in our model the Δ does not give any significant contribution to the total dilepton yield at $E_{\mathrm{kin}} = 3.5\,\mathrm{GeV}$ (without a form factor), this is not so for the two other models. Both of them have a much stronger Δ channel, which even dominates the dilepton spectrum in the intermediate mass region around $600\,\mathrm{MeV}$. We stress here that there are several factors of uncertainty in the Δ channel, for example the inclusive production cross section, but also the parametrization of the Δ decay width (hadronic as well as leptonic) and the completely unsettled question of the electromagnetic N-Δ transition form factor.

To illustrate the uncertainty connected to the Δ form factor, we show in fig. 27 the dilepton mass spectrum with three different assumptions for the Δ channel: 1) Using no form factor at all, 2) using the model of [98] and 3) using the model of [99]. Each of the three cases is shown in a resonance-model and a PYTHIA setup. For the PYTHIA case there is a gap in the intermediate mass region, where the data are underestimated if no form factor is used. However the gap is nicely filled up by the usage of the Iachello form factor. In the resonance-model picture, however, the situation is completely different: Due to the resonance enhancements in the ρ channel, the data can already be described nicely without any form factor, and the use of the Iachello form factor rather deteriorates the agreement. The Ramalho form factor is actually surprisingly close to the "no-form-factor" scenario, so that it also results in a good agreement with the data in the resonance-model approach.
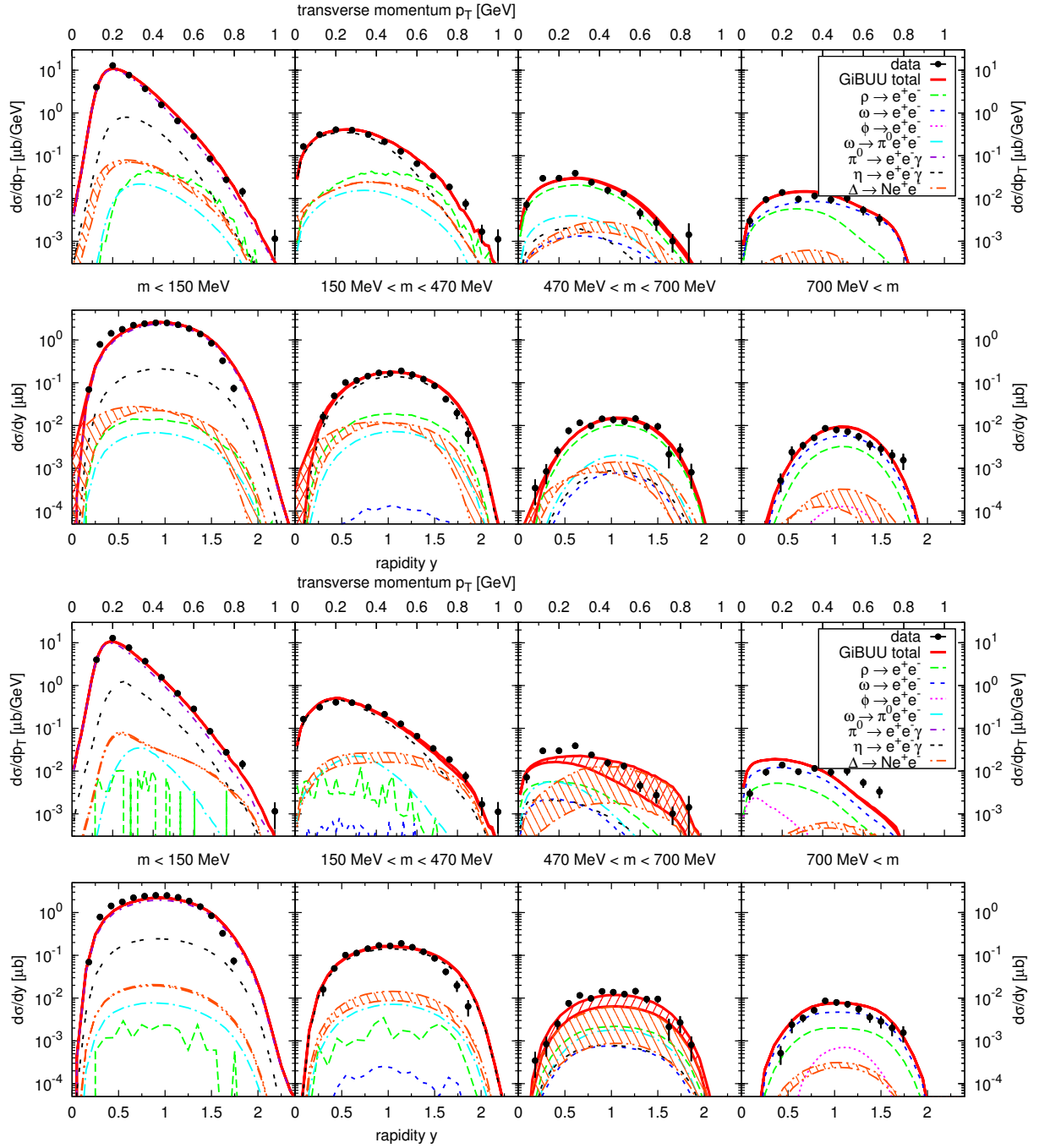
Figure 29: Transverse momentum and rapidity spectra of dilepton pairs from pp at 3.5 GeV in four mass bins. Top: Resonance model with Ramalho form factor, bottom: PYTHIA with Iachello form factor. The hatched area indicates the effect of the Δ form factor. Data from [31].

In order to understand the underlying processes, it is not sufficient to consider only the mass spectrum. Other observables can give further insight into the reaction dynamics and can serve as a cross check for the validation of theoretical models. In order to compare to the data from [31], we examine the transverse momentum and rapidity distributions in four different mass bins (see fig. 29):

- $m < 150\,\text{MeV}$, dominated by the π^0 Dalitz channel,

- $150\,\text{MeV} < m < 470\,\text{MeV}$, dominated by the η Dalitz decay,

- $470\,\text{MeV} < m < 700\,\text{MeV}$, dominated by the ρ and/or Δ channel,

- $700\,\text{MeV} < m$, dominated by the ω and ρ.

Distinguishing several mass bins is useful in order to separate the contributions of different channels. In all four mass bins, we achieve an excellent agreement with the HADES data [31] when using the resonance model (together with the Ramalho/Pena form factor). As an alternative to the resonance model results, we also show the PYTHIA-based simulation with the Wan/Iachello form factor, which gave a similarly good description of the mass spectrum. The description of the p_T data is clearly worse in this case, due to the stronger Δ contribution, which obviously destroys the agreement in the mass bin of 470-700 MeV. The same p_T disagreement was seen in [53], also due to a strong Δ contribution (there, however, already without a transition form factor). From this discrepancy we conclude that the Δ Dalitz decay cannot give a dominant contribution at this energy, and that its contribution is overestimated in HSD (probably due to an isospin mistreatment in FRITIOF). Also the IQMD and UrQMD results published in [53] showed a similarly large Δ contribution as HSD. However, their Δ channel might be overestimated due to different reasons: In UrQMD, a mass-independent lifetime was used, which apparently leads to an overestimation of the dilepton contributions from the high-mass tail of the Δ [161]. IQMD only includes an exclusive production mechanism for the Δ, which could lead to an overpopulation of the high-mass tail (we note that the high-mass contributions dominate the Δ Dalitz channel). The absence of more inclusive production channels also means that IQMD is simply not applicable at energies as high as 3.5 GeV.

Out of the six scenarios we have studied, only the resonance-model approach with the Ramalho form factor is able to fully describe both the mass and the p_T spectra. Using no form factor for the Δ also gives good results, but is not a valid solution from a theoretical point of view, since clearly some kind of form factor is required for the Δ Dalitz decay.

3.1.5   p + Nb at 3.5 GeV

After having discussed all elementary reactions measured by HADES, we now come to the first nuclear collision system: p+Nb. Fig. 30 shows simulated dilepton spectra for p+Nb collisions at 3.5 GeV using vacuum spectral functions, compared to data from [33]. As for p+p at 3.5 GeV, we filter our dilepton events through the HADES acceptance filter and cut on $\theta_{\text{ee}} > 9°$. The single-lepton momentum cut is slightly different here: $0.1\,\text{GeV} < p_{\text{lep}} < 2.0\,\text{GeV}$.

The level of agreement is similar to the p+p reaction at the same energy, for which it it was concluded that the resonance-model scenario (together with the Ramalho form
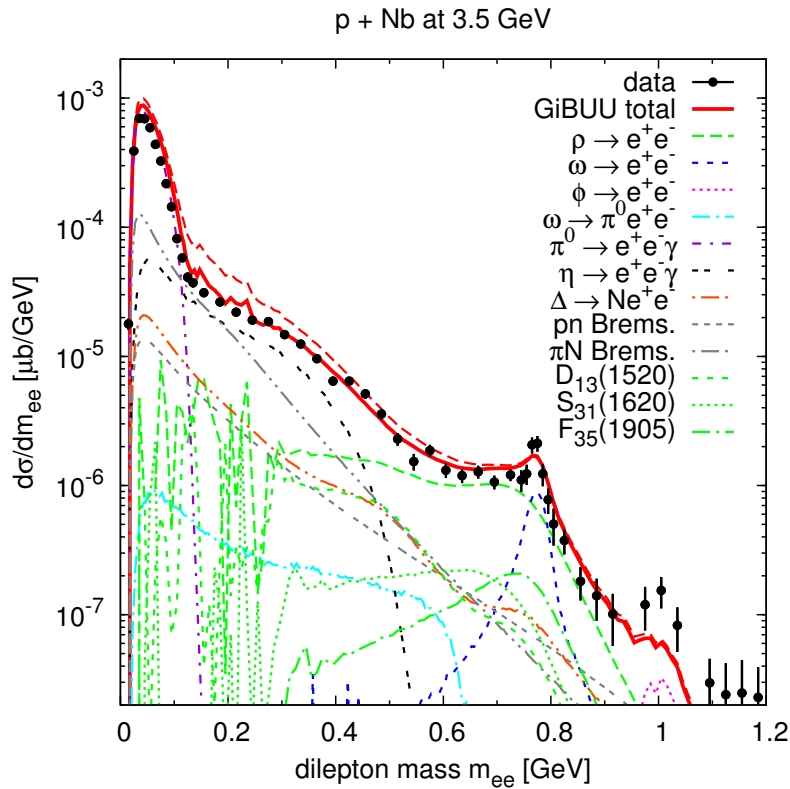
Figure 30: Dilepton mass spectrum for p+Nb at 3.5 GeV, showing all contributing channels with vacuum spectral functions. The solid red line indicates the total without πN bremsstrahlung, while the dashed red line includes πN bremsstrahlung. Data taken from [33].
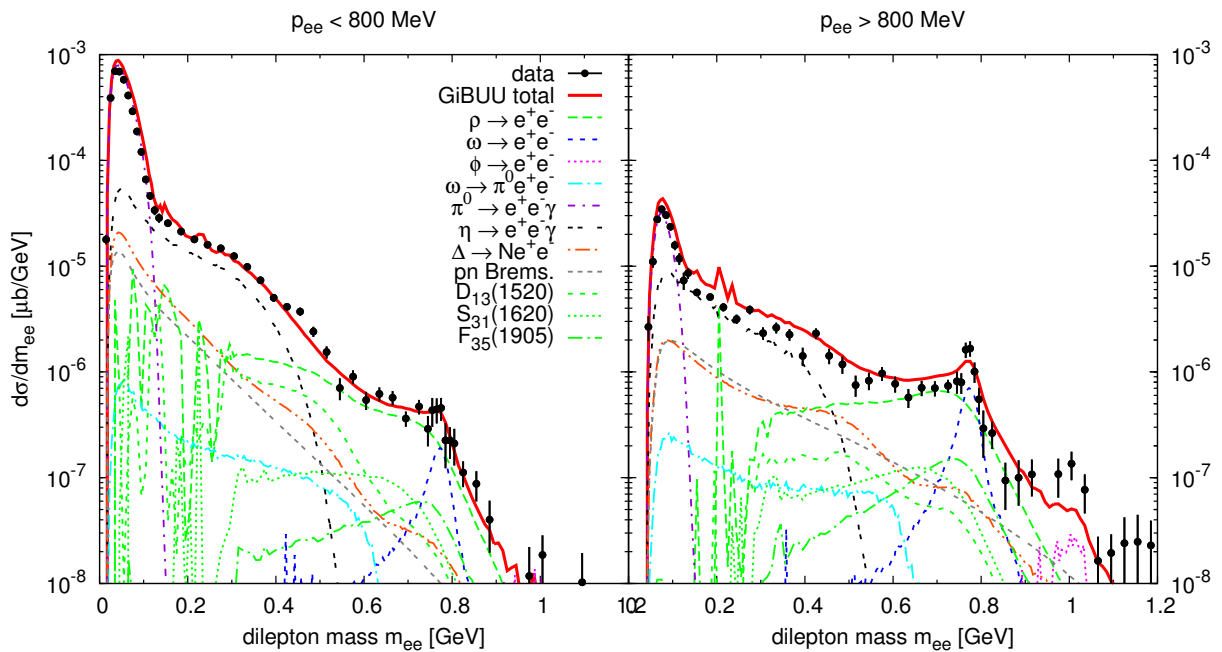
Figure 31: Dilepton mass spectra for p+Nb at 3.5 GeV in two different regions of dilepton momentum. Data from [33].

factor for the Δ) gives the best agreement with the data. Therefore we also use the same scenario here. The largest deviations from the data are a slight overshoot in the pion region and a strong underestimation in the ϕ peak (by roughly a factor 5). While the reason for the pion overshoot can probably be found in the angular distributions (similar discrepancies were observed in pp and dp at 1.25 GeV), the reason for the missing ϕ yield is less clear. There was already a hint of ϕ underestimation in pp at 3.5 GeV. However, the large error bars prevented any final conclusions. The error bars in pNb are smaller, and the deficiency is more pronounced. Apart from the discrepancy in pp, either the $pn \rightarrow pn\phi$ cross section could be underestimated (which is currently assumed to be equal to $pp \rightarrow pp\phi$, although some models predict enhancement factors of 3 – 7 [162].) or the ϕ absorption could be overestimated. We note that PYTHIA yields a somewhat larger ϕ contribution, which is closer to the data [107].

It should be noted that we actually show the 'total' spectrum in two versions in fig. 30, namely including the πN bremsstrahlung (red dashed) and without (red solid). It is apparent that the agreement with data is quite good without the πN bremsstrahlung contribution, and gets much worse when it is added (in particular in the low-mass region). We take this as an indication that the soft-photon approximation that we are using does simply not provide a reasonable description of πN bremsstrahlung (which is indeed expected also from a theoretical point of view, cf. the discussion in section 2.2.2.6).

In fig. 31, the dilepton mass spectrum is plotted for two different momentum regions: A "fast" component ($p_{ee} > 800\,\mathrm{MeV}$), which mostly comes from primary pp collisions, and a "slow" component ($p_{ee} < 800\,\mathrm{MeV}$), which contains more contributions from secondary collisions (e.g. πN). While the mass spectrum of the "slow" sources is quite steep and contains little high-mass contributions, the "fast" spectrum is much flatter and shows more pronounced peaks of the relatively heavy ω and ϕ mesons. Interestingly also the shape of the ρ contribution is affected rather strongly by the momentum cut: The slow part is clearly dominated by light ρ mesons from decays of the $N^*(1520)$, but in the fast part the relative strength of the different baryonic resonances is changed drastically, in favor of heavier states like the $\Delta^*(1905)$. Our model represents the qualitative features of both spectra rather well, which we take as a further confirmation of our hypothesis that ρ production via baryonic resonances is an important ingredient for the dilepton spectrum of this reaction, just as in the pp case. Here, the baryonic resonances are not only produced through pp collisions, but also in secondary πN collisions, both of which seem to be well under control in our model.

Apart from the minor discrepancies mentioned earlier, i.e. a slight overestimation of the pion channel and an underprediction of the ϕ contribution, the fast spectrum also hints at a minor overestimation of the η component (probably due to primary pn collisions), while the η contribution to the slow spectrum (dominated by secondary πN collisions) is more accurate.

It should be noted, however, that a recent analysis of inclusive π^0 and η production from p+Nb collisions at 3.5 GeV showed an excellent agreement of our extended resonance model with the published data [163], which further confirms the validity of our dilepton cocktail. In light of these results, the dilepton disagreement in the pion channel is somewhat surprising and might possibly hint at a slight normalization problem of the dilepton data.

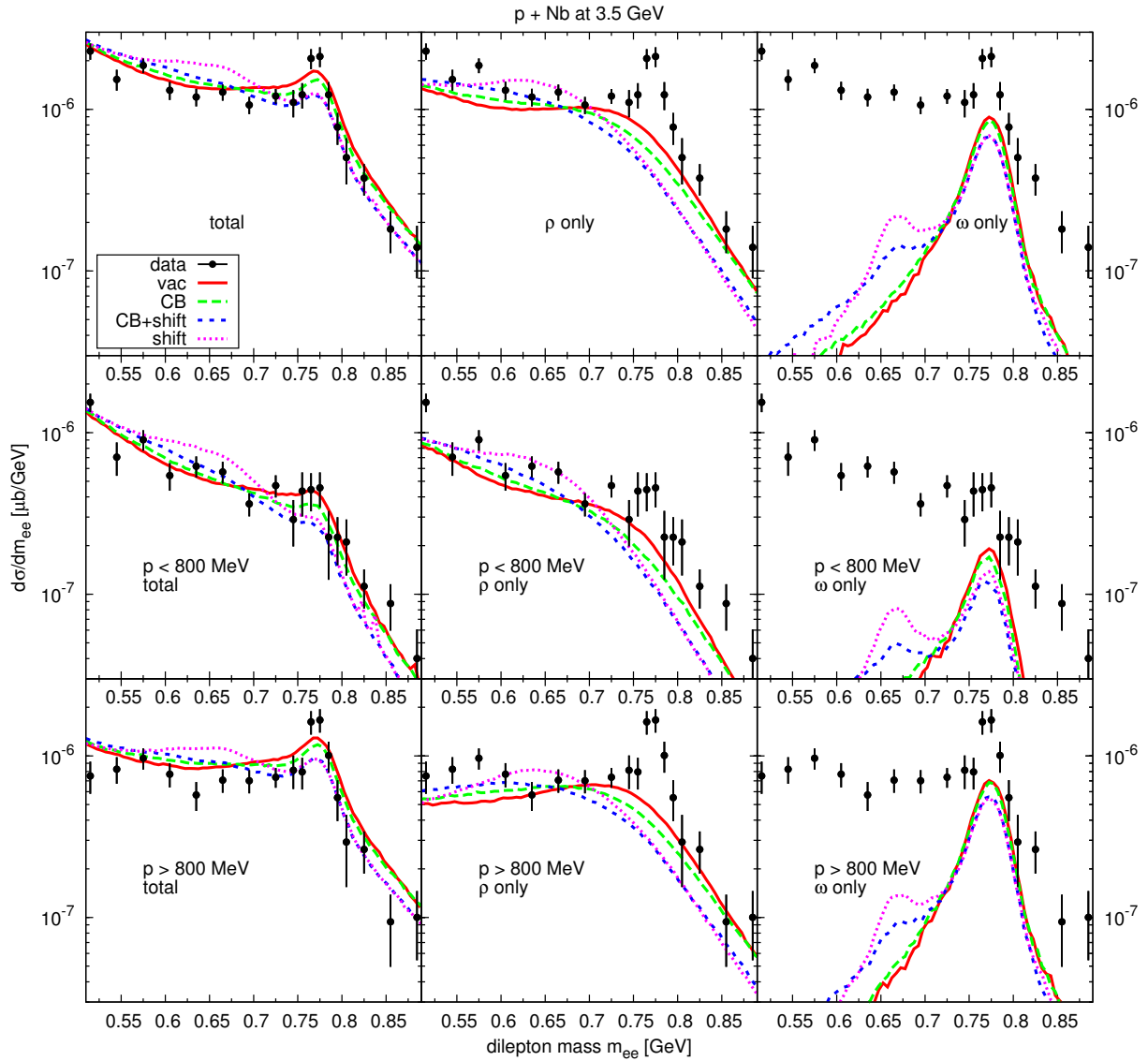It is clear that in p+Nb reactions there are a few additional effects, compared to the

Figure 32: Dilepton mass spectra for p+Nb at 3.5 GeV. Comparison of different in-medium scenarios (vacuum spectral functions for the vector mesons, collisional broadening, 16% mass shift, collisional broadening plus mass shift). Left column: Total spectrum, center column: ρ contribution, right column: ω contribution. Top row: All momenta, middle row: $p_{ee} < 800\,\mathrm{MeV}$, bottom row: $p_{ee} > 800\,\mathrm{MeV}$. Data taken from [33].

elementary p+p reactions. First of all, the primary p+N collisions will be nearly identical, apart from binding effects and some Fermi smearing and Pauli blocking, but besides p+p also p+n collisions play a role. Furthermore, the produced particles undergo final-state interactions within the Nb nucleus, and processes like meson absorption and regeneration may become important. The secondary collisions will on average have lower energies than the primary N+N collisions. Finally also the spectral functions may be modified in the nuclear medium (for example those of the vector mesons, but also of the baryons).

In particular the mass spectrum above 500 MeV can receive modifications from the inclusion of in-medium effects in the vector-meson spectral functions. Fig. 32 shows the typical in-medium scenarios: The first one includes a collisionally broadened in-medium width, while the second one assumes a pole-mass shift according to eq. (92). The third scenario combines both of these effects.

The modifications introduced by these scenarios are roughly on the same order of magnitude as the systematic errors of the data, and so far there is no clear evidence for medium modifications of the vector-meson properties in cold nuclear matter from the HADES data. However, it looks as if a mass shift tends to deteriorate the agreement with the data (mostly at the ω peak, but for a pure mass shift also in the region around 650 MeV). In fig. 32, we do not only show the total dilepton spectrum in the four scenarios, but also the contributions of the ρ and ω channels separately, in order to demonstrate the effect that the in-medium modifications have on both of these mesons. In general the modifications are more dramatic for the ρ meson, since it has a much larger probability to decay inside the nucleus than the ω, due to its short lifetime. The scenarios including a mass shift mainly result in a decrease of the high-mass and on-shell contributions of the ρ spectrum and an increase of the low-mass contributions. The collisional broadening mostly shifts strength from the pole region to lower masses (and does not strongly affect the high-mass region, which is suppressed by phase space). In case of the ω, the peak itself is only weakly modified, since most of the ω mesons actually decay outside of the nucleus (according to their vacuum spectral function). The strongest modification is visible in the case of a pure mass shift, where a sharp in-medium peak emerges, which however is roughly a factor five below the vacuum peak, and therefore not really visible in the total spectrum. In the broadening-plus-shift scenario, this in-medium peak is broadened so strongly that it basically melts away and is not visible as a peak any more, but only as a general enhancement in the low mass tail. The pure broadening scenario only shows a very weak enhancement in the low mass tail. The high-mass tail of the ω is not affected strongly by any of the in-medium scenarios. It is important to note that the in-medium modifications applied here only affect the spectral function itself (which is being 'populated' through particle production in the medium). The scattering and absorption processes which lead to collisional broadening are included in all four scenarios. In this respect the scenarios without collisional broadening of the spectral function are inconsistent, since they include absorption processes, but not the spectral broadening which is connected to it. However, our results also show that the dilepton spectra are not exceedingly sensitive to the spectral broadening, and that in fact the vacuum spectral functions provide a good approximation also in the medium. For the ρ meson, one can argue that collisional broadening of the spectral function only represents a secondary effect, which comes on top of the even stronger modifications which are caused by the production through baryonic resonances. While the top row of fig. 32 shows the mass spectrum for all pair momenta, the middle

and bottom row display the mass spectra of 'slow' and 'fast' sources, with a momentum cut at $p_{ee} = 800\,\mathrm{MeV}$, as used already in fig. 31. As expected, the 'slow' spectrum (with $p_{ee} < 800\,\mathrm{MeV}$) exhibits stronger sensitivity to the in-medium modifications, since the slow mesons have a larger probability of decaying inside the nucleus. This can be seen most clearly in the ω in-medium peak, which is much more pronounced than in the 'fast' spectrum. But unfortunately also the 'slow' spectrum does not allow to draw any more extensive conclusions that the total spectrum, since the data which enters there only represents a subset of the total data set, and therefore the statistical errors are larger. (Of course it should also be noted that the data points can only be compared directly to the curves in the left column, where the total simulated spectrum is plotted. In the other two columns, the data was only added to guide the eye.)

It should be mentioned that the ω absorption in GiBUU has been adjusted to fit the transparency-ratio measurement of CBELSA/TAPS [35], using a factor of $K = 2$ to increase the inelastic ωN cross section (cf. section 2.3.2.2 and 4.2). The HADES dilepton data seem to be roughly compatible with the CBELSA/TAPS transparency ratio, since our simulation agrees reasonably with the HADES data in the ω mass region.

However, one should keep in mind that a statement about ω absorption depends on a number of prerequisites. For example, one needs to have the ρ contribution well under control, since it represents a large background under the ω peak. Given the discussion about resonance contributions to the elementary ρ production, this is already not a trivial task, even more complicated by possible in-medium modifications of the ρ meson. Furthermore, the size of the ω peak in pNb crucially depends not only on the production cross section in pp collisions (which is well determined via the elementary pp data at $3.5\,\mathrm{GeV}$), but also in pn, which is unknown. We assume ω production cross sections which are isospin-independent, i.e. equal in pp and pn. However, there are experimental indications that the ω production in pn is enhanced by roughly a factor of two, while theory predicts even larger factors [164].

In addition to the in-medium modifications of the vector mesons, also the baryonic resonances can receive similar modifications in the medium. Since the production via baryon resonances is particularly important for the ρ meson, in-medium modifications of these resonances can lead to further modifications of the ρ contribution to the dilepton spectrum, which should be considered in future investigations.

The p_T and rapidity spectra for p+Nb are depicted in fig. 33 with the same mass binning as in the p+p case. Overall we get quite a good agreement in both observables. The shown p_T and rapidity spectra do not include any in-medium effects for the vector mesons and are not significantly sensitive to such modifications.

For a further discussion of the nuclear effects, it is useful to consider the quantity

$$R_{\mathrm{pNb}} = \frac{\mathrm{d}\sigma_{\mathrm{pNb}\to e^+e^-X}/\mathrm{d}p}{\mathrm{d}\sigma_{\mathrm{pp}\to e^+e^-X}/\mathrm{d}p} \cdot \frac{\sigma_{\mathrm{pp}\to X}}{\sigma_{\mathrm{pNb}\to X}} \cdot \frac{A_{\mathrm{part}}^{\mathrm{pp}}}{A_{\mathrm{part}}^{\mathrm{pNb}}} \, , \tag{95}$$

i.e., the ratio of dilepton yields in pNb vs. pp (momentum-differential), normalized to the total cross section for these reactions and the average number of participants. If medium effects are negligible, this quantity is expected to be unity. Therefore, any deviation from unity indicates medium effects such as, e.g., absorption ($R < 1$) or secondary production ($R > 1$). Fig. 34 shows R_{pNb} as a function of the dilepton momentum in four different invariant-mass bins, with the contributions from the different source channels. In order
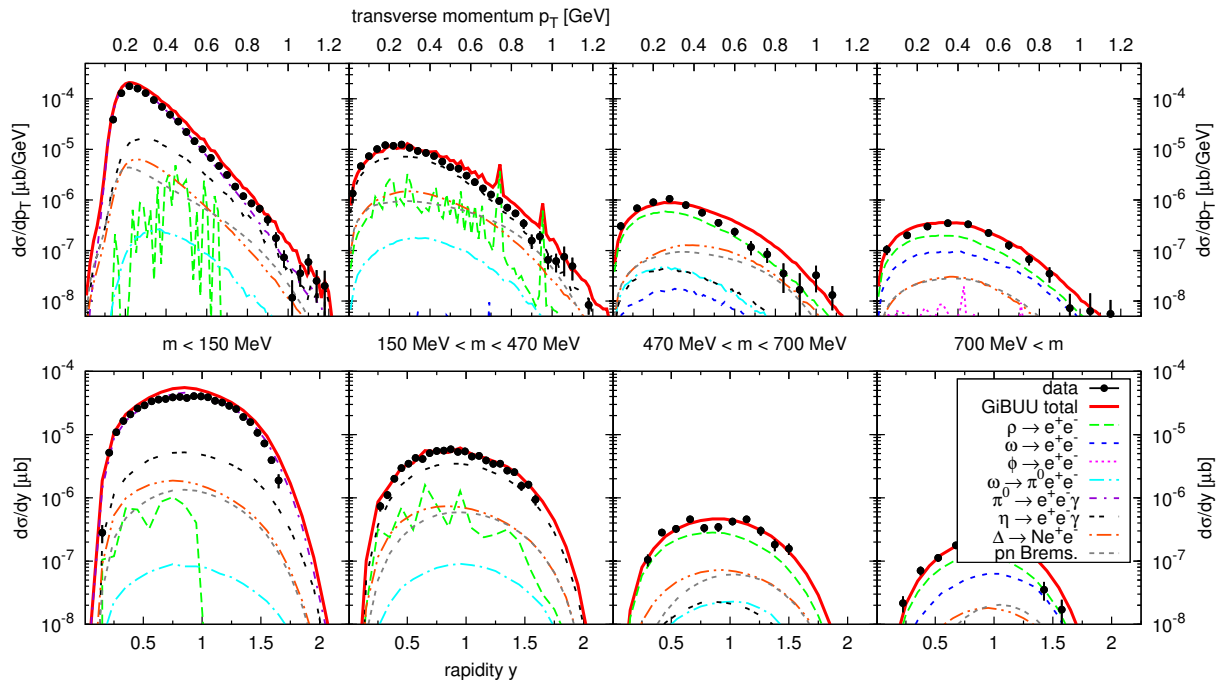
Figure 33: p_T and rapidity spectra of dileptons from p+Nb reactions in four mass bins, in comparison to data from [165].
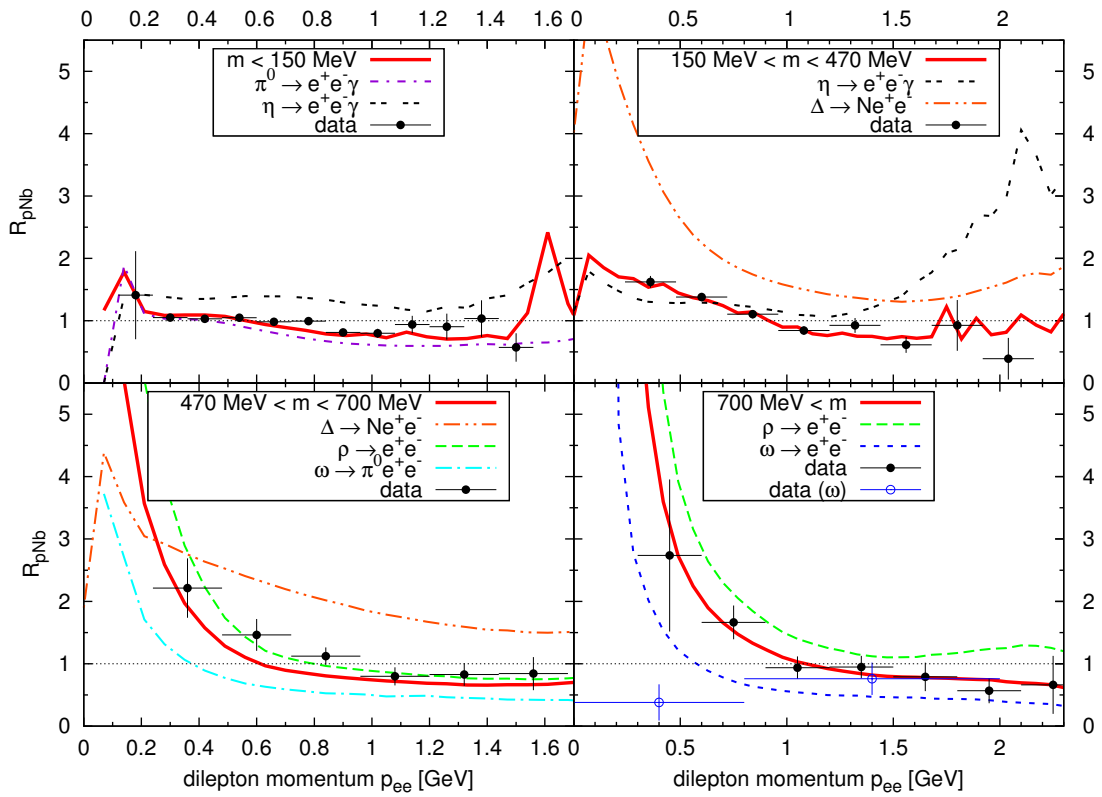
Figure 34: Ratio of dilepton yield from p+Nb and p+p collisions at 3.5 GeV as a function of momentum, in four mass bins, in comparison to data from [33].

to be able to compare our results to the data from [33], we chose to use the same normalization constants as in [33], namely $\sigma_{\text{pp}\to\text{X}} = 43.4\,\text{mb}$, $\sigma_{\text{pNb}\to\text{X}} = 848\,\text{mb}$, $A_{\text{part}}^{\text{pp}} = 2$ and $A_{\text{part}}^{\text{pNb}} = 2.8$.

While R_{pNb} is relatively flat (and close to one) in the π^0 region, the higher mass bins show a strong enhancement at low momenta, which can be understood as secondary particle production and/or elastic rescattering. The high momentum region in all mass bins tends to show a slight depletion, connected to absorption (and, again, elastic rescattering, which tends to descrease the particle momentum). Overall one can see that the simulation nicely follows the qualitative features seen in the data.

One exception to this, however, is the identified ω. Due to the limited statistics, there are only two data points, which are averaged over large momentum bins. Both of these data points are below one, indicating that absorption is the dominant effect for the ω meson, with a slowly rising momentum dependence. In contrast, the simulation yields an R_{pNb} for the ω meson, which clearly falls of with momentum and rises to rather large values for low momenta. While this behavior agrees with the total R_{pNb} data in the highest mass bin, it disagrees with the identified ω which shows an opposite trend.

The observable R_{pNb} could also help to pin down the relative contribution of the Δ Dalitz channel to the dilepton spectrum. As can be seen in Fig. 34, the Δ's ratio is rather large, due to the enhanced production of the $\Delta^{+,0}$ charge states in pn collisions, relative to pp. The isospin factors for $NN \to N\Delta^{+,0}$ are a factor of two larger in pn than in pp.

This isospin dependence could provide additional constraints for distinguishing the ρ and Δ contributions in the intermediate mass range of 470 - 700 MeV. Since the ρ channel dominates our simulated cocktail in this mass range, the total value of R_{pNb} roughly follows the R-value of the ρ channel. If the spectrum would be dominated by the Δ Dalitz channel in this mass range, then the total value of R_{pNb} would be more similar to the Δ's R-value.

Another way to evaluate the cold-nuclear-matter effects in pNb is to consider the excess yield in pNb, by subtracting the pp baseline yield in a suitable way. This has been done with the experimental data in [33], and we do the same with our simulation results here, in order to obtain an interpretation of the experimental excess, and to get an additional check of the validity of our model. For this purpose, we define the "excess yield" in the following way:

$$\left(\frac{\mathrm{d}\sigma}{\mathrm{d}m}\right)_{\text{excess}} = \left(\frac{\mathrm{d}\sigma}{\mathrm{d}m}\right)_{\text{pNb}} - N \cdot \left(\frac{\mathrm{d}\sigma}{\mathrm{d}m}\right)_{\text{pp}} \tag{96}$$

Here, N is a normalization factor, which is defined in the same way as for R_{pNb}:

$$N = \frac{\sigma_{\text{pNb}\to\text{X}}}{\sigma_{\text{pp}\to\text{X}}} \cdot \frac{A_{\text{part}}^{\text{pNb}}}{A_{\text{part}}^{\text{pp}}} \approx 27.35 \tag{97}$$

Further, the ω peak has been subtracted in both pp and pNb (since no significant modification of the ω line shape is expected, due to the rather long lifetime of the ω).

Fig. 35 (top, left) shows the resulting total excess spectrum for 'slow' pairs ($p < 800\,\text{MeV}$), and also the separate excess from different channels in our model. The overall agreement with the data is rather satisfactory. In the mass region from 150 to 400 MeV, the observed experimental excess is well explained by a dominant excess from the η channel (due to
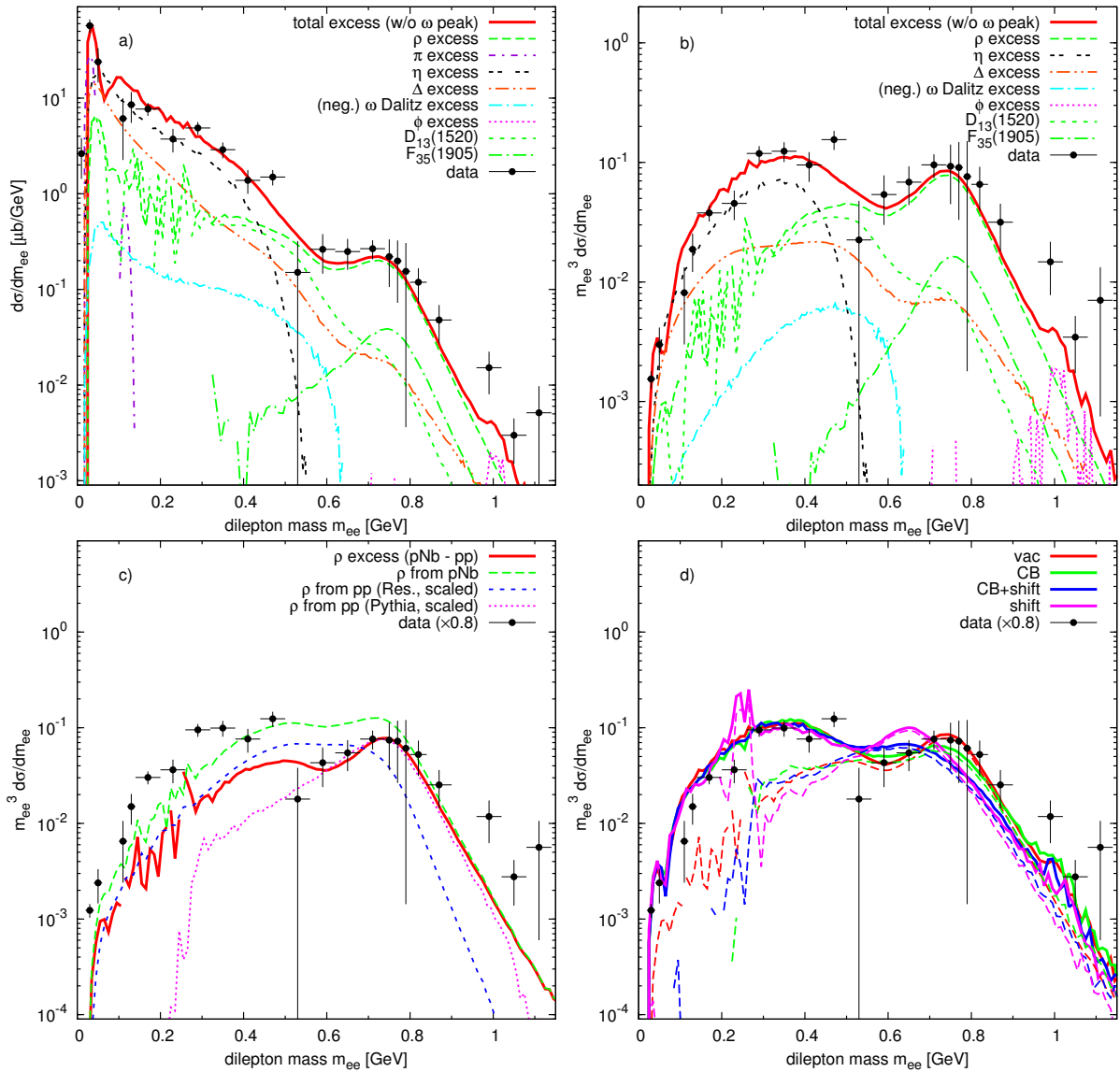
Figure 35: a) Excess of pNb over pp. b) Multiplied with factor m^3. c) ρ excess compared to original pp and pNb spectra. d) With medium modifications. Data from [33].

secondary production of η mesons). Going higher in mass, one first observes a slight dip in the data around 500 - 600 MeV, followed by a shallow bump in the vector-meson region. Both features are seen even more clearly in the simulation, where the peak is obviously attributed to the ρ meson (mostly from secondary ρ production processes, since the pp baseline has been subtracted; no contribution of the ω is visible since it had been subtracted).

The interpretation of the dip is a bit more involved. At first sight it simply appears to be due to the crossover from a dominant η excess to a strong ρ excess. However, the dip structure is already visible in the ρ excess itself. This is a bit surprising, since this sort of dip was not visible in the ρ channel in the original pp and pNb spectra. Apparently this structure is caused by the interplay of the different resonances contributing to the ρ meson production: There is some low-mass excess due to the $D_{13}(1520)$ and also a

significant excess around the ρ peak due to heavier resonances (we show as an example the $F_{35}(1905)$ which gives the largest contribution). In between seems to be a small region where no resonance produces a large excess, which results in the dip of the total ρ excess. It is very interesting that this feature is also visible in the data, although the dip is not as pronounced there and also seems to occur at slightly smaller masses.

The shape of the ρ peak itself is rather well reproduced, although it is slightly underestimated in total. We remind of the fact that the ρ meson in our approach is effectively not a simple vacuum Breit-Wigner function, but includes modifications through effects like production via baryonic resonances (e.g. $NN \to NR \to \rho NN$), secondary production channels (e.g. $\pi N \to R \to \rho N$) and explicit rescattering in the medium (e.g. $\rho N \to R \to \rho N$), even if we do not explicitly utilize in-medium spectral functions.

In fig. 35 (top right) we show the excess spectrum multiplied with m_{ee}^3, in order to compensate the mass dependence of $\rho \to e^+ e^-$, so that one basically sees the ρ spectral function there (including phase-space effects, however, and with additional backgrounds from the other dilepton channels). In this representation, the ρ peak is more clearly visible and the low-mass backgrounds are suppressed.

In the bottom-left part of fig. 35, we have a closer look at the ρ contribution to the excess spectrum: Apart from the ρ excess itself (as the difference between pNb and pp), we also show the ρ contributions to the original pNb and pp spectra (which the excess was derived from). Both of these have a rather flat and broad shape with strong low-mass contributions from light N^* resonances. The 'excess ρ', however, shows a pronounced two-peak structure. We interpret this double peak as a manifestation of the two main sources of excess: Firstly, the Fermi motion in the Nb nucleus generates additional contributions from higher energies than available in pp, which amounts to an additional source of potentially high-mass (i.e. on-shell) ρ mesons, which presumably is responsible for the high-mass peak of the ρ excess. Furthermore, secondary collisions at rather low energies are another source of ρ mesons (e.g. secondary ρ production from πN collisions and rescattering of ρ mesons). Due to the low energies and the limited phase space, these ρ mesons tend to have low masses and are responsible for the low-mass peak of the ρ excess, which is strongly dominated by the light $D_{13}(1520)$ state. This secondary ρ peak cannot be directly confirmed by the data, due to the large background from η Dalitz decays and the sizable error bars of the data. The primary ρ peak, however, is in rather good agreement with the data. If we discard the slight overall underestimation of ρ excess in the simulation by scaling down the data by roughly 20%, we see that the shape is fully compatible with the data (apart from the very-high-mass region above 1 GeV, which should be dominated by other sources, such as the ϕ meson). Interestingly the high-mass part of the ρ excess does not show any deviations from a pure vacuum spectral function. For comparison we show the ρ contribution from pp collisions via PYTHIA, which we use as the baseline for a vacuum ρ, since it includes the correct phase-space effects for this energy, but without any baryon-coupling effects. It is in good agreement with the excess ρ from the data and the simulation above 600 MeV. This we take as an indication that the excess ρ in pNb is fully compatible with a pure Breit-Wigner vacuum spectral function, which is somewhat surprising, since the pNb dilepton spectrum (and even the one from pp) required significant enhancements of the low-mass shoulder of the ρ spectral function due to resonance couplings. In the excess spectrum, the remnant effects of these couplings are minor (basically limited to the $N^*(1520)$) and cannot be clearly identified in the data,

due to the underlying η Dalitz background.

Finally, the lower right part of fig. 35 shows the excess spectrum with additional modifications of the ρ spectral function (collisional broadening, mass shift and broadening plus shift). The solid line shows the total excess, while the dashed shows the excess from the ρ meson. It is apparent that the vacuum spectral function clearly shows the best agreement with the data points. The collisional broadening scenario results in a flatter and more smeared-out ρ peak, which is still compatible with the data within error bars, but seems slightly disfavored. The pure mass-shift scenario (with $\alpha = 0.16$) shows a clearly shifted ρ peak and generates the biggest disagreement with the data. And also the combination of collisional broadening and mass shift is not able to reproduce the behavior of the data points.

We conclude from this that an in-medium mass shift of the ρ meson (as least as large as 16%) can be ruled out. For the collisional broadening the situation is less clear. The excess-yield data do not seem to have sufficient sensitivity to distinguish the collisional-broadening scenario from the simple vacuum spectra function.

3.1.6   C + C at 1.0 AGeV

We start the discussion of the nucleus-nucleus collisions measured by HADES with the light C+C system, beginning with the lowest beam energy of 1 AGeV. Fig. 36 shows the dilepton mass spectrum for ^{12}C+^{12}C at 1.0 AGeV, compared to the HADES data, as well as the p_T spectra for three mass bins. In order to be able to compare to the published data, the simulated dilepton spectra have been normalized by the number of neutral pions N_{π^0} (or rather, to be precise, with the averaged number of charged pions $(N_{\pi^+} + N_{\pi^-})/2$, which is almost the same, as shown in table 7).

As has been argued in [29], C+C is a sufficiently light system, so that it can be regarded, in first order, as a simple superposition of elementary NN collisions, without significant secondary effects or modifications due to the hadronic medium. It has also been shown that both C+C data sets are compatible with a superposition of the NN data (when subtracting the η component, which has a different beam energy dependence) [29].

From this point of view, we can expect our results for the C+C collisions to reflect the quality of our elementary NN results (we recall a good agreement in pp and a significant underestimation in dp at the lowest beam energy of 1.25 GeV). Indeed, the agreement with the CC data is quite good over most of the mass spectrum. The only significant deviation appears around 300 - 400 MeV, where we underestimate the data points up to a factor of two. We note that a similar underestimation was also seen in other models [49, 53]. Because many different channels contribute here with similar magnitude, it is hard to tell where the deviation originates from. However, it seems that a small enhancement of the ρ channel (in particular through the $N^*(1520)$) would improve the agreement. In any case, it is almost a bit surprising that the agreement is not worse here, given the dramatic underestimation of dp at 1.25 GeV. Consequently, improving the description of the dp case would certainly also improve the agreement with the C+C data at 1 AGeV.

We stress that, in contrast to other models [49, 53], the Δ Dalitz channel plays only a minor role in our cocktail, while the ρ production via baryon resonances is much more important. Fig. 36 shows separately the dominant sources of ρ mesons, which are given by decays of the $D_{13}(1520)$ and $S_{31}(1620)$ resonances and the process $\pi\pi \to \rho$. We also note that the latter is the only production process of the ρ which has a physical threshold at $m = 2m_\pi$. All other processes yield dilepton contributions below the 2π threshold (but unfortunately suffer from poor statistics there, due to our numerical treatment).

Looking at the p_T spectra in fig. 36 bottom, it is apparent that the data in the lowest mass bin ($m < 150\,\text{MeV}$) is well described by the simulation. Since the spectrum in this region is completely dominated by the π^0 Dalitz decay, without any significant contributions from other channels, this indicates that the pion production is well under control in this reaction. This is important because the normalization of the dilepton data is done relative to the pion yield. An additional possibility to verify the pion production in GiBUU, would be to compare charged pion spectra to the data published in [153] (transverse mass and momentum, rapidity, polar angle, etc). This has not been done yet, but should be considered in the future.

The p_T spectrum in the highest mass bin is also well described. However, the data is rather sparse there and has large error bars, because this mass region really represents the very high-mass tail of the spectrum with very few counts. It is almost exclusively populated by the ρ channel in our simulation, which shows a good agreement with the data.
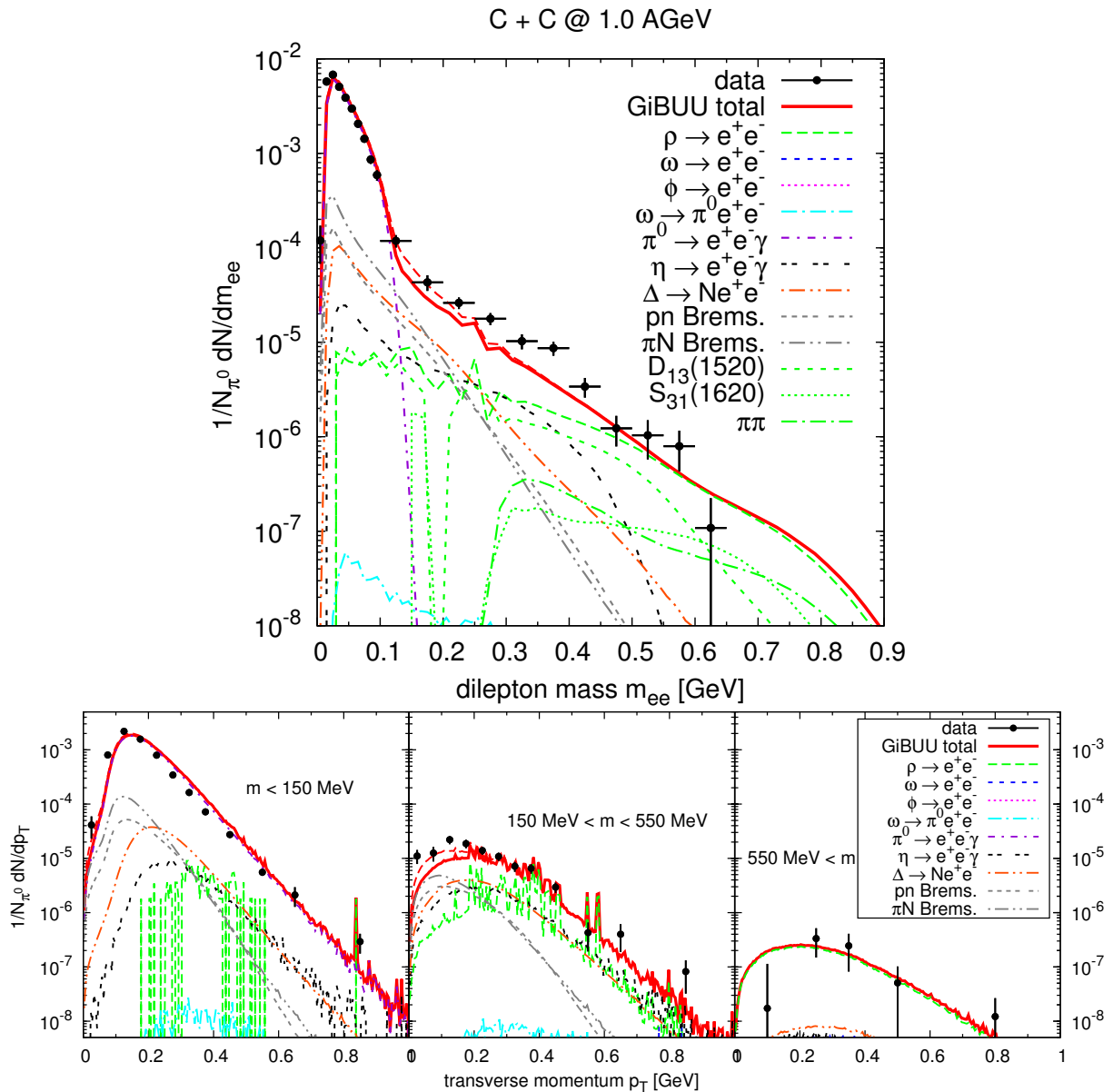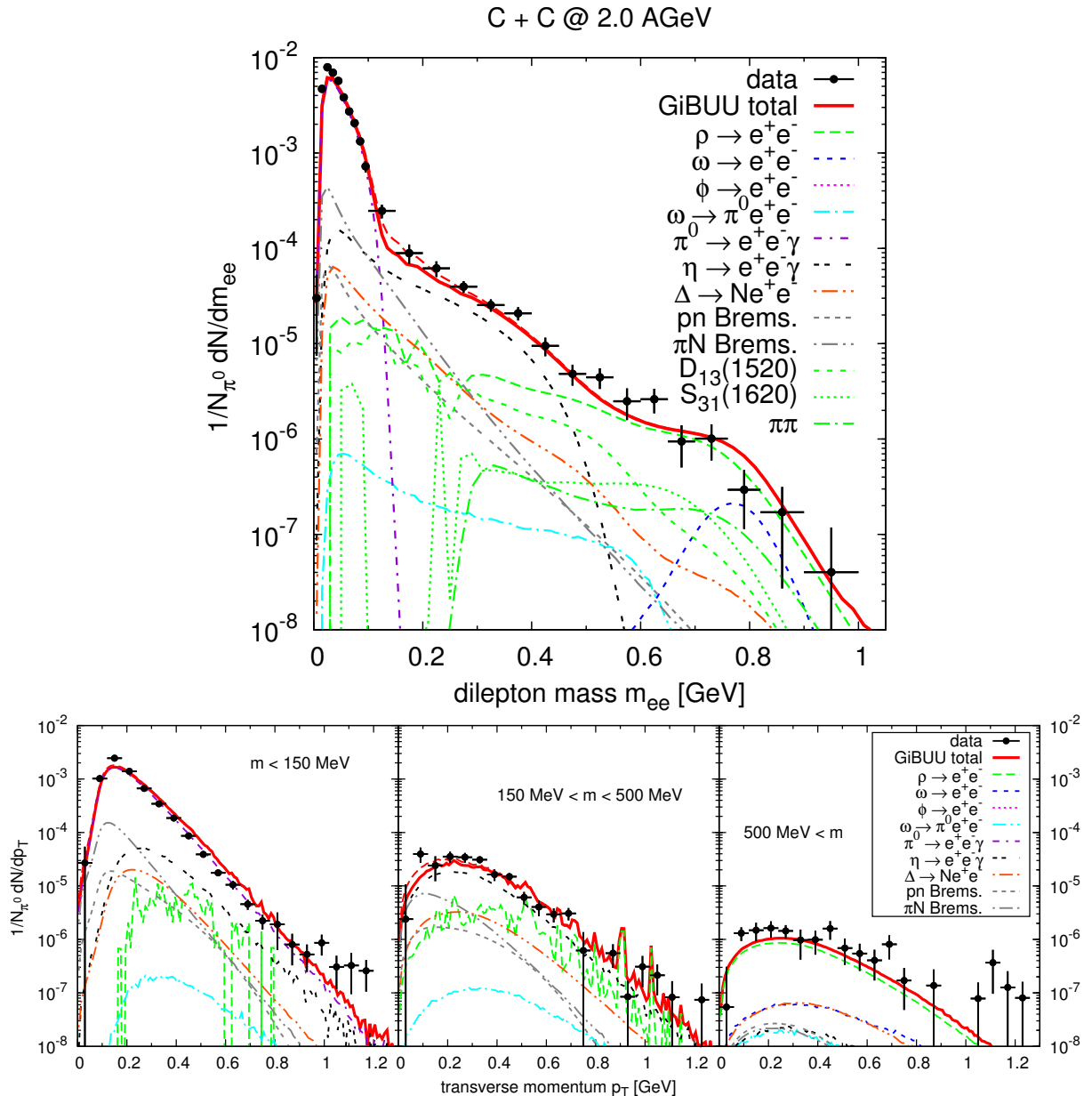
Figure 36: Dilepton spectra for C+C at 1.0 AGeV, normalized to the number of pions per event (top: mass spectrum; bottom: p_T spectra in three mass bins). The solid red line indicates the total without πN bremsstrahlung, while the dashed red line includes πN bremsstrahlung. Data from [28].

In the central mass bin, $150\,\mathrm{MeV} < m < 550\,\mathrm{MeV}$, which also includes the underestimated region, the contributions of ρ, η and Δ are all of similar magnitude, supplemented only by a low-p_T bremsstrahlung contribution (mostly πN). The agreement with the p_T data is still not too bad here and the underestimation mostly concentrates on the low-p_T region. This could be a sign of the bremsstrahlung being underestimated (due to the usage of the soft-photon approximation or the missing electromagnetic form factor). However, while a simple up-scaling of the bremsstrahlung contribution might be able to give an improved description of the p_T spectrum, it would not help so much in the mass spectrum

(due to its steep mass dependence). In any case, we note that the inclusion of the πN bremsstrahlung seems to improve the agreement with the data here, although this was clearly not the case in p+Nb at 3.5 GeV.

3.1.7 C + C at 2.0 AGeV

After discussion of the C+C system at 1 AGeV, we now move to the higher beam energy of 2 AGeV. Since our agreement with the elementary pp data was even better at higher

Figure 37: Dilepton spectra for C+C at 2.0 GeV, normalized to the number of pions per event (top: mass spectrum; bottom: p_T spectra in three mass bins). The solid red line indicates the total without πN bremsstrahlung, while the dashed red line includes πN bremsstrahlung. Data from [27].

energies (2.2 and 3.5 GeV), and also isospin effects are expected to be smaller at high energies, we expect the agreement with C+C to be better at higher energies. And indeed we observe an excellent description of the dilepton mass spectrum of C+C at 2 AGeV, as shown in fig. 37. In particular we achieve a good agreement in the high-mass regime, where most other models showed a severe overestimation [27,50,53]. The largest deviation in the C+C spectrum at 2 AGeV is a slight underestimation of the data in the mass region around 500 – 600 MeV, which is reminiscent of a similar problem in pp at 2 GeV (a system that is very close by in energy).

As in the 1 GeV case, we compare the p_T spectra in three mass bins, see fig. 37 bottom. The lowest mass bin of $m < 150\,\text{MeV}$ is dominated by the π^0 Dalitz. In the middle mass bin of $150\,\text{MeV} < m < 500\,\text{MeV}$ the strongest contribution is given by the η Dalitz decay, with secondary admixtures from the ρ meson and πN bremsstrahlung. In the third mass bin ($m > 500\,\text{MeV}$), the ρ gives by far the largest contribution. All three p_T spectra show a good agreement with the data, which we take as an indication that our cocktail composition is reasonable. It should be noted that the HSD spectra published in [53] provide a similarly good description of the mass-spectrum data as ours. However, they have quite a different composition. In particular the Δ Dalitz channel is much larger than in our case. Also the ρ channel does not have any contributions from decays of baryonic resonances. Therefore, in their cocktail the Δ is more dominant than the ρ in the intermediate mass region around 500 - 600 MeV. Unfortunately, the p_T spectra from HSD have not been published, but it would be interesting to see how they compare to the data, in light of the different cocktail employed there.

We note that, as in the 1 GeV case, a detailed check of pion spectra should be done in order to verify that the normalization to the pion yield does not pose a problem. Further, it should be remarked that the pion numbers listed in table 7 are obtained for a 'minimum-bias' scenario, which does not include any centrality bias, except for the maximum impact parameter (also given in the table). For this reason these numbers are slightly lower than the ones published in [153], where the triggering procedure caused a certain centrality bias, which needs to be taken into account to get proper pion numbers. For the pion-normalized dilepton spectrum, such a centrality bias is not expected to have any significant effect, at least not for the light C+C system.

Further, it should be noted that the correct description of pion spectra, in particular in heavier systems, might require an in-medium modification of the production and absorption cross sections (e.g. a 'quenching' or 'screening' at higher densities), as discussed in [136, 166, 167]. Such modifications are not included in our current simulations, and could in principle modify the relative contributions of different sources to the cocktail in heavy-ion reactions.

3.1.8   Ar + KCl at 1.756 AGeV

The data for this reaction have been obtained by shooting ^{40}Ar ions on a fixed (natural) KCl target. In the simulation we use ^{37}Ar (i.e. the average of ^{35}Cl and ^{39}K) to approximate the composite target. This is a good approximation, since both nuclei in the target material are very similar in mass. Both are equally like to take part in a collision with the beam ions, therefore the experimentally measured cross section is the average of Ar+K and Ar+Cl. Fig. 38a shows a comparison of our simulation results to the data, which clearly exhibits larger deviations than in the C+C case. While there is a slight overshoot it the pion channel, as well as in the high-mass region, the most severe discrepancy is a significant underprediction in the intermediate mass range of 150 to 500 MeV.

As in the C+C case at 1 AGeV, part of the missing yield might be due to disagreement with elementary data. However, it is unlikely that this can account for all of the missing yield, since our agreement with the elementary HADES and DLS data is quite good in the energy regime relevant for the Ar+KCl system (see previous sections). Instead, it seems more plausible that the missing yield represents an actual medium effect. This is supported by the experimental observation that the ArKCl data shows a significant excess over the elementary reference cocktail [30], which is of similar magnitude as the discrepancy to our model. To illustrate this, fig. 38b shows the ArKCl spectrum with the η Dalitz component subtracted, compared to the NN reference spectrum (both normalized to the pion channel, for details see [30]). The subtraction of the long-lived η channel was done mainly to compare the short-lived sources to the elementary reference spectrum, obtained as the average of pp and np at 1.25 GeV. The η contribution which was subtracted from the experimental data was determined by a Pluto simulation (constrained by TAPS data) [30], and seems to agree well with the η Dalitz contribution in the GiBUU cocktail.
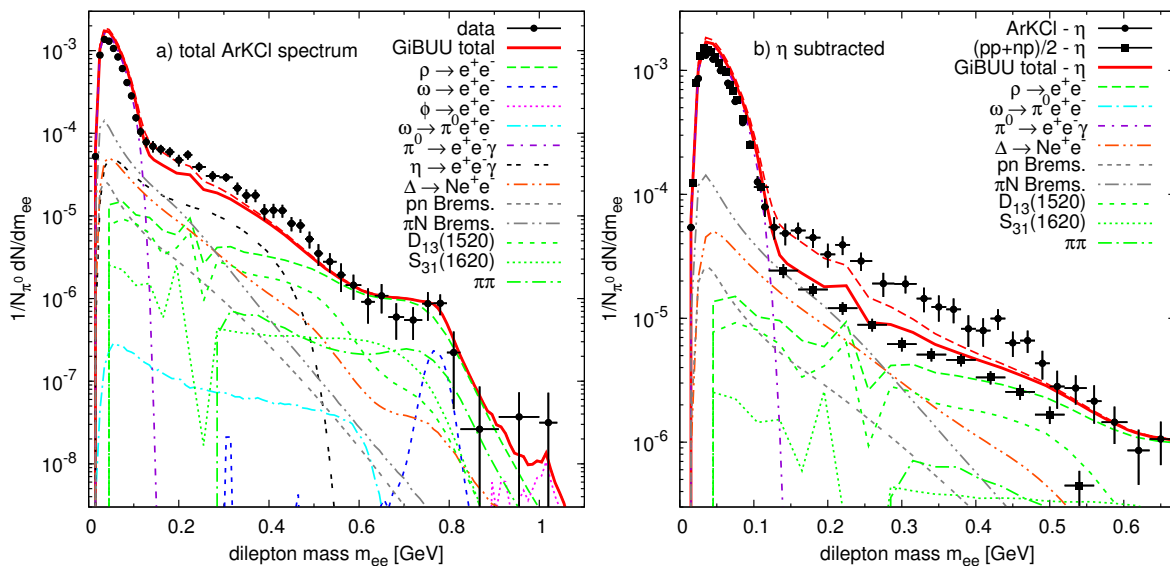
Figure 38: Dilepton mass spectra for Ar+KCl at 1.756 GeV, normalized to the number of pions per event. a) Total spectrum, b) η Dalitz contribution subtracted. The solid red line indicates the total without πN bremsstrahlung, while the dashed red line includes πN bremsstrahlung. Data from [30].

While our model underestimates the subtracted ArKCl data, it lies close above the elementary reference spectrum.

The excess yield could in principle come from two distinct sources:

1. Dilepton emission from secondary collisions (e.g. πN), which is in principle covered by our model but could be underestimated. Apart from processes like $\pi N \to \Delta$, $\pi N \to \eta N$ or $\pi N \to \rho N$, also πN bremsstrahlung can play a role, which is treated in our model only in soft-photon approximation (SPA).

2. An in-medium modification of the spectral functions, e.g. a broadening of the ρ meson or modifications of the nucleon resonances, which are involved in the production dynamics of the ρ, most prominently the $D_{13}(1520)$. Such spectral modifications are not included in fig. 38, which fully relies on vacuum spectral functions.

Since it was claimed in [53] that the ArKCl data in the intermediate mass can be described by virtue of a strong Δ contribution (which was demonstrated via the HSD and IQMD models), we also varied our description of the Δ Dalitz channel (see fig. 38c), in order to try to reproduce the large Δ contribution shown in [53]. As mentioned earlier, there are several factors which influence the Δ Dalitz channel, e.g.

1. the inclusive Δ production cross section $\sigma(NN \to \Delta X)$, as well as the secondary production from e.g. $\pi N \to \Delta$,

2. the hadronic width $\Gamma(\Delta \to \pi N)$,

3. the radiative width $\Gamma(\Delta \to e^+ e^- N)$,

4. the electromagnetic transition form factor entering the radiative width.

5. possible in-medium modifications of the Δ spectral function

In chapter 2.3.1.2, we have investigated the Δ production cross section in NN collisions, and have concluded that it is reasonable in our model (while probably overestimated by FRITIOF and HSD). Therefore we do not care to vary it here and instead focus our variations on item 2-4, all of which have already been discussed earlier (see chapters 2.2.1 and 2.2.2.3). By default, our simulations, as shown in fig. 38a, rely on the combination of the Manley parametrization for the hadronic width and the Krivoruchenko parametrization for the radiative width (plus the Ramalho form factor). In fig. 39a we vary both of these widths. As expected, one gets the largest contributions from the combination of the Verwest parametrization of the hadronic width and the Ernst parametrization of the radiative width, which at small dilepton masses is up to a factor of two larger than our default approach. However, this is obviously not enough to bring the simulation up to the data in the intermediate mass range, and so still a sizable discrepancy remains, even when maximally varying the hadronic and radiative Δ width. Adding a form factor can further increase the Δ Dalitz contribution. But while the Ramalho form factor only gives moderate modifications, the one by Wan/Iachello will yield large modifications only at masses around 600 MeV, and not in the range of 200 - 500 MeV. So none of them can solve the discrepancy. Therefore we conclude: The fact that HSD can describe the ArKCl data in the intermediate mass range is caused by its overestimation of the Δ production
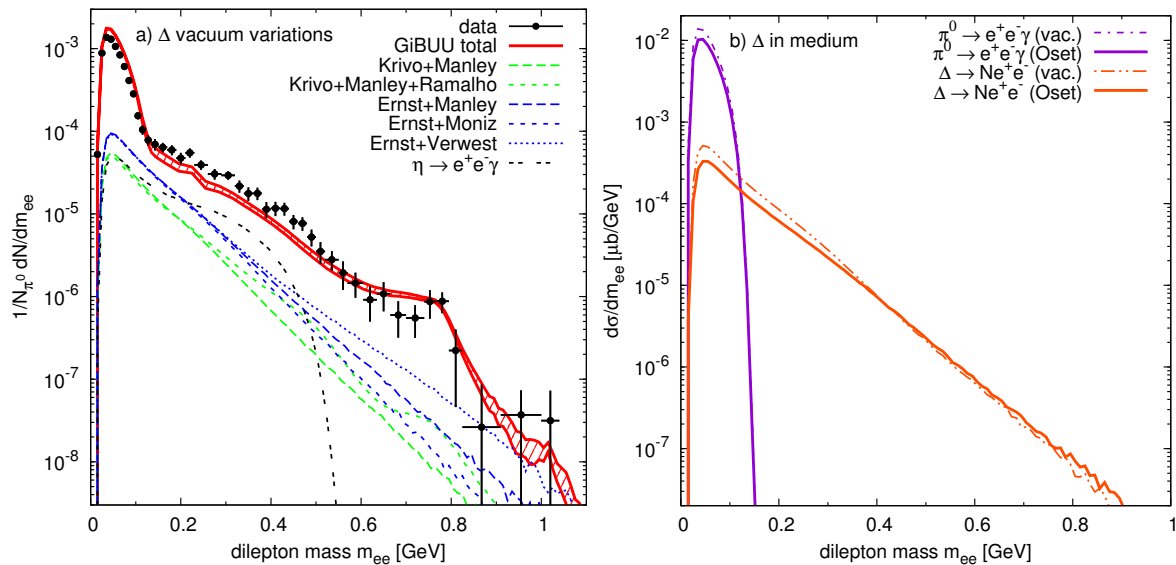
Figure 39: Dilepton mass spectra for Ar+KCl at 1.756 GeV. a) using different vacuum prescriptions for the Δ Dalitz channel, b) with Δ in-medium width according to Oset et al. [149]. Data from [30].

cross section, which results in an extremely large Δ Dalitz contribution to the dilepton spectrum.

An additional problem in the string-model based approach of HSD could be detailed balance: A string model like FRITIOF heavily relies on many-body production channels $(2 \to 3, 2 \to 4, ..., 2 \to N)$. However, usually the back reactions for all these channels are not implemented, since it is not straightforward to treat N-body collisions $(N \to 2)$. For a particle like the Δ, in particular, the production in a string model frequently proceeds via channels like e.g. $NN \to \pi N \Delta$, but the corresponding back reaction is missing, so that production and absorption of the Δ are not balanced, which can lead to further overestimation, in particular in heavy-ion collisions like ArKCl. In our resonance-model approach this problem does not exists, since the production is based on $2 \to 2$ reactions like $NN \to R_1 R_2$ (with $R = N, \Delta, N^*, \Delta^*$), for each of which the corresponding back-reaction is implemented to satisfy detailed balance.

In addition to the variation of the vacuum description of the Δ Dalitz decay, we have also evaluated the effect of using the in-medium width of the Δ according to [149]. This is shown in fig. 39b for central ArKCl collisions, without an electromagnetic form factor and in absolute normalization. The Δ in-medium width of Oset et al. has several effects on the dilepton spectrum: Firstly, it brings down the π^0 Dalitz channel, since it lowers the overall pion multiplicity. Secondly, the broadening of the Δ spectral function leads to a modification of the Δ Dalitz dilepton contribution: It is suppressed at low masses and enhanced in the high-mass tail. Apparently this effect is rather small compared to the effects which were obtained by varying the vacuum description of the Δ. When normalized to the pion yield, the dilepton contribution of the Δ is basically unchanged at low masses, and the only surviving effect is a moderate enhancement of the high-mass tail, which means that an in-medium treatment of the Δ is not able to explain the missing yield in the intermediate mass range, either.
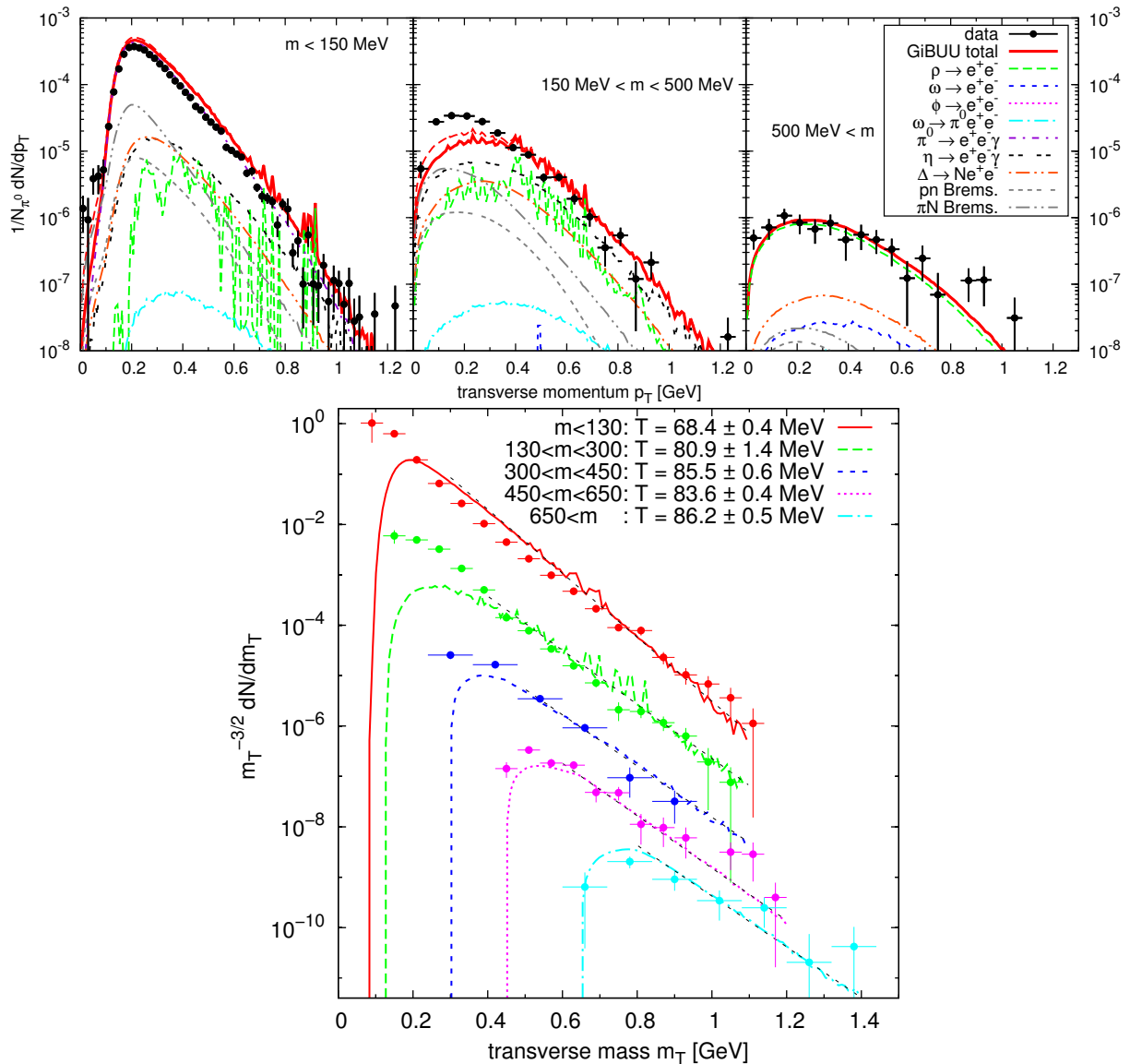
Figure 40: Transverse momentum (top) and transverse mass spectra (bottom) for Ar+KCl at 1.756 GeV in several mass bins. Data from [30].

In fig. 40 we show the transverse momentum and transverse mass spectra for Ar+KCl. The p_T spectra, as for C+C, are plotted in three mass bins. The lowest mass bin, dominated by the π^0 Dalitz decay, shows an overall offset of about 20%, but an almost perfect agreement in shape. The offset is still within the systematical errors of the data, which is quoted as 25% in [30]. Also the highest mass bin, dominated by ρ^0 decays, displays a good agreement in shape, although the overall yield seems slightly too low in the simulation. Unsurprisingly, the central mass region, which showed the largest disagreement in the mass spectrum, also deviates significantly from the data in the p_T spectrum. However, it is interesting that the disagreement is limited to the low-p_T region, while the data is well reproduced above $p_T \approx 400\,\mathrm{MeV}$. This means that the missing yield, wherever it originates from, must have rather low p_T. Looking at the different contributions in the

p_T spectrum, it is apparent that the bremsstrahlung channels are the sources with the lowest average p_T. So possibly our underestimation of the low-p_T yield could be due to an underestimation of the bremsstrahlung contribution. However, the πN bremsstrahlung, which dominates over the NN bremsstrahlung in our simulation, would have to be boosted up by roughly a factor of six, in order to provide a proper description of the p_T data. This seems unlikely, even though it is clear that the soft-photon approximation employed in our simulation is not fully correct. In fact, as we saw for p+Nb, the πN bremsstrahlung might even be overestimated already. Moreover, the bremsstrahlung has a too steep slope in the mass spectrum to be able to fully explain the underestimation there: It would mostly fill up the low-mass part of the spectrum, but cannot explain the underestimation at high masses of 400 - 500 MeV.

In fig. 40 bottom, we show the transverse mass spectra for five different mass bins. Since the transverse mass is related to the transverse momentum via $m_T^2 = m_{ee}^2 + p_T^2$, it shows similar features: While the upper three mass bins show a reasonable agreement, the lower two mass bins show some underestimation at low m_T, which is certainly connected to the deficiencies seen at low p_T. (Note that the m_T distribution for each mass bin has of course a kinematic cutoff given by the lower bound of the corresponding mass interval.)

Following [30], we have determined the temperature T from our m_T distributions, by fitting the simulated spectra with an exponential function:

$$\frac{1}{m_T^{3/2}} \frac{\mathrm{d}\sigma}{\mathrm{d}m_T} \propto exp\left(-\frac{m_T}{T}\right) \tag{98}$$

With the pre-factor of $m_T^{-3/2}$, the inverse slope of the rapidity-integrated m_T spectrum in semilogarithmic representation can be identified with the temperature T (for a thermalized system, and in the limit $m_T \gg T$) [168]. The fits exclude the low-m_T region, where the spectra obviously deviate from the exponential behavior. The resulting (inverse) slopes T are indicated in fig. 40 for each mass bin, and except for the lowest bin all of them lie in the range of 80 - 86 MeV. It should be noted that the values determined from the simulated spectra do not perfectly coincide with the fits to the experimental data obtained in [30], which often turn out to be somewhat larger, in particular in the two uppermost mass bins, but also in the lowest one. In the lowest bin, it is easy to see that the slope is not quite the same (although it is a bit surprising – in light of the good p_T agreement in the lowest mass bin). In the high mass bins, however, the disagreement does not look too dramatic (visually), and the difference in the fitted slopes may partially be due to the large experimental error bars (which are also reflected by the rather large error bars of the experimentally determined slopes).

Since our model is not a thermal model, but instead based on microscopic particle collisions and decays, the interpretation of the inverse-slope parameter as an actual temperature is certainly questionable. In particular it is not clear whether a medium-size system like Ar+KCl at the rather low energy employed here will actually be able to fully 'thermalize' at all. Also the rather large spread of temperature values determined from the experimental m_T spectra may be an indication that the system cannot be characterized by a unique freeze-out temperature. However, it should be noted that both the experimental m_T spectra as well as the simulated ones clearly exhibit exponential behavior to a good approximation (at least in the large-m_T regime), which obviously justifies the fitting procedure, even if the interpretation of the slope parameter as a temperature

is not obvious. Further, one could even interpret the observed increase of T with mass as being connected to the continuous cooldown of the system: Heavy particles can only be produced via high-energy collisions in the early (hot) phase of the collision, therefore the temperature in the high mass bins is larger than in the lower mass bins, whereas the lighter particles (such as pions) are mostly produced in the later and cooler stage of the collision. This trend is slightly visible in the simulated sprectra and even stronger in the experimental data, where the highest mass bins were attributed with temperatures of up to 130 MeV [30].

In fig. 41, we show the dilepton mass spectrum from ArKCl with in-medium modifications of the vector-meson spectral functions, using the scenarios described in section 2.5 and previously applied to the pNb results in section 3.1.5. It is apparent that the total spectrum is most sensitive to the modifications in the high-mass regime above 500 MeV. In the region of 500 - 700 MeV, the collisional broadening scenario gives a slight improvement over the vacuum case, while the mass-shift scenario tends to overshoot the data. In the ω peak, all scenarios seem to give a deterioration over the vacuum case. However, this could also mean that the ω production cross sections, e.g. from pn or πN collisions, are underestimated. A similar trend was already seen in p+Nb, and might be due to a missing enhancement of ω production in pn over pp. We note that all scenarios in fig. 41 use the factor of $K = 2$ for ω absorption (cf. section 2.3.2.2), in line with the TAPS transparency ratio data [35]. Above the ω peak, the spectrum still shows significant sensitivity to in-medium modifications. However, the error bars of the data are too large to resolve these modifications.

The lower part of fig. 41 shows the modifications of the ρ and ω mesons separately. It is clear that any modifications of the ρ meson are more important for the total spectrum, since the ρ is the dominant source above 500 MeV, and moreover it has a larger probability of decaying inside the medium.

For the ω, the in-medium modifications only cause a minor drop of the peak and an enhancement of the low-mass tail, which is most pronounced for the pure-shift scenario. In contrast to the pNb case, no clear in-medium peak can be observed here, because the density is not constant and can vary over a larger interval (roughly up to $3\rho_0$). In consequence, it's basically impossible to learn anything about the ω in-medium properties from the dilepton mass spectrum of ArKCl, and even harder than in a cold-nuclear-matter setup (like pA or γA).

For the ρ meson, however, one can observe significant modifications of the mass shape, which are in fact larger than in the pNb case. This is of course expected, since the ArKCl collisions probe larger densities and many of the ρ mesons will actually decay at finite densities. Almost all of the in-medium scenarios cause an enhancement of the spectrum around 600 MeV as well as a decrease at higher masses (around 800 MeV). Below 500 MeV, they either show little change or even a decrease. This is unfortunate, since we were of course hoping that a modification of the ρ meson might be able to cure the underestimation of the data in the intermediate mass range of 200 - 500 MeV.

However, it might certainly be that the misbehavior we are seeing is just due to the fact that our treatment of the in-medium modifications is just not refined enough at this point. To illustrate this, we show not only the total ρ channel, but also the separate contributions from two of the most important sources of ρ mesons in the ArKCl system: $\pi\pi$ collisions and decays of the $D_{13}(1520)$ state. Looking at the $\pi\pi$ channel, one can see that all in-medium
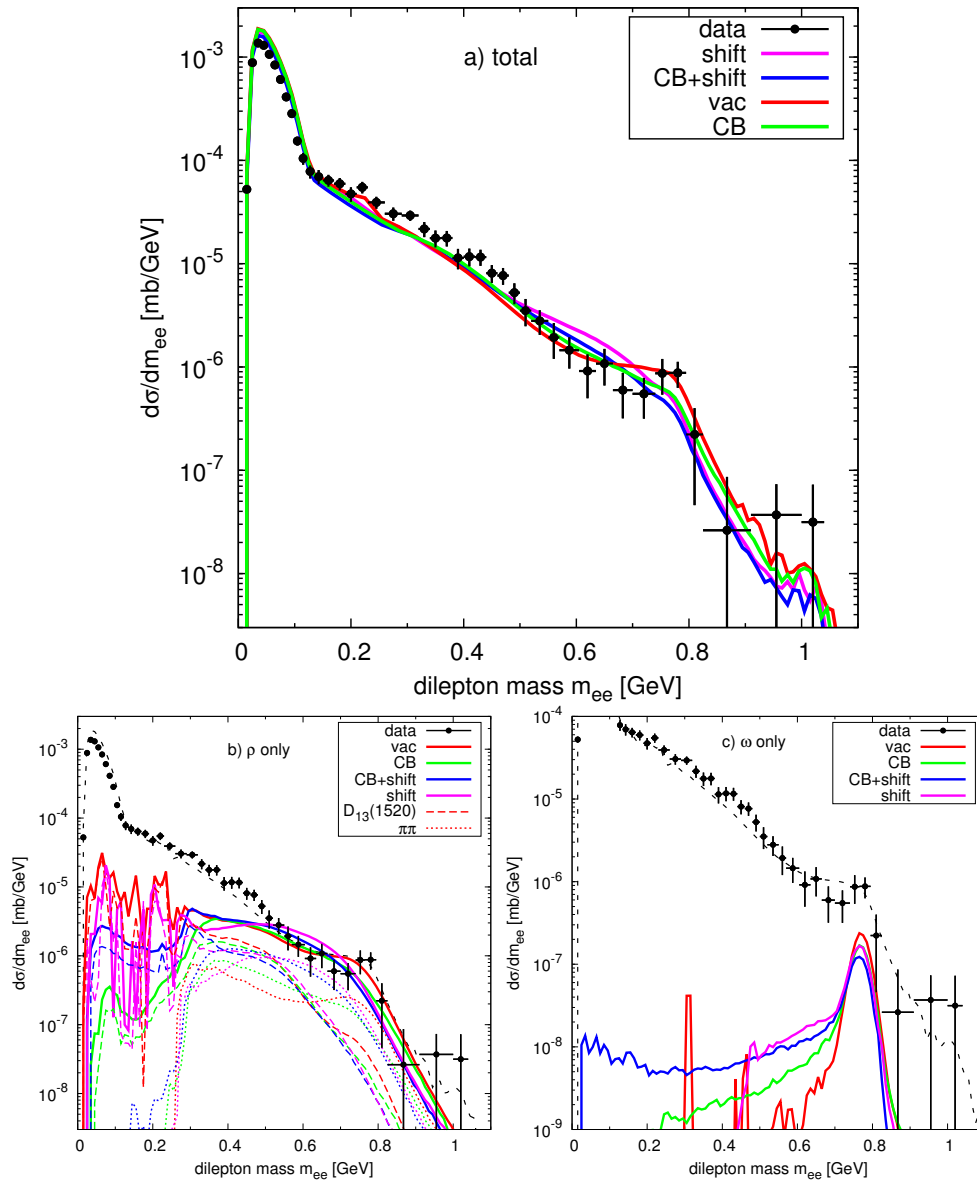
Figure 41: Mass spectrum for Ar+KCl at 1.756 GeV with in-medium spectral functions for the vector mesons. Top: Total spectrum, bottom: separate ρ and ω contributions. Data from [30].

scenarios enhance the low-mass part of of the spectrum. However, it is also visible that in the pure-shift scenario the spectrum falls off quickly when approaching the 2π threshold. This is due to low-mass ρ mesons being produced at high densities, which increase their mass when propagating out into the vacuum, so that right above the 2π threshold the pure-shift scenario is actually lower than the vacuum scenario. This is probably a fake effect, which should go away e.g. if one also applies in-medium modifications to the pions, which is currently not done but would lower the threshold for $\pi\pi \to \rho$ below the vacuum threshold of $2m_\pi$.

The modifications of the $D_{13}(1520)$ contribution are overall much smaller than in the $\pi\pi$ case. This is because we take into account the modified ρ mass distribution in the

kinematics of the decay etc, but we do not respect it e.g. for the branching ratios. These are obtained by calculating the decay widths for different channels in the vacuum, and are then tabulated as a function of the mass of the decaying particle. Therefore they are density-independent. Doing a two-dimensional tabulation (as a function of mass and density) should further modify the resonance-decay contributions to the ρ mass spectrum, and in particular might give additional yield at low masses.

Further modifications could be obtained by taking into account possible in-medium modifications of the decaying baryon resonances themselves. For example a broadening of the baryons would enhance the low-mass part of the baryon spectral function, which could in turn give enhanced contributions of low-mass ρ mesons.

Further, one might think about going beyond the simple in-medium scenarios treated here, namely a linear density-dependent increase of the width or a linear decrease of the pole mass. It is known that realistic scenarios are more complex and exhibit a much richer structure, as shown e.g. by the works of Post et al. [9], Eletsky et al. [11] and Rapp et al. [3].

A fully consistent in-medium treatment of all pions, rhos and N^* resonances poses a significant effort, and may require an iterative scheme, where the modification of one particle species acts back on the others. It is not clear if this is feasible in the scope of a transport calculation, and whether methods like the off-shell-potential treatment can handle such a complex scenario.

3.1.9   Au + Au at 1.25 AGeV

The last system in our series of HADES-related results is in fact the largest one, however at a somewhat lower energy than the previously discussed Ar+KCl system: Au+Au at a beam energy of 1.25 AGeV. The data-taking for this reaction with the HADES detector has already been completed, however the results are presently still being analyzed and the final data have not been published yet. Therefore we can only show here the prediction of the GiBUU model for this reaction, without making a comparison to data. All we can do at this point is to compare our results for AuAu to other already published data sets, such as the elementary reference spectrum and ArKCl.

Fig. 42 shows the dilepton mass and p_T spectra for the Au+Au system. The first plot on the top left depicts the total dilepton mass spectrum for an almost-minimum-bias setup ($b < 9\,\mathrm{fm}$). It has been filtered through the HADES acceptance filter [151] using
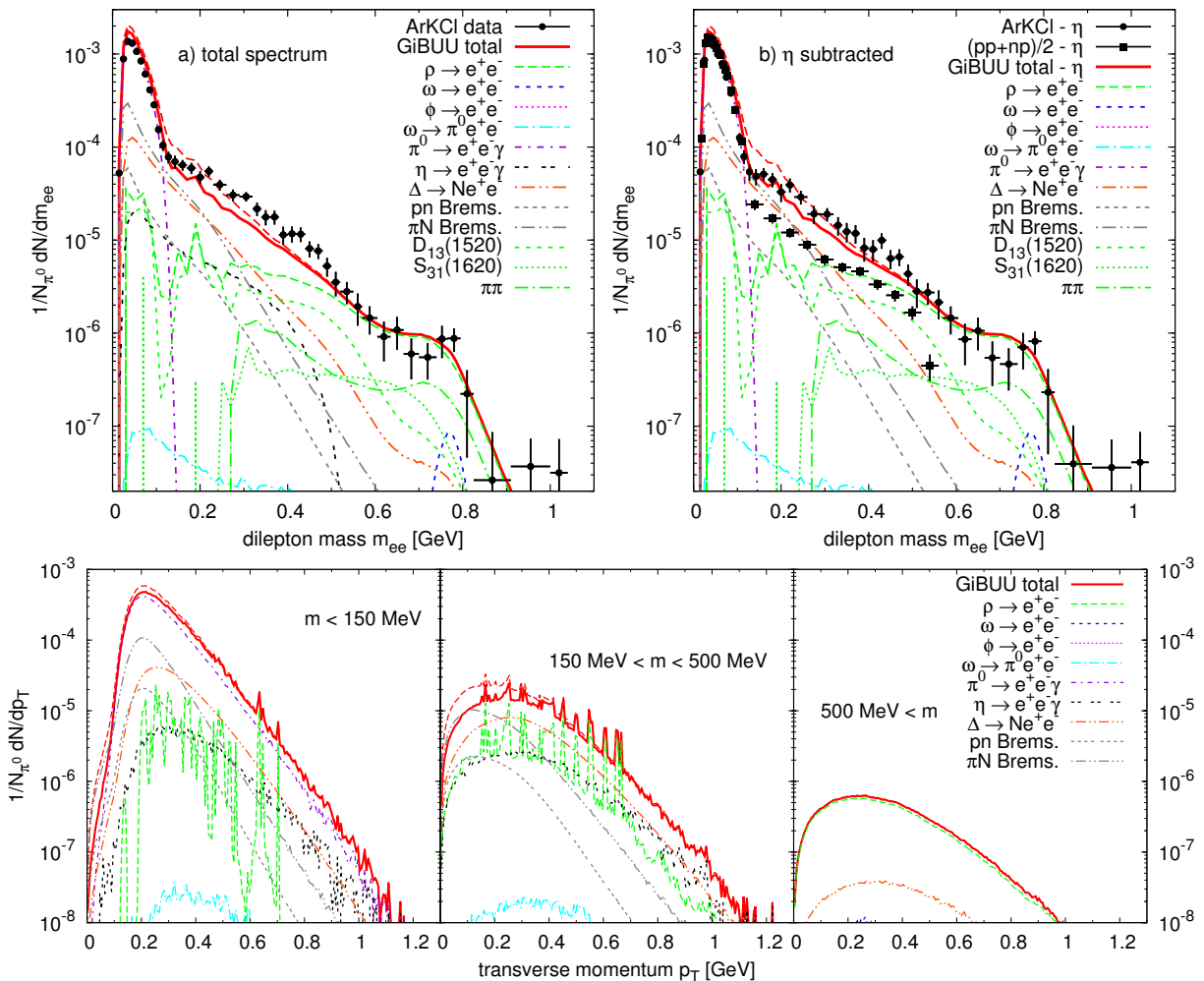
Figure 42: Dilepton mass (top) and p_T spectra (bottom) for Au+Au at $1.25\,\mathrm{GeV}$ (minimum bias) in ArKCl acceptance, normalized to the number of pions per event. a) Total spectrum, b) η Dalitz contribution subtracted, in comparison to ArKCl and elementary reference data [30]. The solid red line indicates the total without πN bremsstrahlung, while the dashed red line includes πN bremsstrahlung.

the settings for ArKCl, in order to be able compare to the ArKCl data (as well as the elementary reference spectrum, which has also been published in ArKCl acceptance).

The overall features of the AuAu spectrum in ArKCl acceptance are amazingly similar to the ArKCl spectrum. However, since the Au+Au system is relatively large, the resulting 'fireball' (i.e. the hot and dense collision region) is more extended (both spatially and temporally) than for the smaller systems. As a consequence, short-lived resonances like the Δ and the ρ are frequently recreated by NN, πN and $\pi\pi$ collisions. Therefore these sources show up more prominently in the dilepton spectrum. On the other hand, long-lived but heavy sources like the η and the ω are somewhat suppressed due to the rather low energy. In the intermediate mass range, the enhancement of the short-lived ρ and Δ and the suppression of the η are almost balanced, so that the total Au+Au spectrum is quite close to the ArKCl data.

Also the πN bremsstrahlung gives relatively large contributions in the low-mass range. However, we have observed previously that the πN bremsstrahlung in SPA often over-shoots the available data, most severely in p+Nb at 3.5 GeV (see fig. 30). Therefore we show the Au+Au results here with (dashed red curve) and without (solid red curve) the πN bremsstrahlung contribution.

In the lower part of fig. 42, we show p_T spectra for Au+Au in three mass bins (also in a minimum-bias setup). While the lowest mass bin of $m < 150\,\mathrm{MeV}$ is of course dominated by the pion Dalitz channel, the second one ($150\,\mathrm{MeV} < m < 550\,\mathrm{MeV}$) shows a strong Δ Dalitz contribution and the highest bin of $m > 550\,\mathrm{MeV}$ is dominated by the ρ meson, which is either produced through baryonic resonances (like the $D_{13}(1520)$ and others) or through $\pi\pi$ fusion.

Further we show in the top right part of fig. 42 the dilepton mass spectrum for Au+Au at 1.25 GeV with the η Dalitz contribution subtracted. This is done in order to be able to compare to the η-subtracted spectra published in [30], namely the Ar+KCl spectrum and the elementary reference spectrum, i.e. (pp+np)/2.

While in the ArKCl case we saw only a marginal excess over the elementary reference spectrum when using vacuum spectral functions, the enhancement in AuAu is somewhat larger due to the enhanced short-lived sources, which clearly lift the AuAu spectrum over the reference cocktail. However, it does not quite reach the ArKCl data.

For the Au+Au system, no experimental data are available yet. However, already in ArKCl an experimental excess of roughly a factor three over the reference spectrum was observed. Although the energy of the ArKCl system (1.76 GeV) was slightly higher than in the elementary reference measurements (1.25 GeV), the excess was mainly attributed to a system-size effect (since the beam energy dependence in the intermediate mass range is assumed to be rather flat, which is confirmed by GiBUU simulations).

Still, the effect of the energy-dependence is not fully negligible, and it has been shown in [30] that correcting for the energy dependence leaves about a factor of two enhancement in ArKCl over CC, which is then supposed to be a pure system-size effect. This system-size effect is expected to be even larger for the heavy AuAu system, of course. This is confirmed by our simulations which show a larger excess over the reference spectrum for AuAu than for ArKCl. However, since we still underestimate the enhancement in ArKCl and even our AuAu spectrum does not reach the enhancement observed in ArKCl, it is to be expected that the AuAu data will show an even larger enhancement, which is not compatible with our current simulations. Therefore we conclude that such an excess,
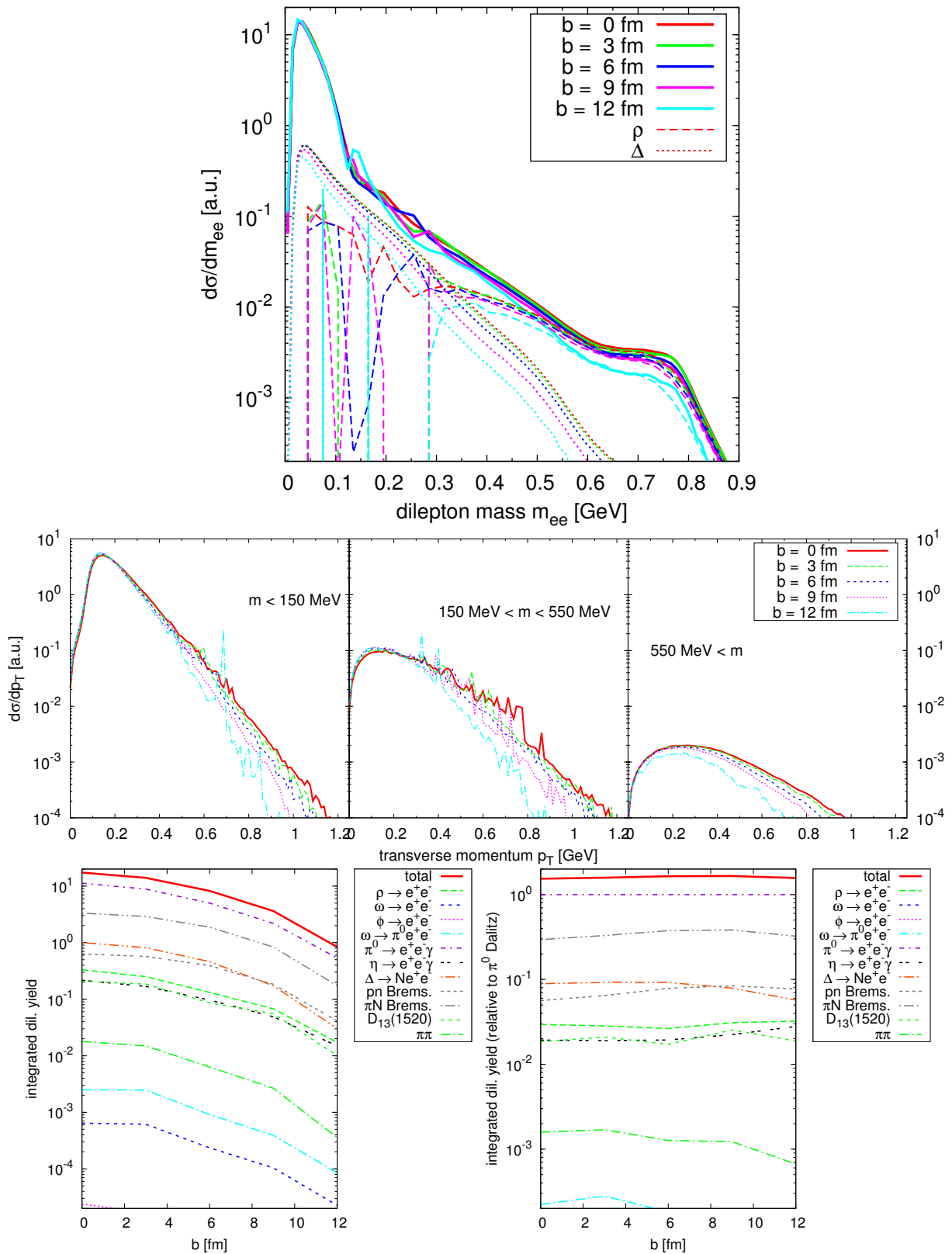
Figure 43: Top: Dilepton mass spectrum of Au+Au at 1.25 GeV for different centralities, normalized to the π^0 channel. Center: p_T spectrum for different centralities. Bottom: Integrated centrality dependence (right: relative to π^0 channel).

as already measured in ArKCl, can only be explained by significant modifications of the dilepton spectrum caused by changes of the spectral functions in the medium (both vector mesons as well as baryons could play a role here and should be further investigated in the future).

Fig. 43 shows the centrality dependence of the dilepton mass spectrum, comparing five different calculations with fixed impact parameters of $b = 0, 3, 6, 9$ and 12 fm, respectively. In contrast to fig. 42, the AuAu spectrum is shown in the acceptance of pp at 1.25 GeV here, which is supposed to be closest to the Au+Au running conditions [152]. In the plot the different curves are normalized to have the same yield in the pion region, in order to compare their shapes. Of course the pion yield (same as the general particle multiplicity) strongly depends on centrality: For central events basically all of the nucleons will be involved in the collision, leading to a large multiplicity of produced particles, while for very peripheral events only few nucleons will collide (most nucleons just being spectators) so that the multiplicity will be rather low. The general centrality dependence of the integrated dilepton yield is shown at the bottom fig. 43. In the dilepton mass spectrum at the top of the figure, we discard the 'trivial' pion multiplicity effect by normalizing to the pion yield, in order to concentrate on the shape of the spectrum. In fact the differences in shape are most severe in the high-mass region, which is dominated by ρ-meson contributions. For the more central events these ρ contributions are enhanced relative to the pion yield, since, as already noted above, the larger fireball leads to an enhanced production and regeneration of short-lived resonances (like the ρ). In the ρ-mass region, the difference between perfectly central ($b = 0$) and very peripheral collisions ($b = 12$ fm) is about a factor of 2-3. We remind of the fact that in absolute terms, this difference will be even larger (due to the general multiplicity scaling that has been taken out here).

The centrality dependence of the p_T spectra looks as expected: More central events yield 'harder' p_T spectra, which have a flatter slope and extend to higher p_T values. This holds in a similar fashion for all three mass bins.

We note that an even stronger centrality dependence will be generated by using in-medium spectral functions for the ρ meson (and other resonances), which has not been done here. Therefore the shown centrality dependence is only the 'trivial' dependence due to the kinematics and dynamics of collisions of different centrality, but without an additional density dependence of the spectral functions. Including such a density dependence is expected to generate a much stronger centrality dependence, since the densities which are probed strongly depend on the centrality of the collision, and should be investigated in the future.

3.1.10 Density evolution

In this section we give a short comparison of the density evolution of the different A+A collisions measured by HADES, in order to get an estimate of the densities reached in these reactions and for the lifetime of the generated region of high density and/or temperature (the so-called 'fireball'). For this purpose we show in fig. 44 the baryon density in units of ρ_0 at the center of the collision as a function of time. The four panels show this quantity for C+C at 1 and 2 GeV, Ar+KCl at 1.76 and Au+Au at 1.25 GeV, respectively, where for each of those we show collisions at different impact parameters, which are distinguished by color.
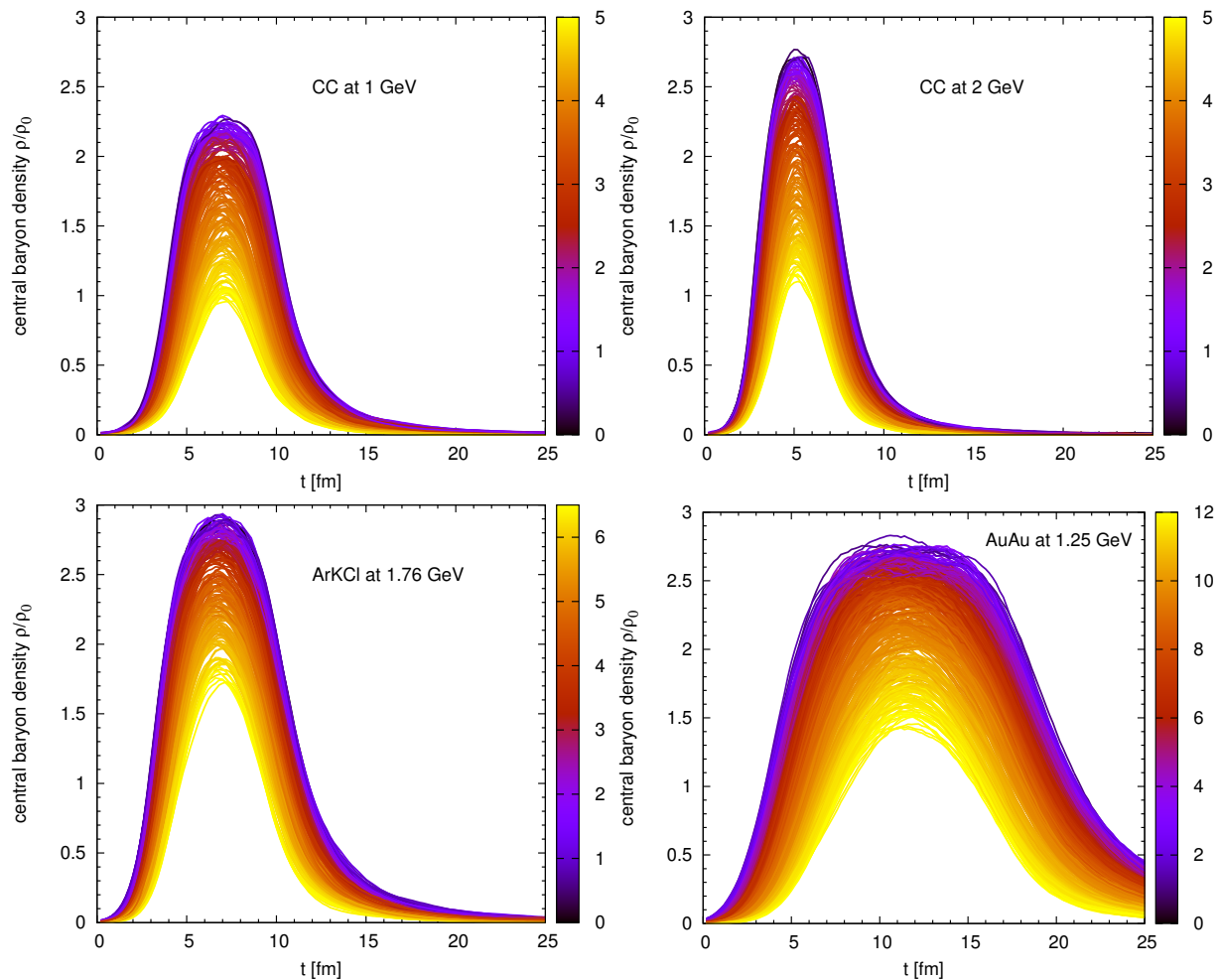
Figure 44: Baryon density evolution of different collision systems. The color code indicates the impact parameter (in fm).

Comparing first the two C+C systems in the top row, it is clearly visible that higher beam energy causes a stronger compression of the system (i.e. higher densities), but at the same time leads to a shorter lifetime of the compression zone. Of course there is a clear correlation between the centrality and the maximum density: While the very peripheral collisions ($b \approx 5\,\mathrm{fm}$) only show a maximum density around ρ_0 (i.e. no compression), the central collisions reach densities up to $2.3\rho_0$ at 1 GeV and up to $2.7\rho_0$ at 2 GeV. The lifetime of the $\rho > \rho_0$ region in the most central collisions is around 7 fm/c at 1 GeV and only slightly shorter (i.e. roughly 6 fm/c) at 2 GeV.

For the ArKCl case, the lifetime of 9 fm/c is only slightly larger than for C+C at 1 GeV (due to the combination of larger system and higher beam energy), but the maximum density is significantly larger (almost up to $3\rho_0$). From this direct comparison it appears that the large excess that is seen in the dilepton spectrum of ArKCl compared to CC, might be primarily caused by the higher density and not not so much by the lifetime of the 'fireball' (which is comparable). However, it might be that the spatial extent of the fireball (which is not shown here) could also play a role.

The last panel shows the density evolution for Au+Au at 1.25 GeV, where the density does not get any larger than in ArKCl (due to the lower energy), but the fireball lives much

longer: The $\rho > \rho_0$ phase lasts for almost 18 fm/c in central collisions, which is roughly twice as long as in the ArKCl case. Since already the dilepton signal from ArKCl showed a significant enhancement over the elementary and CC reactions, one should expect that any such density- and/or system-size dependent effect shows up even stronger in AuAu. With the large amount of measured events for AuAu, there is even hope to directly determine the centrality dependence of the excess, which, as fig. 44 illustrates, directly translates into a dependence on the density and lifetime of the fireball of hadronic resonance gas that is being created in these collisions.

3.2 DLS at Bevalac

The DLS collaboration was the first to observe dilepton production at incident energies below 10 GeV. They measured a variety of systems in a large energy range, roughly from 1 to 5 AGeV [16, 17]. For a long time, however, none of the available models was able to properly describe the DLS dilepton data, and so the term "DLS puzzle" was coined in the late 90s to characterize this discrepancy [23–26]. At first, the origin of the puzzle was unknown: Was there some problem in the data taking process? Was the detector and its acceptance and effiency not understood in all detail? Or was the data correct, and instead the theoretical models missed some ingredient to achieve agreement with the data? This question was later answered by the HADES collaboration, whose data fully verified the correctness of the old DLS data, and in this way shifted the DLS puzzle into the theory sector.

Originally, the term "DLS puzzle" was mainly used to refer to the disagreement between theory and experiment in the C+C and Ca+Ca systems, but we will argue here that most models already failed to describe the elementary p+p and p+d data in some ways, and that a large part of the "puzzle" was probably due to an improper understanding of the elementary data (and not due to additional effects of the nuclear medium).

In order to compare to the DLS data, the GiBUU dilepton events have been filtered throug the DLS acceptance filter, version 4.1, as available from [169]. In addition to the acceptance filtering, the events have been smeared with a Gaussian of width $\sigma = 0.1 m_{\mathrm{ee}}$, in order to account for the mass resolution of the detector. No further cuts have been applied.

3.2.1 Elementary NN reactions

We start here by comparing the results of our model to the elementary data measured by the DLS collaboration [17]. Unfortunately they are of inferior quality than the HADES data in terms of statistics and acceptance. However, more beam energies have been measured than in the case of HADES, so that they can still provide additional contraints, which are useful for understanding the elementary cocktail.

E_{kin}	$\sqrt{s}$	p_{lab}
1.04	2.34	1.74
1.27	2.43	2.00
1.61	2.56	2.37
1.85	2.64	2.63
2.09	2.73	2.88
4.88	3.56	5.74

Table 9: Kinematic conditions of the elementary collisions measured by DLS (in GeV).

The kinematics of the reactions measured by DLS are summarized in table 9. At each of the given energies, a p+p and p+d reaction was measured.

The comparison of the GiBUU model results to the DLS data is shown in Figs. 45 and 46. For each reaction, mass, p_T and rapidity spectra have been published. The p_T and
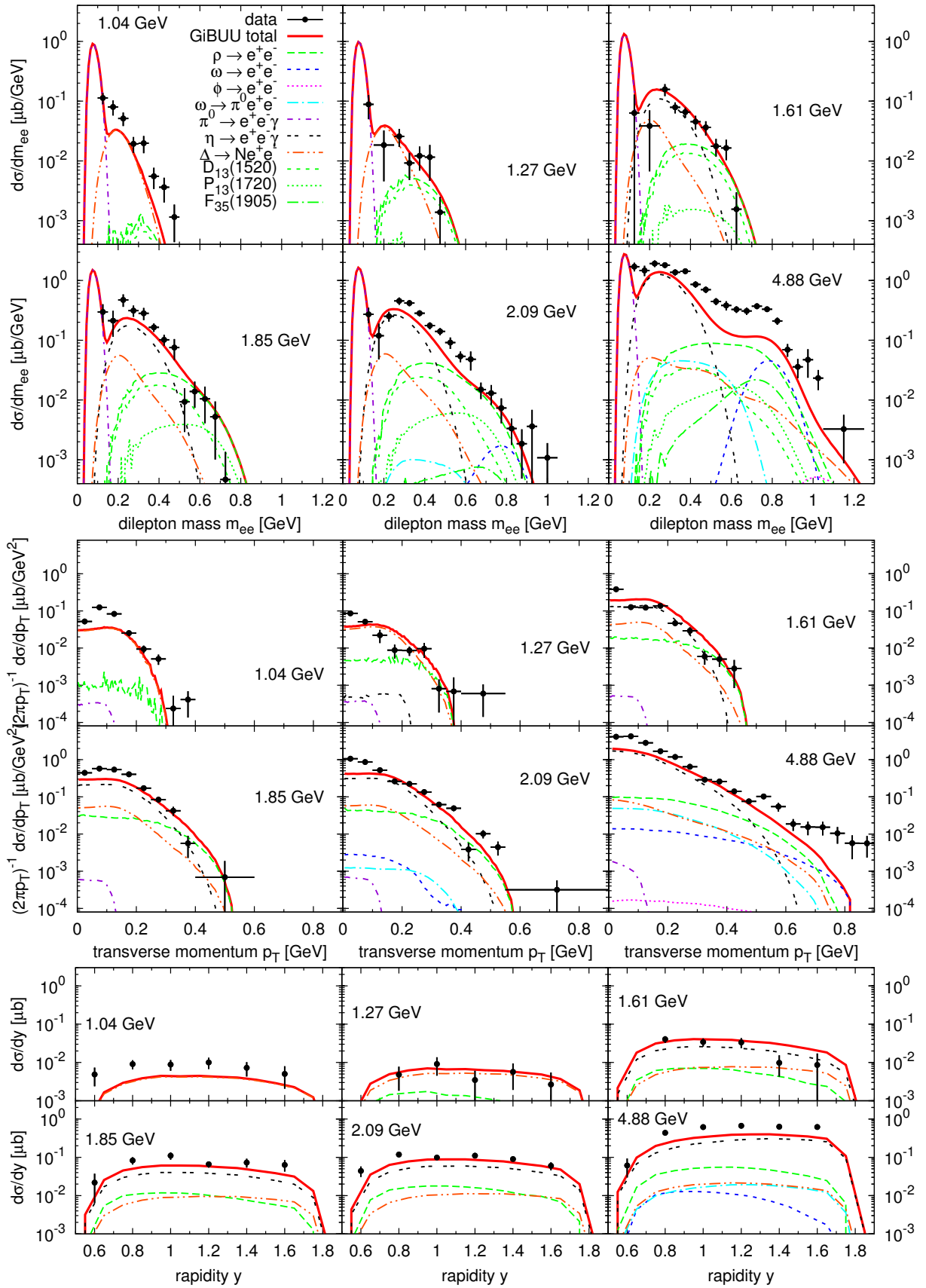
Figure 45: Dilepton spectra from pp collisions at six different beam energies in comparison to DLS data [17]. Top: Mass spectra; center: p_T spectra; bottom: rapidity spectra.
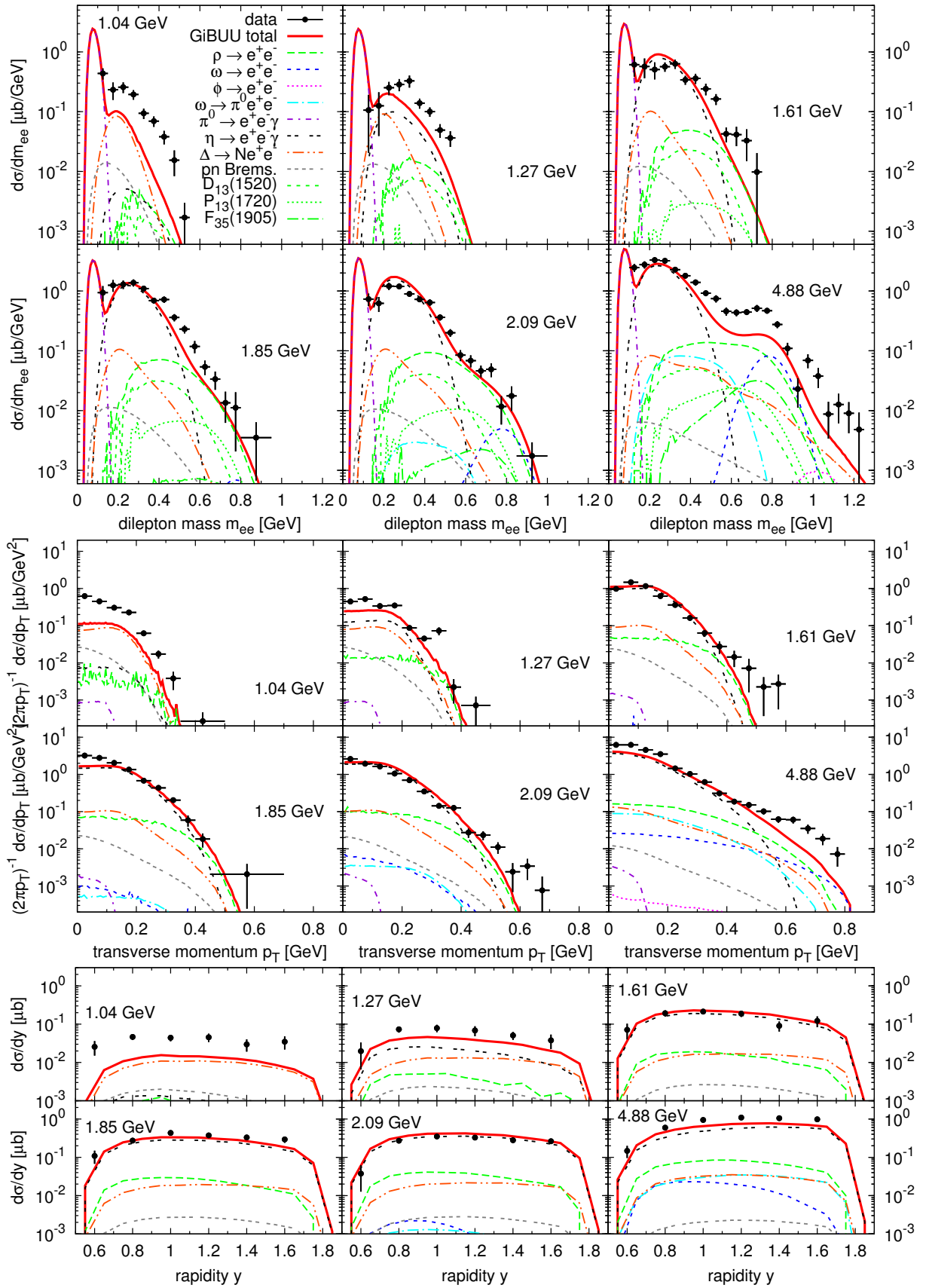
Figure 46: Dilepton spectra from pd collisions at six different beam energies in comparison to DLS data [17]. Top: Mass spectra; center: p_T spectra; bottom: rapidity spectra.

rapidity spectra are limited to masses $m_{ee} > 0.150\,\mathrm{GeV}$. Again, we use the model of Ramalho et al. [99] as the best available calculation of the Δ transition form factor.

It is apparent that at the medium beam energies there is a reasonable agreement, both in p+p and p+d. The largest deviations are visible at the highest beam energy of $4.88\,\mathrm{GeV}$, which is already at the border of validity of our resonance model. Apparently the inclusive production of ρ and ω mesons is underestimated there.
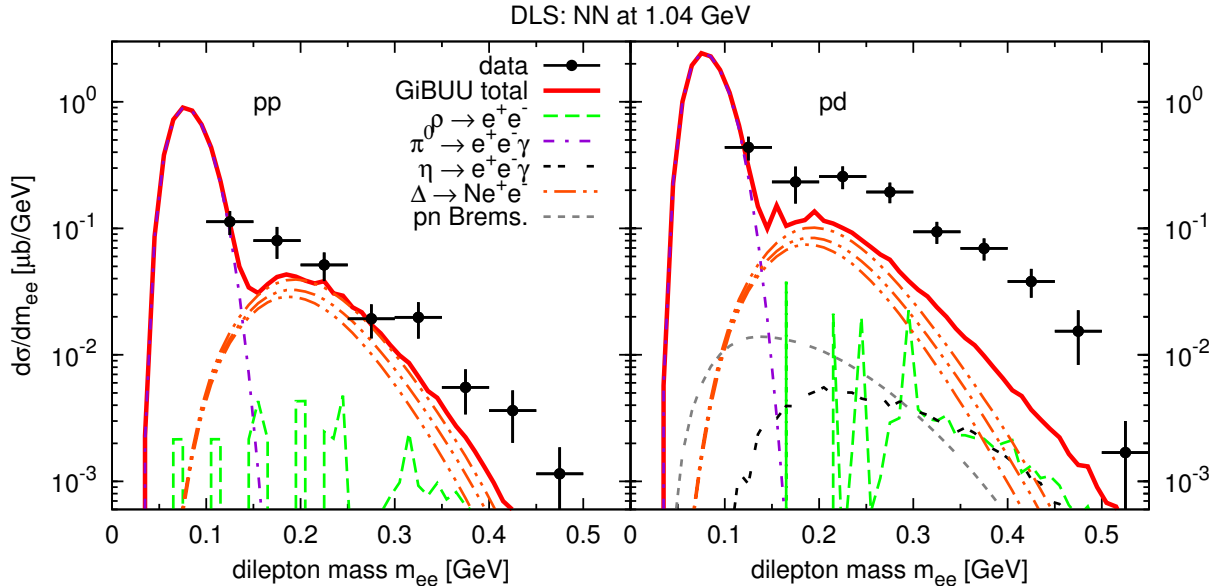
Figure 47: Dilepton mass spectra from pp and pd collisions at 1.04 GeV in comparison to DLS data [17], with different Δ form factor prescriptions.

The underestimation at the lowest energy of $1.04\,\mathrm{GeV}$ is similar to that seen in the HADES experiment at 1.25 GeV (see e.g. fig. 25). Since, at this even lower energy, the η production does not play any role, the discrepancy seems to indicate a problem with the Δ or bremsstrahlung contributions. However, we note again that the population of the Δ resonance is constrained rather well by the pion and total cross sections, which we describe rather well (see Fig. 10). On the other hand, the decay of the resonance is fixed by the electromagnetic coupling at the photon point, so that there is no ambiguity there (at least around the Δ mass pole). Further, form factors have only little influence at such low energies, as seen in fig. 47 (which shows the the Δ from top to bottom with the form factors of Iachello et al. [98], Ramalho et al. [99] and a 'constant' form factor). We thus have to conclude that we have no explanation for the discrepancy yet and note that related, earlier calculations similarly underestimated the DLS dilepton yield at this lowest energy [26].

As observed previously in the HADES case at 1.25 GeV, the discrepancy is much larger on the deuteron than on the proton, which shows that the isospin effects are still not completely under control. Possible isospin enhancements on the neutron could be provided e.g. by the charged-pion exchange diagrams included in the OBE model of [51] or by the isospin factors for ρ production via baryon resonances (cf. sec. 2.3.1.4).

The highest DLS energy of $4.88\,\mathrm{GeV}$, on the other hand, is in fact slightly beyond the limit of applicability of our resonance model (which lies roughly at $\sqrt{s} = 3.4\,\mathrm{GeV}$). As seen in the previous figures, the pp and pd data are strongly underestimated at this

DLS: NN at 4.88 GeV
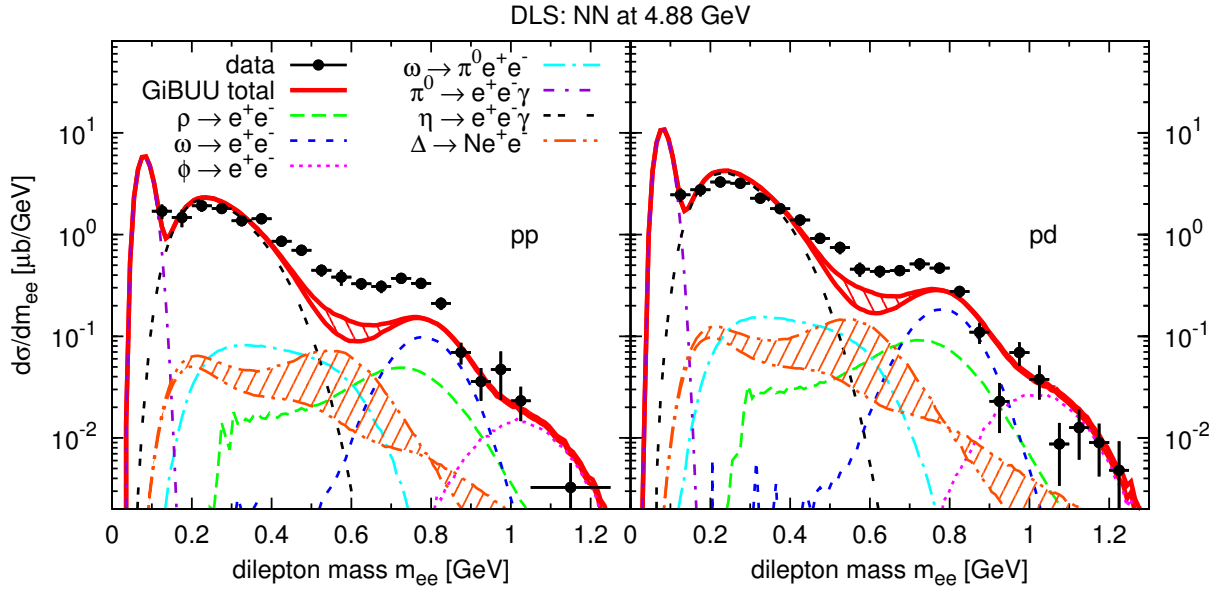
Figure 48: Dilepton mass spectra from pp and pd collisions at 4.88 GeV in comparison to DLS data [17], using PYTHIA cross sections. The Δ Dalitz contribution is shown with the Ramalho and Iachello form factors and the difference between both is indicated by the hatched band.

energy, in particular in the vector-meson region. As an alternative, we try to describe the data at this energy with PYTHIA-based production cross sections, using the same tuning previously applied to the pp reaction at 3.5 GeV measured by HADES, cf. section 3.1.4. The resulting mass spectra for pp and pd are displayed in fig. 48, which shows that the PYTHIA simulation in particular gives a better description of the high-mass region (dominated by the ω and ϕ mesons), due to its proper inclusive production cross sections. However, it still fails to describe the mass region around $0.6 - 0.7$ GeV. The Iachello form factor for the Δ Dalitz decay gives some improvement there, but can not fully fill up the gap. The same problem was previously encountered for the HADES data at 3.5 GeV, and could only be solved satisfyingly via baryon-resonance contributions to the ρ meson production, which filled up the intermediate-mass gap. Therefore we conclude that also the DLS data at 4.88 GeV can only be explained properly in a resonance-model description. However, our resonance-model implementation already starts to fail at this energy, and would need to be extended further (for example with additional resonance production channels like $NN \rightarrow RR$, or with heavier resonances).

3.2.2 A + A at 1 GeV

In addition to the elementary p+p and p+d collisions, the DLS collaboration has also measured four different nucleus-nucleus collisions at a beam energy of approximately 1.0 GeV [16]. These include two symmetric systems (the light C+C and the heavier Ca+Ca), as well as two asymmetric ones (d+Ca and He+Ca). It should be noted that the beam energy of 1.06 AGeV for the d+Ca case is slightly different from the other three systems, where it was determined as 1.04 AGeV. This difference was accounted for in the simulation, although the effect is expected to be minimal. All systems have been

measured in a fixed-target setup without any centrality selection ('minimum bias'). While the experiment used 'natural' C and Ca targets (possibly including a mixture of different isotopes), pure ^{12}C and ^{40}Ca isotopes were used in the simulation (which are certainly a good approximation to the natural targets).

proj.	target	E_{kin}	b_{max}
^{12}C	^{12}C	1.04	6.56
^{40}Ca	^{40}Ca	1.04	9.34
^{2}H	^{40}Ca	1.06	6.67
^{4}He	^{40}Ca	1.04	5.86

Table 10: A+A collisions measured by DLS (in GeV).

The mass spectra for all four A+A systems are shown in fig. 49, comparing the published DLS data from [16] to the corresponding GiBUU simulations in DLS acceptance. Since the beam energy for all four systems is (almost) equal, they all show similar features. The pion Dalitz peak is much smaller here than in the HADES case, due to the limited acceptance in this mass region (cf. also the following section). Despite of this limited acceptance and the resulting uncertainty due to angular distributions etc., the simulations agree surprisingly well with the three data points in the pion region (for all four systems), although there is usually a small overshoot. Note that the data have been published in absolute normalization, and fig. 49 actually compares them to the simulations on an absolute scale (without any scaling factors).

Going higher in dilepton mass, the simulation typically underestimates the data in the region from 150 to 500 MeV. Above this region, we again get a reasonable agreement with most of the data points (within error bars). Since this region is clearly dominated by the ρ contribution, we take this as a further indication that the ρ meson production via resonances is quite well under control in our model.

The underestimation of the data in the intermediate mass region is clearly the biggest issue here, and it's basically what the original DLS puzzle was about. In fact such an intermediate-mass underestimation is also visible for some of the HADES spectra, e.g. in C+C at 1 GeV (to a minor extent, see fig. 36) and in Ar+KCl (quite severely, cf. fig. 38). For the DLS A+A results in fig. 49, one can see that the intermediate mass region is really populated by a number of different channels with similar magnitude: For C+C and Ca+Ca, the Δ, η and $D_{13}(1520)$ channels appear to be most important in the underestimated region, while for d+Ca and He+Ca also bremsstrahlung contributes significantly. Judging from the mass-spectrum shape of the missing yield alone, it seems as if an increased η contribution would be the most promising candidate to fill the gap. However, it is far from clear where such an increased η production should originate from. In principle all relevant production mechanisms in this energy regime should be covered by our model (i.e. $pp \to pp\eta$, the isospin-increased $pn \to pn\eta$, as well as $\pi N \to \eta N$ and even $pn \to d\eta$). A mistreatment of the angular distributions in these processes is indeed a possibility (e.g. our assumption that all η production from NN collisions proceeds via the $N^*(1535)$ is certainly not a fully valid approximation, and also we do not properly treat the formation of a deuteron in $pn \to d\eta$), but these effects are not expected to be large enough to explain the full discrepancy with the data.
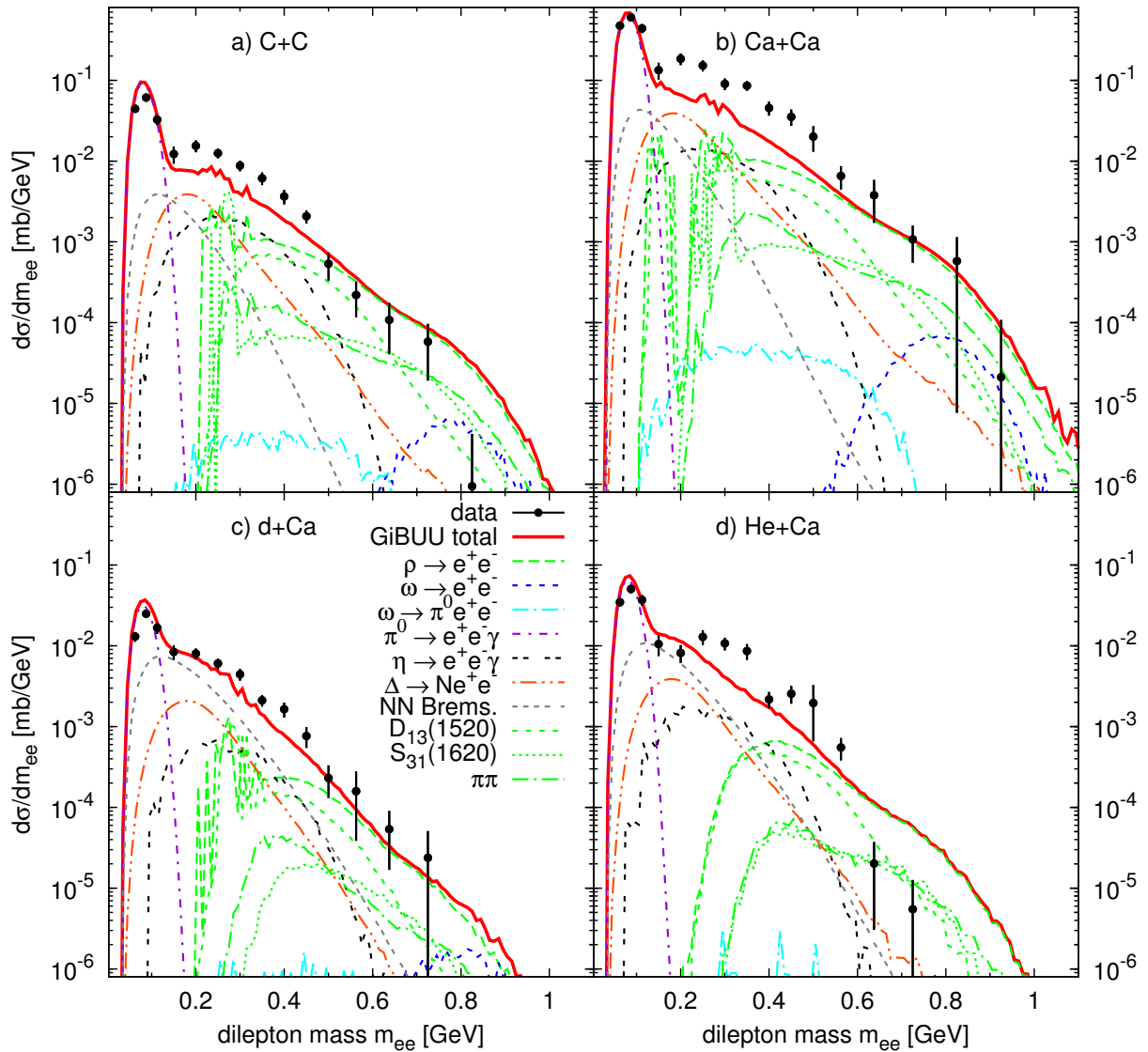
Figure 49: Dilepton mass spectra of A+A collisions at 1.0 GeV in DLS acceptance. Data from [16].

Increased Δ and bremsstrahlung contributions (as proposed in [47]) do not seem to have the right mass shape to explain the discrepancy observed here. Moreover, the methods of treating these channels, as used in [47], are extremely questionable, and it seems that they strongly overestimate e.g. the inclusive Δ production cross section from NN collisions (connected to erroneous isospin factors of $NN \to \Delta\Delta$ from the FRITIOF model, cf. section 2.3.1.2).

From our point of view, the discrepancy between the simulations and the DLS data is very like to be connected with the $D_{13}(1520)$ contribution. Neither its production amplitude in NN collisions is very well known, nor is its coupling to the ρ meson fixed to extremely good precision (according to recent JLab data, the latter might be a bit smaller than previously assumed [77]). It has often been neglected in other transport approaches, and also our treatment of this contribution is on a rather basic level and several uncertainties

are involved. Apart from the already mentioned production cross section and the 'on-shell' branching ratio into ρN, also the off-shell behavior of the $N^*(1520)$ and its partial widths are important. This is not well constrained by experiments and based on theoretical assumptions, which are not necessarily fully accurate. Therefore a stronger contribution of the $N^*(1520)$ seems plausible and may explain at least a part of the discrepancy. And in fact recent investigations of πN spectra seem to indicate an underestimation of the $N^*(1520)$ contribution in the GiBUU resonance model [170].

In addition to the mentioned factors, it should be noted that at such low energies as probed by the DLS A+A measurements, interferences between different contributing channels as well as angular distributions of particle production are becoming increasingly important. The angular distributions are often not well-constrained experimentally, and interferences are neglected in most simulations, since it is very much nontrivial to treat them properly in a transport approach.

Apart from all these sources of uncertainty in the elementary dilepton production mechanisms, additional effects can come from the density and system-size dependence. Indeed it seems that the underestimation of the data increases with growing system size. It is below a factor of two for d+Ca, but in the range of 3-4 for Ca+Ca. That is a clear indication that a density-dependent effect is involved. We have already discussed some of the possible medium modifications in the context of the HADES data, and have observed that our present approach cannot fully explain the ArKCl data points. Therefore we will not add any further discussion here, but rather leave that to future investigations.

3.2.3 HADES vs DLS

In this section, we want to evaluate the effects of the detector acceptance on the dilepton spectra. Neither of the two detectors is a full 4π detector, and so both cover only a certain region of phase space. This means that any model that is to be compared to the data has to undergo a procedure to restrict the full event sample to the same region of phase space that is accessible to the detector. This has been done for our results in the preceding sections, by filtering them through an acceptance filter provided by the experimental collaborations. Since we have so far mostly showed filtered results, we want to compare here the effects of both filters to an unfiltered "4π" spectrum.

For this purpose, the C+C reaction at 1 GeV is particularly suited, since it has been measured by both experiments, and we can obtain from our model both the full 4π spectrum as well as the filtered spectra for the DLS and HADES setups. All of this is shown in fig. 50a. Since the DLS data has been published in absolute normalization, it can be directly compared to the simulation (although a sizable systematic error is introduced by the normalization procedure). The HADES data, however, has only been published in relative normalization, and so we had to scale it by an arbitrary factor to match our pion channel in absolute normalization. In that sense, the absolute scale obtained from the simulation represents the 'glue' necessary to directly compare the HADES and DLS data. The comparison shows that, while the HADES detector has a much better acceptance in the pion-Dalitz region, the acceptance of the DLS detector is actually slightly larger in the high-mass region (above the pion mass). This can be seen both in the data points and in the simulated spectra. The fact that the DLS-filtered spectrum even lies above the 4pi spectrum at very large masses, is simply due to the low mass resolution of the DLS detector, which smears many events to higher masses, where the spectrum drops
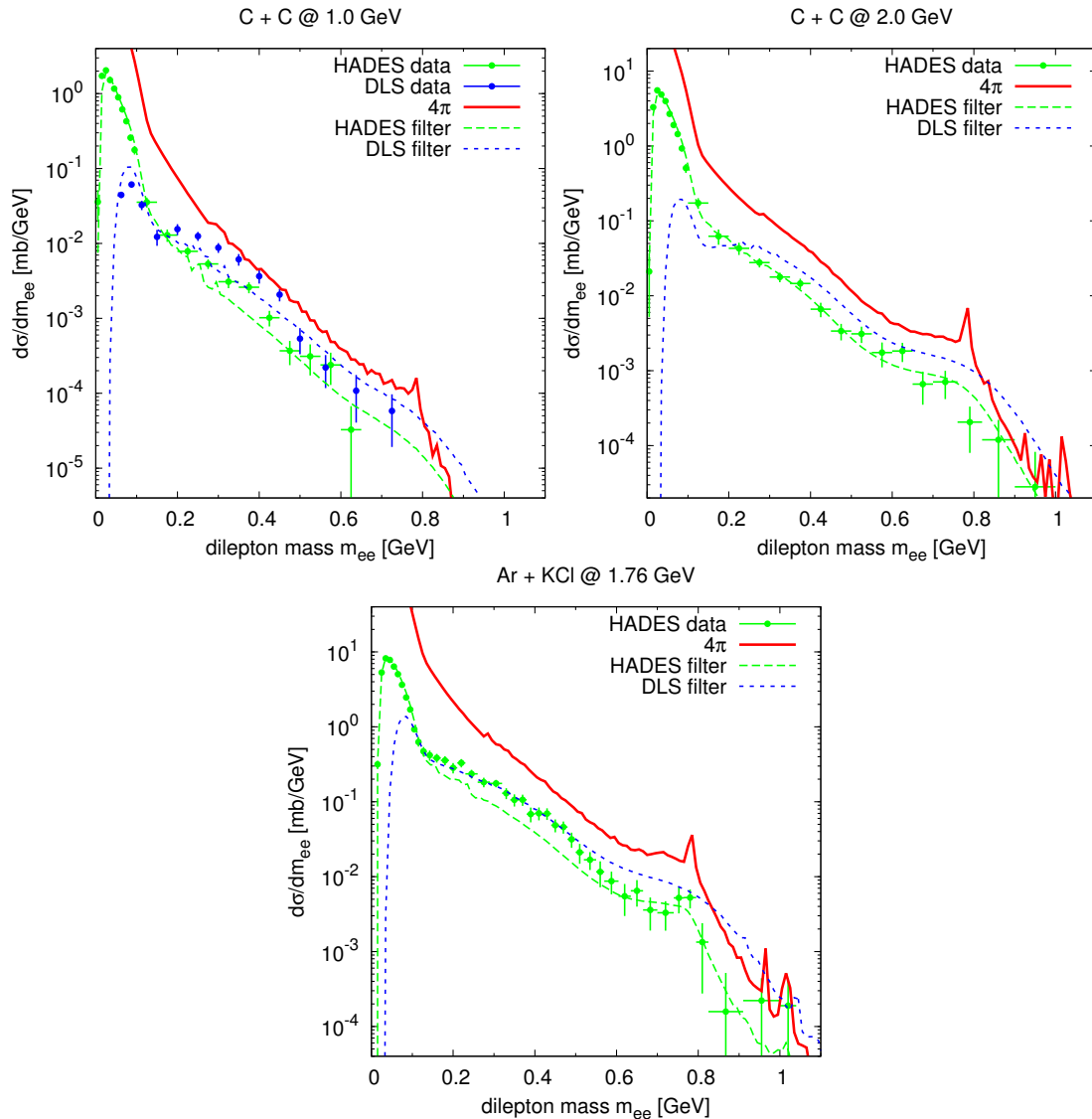
Figure 50: Comparison of HADES and DLS acceptance.

very rapidly.

Further, it is visible in the region around 300 - 400 MeV, where the discrepancy between data and simulation is largest (both for the DLS and HADES case), that the DLS data is actually closer to the 4pi simulation than to the filtered one. This can either mean that the phase-space distribution of events is not properly treated in the simulation, so that too many events are cut away by the filter; or alternatively it could be due to an underestimation of the 4π yield (missing sources). The latter seems more probable, since the deviation is quite large. But since the data is still below the 4π result, it could still just be due to a wrong phase-space distribution. In any case, the comparison shows the significant effect of the filtering procedure, which documents the need for correct angular distributions and the importance of a good knowledge of acceptance effects.

In addition to the C+C at 1 GeV case, we also show in fig. 50 the filter effects for the other heavy-ion reactions measured by HADES (C+C at 2 GeV and Ar+KCl at 1.76 GeV).

For those systems, no DLS data are available. Nevertheless we show the DLS-filtered simulation results for comparison. Both show similar features as C+C at 1 GeV, namely a larger HADES acceptance in the pion region and a slightly larger DLS acceptance above. As seen before, the ArKCl data overshoot the simulation in the intermediate mass region and, by coincidence, are compatible with the DLS-filtered simulation there. While this is certainly not more that a coincidence, it shows the significant effect of the filtering process.

3.3 Pion-induced reactions

Pion-induced reactions are a supplementary source of information, in addition to the proton-induced and heavy-ion reactions discussed in the preceding sections. One particular advantage is that they are considerably cleaner in a certain sense and give a more well-defined access to resonance properties. While a NN collision at a particular energy usually excites a broad variety of resonance states with overlapping and possibly interfering contributions to pion and dilepton production, the energy in a πN collision can be tuned to sit on top of a particular resonance peak, which allows for a comparably clean separation of individual resonance contributions.

Of course it is not possible to completely avoid the problem of overlapping resonances, not even in pion-induced reactions. Therefore the separation of individual resonances usually requires a detailed partial-wave analysis of the measured data, where additional information is drawn from the angular distribution of the resonance's decay products, so that resonances contributing to different partial waves can be separated. Moreover the variation of the charge of the projectile pion allows the separation of different isospin states: While e.g. a $\pi^+ p$ collision can only excite $I = 3/2$ resonances, $\pi^- p$ has contributions from both $I = 1/2$ and $I = 3/2$. For dilepton measurements, however, the charge states $+1$ and 0 are most interesting (corresponding to $\pi^- p$ or $\pi^+ n$), since Δ^{++} and Δ^--type resonances have no dilepton decay modes (except for a possible $\Delta^* \to e^+ e^- \Delta$, which is experimentally unknown at present, but could be constrained via such $\pi^+ p$ reactions).

Since we have argued earlier that resonance contributions are an important ingredient for the dilepton spectra measured by HADES and DLS, pion-induced reactions may help to give additional constraints on these resonance contributions. Two possible approaches come to mind: Firstly, one could directly measure dilepton spectra from pion-induced reactions, tuning the beam energy to hit a certain resonance peak, in order to get maximum contribution from this particular resonance, thereby getting a direct measurement of the dilepton yield from this resonance. Obvious candidates would be the $\Delta(1232)$ and the $N^*(1520)$, both of which are much debated in terms of dilepton contributions, and are expected to be dominant at low energies. And second, the precise measurement of pionic final states (in particular 2π) over a range of beam energies could improve the existing data base, which is the crucial input for partial-wave analyses. In the following we will mostly focus on the dilepton analysis, but will shortly come back to pions at the end of this section.

Fig. 51 shows the dilepton excitation function of $\pi^- p$ collisions, i.e. the energy-dependent integrated cross section for dilepton production. It is clear that the total dilepton production is strongly dominated by the π^0 Dalitz decay, which fortunately is limited to small invariant masses ($m_{ee} < m_\pi$) and can therefore be easily be identified in the mass spectrum. The π^0 Dalitz of course follows the π^0 production cross section, and therefore shows some clear resonance structures: the $\Delta(1232)$ as well as some peaks in the second resonance region. The same structures can also be observed in the bremsstrahlung channel, which in SPA follows the elastic πN cross section. Since this also has strong resonance contributions, the SPA bremsstrahlung given here might be overestimated or have issues with double counting (as discussed earlier), so it should only be regarded as a very rough estimate. For a proper treatment of πN bremsstrahlung, one probably needs to rely on an effective-Lagrangian model like the one recently discussed in [103], instead of the simple soft-photon approximation.
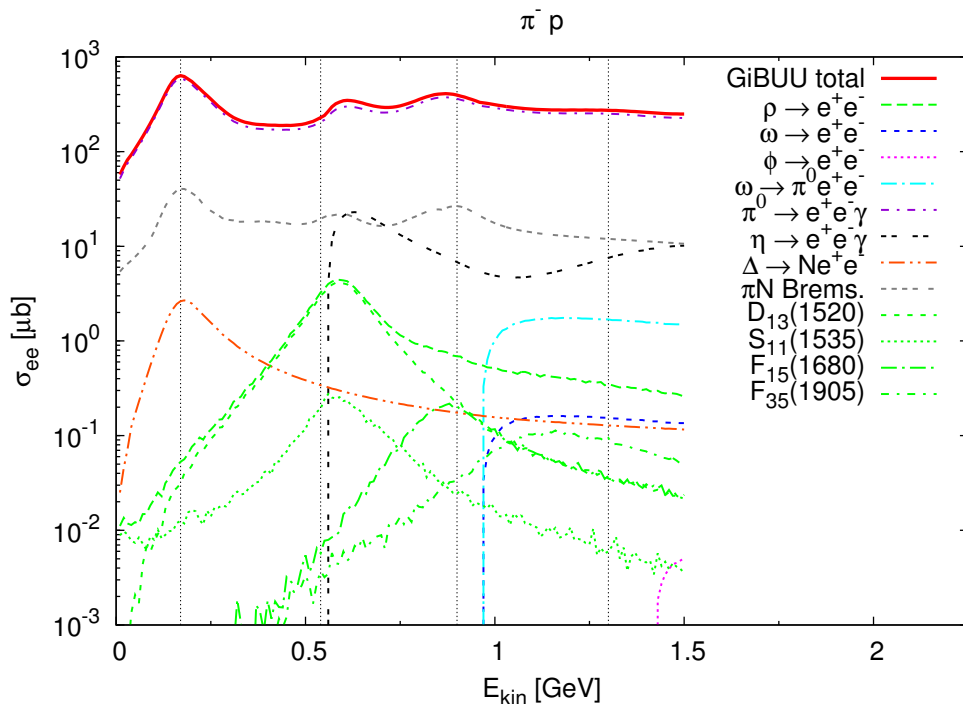
Figure 51: $\pi^- p \to e^+ e^- X$ excitation function.

On the same order of magnitude as the bremsstrahlung is also the η Dalitz decay, which only opens up for pion energies above 500 MeV. Further below are the actual resonance contributions: the Δ Dalitz as well as other resonances contributing through the $R \to \rho N$ decay. Of those resonances contributing through the ρ decay, the $D_{13}(1520)$ gives by far the largest contribution, and clearly dominates the ρ production at low energies. The $N^*(1520)$ peak in the dilepton excitation function is even larger in magnitude than the Δ peak, which confirms its important role for dilepton production, which we already observed in NN collisions.

We note here that the ρ production cross section from πN collisions in our model includes only resonant s-channel production, i.e. $\pi N \to R \to \rho N$, but neglects t-channel processes, which could in principle give additional contributions to pion-induced dilepton production. However, it was concluded for example in [120] that the process $\pi N \to 2\pi N$ is dominated by baryon resonance contributions, which indicates that t-channel contributions are supposed to be small.

E_{kin}	$\sqrt{s}$	p_{lab}
0.17	1.215	0.275
0.54	1.473	0.664
0.90	1.687	1.029
1.30	1.896	1.431

Table 11: $\pi^- p$ reactions considered in this section. All values in GeV.

In light of a possible measurement of dilepton spectra from pion-induced reactions with the

HADES detector, which might be carried out with a pion beam at GSI in the near future, we try here to identify those regions of pion energy that would be most interesting to be investigated experimentally. For this reason we picked out four different pion energies which we want to discuss in more detail, namely $E_{kin} = 0.17, 0.54, 0.90$ and $1.3\,\mathrm{GeV}$ (see also table 11). These are marked by vertical lines in fig. 51, and the corresponding mass spectra are shown in fig. 52.

The first energy of $E_{kin} = 0.17\,\mathrm{GeV}$ was chosen to sit right on top of the Δ peak. After it turned out that the popular transport models yield very different results for the Δ contribution to the HADES dilepton spectra, it was argued that pion-induced reactions might help to pin down the contribution of the Δ Dalitz decay. And indeed, as shown in fig. 52a, this energy provides a rather clean probe of the Δ contribution: The pion Dalitz and bremsstrahlung channels are essentially limited to masses below m_π and contributions of heavier resonances are strongly suppressed (by more than one order of magnitude).
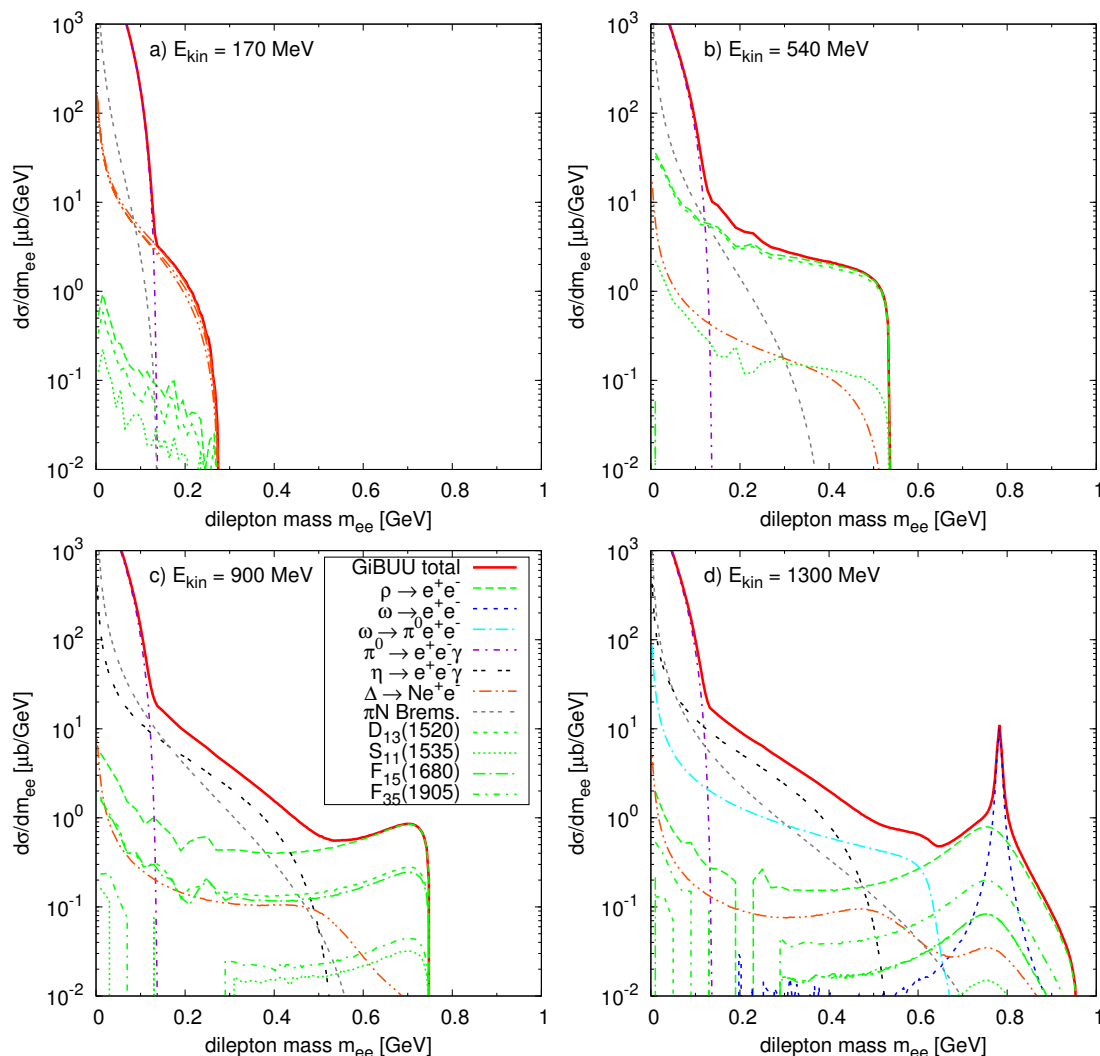
Figure 52: Dilepton mass spectra of $\pi^- p$ collisions at four different energies.

However, the problem is that a dilepton measurement from πN collisions at this energy would not be able to settle the biggest issues connected with the Δ channel: It can neither

fix the inclusive Δ production cross section in NN collisions, nor the off-shell behavior of the dilepton width and Δ spectral function (since the Δ is essentially produced on-shell). Also the differences between different form factor models are not extremely large at this energy, as shown in fig. 52a (from top to bottom: Iachello et al. [98], Ramalho et al. [99] and constant). This severely limits the usefulness of this system regarding constraints on the Δ channel.

Apart from the Δ, another particularly interesting resonance is the $D_{13}(1520)$, which is expected to be very important for the dilepton spectrum due to its large coupling to the ρ meson and its rather low mass. Since the η channel has just opened up at the $N^*(1520)$ peak, we recommend to go to a slightly lower energy of $E_{kin} = 0.54\,\mathrm{GeV}$, which is just below the η threshold and slightly off the $N^*(1520)$ peak. Here one has a very clean testing ground for the $N^*(1520)$ contribution, cf. 52b. Other resonances like the $\Delta(1232)$ and the $N^*(1535)$ are suppressed by roughly an order of magnitude, and bremsstrahlung is limited to small masses, so that the $N^*(1520)$ cleanly dominates the spectrum at masses larger than 300 MeV. Doing this measurement would therefore give a tight constraint on the dilepton contribution from this resonance. At the same time it could yield a direct determination of the $N^*(1520) \rightarrow \rho N$ branching ratio, which so far has only been measured through pionic observables [74,77], and a measurement via dileptons would give an independent check of this quantity. Further it would provide a handle on the transition form factor involved in the $N^*(1520) \rightarrow e^+e^- N$ decay, and a check of the strict-VMD assumption employed in our simulations.

Going higher in energy, we move to $E_{kin} = 0.9\,\mathrm{GeV}$, which is in the region of the $F_{15}(1680)$ resonance and slightly below the ω threshold. Here one has a considerable background from the η Dalitz and bremsstrahlung channels, as seen in fig. 52c, but above the η mass both of these die out and one is left with a rather clean ρ contribution, which however is given by a mixture of several resonance decays here (the dominant ones are the $N^*(1520)$ and $N^*(1680)$, both contributing with roughly equal magnitude). Having determined the $N^*(1520)$ contribution at lower energy, a measurement at this energy could help to establish secondary contributions to the ρ channel from other resonances, such as the $N^*(1680)$. It should be noted that the ρ shape in πN differs from the case of NN collisions, in that it does not contain any low-mass resonance contributions. The reason for this is of course given by the fact that in a πN collision at a fixed energy, all resonances are excited with a fixed mass $W = \sqrt{2m_N E_{kin} + (m_N + m_\pi)^2}$, which is fully determined by the kinetic energy E_{kin} of the pion beam. So, although different resonance states can still contribute at the same energy, they will all have a fixed (off-shell) mass W. Therefore no low-mass contributions are present, and consequently all resonance contributions to the dilepton spectrum have the same shape (as seen in the figure).

Side note: It is conceivable that the ρ mass shape could still be modified, e.g. by different angular momenta of the $R \rightarrow \rho N$ decay. These angular momenta are currently only taken care of in the determination of the decay widths, cf. chapter 2.2.1, but not in the actual kinematics of the decay. Implementing these angular momenta in the decay kinematics would supposedly give a certain modification of the mass shape. This effect should be investigated in future studies.

As a last region of interest, we picked a pion energy of $E_{kin} = 1.3\,\mathrm{GeV}$, which is well above the ω production threshold. This particular energy was mainly chosen because previous results by Weidmann [171] and Effenberger [55] are available at this energy, which can be

compared to our present results. Since the energy is above the ω threshold, the spectrum in fig. 52d shows a clear ω peak (which is shown in full sharpness here, without any detector resolution smearing), and also the ω Dalitz decay gives quite a significant contribution to the spectrum. Furthermore the energy is large enough for the ρ channel to fully develop its peak here (which was not the case for the lower energies).

Comparing our $\pi^- p$ spectrum at $E_{kin} = 1.3\,\mathrm{GeV}$ to that of Effenberger [55], it seems that the η and ρ contributions are roughly comparable, but our ω is somewhat larger. The reason for this is not clear, since we use the same elementary $\pi N \to \omega N$ cross sections as given in [66], section A.2.1 (which we assume are also used in [55]). Also our Δ Dalitz channel is considerably different, which is explained by our usage of a form factor [99], which is missing in [55]. There also a bremsstrahlung contribution is missing, and the contributions of the ρ meson below $m = 2m_\pi$ are neglected, both of which are included in our results.

Finally, it should be mentioned that all the results shown here, as in the previous chapters, are based on the usual transport approximations. In particular, all interferences between contributing amplitudes are neglected and only an incoherent addition of cross sections is performed. However, it has been shown (for example in [172]) that interference terms, in particular ρ-ω interference, can possibly become important in πN reactions.

In addition to the elementary $\pi^- p$ collisions, we also show in fig. 53 dilepton spectra for $\pi^- Pb$ collisions at 1.3 GeV. At first sight the mass spectrum at the top of the figure is qualitatively similar to the $\pi^- p$ spectrum. However, certain differences are visible. For example, a small ϕ peak is present in the nuclear target, due to the additional energy from the Fermi motion of the nucleons. In addition, the contribution of the ω (which suffers from absorption in the nucleus) is diminished relative to short-lived sources like the ρ and the Δ, which are enhanced by secondary production. And finally the mass distribution of the ρ channel is altered significantly. This is actually not an effect of using in-medium spectral functions (the shown spectrum relies purely on vacuum spectral functions), but rather a phase-space effect related to secondary collisions.

To illustrate this, we show in the middle part of fig. 53 the dilepton mass spectrum separated into primary and secondary contributions. That is, the left part (labeled 'primary') contains only dilepton decays from source particles, which have been created in a primary πN collision of the beam pions. The right part (labeled 'secondary'), on the other hand, contains only contributions from source particles which have been created in a secondary collision of any type. In the secondary collisions, the available energy is typically lower than in the primary ones. This is demonstrated by the fact that fewer high-mass contributions are present. In particular, ϕ mesons are too heavy to be produced in secondary collisions, and also the ω peak is much smaller than in the primary spectrum. For the ρ meson, a clear difference in mass shape is visible: While the primary spectrum exhibits a nearly 'free' mass shape (very similar to the elementary $\pi^- p$ reaction), the secondary spectrum has strongly-enhanced low-mass contributions, due to the lower available energy. In particular, contributions of light resonances like the $D_{13}(1520)$ become much more important than those of the heavier ones, like e.g. the $F_{35}(1905)$. Due to the interplay of primary and secondary contributions, the total ρ shape develops a characteristic kink around 600 MeV, which marks the transition from the heavy primary ρs to the light secondary ρs.

This means that the ρ shape in $\pi^- Pb$ is significantly modified over the the $\pi^- p$ ('vacuum')
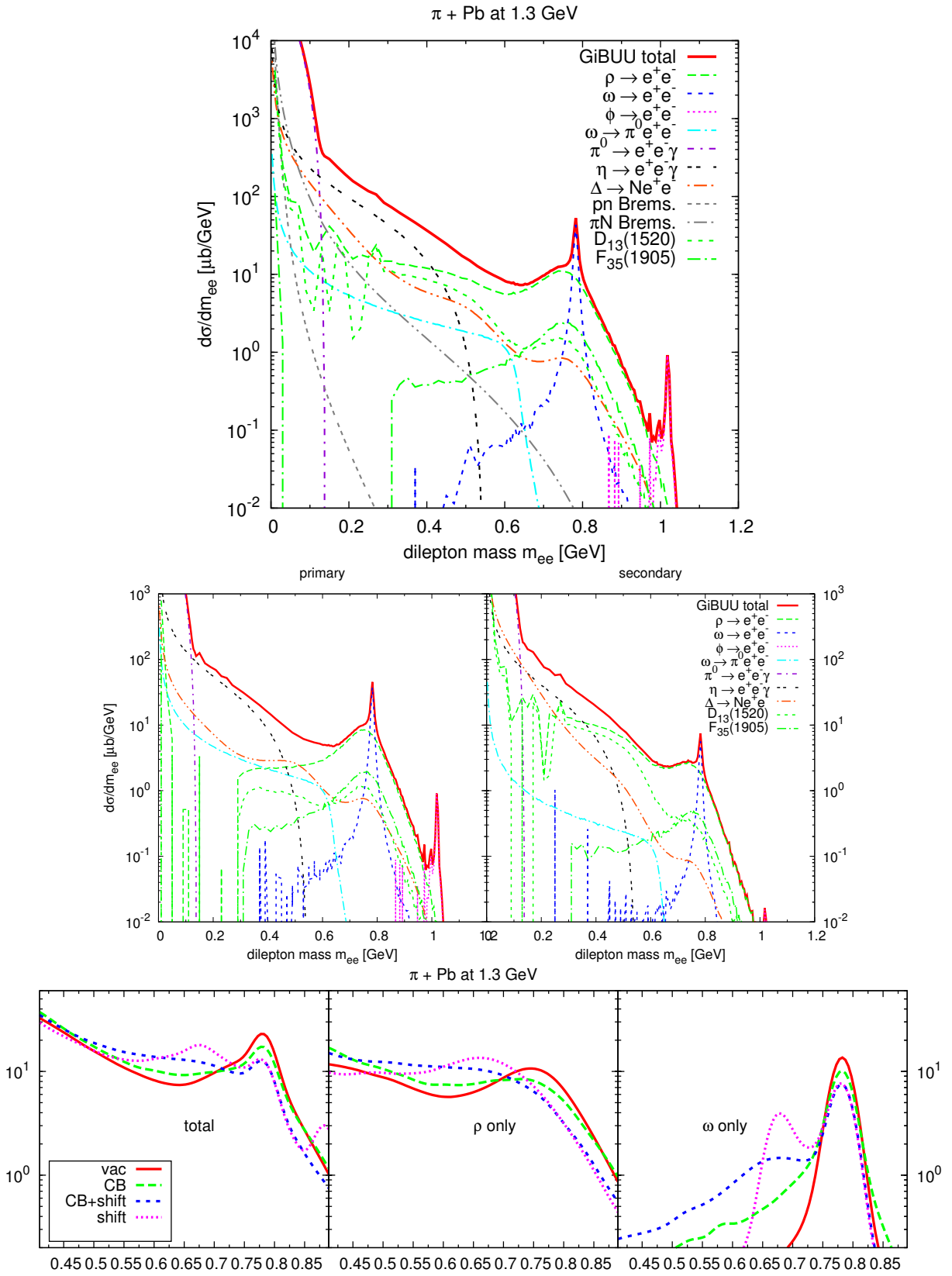
Figure 53: Dilepton mass spectrum of π^-Pb collisions at 1.3 GeV. Top: Total spectrum. Middle: Split into primary and secondary contributions. Bottom: With medium modifications (and smeared with a resolution of 15 MeV).

case, already without explicitly applying in-medium spectral functions. By the way a similar effect is present also in pA vs pp collisions, where it is much weaker, however, due to the fact that pp already contains a mixture of resonance decays of different masses (while πp is always tuned to a particular resonance mass).

In addition to the aforementioned phase-space effect of secondary collisions, the ρ mass spectrum can in principle be further modified by actual in-medium changes of its spectral function. The lower part of fig. 53 shows the modifications of the dilepton mass spectrum with different scenarios for the in-medium spectral function of the ρ and ω meson. As before, we consider collisional broadening, a negative mass shift or a combination of both. The observed effects are similar to the p+Nb case we have studied in section 3.1.5, but somewhat larger, due to two reasons: First, it is slightly easier to produce low-momentum vector mesons in a pion-induced setup (which have then a larger chance of decaying in the medium), and second the ^{208}Pb nucleus used here is larger than the ^{93}Nb nucleus in the proton-induced case. For the ω meson, the in-medium peak even becomes comparable in size to the vacuum peak, but only in the pure-shift scenario, which is unrealistic. With the collisional broadening established by CBELSA/TAPS, the in-medium peak melts considerably, so that there is little hope to observe it directly. For the ρ, however, also the CB+shift scenario generates significant modifications of the dilepton spectrum (primarily filling up the kink in the ρ channel), which might be well-distinguishable from the vacuum case with sufficiently precise data.

A second important strategy for a pion-beam setup at GSI, apart from dilepton measurements, could be to measure pionic observables (instead of dilepton spectra) in order to get better constraints on resonance properties. Here the reaction $\pi N \to 2\pi N$ is of particular interest, for two reasons: Firstly, data for this reason are quite rare and often very old. Many modern PWAs do not take into account sufficient amounts of 2π production data. Secondly, the 2π channel is essential to get information on $R \to \rho N$ decay modes, which are of vital interest for dilepton spectra at SIS energies, as we have showed in the preceding chapters. The branching ratios of the ρN decays are a crucial input for dilepton calculations, and their error bars are often a limiting factor.

For example, the decay $D_{13}(1520) \to \rho N$ is listed in the PDG's current 'Review of Particle Physics' [78] with a branching ratio of $15 - 25\%$. Manley's value of 21 % [74] is obviously compatible with this range, but more recent measurements [77] seem to indicate slightly smaller values ($8 - 17$ %), however still with considerable error bars. Tighter constraints on this value, as well as the ρN branching ratios of other resonances, are urgently needed!

3.4 Dileptons at higher energies

Apart from the low-energy regime available to the SIS18 and Bevalac accelerators, dilepton spectra have also been measured at higher energies, of course. We will not show here any actual results for high-energy collisions, but only give some outlook on what might be done in the future.

As a first example of dilepton spectra at slightly higher energies, the E325 experiment at KEK (Japan) has measured dilepton spectra from proton-induced reactions on nuclei, such as p+C and p+Cu, at kinetic beam energies of $E_{kin} = 12\,\mathrm{GeV}$ (corresponding to $\sqrt{s}_{NN} \approx 5.1\,\mathrm{GeV}$) [15]. The results obtained there have been proposed to indicate a mass shift of the ρ and ω mesons of about 9% at normal nuclear matter density. However, it was also claimed that the E325 analysis suffers from severe background-subtraction problems, which would render this result a fake [12]. From a theoretical point of view, the KEK result seems questionable, since it does not see any sign for broadening of the vector mesons, which is a well-established effect [13, 35].

In a similar energy regime, experiments with the HADES and CBM detectors are planned at the future FAIR facility. As with HADES at SIS 18, reactions such as pp, pA and AA will be studied there in a fixed-target setup, however at significantly higher energies: For the heavy Au+Au system, beam kinetic energies of up to $E_{kin} = 11\,\mathrm{GeV}$ will be available in the first configuration of SIS100 (corresponding to $\sqrt{s}_{NN} \approx 4.9\,\mathrm{GeV}$). With an upgrade to SIS300, this will be raised further to $E_{kin} = 35\,\mathrm{GeV}$ (corresponding to $\sqrt{s}_{NN} \approx 8.0\,\mathrm{GeV}$).

Both E325 at KEK and HADES/CBM at FAIR are situated at energies which clearly reach beyond the low-energy regime that can be covered by a resonance model like the one we have applied in this work. In order to properly describe such reactions in a transport approach, one will certainly need to facilitate a string-model approach for the elementary hadron-hadron collisions. In GiBUU, the PYTHIA 6.4 event generator [104, 105], which is a state-of-the-art string-model implementation, is used to model high-energy collisions. However, the energies at FAIR and KEK are still low enough that resonances could still play a role there. Therefore the most desirable treatment would be to not switch between resonance and string model at a fixed energy (or with a small transition window, as it has been done in GiBUU in the past [61]), but combine both models in a well-defined way, e.g. by treating low-multiplicity collision channels with the resonance model, and use the string model only for those high-multiplicity final states which are not covered by the resonance model.

Such a setup would ensure on the one hand that one can carry the resonance effects, which have proven to be so important at SIS energies, over to higher energies (although they are expected to be less dominant there), and on the other hand that one can describe the full reaction dynamics, including all of the high-multiplicity channels which become available. Except for some minor technical intricacies, no principal problems are to be expected for such an implementation.

Going even higher in energy, various other dilepton measurements are available, e.g. from NA60 [19, 89, 173] and CERES [18, 174, 175] at SPS, PHENIX [176–178] and STAR [179] at RHIC and soon also from ALICE at LHC [180]. The PYTHIA model employed for the high-energy elementary collisions in GiBUU should in principle be able to cover basically the complete energy range from SPS over RHIC up to the LHC. However, one of the limitations of the GiBUU model is that it is purely based on hadronic degrees of freedom

at the moment. As one goes to higher energies (resulting in higher temperatures of the fireball created in heavy-ion collisions), one gets more and more into a regime where the confinement of quarks and gluons inside hadrons is suspended, and a hot soup of quasi-free quarks and gluons is created, the so-called quark-gluon plasma (QGP). In order to describe a heavy-ion collision at such high energies, it is necessary to treat both the hadronic phase, which is expected to dominate at the beginning of the reaction and in peripheral regions where the energy density is not so large, as well as the partonic phase, which is expected to emerge at some point in the central region of the collision, where the highest temperatures and densities are reached. But of course this QGP phase will only have a short lifetime and should freeze out into hadrons again as it expands and cools down. Therefore the final stage of the collision must again be treated via hadronic degrees of freedom. Moreover, the phase transition from the hadronic to the partonic phase (and back) must be treated properly, and in principle also regions of mixed phases might occur.

All of this can be approached either by introducing a microscopic partonic phase and modeling the propagation and collisions of quark and gluon quasiparticles in a transport approach (as e.g. done in pHSD [181]), or by discarding a 'microscopic' description of the QGP phase and instead using a hydrodynamical approach, which is based on collective degrees of freedom (as done in the hybrid UrQMD model [182]).

4 Photoproduction of ω mesons detected via $\pi^0\gamma$

In this chapter we will discuss in some detail the ω meson and its possible modification in cold nuclear matter, which has not only been studied via the dilepton channel, but also via the semi-hadronic $\pi^0\gamma$ decay.

When studying in-medium effects of the ω meson by observing its decay products, one has to remember that the invariant mass reconstructed from the four-vectors of the decay products always contains a product of spectral function and branching ratio. In choosing the decay channel one has the choice between the rare dilepton decay mode, which is free of final-state interactions, and the more prominent hadronic or semi-hadronic decays, like $\omega \to \pi^0\gamma$. While the latter has the advantage of a much larger branching ratio of 8.3% (roughly three orders of magnitude above the dilepton channel), it suffers from the fact that of one the decay products (namely the π^0) undergoes strong final-state interactions (FSI). For a long time it was commonly assumed that there are ways to cope with this issue, but we will show here that the pion FSI poses a major obstacle and in fact makes the $\pi^0\gamma$ decay unsuitable for certain in-medium studies.

Experimentally, the decay $\omega \to \pi^0\gamma$ has been studied intensively by the CBELSA/TAPS collaboration in photoproduction reactions on nuclei [34–37]. Moreover, ω mesons in cold nuclear matter have been investigated via the dilepton decay channel by E325 at KEK [15], CLAS at JLAB [12–14] and most recently by HADES at GSI [33]. While the CLAS data indicate a broadening of the ρ and ω, but no shift, E325 claimed an ω mass shift without any broadening (however, it has been claimed that the E325 analysis suffers from background-subtraction problems [13]). For the HADES data, no consistent interpretation is available yet regarding the ω meson: So far the p+Nb data only seem to show indications for an absorption of the ω meson [110], cf. also section 3.1.5. Overall, the in-medium mass shift of the ω meson is still an open issue from an experimental point of view. If one discards the KEK result, it seems that a mass shift is rather unlikely. However, the question is also whether the mentioned experiments actually have the sensitivity to detect a mass shift (if it exists), which we try to answer here at least for the CBELSA/TAPS experiment.

In the following, we will give an overview over several methods for determining the in-medium properties of ω mesons in cold nuclear matter, such as invariant mass spectra, transparency ratios and excitation functions. As a new method we propose a study of the ω meson's momentum distribution.

4.1 Invariant Mass Spectrum

The idea to study in-medium properties of the ω meson via the $\pi^0\gamma$ invariant mass spectrum was first proposed in an early exploratory study by Messchendorp et al. [57], and further studied theoretically in a subsequent transport investigation [58]. The first measurement followed soon [34] and indeed claimed to observe a shifted in-medium peak in the $\pi^0\gamma$ invariant mass spectrum. This claim was withdrawn later, after follow-up analyses [36,37] with systematic studies of the background could not confirm the finding. The problems that one has to deal with when studying the in-medium spectral function of the ω meson via the reconstructed $\pi^0\gamma$ invariant mass involve e.g. the rather long lifetime of the ω (which means that only a fraction of the ω mesons will actually decay in the

medium) as well as the final-state interaction of the decay pion (which can severely distort or damp the in-medium signal).

The results of our present transport study indicate that about 20 – 30 % of all $\omega \to \pi^0\gamma$ decays occur in the medium (i.e. at densities above a threshold of $0.1\rho_0$). However, there are several effects which affect the actual observability of any in-medium effect. First of all, one expects a significant 'melting' of the in-medium peak due to collisional broadening. From the transparency ratio measurement of Kotulla et al. [35] a collisional width of $\Gamma_{coll} \approx 130 - 150\,\text{MeV}$ was extracted, which exceeds the ω decay width in vacuum by more than a factor 10. This means that the in-medium peak should be considerably smeared out, making it much harder to observe [183].

Moreover, not all of the in-medium decays happen at full nuclear density ρ_0 in the center of the nucleus. Every nucleus has a diffuse surface with a slowly dropping density distribution. The fraction of ω mesons decaying at the surface will further smear out the in-medium peak, if we expect a density-dependent mass drop. This holds for any decay mode of the ω meson.
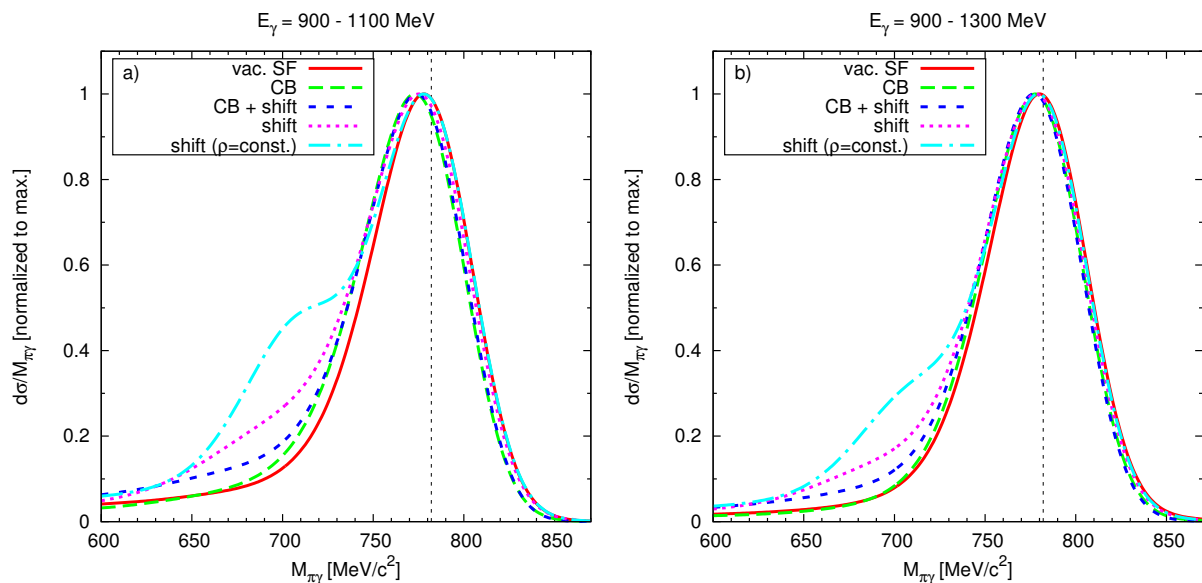
Figure 54: ω meson line shape predicted for a Nb target for different in-medium modification scenarios. a) incident photon energies of 900 - 1100 MeV; b) incident photon energies of 900 - 1300 MeV.

Both of the just mentioned effects, i.e. the 'damping' of the in-medium peak as well as the density smearing, are illustrated by fig. 54, which shows the $\pi^0\gamma$ invariant mass distributions for ω photoproduction on a ^{93}Nb nucleus, for two different photon energy ranges close to the free production threshold.

The signals are folded with the detector response given by the Novosibirsk function [184]

$$f(x) = A \cdot \exp\left[-\frac{1}{2}\left(\frac{\ln q_x}{\tau}\right)^2 + \tau^2\right],\tag{99}$$

with

$$q_x = 1 + \frac{(x - x_0)}{\sigma} \cdot \frac{\sinh(\tau\sqrt{\ln 4})}{\sqrt{\ln 4}}, \tag{100}$$

using a width parameter of $\sigma = 25$ MeV and a skewness of $\tau = -0.09$ [37] (note that the Novosibirsk function transforms into a Gaussian function for $\tau \to 0$). Furthermore the simulation takes into account a $1/E_\gamma$ weighting of the bremsstrahlung spectrum of the incident photon energy.

For both energy ranges we show the spectrum in different in-medium scenarios (all of which have been normalized to the same vacuum peak height): Vacuum spectral function (solid), collisional broadening of $\Gamma_{coll} = 140$ MeV (long dashed), collisional broadening and an attractive mass shift of -16% at nuclear matter density (short dashed) and mass shift without broadening (dotted). The modifications in all these scenarios are relatively modest, however they are slightly larger for the lower photon energy range, since the mesons are produced on average with lower momenta and therefore have an increased chance of decaying inside the nucleus.

Obviously the largest modifications are obtained in a pure mass-shift scenario, where additional strength accumulates at the left shoulder of the ω peak, due to decays in the medium with lowered masses. Adding collisional broadening on top of the mass shift, the enhancement weakens since the in-medium peak is broadened and smeared out. And in the pure broadening scenario only a marginal difference to the vacuum curve is visible.

In addition to the four curves already discussed, the dashed-dotted curve shows the pure-mass-shift scenario for a constant nuclear density of $\rho = 0.6\rho_0$ (which obviously is not a realistic scenario, but was only included to illustrate the density-smearing effect). This significantly increases the enhancement effect, since the nucleus has no diffuse surface any more and all 'in-medium' decays really happen at the same density (i.e. with the same mass), which avoids the density-smearing effect mentioned earlier. Even with a reduced density of $0.6\rho_0$ (which should be close to the average density in a Nb nucleus), this enhances the observable in-medium modifications, which shows the large effect of decays in the surface region. However, it should be mentioned that a part of this effect is also caused by a slightly larger size of the nucleus (due to the lower central density).

The results in fig. 54 also show that we are not able to reproduce the spectra shown in [56], which showed much larger low-mass tails (see e.g. fig. 9.28 there). The most significant difference between our simulations and those of [56] (which were done with a predecessor of the current GiBUU code) is the treatment of the off-shell propagation, i.e. the dynamical changes of the test-particle masses according to density-dependent spectral functions. As discussed in section 2.4, we rely on an 'off-shell potential' ansatz based on the equations of motions from [144], whereas the off-shell treatment in [56] is based on the earlier ad-hoc ansatz of [66].

It seems that the large tails in [56] are an artifact of this ad-hoc ansatz, related to particles not properly returning to the vacuum mass shell as they propagate out of the nucleus. In particular fig. 9.27 in [56] shows that the percentage of actual in-medium decays is quite small and cannot be responsible for the large tails, which therefore have to be caused by vacuum decays. The results of [56] also suggest that the off-shell treatment applied there is only problematic at threshold energies, but not for higher energies, where such strong tails are not observed.

To illustrate the problem and the difference to our new simulations, we show in fig. 55
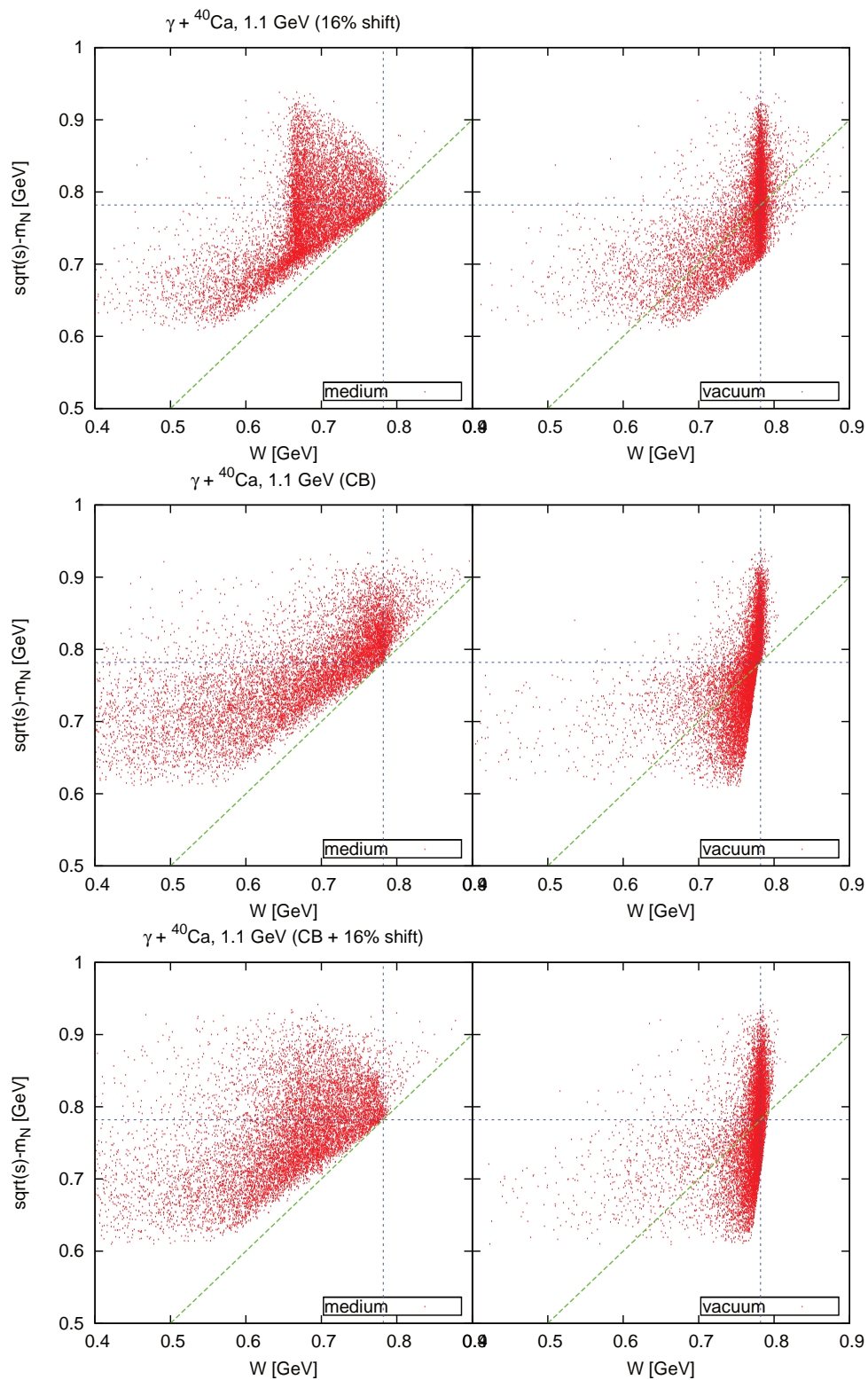
Figure 55: 2-dimensional distributions of effective mass W versus production energy $\sqrt{s} - m_N$ of ω mesons in the medium (i.e. at production) and in the vacuum (i.e. after having propagated out of the nucleus) for three different in-medium scenarios. Top: Mass shift; center: collisional broadening; bottom: broadening plus shift.

three plots equivalent to fig. 9.14 in [56], which shows a scatter plot of the mass-vs-energy distribution of ω mesons in $\gamma+^{40}$Ca collisions at $E_\gamma = 1.1$ GeV. The distribution of the invariant ω mass W and the center-of-mass energy $\sqrt{s}$ available in the production process $(\gamma N \to \omega N)$ is shown both in the medium (i.e. at production time, left) and in the vacuum (i.e. after having propagated out of the nucleus, right). We show these distributions for three different scenarios (top: mass shift of 16%, center: collisional broadening, bottom: broadening plus shift), while they are only given for a broadening-plus-shift scenario in [56]. The diagonal green dashed line represents a kinematical limit in the production process $\gamma N \to \omega N$, where the ω mass is obviously limited to $W < \sqrt{s} - m_N$. It is apparent that all our in-medium distributions obey this limit, and so does the one from [56]. However, we stress that this limit applies only to the production process, but does not necessarily need to hold for later times, if the ω mass changes dynamically during its propagation through the nucleus. Such a dynamical change in our simulations is either due to the scalar potential which causes the mass shift or the off-shell potential connected to the collisional broadening (or both). It results in a horizontal movement of the dots in the scatter plot, which also abolishes the original production-process limit: In the pure-mass-shift scenario, all points move to the right as the ω mesons gain mass when propagating outward, and therefore also the diagonal line of maximally-possible mass shifts to the right, and in the vacuum is different from the original kinematical limit in the medium. Also the other scenarios are affected in a similar fashion: For the collisional broadening, the line of maximum mass in the vacuum is not shifted but rotated, since the off-shell potential is proportional to the 'offshellness' (which means it is stronger for particles which are further off the mass shell). However, the kinematical limit is only in full effect for subthreshold energies, where the ω can only be produced below its mass shell. For $\sqrt{s} - m_N > 782$ MeV, the ω mass can reach the on-shell value of 782 MeV, so that no strong limitation of the spectral function is observed any more. For the broadening-plus-shift scenario, the combination of both effects leads to a rotation plus shift of the maximum-mass boundary. We note that for each of the three scenarios, the final mass distribution of the ω mesons always goes beyond the original production limit.

In fig. 9.14 of [56], however, the production limit is still obeyed in the vacuum distribution. We believe that this is an artifact in the off-shell transport implementation employed there, which is possibly due to the fact that both the in-medium as well as the vacuum mass are chosen independently by Monte-Carlo already at production time. Therefore the same kinematical limit is applied to both, and the fact that dynamically-changing masses also alter the kinematical limit was apparently dismissed. This explains also why this problem is only acute at threshold energies: Here one is close to the kinematical limit, while at higher energies it does not really play a role any more.

Our new treatment of the off-shell propagation does not suffer from such problems at threshold. Only the in-medium mass is fixed at production time, and subsequently the dynamic evolution of the effective mass is goverened by potentials. This makes sure that the vacuum spectral function is (approximately) restored for particles propagating out of the nucleus, which leads smaller modification effects in the $\pi^0\gamma$ mass spectrum (as compared to [56]).

Although the new treatment clearly represents an improvement over the previous ad-hoc ansatz, we emphasize that there are still problems and limitations in several areas (as discussed in section 2.4.2). In particular, the off-shell potential approach is not perfect

for very far-off-shell particles, cannot properly handle momentum dependencies of the in-medium self energy and introduces limitations even on the vacuum width. However, within the approximations applied here and in the mass range around the pole mass, it is supposed to give a rather reliable estimate of the expected medium modifications.
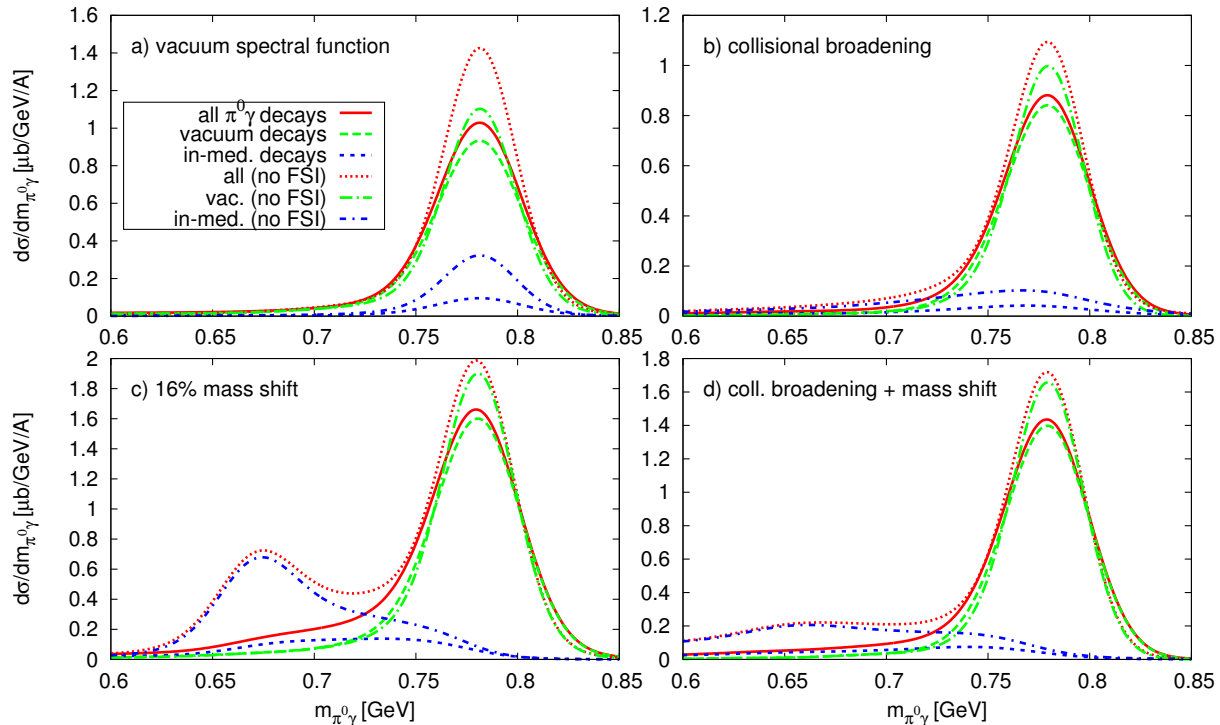
Figure 56: Calculated $\pi^0\gamma$ mass spectrum for γ+Nb at 0.9 - 1.3 GeV, in four different in-medium scenarios. Shown are the total spectrum as well as the contributions from in-medium ($\rho > 0.1\rho_0$) and vacuum ($\rho < 0.1\rho_0$) decays, with and without pion FSI.

After some discussion of the off-shell propagation, we now return to the question of why the medium modifications observed in fig. 54 are actually so small for realistic scenarios. Apart from the already mentioned density-smearing and the damping of the in-medium peak, the $\pi^0\gamma$ channel suffers from an additional limitation of the usefulness of the invariant mass spectrum as an indicator for in-medium effects, namely the strong final-state interaction (FSI) of the π^0 daughter particle. Most previous studies concentrated on the fact that the background created by rescattered pions can be suppressed by kinetic energy cuts [57]. Little attention was paid to the fact that the pion FSI selectively favors decays at small densities, as far as observability is concerned. If a π^0 from an ω decay scatters with a nucleon, there are two possibilities: Either the collision is inelastic, leading to an absorption of the π^0 ($\pi^0 N \to NX$), possibly due to charge exchange (e.g. $\pi^0 p \to \pi^+ n$); or the collision is elastic ($\pi^0 N \to \pi^0 N$), which typically causes an energy loss of the pion in the laboratory, so that the reconstructed $\pi^0\gamma$ invariant mass is changed dramatically. In both cases the event is basically unusable for the ω reconstruction, since the original ω in-medium mass is lost.

The FSI has dramatic consequences for the in-medium part of the $\pi^0\gamma$ mass spectrum. Decay products coming from high densities at the center of the nucleus have little chance

of making it outside without rescattering, so that mostly those from the surface will be observed, which carry little information on medium modifications. This means that the pion FSI cuts away most of the in-medium peak, as can be seen in fig. 56, and even in the very unlikely scenario of a pure mass shift, only a minor in-medium contribution to the spectrum is left. In the scenarios including collisional broadening, the in-medium peak is already broadened so strongly, that even without any FSI of the decay products, it would be hard to unambiguously measure a medium modification of the spectrum and to distinguish it from the background.

Although a much smaller effect of pion FSI was obtained in [185], this calculation also supports our conclusion that the $\pi^0\gamma$ invariant mass distribution is not very sensitive to in-medium modifications of the ω meson.

Note that fig. 56 includes the mass resolution of the CBELSA/TAPS detector, incorporated by folding the spectrum with a Gaussian distribution of 19 MeV width (the small skewness, which was previously incorporated through a Novosibirsk function, is neglected here). However, we have verified that the mass resolution of the detector is not a limiting factor, and that even an improvement of this resolution would not dramatically increase the chances of being able to observe any in-medium modification.
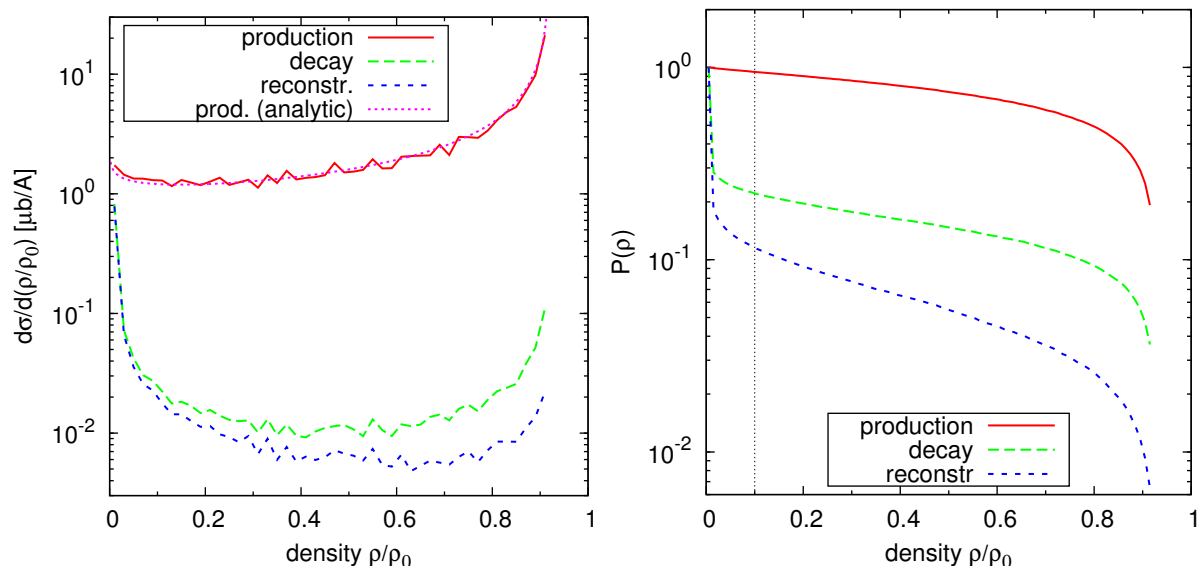
Figure 57: Left: Distribution of the production points of ω mesons in photoproduction on Nb, $E_\gamma = 0.9 - 1.3\,\mathrm{GeV}$, as a function of density (topmost line). Also shown are the $\omega \to \pi^0\gamma$ decay points without (middle line) and with (lowest line) pion FSI. Right: Probability $P(\rho)$ for a process happening at densities larger than ρ.

The density distributions of the production and decay point (with and without FSI) are shown in fig. 57. While the production density has a clear peak at full nuclear density, the decay point tends to lie in the vacuum due to the rather long lifetime of the ω meson ($\tau \approx 23.2\,\mathrm{fm/c}$). On top of this, the FSI of the decay pion further decreases the sensitivity to high densities (as seen in the difference between the long-dashed green curve and the short-dashed blue curve in the figure). Additional cuts on the pion kinetic energy or the $\pi^0\gamma$ invariant mass can further reduce the reconstructed events from high densities.

The production density distribution is rather easy to calculate analytically. We start with the ansatz

$$\frac{\mathrm{d}N}{\mathrm{d}r} = \rho(r) \cdot 4\pi r^2.$$

This represents the assumption that an ω meson is produced with equal probability on each nucleon, which means that effects like shadowing are neglected (which should only play a role at higher energies), so that the production probability simply follows the nuclear density. Further, we use a Woods-Saxon density profile for the nucleus:

$$\rho(r) = \frac{\rho_c}{1 + e^{(r-r_0)/a}}$$

where $r_0 = 1.2\,\mathrm{fm} \cdot A^{1/3}$ is the nuclear radius and $a \approx 0.5\,\mathrm{fm}$ is the so-called diffuseness. ρ_c approximately equals the central density in large nuclei, since $\rho(0) = \rho_c/(1 + e^{-r_0/a}) \approx \rho_c$ for large r_0, and can be determined by the normalization condition

$$\int \rho(r)\mathrm{d}^3 r = A.$$

Under these assumptions, one finally arrives at

$$\frac{\mathrm{d}N}{\mathrm{d}\rho} = \frac{4\pi a r^2}{1 - \rho/\rho_c} = \frac{4\pi a}{1 - \rho/\rho_c} \left[r_0 + a\ln(\rho_c/\rho - 1)\right]^2 . \tag{101}$$

This analytic distribution of the production density is also plotted in fig. 57 as a thin dashed line and agrees nicely with the numerical result obtained from GiBUU. We note that the density distribution does not reach up all the way to $\rho_0 = 0.168\,\mathrm{fm}^{-3}$, since the central density in Nb is slightly smaller than the theoretical value of the saturation density of infinite nuclear matter ($\rho_c \approx 0.92\rho_0$).

Furthermore, we define the quantity

$$P(\rho) = \frac{1}{\sigma} \int_\rho^{\rho_0} \left(\frac{\mathrm{d}\sigma}{\mathrm{d}\rho'}\right) \mathrm{d}\rho', \tag{102}$$

$$\sigma = \int_0^{\rho_0} \left(\frac{\mathrm{d}\sigma}{\mathrm{d}\rho'}\right) \mathrm{d}\rho', \tag{103}$$

where σ represents the full (density-integrated) cross section for a particular process, and $P(\rho)$ is the probability for that process (ω production or decay) happening at a density larger than ρ. This is illustrated in the right-hand side of Fig. 57, which shows that while about 22% of all ω mesons decay at densities larger than 0.1ρ, the fraction of reconstructed $\pi^0\gamma$ pairs from such densities is only about 12%, due to the pion FSI.

In summary, we conclude that the $\pi^0\gamma$ decay channel is clearly inferior for invariant mass analyses compared to e.g. e^+e^-, mainly due to pion FSI. Moreover, we note that in general mass spectrum analyses are much better suited for more short-lived mesons (like the ρ), which have a larger probability of decaying in the medium.

In fig. 58 we show again our simulations for $\gamma + ^{93}\mathrm{Nb}$ in a photon energy range of $0.9 - 1.3$ GeV, in comparison to the data from [37]. The realistic scenarios including collisional broadening are in fact very close to the vacuum curve, due to the reasons discussed
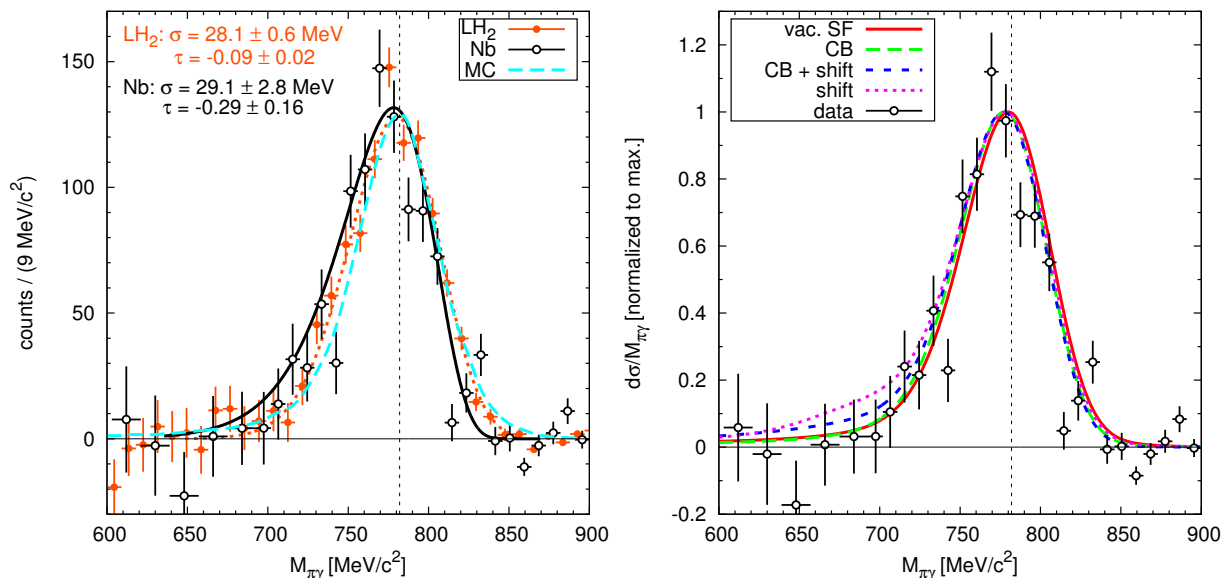
Figure 58: a) ω signal (solid points) for the Nb target (1 mm thick) and incident photon energies from 900 - 1300 MeV. The errors are purely statistical. A fit curve to the data points (see text) is shown in comparison to the ω lineshape measured on a LH_2 target and a Monte Carlo simulation; b) ω signal for the Nb target in comparison to recent GiBUU simulations for the following scenarios: no medium modification (solid), in-medium broadening of $\Gamma_{coll} = 140$ MeV at nuclear saturation density (long dashed), an additional mass shift by -16% (short dashed) and mass shift without broadening (dotted). From [37].

above. And even the theoretically very unlikely scenario of a pure mass shift without any broadening does not yield much larger effects. None of three scenarios is in clear conflict with the data, which have rather large systematic errors on the left shoulder of the peak, mainly due to background subtraction. One can try to further enhance the fraction of in-medium decays by applying momentum cuts or going to even lower photon energies (which is currently being investigated at MAMI), but this will also reduce the overall statistics of the available data samples, so that statistical errors can become a limiting factor.

4.2   Transparency Ratio

Another way of investigating the in-medium properties of the ω meson is to measure its absorption as a function of nuclear mass number A. This method only gives information on the collisional width, but not on a possible mass shift. It does not require the measurement of actual in-medium decays, as is the case for the mass spectrum, but can rely completely on the four-momenta of the final decay products in vacuum. However, since pion FSI may decrease the number of finally reconstructed ω mesons the transparency itself does not give directly the attenuation of ω mesons alone, but has to rely on state-of-the-art transport calculations to extract the actual in-medium width. Only in the case of large collisional widths the pion FSI become negligible [59].
The so-called transparency ratio (here normalized to ^{12}C) is defined as:

$$T_A = \frac{12\,\sigma_{\gamma A \to \omega X}}{A\,\sigma_{\gamma^{12}C \to \omega X}}\ . \tag{104}$$

The first measurement of this quantity was performed by the CBELSA/TAPS collaboration via $\pi^0\gamma$ decays in photoproduction experiments [35]. By assuming a low density approximation, an inelastic ωN cross section of about $70\,\mathrm{mb}$ and its momentum dependence were deduced from the measured transparency.

More recently, it was claimed in [186] that the CBELSA/TAPS data can be described by a much lower inelastic ωN cross section on the order of $20\,\mathrm{mb}$. However, we note that the treatment presented there assumed a fixed photon energy of $1.5\,\mathrm{GeV}$ for comparison with the CBELSA/TAPS data, instead of the full bremsstrahlung energy spectrum of $E_\gamma = 1.2 - 2.2\,\mathrm{GeV}$ used in the experiment. Using a fixed photon energy might be sufficient to describe the momentum-integrated transparency ratio, but it will certainly distort the momentum dependence. Moreover, we note that the latest results of Rodrigues et al. indicate a much larger absorption cross section than claimed previously: In [187] an inelastic ωN cross section of $\sigma_{\omega N}^{\mathrm{inel}} \approx 40\,\mathrm{mb}$ is given (for $p_\omega \sim 1.1\,\mathrm{GeV}$), which is roughly
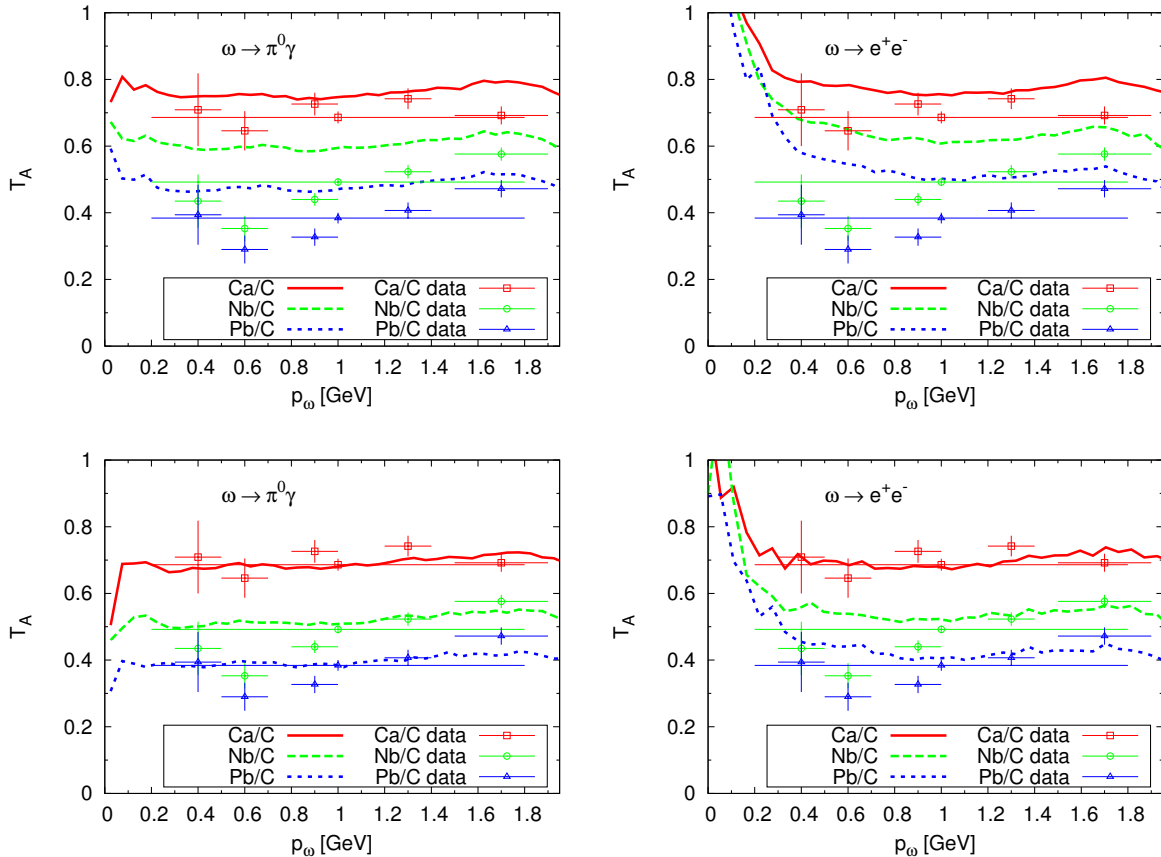
Figure 59: Transparency ratio for three different nuclei relative to ^{12}C; top: using $K = 1$, bottom: using $K = 2$. Left: Obtained via the $\pi^0\gamma$ decay, with $T_\pi > 150\,\mathrm{MeV}$; right: obtained from the dilepton decay, in comparison to the $\pi^0\gamma$ data from [35].

a factor of two higher than the previously claimed range of $15\,\mathrm{mb} \leq \sigma_{\omega N}^{\mathrm{inel}} \leq 24\,\mathrm{mb}$ [186] and much closer to the cross section used in our simulations, cf. Fig. 15.

The results obtained with the GiBUU model are shown in Fig. 59. It is apparent that the transparency ratio obtained with the default GiBUU treatment (i.e. $K = 1$, shown in the top row of the figure) exhibits too little absorption, and is not compatible with the data points. To properly describe the data, we need to modify the inelastic ωN cross section by a factor of $K \approx 2.0$. Our model yields a rather flat momentum dependence for the $\pi^0\gamma$ transparency ratio. While it does not fully follow the slight upward trend visible in parts of the data, it is also not in clear conflict with this trend. Furthermore, it should be noted that the transparency ratio obtained via dilepton decays (as shown in fig. 59 bottom) is mostly compatible with the $\pi^0\gamma$ result, and only shows slight deviations at low momenta, which confirms that this observable is not strongly affected by pion FSI.

In fact, the ω transparency ratio has also been measured via dilepton decays from photon-induced reactions on nuclei by the CLAS collaboration at Jefferson Lab [14]. However, the CLAS data show a significantly larger absorption than the CBELSA/TAPS data, which currently cannot be explained by any of the theoretical models (including ours).

Moreover, the dilepton data recently measured by the HADES collaboration [33] could provide further constraints on the ω absorption in nuclear matter. An ω peak has been identified in both pp and pNb reactions at the same beam energy of 3.5 GeV. However, there are two obstacles for extracting the ω absorption cross section: First, the ω peak needs to be separated from an underlying background (mostly due to the ρ meson), whose shape is nontrivial already in pp, and might be further modified in pNb [110]. Second, only a reference from pp collisions is available, and the ω production from pn collisions in not well constrained.

4.3   Excitation Function

It was argued in [60] that the ω excitation function, i.e. the total ω photoproduction cross section on a nucleus $d\sigma_{\gamma A \to \omega X}/dE_\gamma$, is sensitive to in-medium modifications of the ω meson. In particular, a downward mass shift of the ω in medium would lower the threshold for ω photoproduction and increase the cross section due to the enlarged phase space, which could be determined in an excitation function measurement.

Fig. 60 shows the energy-dependent ω photoproduction cross section on C and Nb (observed through the $\pi^0\gamma$ decay) for photon energies from threshold up to 1.5 GeV. While the collisional broadening scenario only slightly enhances the subthreshold contributions (which presumably would be hard to measure, since the cross sections become very small there), the scenarios including a mass shift exhibit a much stronger enhancement, also above the free ω production threshold of $E_\gamma \approx 1.1\,\mathrm{GeV}$.

It is important to note that the modification of the excitation function is proportional to the density at the production point, in contrast to the mass spectrum modifications discussed above, which are proportional to the density at the decay point.

Further, it should be pointed out that a number of theoretical uncertainties are involved in the calculation of the ω excitation function: In particular at subthreshold energies, where the simulations are in fact most sensitive to in-medium modifications, also other effects can start to play a role, such as nuclear clustering, short-range correlations and the associated high-momentum tails, which are hard to capture in transport simulations.
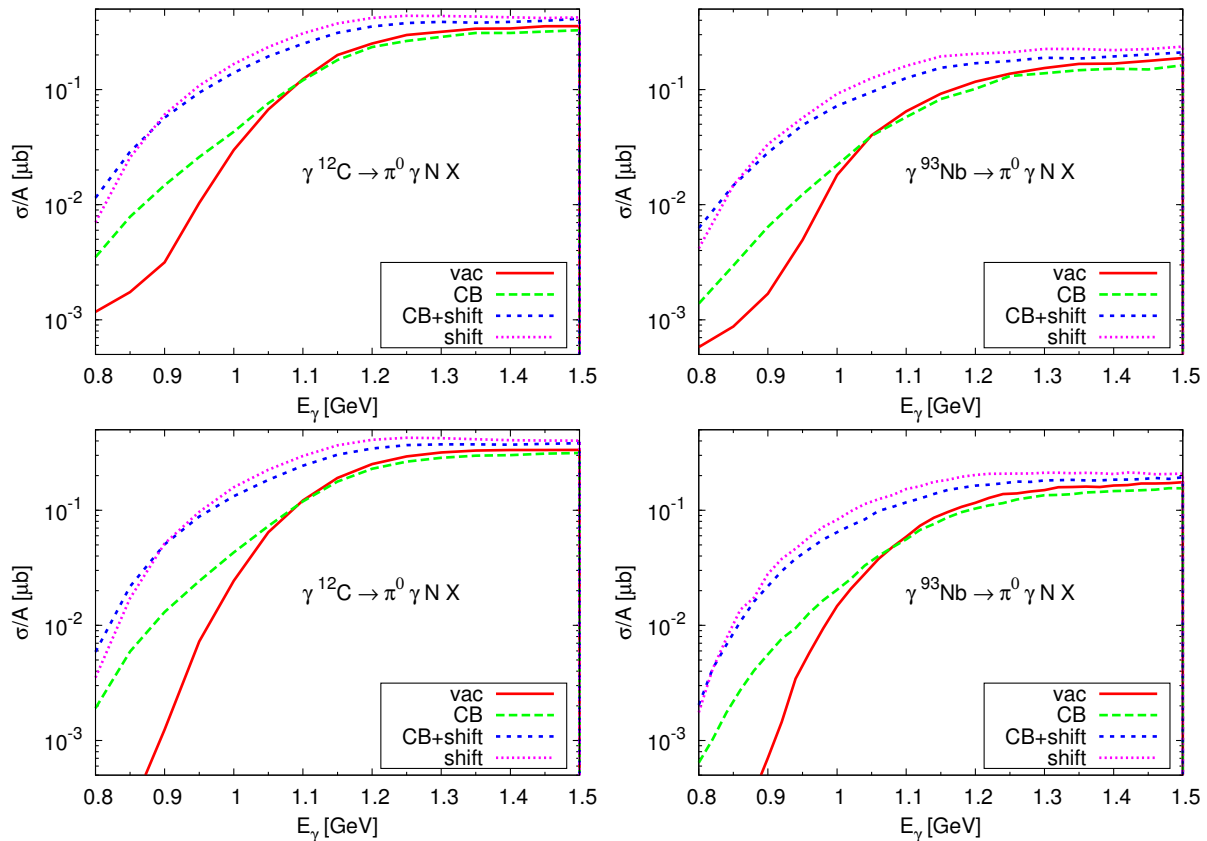
Figure 60: Calculated excitation function for photoproduction of ω mesons in the $\pi^0\gamma$ decay channel on ^{12}C and ^{93}Nb nuclei. The different curves represent the same in-medium scenarios as those used in fig. 56. Top: without mass cut; bottom: with mass cut $650\,\mathrm{MeV} < m_{\pi^0\gamma} < 850\,\mathrm{MeV}$.

4.4 Momentum Spectrum

In addition to the previously established methods discussed in the preceding sections, we propose here a new method for extracting in-medium properties of the ω meson from photoproduction data. Our simulations show that the momentum spectrum of ω mesons produced on a nucleus is sensitive to medium modifications of the ω properties.

This effect is due to the kinematics in the ω production process, which is altered by the ω's medium modifications. When an ω is produced with a lower mass, then, on average, it's total energy is lower. Furthermore, the meson has to come back to its free vacuum mass on its way out of the nucleus; the necessary energy is obtained by converting kinetic energy into mass. This conversion process lowers the momentum.

In order to illustrate the modification of the production kinematics, we plot in fig. 61 the kinematically allowed energies of the ω meson in the lab frame for a photoproduction process as function of the photon energy (neglecting Fermi motion). We do this for ω mesons with vacuum mass (red), as well as a mass-shift of 16% (green). For each of the two scenarios, there are three solid lines (meeting at threshold) which mark the extreme cases: The upper one corresponds to forward production of the ω meson (and maximum lab energy), the lower one corresponds to backward production (and minimum

lab energy), and the central one corresponds to 'transverse' production (i.e. $\theta = 90°$ in the c.m. frame). The hatched area indicates the space of kinematically allowed values between these extreme cases. How this space will be populated depends on the angular distributions in the production process, of course.
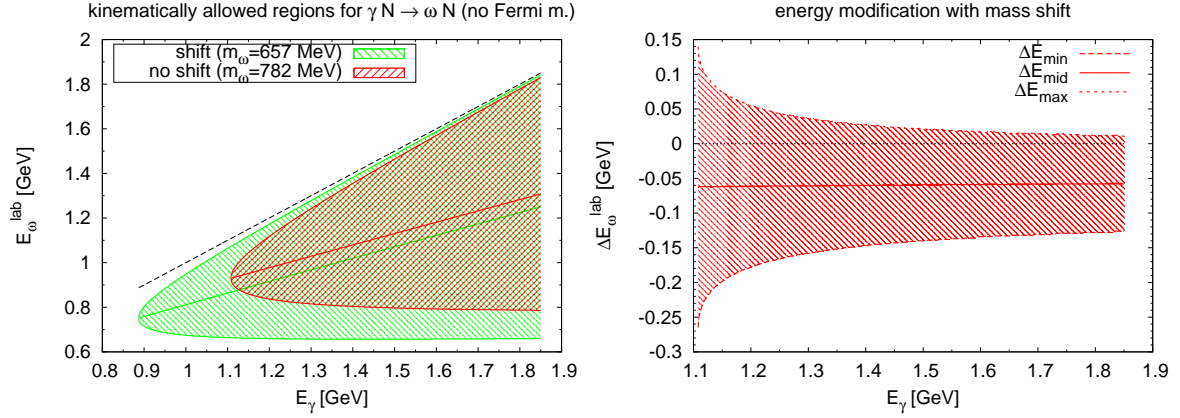
Figure 61: Left: Kinematically allowed regions for $\gamma N \to \omega N$ (without Fermi motion), with and without mass shift. Right: Difference in energy of the ω meson between shift and no-shift scenario.

When neglecting the Fermi motion of the target nucleons, the laboratory energies for the three extreme cases can be derived by a simple Lorenz boost from the center-of-mass quantities p_{cm} and $E_{cm} = \sqrt{m_\omega^2 + p_{cm}^2}$:

$$E_{lab}^{max} = \gamma(E_{cm} + \beta p_{cm}), \tag{105}$$

$$E_{lab}^{mid} = \gamma E_{cm}, \tag{106}$$

$$E_{lab}^{min} = \gamma(E_{cm} - \beta p_{cm}), \tag{107}$$

where $\beta = E_\gamma/(m_N + E_\gamma)$ and $\gamma = 1/\sqrt{1 - \beta^2}$. At threshold p_{cm} goes to zero and the three lines meet. In the high energy limit, E_{lab}^{max} approaches the incident photon energy E_γ (indicated by the dashed line), and E_{lab}^{min} tends to become constant.

Apart from showing the trivial fact that a lowered ω mass lowers the production threshold, fig. 61 also demonstrates that a lowered ω mass modifies the ω's energy energy distribution, by expanding the range of allowed energies (most significantly in downward direction). As the right-hand side of fig. 61 shows, this results on average in a lowered total energy of the ω in the lab frame, when a mass shift is assumed.

Since there are small parts of the distribution which also show a upward shift of the ω energy, the statement about the net effect depends somewhat on the angular distributions. At least at higher energies, where the angular distribution is usually very forward-peaked, a downward energy shift is well established, since the upward-shift region becomes smaller and smaller. At low photon energies, the upward-shift regions gets larger, but there the angular distributions are not so strongly forward-peaked, therefore the net effect should still be a downward shift of the energy distribution of ω meson.
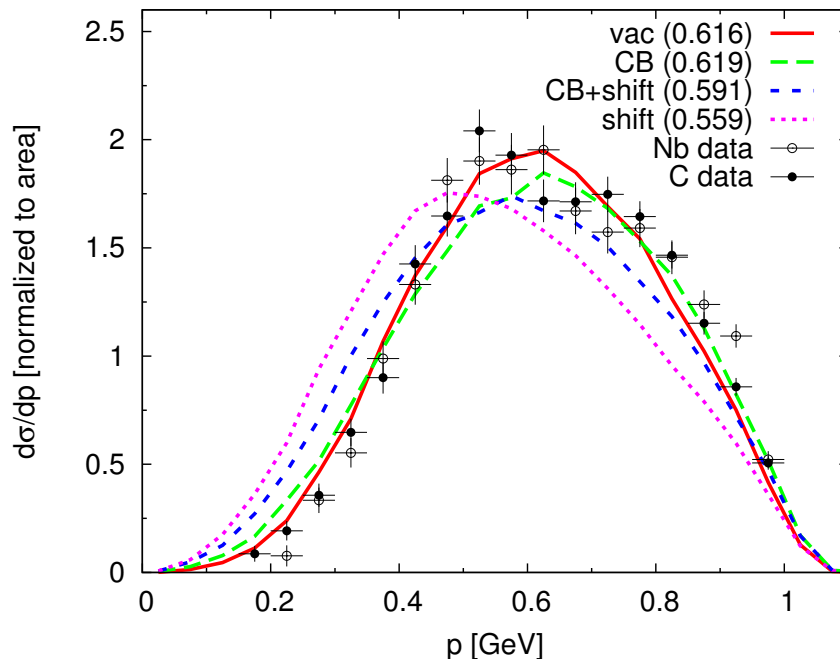
Figure 62: Calculated $\pi^0\gamma$ momentum distribution for $\gamma+$Nb at $E_\gamma = 0.9 - 1.3$ GeV, compared to preliminary data for C and Nb targets [188, 189]. The average momenta for the different in-medium scenarios are given in brackets (in GeV).

After we have established such a downward shift of the ω energy distribution, this directly leads to a downward momentum shift of the ω mesons decaying in vacuum, since they have all return to the mass shell (and therefore lower energy translates directly into lower momentum). In summary: A downward mass shift of the ω in medium should also lead to a downward shift of the momentum distribution. Although our argumentation relied on some simplifying assumptions (e.g. neglecting Fermi motion etc), this should not influence strongly the conclusions.

Fig. 62 shows the momentum spectrum of a $\gamma+$Nb reaction with photon energies in the range of 0.9 - 1.3 GeV. An invariant mass cut of $650\,\text{MeV} < m < 850\,\text{MeV}$ was used to select the relevant ω mass region and to remove events with π^0 rescattering. It should be noted that the momentum distribution is quite sensitive to the angular distribution of the ω production process. The angular distributions used in the simulation properly reproduce the measurements on the free proton [134, 190]. For better comparison, the different curves are normalized to have the same integral. One can see that, while the collisional broadening scenario is hardly distinguishable from the vacuum curve, in the scenarios involving mass shift the momentum distribution is clearly shifted (the maximum of the distribution shows a clear offset and also the average is shifted by about 25 - 50 MeV).

This means that a measurement of the $\pi^0\gamma$ momentum distribution might be used to determine the existence and magnitude of an in-medium mass shift of the ω meson. Preliminary data seem to indicate that the in-medium scenarios involving mass shifts are disfavored [188], as shown in fig. 62, and a publication of the final data is in preparation [189].

4.5   Conclusions

In summary of this chapter, we have evaluated various approaches for the determination of in-medium properties of the ω meson in cold nuclear matter via the $\pi^0\gamma$ decay in photoproduction experiments. Our analysis shows that the lineshape analysis of the $\pi^0\gamma$ invariant mass spectrum suffers mainly from the hadronic FSI of the pion, which drastically reduces the sensitivity to medium modifications. This means that even if the ω mass was shifted in the medium, it would be very hard to detect it via the $\pi^0\gamma$ mass spectrum.

Potentially larger effects could be expected from two other methods of determining the in-medium mass of the ω: the excitation function and the momentum spectrum. Both are sensitive to the density at the production place of the meson, and not at the decay location (as is the case for the lineshape).

Also the transparency ratio, which yields a reliable determination of the ω absorption cross section, is not as sensitive to pion FSI, since it relies mostly on decays of ω mesons outside the medium. However, it cannot make any statement about an in-medium mass shift of the ω.

5   Summary and Outlook

Following the presentation of our results in the previous two chapters, we want to close this thesis with a short summary and some concluding remarks on these results as well as an outlook to possible future investigations.

5.1   Summary

After laying out the basic ingredients of the GiBUU model, we have discussed in the first result chapter dilepton production in the few-GeV regime. We have presented dilepton spectra (invariant mass, p_T and rapidity) of pp, pA and AA reactions at various beam energies, simulated with the GiBUU transport model. We have compared our simulated spectra to data published by the HADES and DLS collaborations, which was only possible by feeding the dilepton events generated by the model through the acceptance filters provided by the experimental collaborations.

Regarding the elementary reactions, we have demonstrated that our model is able to give a rather good description of the spectra from both pp and dp collisions. By tendency, the agreement with the data is better at higher energies. In particular we have shown that a resonance-model description is superior over a string-model treatment, even at the highest HADES energy of 3.5 GeV. Further we have emphasized that in order to learn about the underlying processes and to fix the composition of the dilepton cocktail, it is important to use one consistent model for all energies, instead of switching between resonance and string model right in the middle of the relevant energy range, as it was done in earlier versions of the GiBUU model and is still done in HSD. We have set up an extended resonance model based on the earlier Teis model and have shown that contributions of higher N^* and Δ^* resonances can be important at almost all considered energies. In many publications contributions of the resonances are underestimated, e.g. by neglecting form factors or considering only one particular resonance, but not the full spectrum of known nucleon resonances.

We have tried to overcome these limitations by considering a large number of resonances and including electromagnetic form factors (under the assumption of strict VMD). The form factors were implicitly included in the transport model by treating the dilepton Dalitz decays of the resonances as a two-step process ($R \to \rho N \to e^+e^- N$). In this way we also incorporate the couplings of the baryon resonances to the ρ meson, which are known to be crucial for the in-medium properties of the ρ, but in our analysis have proven to be important also for elementary reactions, since the production of ρ meson through resonance decays influences the ρ mass distribution via the limitation of phase space. The couplings have been taken from the Manley/Saleski partial-wave analysis, which infers these couplings from large amounts of hadronic data.

With this approach we have shown that the contributions of nucleon resonances are indeed important at basically all HADES/DLS energies, and that resonance-model based simulations yield the best agreement with data. This is one of the central results of our studies, together with the finding that baryon-resonance couplings of the ρ meson do not only determine its in-medium properties, but already play a role in elementary collisions at SIS energies.

While our results for the higher HADES energies (2.2 and 3.5 GeV) are quite satisfactory,

the lower energy of 1.25 proved to be somewhat more puzzling. In pp the agreement
is still quite good (although minor deviations are present), but the dp measurement at
the same energy turned out to be the most challenging. It was not possible to achieve a
sufficient description in the transport approach, and the only way to change that might
be to use an OBE model as input, which can properly describe the isospin differences
(caused e.g. by charged-pion exchange in pn, which yields additional contributions).

Also for the elementary DLS measurements we found a rather good agreement. Only the
very highest and very lowest energies showed significant underestimations: The highest
because not all inclusive production channels are included, and the lowest probably be-
cause a proper treatment of bremsstrahlung is missing and because of other uncertainties
(e.g. possible interferences and mistreatment of angular distributions).

Moving from the elementary to the nuclear reactions, we showed that, based on the good
description of the HADES pp data at 3.5 GeV, we also get a good agreement with p+Nb
data at the same energy. As already demonstrated by the DLS data, no large isospin
effects are expected at such high energies. Also the medium modifications of the vector
mesons turned out to yield only moderate effects in our model, which are roughly on
the same order of magnitude as the error bars of the data, so that it's not possible to
distinguish different scenarios unambiguously.

For the light nucleus-nucleus collisions, such as C+C, we get results consistent with the
elementary ones: A very good agreement at high energies (i.e. HADES 2 GeV) and a
slight underestimation at lower energies (1 GeV, HADES and DLS), possibly related to
the underestimation of d+p.

For the heavier ArKCl system, things get more interesting: We see a significant disagree-
ment between the simulation results and the data here, which is close to a factor 2 in the
intermediate mass region and therefore much larger than for the CC cases (although the
beam energy is between both CC energies here). From this we conclude that the major
part of this discrepancy is due to a system-size (and possibly density-dependent) effect,
although a minor part might be related to the problems in some of the elementary colli-
sions (in particular d+p at 1.25 GeV). Interestingly, the discrepancy between our model
and the ArKCl data is roughly the same as the difference between the ArKCl data and
the elementary reference spectrum (which has been obtained from the average of the pp
and dp data at 1.25 GeV), which means that our results are basically consistent with the
elementary reference spectrum and do not show any significant enhancement.

In [53] it was claimed that the enhancement in ArKCl is mostly due to the Δ Dalitz
channel. However, we suspect that the Δ Dalitz in [53] is actually overestimated quite
strongly due to various reasons, most severely an isospin mistreatment of the Δ produc-
tion in FRITIOF (as discussed in section 2.3.1.2), and cannot be the sole source of the
enhancement. This overestimation of the Δ channel is also visible in the elementary reac-
tions, e.g. p+p at 3.5 GeV, where it causes a clear disagreement with the p_T data [53]. We
doubt that this approach can provide a solution of the DLS puzzle (as claimed in [47]).

Instead the enhancement in ArKCl could be caused e.g. by modified in-medium spectral
functions of the vector mesons (most notably the ρ) and/or the baryon resonances. Our
current off-shell treatment only allows to treat modifications of the vector mesons in a
rather simplified way, using a mass shift or broadening which is linear in density. Due to
several limitations in the off-shell propagation scheme it is currently not possible to treat
more involved scenarios (including momentum dependencies etc), and also the accuracy

of the current method is only guaranteed to be good in the region close to the pole mass. These limitations are probably the reason why the ArKCl spectrum does not achieve a much better agreement with the data when including medium modifications. It is clear that more work is needed in this direction, in order to achieve a better treatment of in-medium modifications, including also off-shell transport of baryons and modified branching ratios in medium.

In the end, we conclude that the old DLS puzzle is still not fully solved at present, since there is no model which can fully describe all the DLS and HADES data. But at least the experimental part of the puzzle has been solved by the HADES collaboration by reproducing the DLS data and thereby confirming its validity. With this confirmation it has finally become clear that the DLS puzzle is a theory puzzle and that the available models still fail to describe a part of the observed dilepton yield. However, the HADES detector has greatly enhanced the available set of data, both in quantity and quality, which has helped to better understand and constrain the elementary input that enters in the transport models. As a consequence, the description of the elementary dilepton spectra has improved significantly, so that the 'elementary' component of the DLS theory puzzle is close to being solved by now. However, this is not fully the case yet, and more experimental constraints on resonance properties and their dilepton decay modes are needed, which will hopefully be provided by a pion-beam measurement with HADES in the near future. Moreover, more theoretical work (e.g. on the form factors of the baryon resonances) is needed to complete the picture, and it would certainly be desirable to achieve a proper coupling of OBE models to transport.

From our point of view, the largest remaining puzzle is the significant underestimation of the heavy systems, like ArKCl at 1.76 GeV (HADES) and CaCa at 1.04 GeV (DLS), which cannot be explained by the minor deviations that are left in the elementary reactions, and seems to indicate that the dilepton radiation from the hot and dense phase of the collisions has not been properly understood yet. The soon-to-be-published AuAu data are expected to show an even larger enhancement, and the challenge for the transport models will be to provide an improved treatment of the in-medium component of the dilepton spectum. For this, proper hadronic models of in-medium spectral functions are needed, both for the vector mesons and the baryonic resonances. These models then need to be coupled to transport models, either by a coarse-graining approach, which extracts thermodynamical quantities from the transport simulation and uses those as an input to the spectral-function models, or even by a fully microscopic off-shell transport scheme, which treats the transition between in-medium and vacuum spectral functions in a dynamical fashion. We also note that the models used for the in-medium spectral functions should be consistent with the cross sections of the resonance model used in the transport part. Both for the in-medium spectral function of the ρ meson as well as its vacuum production, baryon resonances are expected to play an important role, and therefore cross links must be used carry over constraints from one area to the other. A proper treatment of resonance-coupling effects in both sectors could be the last missing piece to finally solve the long-standing DLS puzzle, which has remained unsolved for more than a decade now.

While dilepton spectra from pA and AA collision are primarily sensitive to in-medium modifications of the ρ meson (which has a very short lifetime and therefore a large probability to decay in the medium), another interesting question is whether it is possible to extract in-medium information also for the ω meson. This is more challenging than for

the ρ, since any invariant-mass reconstruction (be it based on e^+e^- or $\pi^0\gamma$ decays) suffers from the ω's long lifetime, which severely limits the fraction of in-medium decays. On top of this come additional problems: In the dilepton case, there is a large background of $\rho \to e^+e^-$ decays under the $\omega \to e^+e^-$ peak, whose shape is already nontrivial in the vacuum (due to the production via baryon resonances) and can be further modified in the medium. Therefore any hope to learn something about the ω in medium from the dilepton mass spectrum strongly depends on a good understanding of the dilepton signal from the ρ meson, which is a very involved topic as the ongoing DLS puzzle shows.

Relying on the $\omega \to \pi^0\gamma$ decay instead of $\omega \to e^+e^-$ has the advantage of getting rid of the complex ρ background that is present in the dilepton spectrum. However, other ('nonphysical') backgrounds are presents when detecting the ω via $\omega \to \pi^0\gamma \to 3\gamma$, which are mostly related to misidentifications of particles in the detector or detection inefficiencies. Moreover, the $\pi^0\gamma$ channel has the disadvantage that one of the decay products, namely the π^0, undergoes strong final-state interaction. This further suppresses or distorts the signal from in-medium decays, which is already small for the ω to begin with. Our simulations have shown that the remaining observable effects of in-medium modifications are very small, and that it is experimentally very challenging to reach the required precision.

Another method of getting a hold on the ω's in-medium properties is the transparency ratio. It does not rely on actual in-medium decays and basically quantifies the absorption of ω mesons as a function of nuclear mass number. This also means that it cannot make statements about the full in-medium spectral function (and in particular about any kind of mass shift), but only about the collisional broadening, which is related to scattering and absorption processes. Via this method (and using $\pi^0\gamma$ decays) the CBELSA/TAPS collaboration has established a strong broadening/absorption of the ω meson. The microscopic source of this broadening is still a challenge and it can only be accounted for in the GiBUU model by introducing a scaling factor for the inelastic ωN cross section.

The transparency ratio can also be measured via dilepton decays, which has been done e.g. by the g7 collaboration at JLab. However, their results are not compatible with those of CBELSA/TAPS and indicate an even stronger absorption, which currently cannot be explained by any model.

In principle a transparency-ratio analysis of the ω meson could also be performed with the HADES dilepton data. However, the problem is that only pp and pNb have been measured, and therefore the isospin effect from pn collisions in not well under control (this is the reason why in the CBELSA/TAPS case an isospin-symmetric ^{12}C nucleus was used as a baseline). Under the assumption of equal ω production cross sections in pp and pn, our simulations slightly underestimate the ω peak in pNb (when using the absorption cross sections inferred from the CBELSA/TAPS data). However, this does not necessarily mean that the HADES data are inconsistent with the CBELSA/TAPS transparency, since possibly the ω production cross section on the neutron could be enhanced over pp (which is not treated in our model).

Finally we have described two further methods of obtaining in-medium information of the ω meson: The excitation function and the momentum spectrum. Both of these are sensitive to the density at the production place (instead of the decay location, as in the case of the invariant mass spectrum), which can potentially yield larger effects, since it avoids the problem of the long ω lifetime. In case of the excitation function, the production

cross section is sensitive to in-medium modifications of the spectral function (such as a mass shift), since such a modification alters the available phase space in the production process. E.g. a downward mass shift would shift the production threshold to lower energies in medium. Such a mass shift would also alter the production kinematics in such a way that the ω meson on average obtains a lower total energy in the lab frame. This would lead to a modified momentum spectrum, which could be measured via $\pi^0\gamma$ decays. After the $\pi^0\gamma$ invariant mass spectrum has turned out to suffer from a very limited sensitivity to in-medium modifications, these two methods might be the only way to learn about a possible in-medium mass shift of the ω meson.

5.2 Outlook

After summarizing the results of this thesis and discussing the conclusions, the final words are devoted to an outlook to what could and should be done in the future. In the dilepton sector, we have achieved a significant improvement in the description of the HADES and DLS data. However, not all puzzles have been solved, and therefore there is much room for future investigations. For one thing, it would be great to achieve a coupling between the popular OBE and transport models, and use the output of an effective-Lagrangian OBE model as an input for the elementary cross sections in transport. This has never been done and would basically represent a new type of model that is not available presently. We note there have been efforts to use OBE results as an input for transport, but those only involved simple parametrizations of the OBE output, which have been used as a correction factor for SPA bremsstrahlung. This is clearly not enough and in particular does not take into account the full differential information from the OBE model (which can be important, in particular in connection with limited detector acceptance). Furthermore, better experimental constraints on the nucleon resonances and in particular their ρN decay modes are required, as well as a better theoretical understanding of baryon formfactors in the time-like region. All these things already affect the description of elementary spectra. Going into the medium, the primary challenge is to improve the available methods for treating density-dependent spectral functions (which goes under the buzzword 'off-shell transport'), since there are various problems in this area, several of which have been discussed in this thesis. Once such methods are established for a consistent treatment of dynamically changing spectral functions, these need to be applied by using realistic hadronic-model spectral functions in the transport simulation. All of this would hopefully lead to a better understanding of dilepton spectra at SIS energies and could finally provide a solution to the infamous DLS puzzle.

Another major challenge for the transport community is not directly related to physics, but concerns the management and development of the large code bases that all present-day transport models have grown into. Most of the popular transport models have originally been implemented in FORTRAN 77, which is a very ancient and outdated programming language by now and does not provide the necessary facilities and structures to properly support scientific code bases on the order of tens to hundred thousands lines of code.

Popular ideas for coping with the increasing complexity of transport codes include rewriting these codes from scratch in a more modern object-oriented language (like C++) and/or leveraging the massively parallel capabilities of modern CPUs and GPUs. While such 'revolutionary' new ideas offer great opportunities, one has to be careful not to pre-

maturely throw overboard the large amounts of well-tested code that has been developed and maintained over many years. Therefore a compromise needs to be found between renewal and conservation.

Such a compromise (and the corresponding upgrade path) could be provided by modern Fortran dialects, such as the ISO-certified standards of Fortran 95, Fortran 2003 and Fortran 2008. The GiBUU project has already taken the step from the ancient FORTRAN 77 to the somewhat more modern Fortran 95, which provides modularization, pointers and derived types (to just name a few of the new features). The main advantage of moving to modern Fortran dialects instead of a completely new language is that the former are backward-compatible with earlier Fortran versions and therefore provide a smooth step-by-step upgrade path instead of requiring a disruptive rewrite of the whole code base.

Since GiBUU has already made the move to Fortran 95, the next step would be to fully embrace the new capabilities of Fortran 2003, the most important of which is certainly the possibility to write fully object-oriented code (similar to C++ or Java). This will further improve the structuring of the code base and greatly simplifies the task of maintaining and extending the code. For some time the availability of Fortran 2003 features in compilers was a problem, but nowadays writing object-oriented code in Fortran is not a problem any more and many compilers (both commercial and open-source) support this by now.

Object orientation will mainly improve the structure and modularization of the code base and improve its readability and flexibility, but one should not stop there. Modern computer architectures are moving more and more into the direction of massive parallelization, where already a single machine consists of a large number of CPU or GPU computing cores, and many such machines are connected by high-bandwidth low-latency networks to form supercomputers. Traditional programming languages provide only a single thread of execution and cannot fully utilize the massively parallel capabilities of modern computers. However, the latest Fortran standard (Fortran 2008) offers intrinsic support for parallel computation in the form of 'coarrays' (i.e. concurrent arrays). These represent an abstract model for parallel execution, which can, depending on the compiler support, handle both shared-memory and distributed-memory setups. Such a high-level abstraction, directly incorporated on the language level, is clearly preferable over specific vendor solutions, which keep popping up lately and are sometimes even hardware specific. The usage of coarrays would greatly improve the performance of the code on modern multi-core architectures, while at the same time maintaining hardware independence and the flexibility to potentially run on both CPUs and GPUs (the distinction between which will anyway fade away in the future).

Apart from the usage of a modern programming language, additional infrastructure can aid the development of large codes. First and foremost the usage of a proper version-control system (e.g. svn or git) is indispensable, but unfortunately this aspect is still being underestimated by large parts of the transport community. Further a semi-automatic documentation system and other facilities (e.g. a wiki) are important for providing documentation of the source code, input parameters, etc. The GiBUU project has been successfully using such tools for some time already and this should be further extended and improved in the future, in order to facilitate the maintenance and development of the transport code in the long run.

A Numerical Details & Jobcards

A.1 pp

For elementary p+p runs, we usually do not perform a full transport simulation with time evolution, but just the primary collision plus any subsequent decay chains of unstable particles. This means that secondary collisions, such as $pp \to \Delta\Delta \to NN\pi\pi$ with $\pi\pi \to \rho$ are neglected, but it was verified by a full simulation that their contributions are indeed extremely small.

Furthermore, we increased the high-energy string-model threshold for baryon-baryon collisions to $\sqrt{s} = 4\,\mathrm{GeV}$ in all elementary p+p collisions, unless otherwise indicated, in order to get pure resonance-model results.

In the following we show a typical jobcard with the necessary input for p+p at 3.5 GeV:

```
!*******************************************************************************
!       General Input :
!*******************************************************************************

&Input
  numEnsembles = 40000          ! number of ensembles
  eventtype    = 12             ! 2=PionA, 3=photon A, 12=HiPion A
  numTimeSteps = 0              ! number of time steps
  delta_T      = 0.2            ! time step size
  num_runs_SameEnergy = 500     ! number of runs
  num_Energies = 1
  length_perturbative = 150
  freezeRealParticles = .true.
  ! localEnsemble = .true.      ! default: parallel ensemble
  path_to_input = "~/GiBUU/buuinput"
/

&Target
  target_Z = 1, target_A = 1
/

&initDatabase
  rho_dilep = .true.
/


!*******************************************************************************
!       Input specific for the reactions
!*******************************************************************************

&HiPionNucleus
  ekin_lab          = 3.5
  DoProton          = .true.
  Charge            = 1
  distance          = -1.
  numberPions       = 50
  impact_parameter  = -1.
  doPerturbativeInit = .true.
  minimumMomentum   = 0.0
/

&insertion
  minimumEnergy = 0.0
/


!*******************************************************************************
!       Analysis :
!*******************************************************************************

&DileptonAnalysis
  enable          = .true.
```

```
  nEvent          = 1
  binsz           = 0.005
  filter          = 4                        ! 4 = HADES(full,single)
  hadesFilterFile = "../HadesSingleAcc-p35p-APR07-effgt5-RK-v2.acc"
  massBinning(1:3)= 0.150, 0.470, 0.700
  DeltaDalitzFF   = 6                        ! 1 = const, 5 = Iachello, 6 = Ramalho
/

&HiPion_Analysis
  Enable        = .true.
  DoOutChannels = .true.
  DoInvMasses   = .true.
/


!*****************************************************************************
!      Collision Term :
!*****************************************************************************

&master_2body
  usePythia = 1                     ! 0=Fritiof, 1=Pythia
  HiEnergyThresholdBarBar      = 4.0
  HiEnergyThresholdBarBarDelta = 0.0
/

&baryonBaryon
  NNpi_BG = 3
/

&angular_distribution
  NN_NR_noniso = .true.
/

&decayChannels
  rhoDelta_is_sigmaDelta = .true.
/

&finalState_Full
  silentMode = .false.
/


!*****************************************************************************
!      Temperature and thermodynamics
!*****************************************************************************

&InitDensity
  densitySwitch = 2        ! 1=dynamic, 2=analytic, 0=no density
/

&InitPauli
  pauliSwitch = 2          ! 1=dynamic, 2=analytic, 0=no pauli blocking
/
```

A.2   pA, AA

For hadronic nuclear reactions like p+A and A+A, the typical time step size is $\Delta t = 0.2\,\text{fm}$ and the time evolution proceed over an interval of about $t_{max} = 20 - 40\,\text{fm}$ (depending on the size of the nuclei etc). Usually the "parallel ensemble" technique is used with roughly 10000 ensembles. In particular for A+A, 'real' particles and a dynamic density is used, while for low-energy p+A collisions, sometimes a 'perturbative' treatment with a frozen nucleus can be sufficient. We typically use a medium-stiff momentum-dependent Skyrme potential for nucleons and Deltas, but neglect the Coulomb potential.

In the following we show a typical jobcard with the necessary input for a C+C collision

at 2 GeV:

```
!*****************************************************************************
!       General Input
!*****************************************************************************

&input
  numEnsembles          = 30000  ! number of ensembles
  eventtype             = 1       ! HeavyIon collision
  numTimeSteps          = 100     ! number of time steps
  delta_T               = 0.2     ! time step size
  num_runs_SameEnergy   = 1
  num_Energies          = 1
  path_to_Input         = '/home/gibuu/buuinput'
  checkGridSize_Flag    = .true.          ! check grid dimensions
  length_real           = 100
  length_perturbative   = 0
  !fullensemble = .false.                 ! default: parallel ensemble
/

&initDatabase
  rho_dilep = .true.
/

&DileptonAnalysis
  enable          = .true.
  binsz           = 0.01
  writeEvents     = 0
  filter          = 4                     ! 4=HADES(full,single)
  hadesFilterFile = "../HadesSingleAcc-c20c-NOV02-effgt0-KP-v1.acc"
  massBinning(1:2) = 0.150, 0.500
  DeltaDalitzFF   = 6                     ! 1 = const, 5 = Iachello, 6 = Ramalho
/


!*****************************************************************************
!       Heavy-Ion
!*****************************************************************************

&projectile
  projectile_Z=6, projectile_A=12     ! C12
/

&target
  target_Z=6, target_A=12             ! C12
/

&heavyIon                           ! Eventtype=1
  impact_Parameter    = -5.
  distance            = 0.
  ekin_lab_Projectile = 2.0     ! kinetic Energy/nucleon of projectile
  ekin_lab_Target     = 0.      ! kinetic Energy/nucleon of target
  cmsFlag             = .true.
  adjustGridFlag      = .true.
/

&HICanalysis_Input
  flag_outputReal     = .false.
  flag_outputPert     = .false.
  flag_outputDetailed = .false.
  pionAnalysis        = .true.
/

!*****************************************************************************
!       Misc
!*****************************************************************************

&initDensity
  densitySwitch = 1                 ! 1 = dynamic, 2 = analytic
  splineExtraPolation = .true.
  gridSize(1:3)   = 20., 20., 40. ! Size of density grid in x/y/z direction [fm]
```

```
  gridPoints(1:3) = 40, 40, 80    ! Number of grid points in x/y/z direction
/

&initPauli
  pauliSwitch = 1                 ! 1=dynamic, 2=analytic
/


!*****************************************************************************
!      Potentials
!*****************************************************************************

&Coulomb
  CoulombFlag = .false.
/

&baryonPotential
  symmetriePotFlag = .false.
  EQS_Type = 5   ! equation of state for nucleon resonances spin=1/2
  DeltaPot = 1   ! potential of spin=3/2 resonances
/


!*****************************************************************************
!      Collision term
!*****************************************************************************

&master_2body
  usePythia = 1                   ! 0=Fritiof, 1=Pythia
  HiEnergyThresholdBarBar      = 4.0
  HiEnergyThresholdBarBarDelta = 0.0
/

&baryonBaryon
  NNpi_BG = 3
/

&angular_distribution
  NN_NR_noniso = .true.
/

&decayChannels
  rhoDelta_is_sigmaDelta = .true.
/

&insertion
  minimumEnergy = 0.
/

&collisionTerm
  energyCheck = 0.1
  maxout      = 10
/
```

A.3 γA

For γA reactions, we use a similar time-evolution setup as for pA, with $\Delta t = 0.2$ fm, $t_{max} \approx 40$ fm and the "parallel ensemble" technique. But here we typically rely on the approximation of a frozen nucleus, perturbative particles and an analytic density distribution.

In the following we show a typical jobcard with the necessary input for γ+Nb at 1.2 GeV:

```
!************************************************
! general input
!************************************************
```

```
$input
  numEnsembles = 100            ! number of ensembles
  eventtype    = 3              ! 3=photon A
  numTimeSteps = 200            ! number of time steps for a nuclear target
  delta_T      = 0.2            ! time step size
  num_runs_SameEnergy = 1       ! Number of runs with the same energy
  num_Energies       = 9        ! Number of different energies
  length_perturbative = 6000
  path_to_input='/home/gibuu/buuinput'     ! Path to input directory
  fullensemble           = .false.
  FinalCoulombCorrection = .false.
  PrintParticleVectors   = .false.
$end

$target
  target_Z=41, target_A=93,          ! Nb93
  fermimotion = .true.
$end

!*****************************************************
!   photon induced reactions
!*****************************************************

$low_photo_induced
  energy_gamma     = 0.9
  delta_energy     = 0.05
  energy_weighting = 1
  ! switches for specific initial channels
  vecmes(2)       = .true.    ! (omega only)
  vecmes_delta(2) = .true.
  pi0eta          = .false.
  twopi           = .false.
  resonances      = .false.
  singlePi        = .false.
$end

$lowPhotonAnalysis
  ! Analysis flags
  outputEvents          = .false.    ! Print events to file
  outputEvents_onlyFree = .true.     ! Prints only "free" nucleons to file
  photonAnalyse         = .false.    ! Generate analysis for final state photons
  pi0gamma_analysis     = .true.
  pi0gamma_momcut       = 0.4
  pi0gamma_masscut      = 0.65, 0.85
  pi0gamma_massres_sigma = 0.019
  ! Ekin_pi0_cut = 0.150
  ! Switch off unnessary analysis
  KruscheOutput  =.false.
  fissumOutput   =.false.
  twoPiOutput    =.false.
$end

!*********************************************************
!     collision term
!*********************************************************

$master_1Body
  omegaDecayMediumInfo   = .true.
  omegaDecay_restriction = 0        ! 0=all, 1=vacuum, 2=medium
$end

$master_2body
  omega_K_factor = 2.
  ! OverideSigma_PiN = 0.  ! no pion FSI
$end

$angular_distribution
  iParam_gammaNVN = 2
$end
```

140

```
!**********************************************************
!       potentials
!**********************************************************

$baryonPotential
  symmetriePotFlag = .false.
$end

$coulomb
  coulombFlag = .false.
$end


!*********************************************************
!       photon propagation
!*********************************************************

$insertion
  propagateNoPhoton = .false.     ! Photons are propagated
$end


!*************************************************************
!       ground state
!*************************************************************

$initDensity
  densitySwitch=2             ! 1=dynamic, 2=analytic
  splineExtraPolation=.true.
$end

$initPauli
  pauliSwitch=2             ! 1=dynamic, 2=analytic
$end
```

References

[1] S. Leupold, V. Metag, U. Mosel, Int. J. Mod. Phys. E **19**, 147 (2010), `arXiv: 0907.2388 [nucl-th]`

[2] R.S. Hayano, T. Hatsuda, Rev. Mod. Phys. **82**, 2949 (2010), `arXiv: 0812.1702 [nucl-ex]`

[3] R. Rapp, J. Wambach, H. van Hees, Landolt-Börnstein **I/23**, 4 (2010), `arXiv: 0901.3289 [hep-ph]`

[4] T. Hatsuda, S.H. Lee, Phys. Rev. C **46**, 34 (1992)

[5] M. Kotulla, V. Metag, U. Mosel, Physik J. **8N3**, 41 (2009)

[6] S. Klimt, M.F. Lutz, W. Weise, Phys. Lett. B **249**, 386 (1990)

[7] S. Leupold, W. Peters, U. Mosel, Nucl. Phys. A **628**, 311 (1998), `arXiv: 9708016 [nucl-th]`

[8] Z. Fodor, S. Katz, JHEP **0203**, 014 (2002), `hep-lat/0106002`

[9] M. Post, Ph.D. thesis, Justus-Liebig-Universität Gießen (2004), available online at `http://theorie.physik.uni-giessen.de/`

[10] M. Post, S. Leupold, U. Mosel, Nucl. Phys. A **741**, 81 (2004), `arXiv: 0309085 [nucl-th]`

[11] V. Eletsky, M. Belkacem, P. Ellis, J.I. Kapusta, Phys. Rev. C **64**, 035202 (2001), `nucl-th/0104029`

[12] R. Nasseripour et al. (CLAS Collaboration), Phys. Rev. Lett. **99**, 262302 (2007), `arXiv: 0707.2324 [nucl-ex]`

[13] M. Wood et al. (CLAS), Phys. Rev. C **78**, 015201 (2008), `arXiv: 0803.0492 [nucl-ex]`

[14] M. Wood et al. (CLAS Collaboration), Phys. Rev. Lett. **105**, 112301 (2010), `arXiv: 1006.3361 [nucl-ex]`

[15] M. Naruki, H. Funahashi, Y. Fukao, M. Kitaguchi, M. Ishino et al., Phys. Rev. Lett. **96**, 092301 (2006), `arXiv: 0504016 [nucl-ex]`

[16] R. Porter et al. (DLS Collaboration), Phys. Rev. Lett. **79**, 1229 (1997), `arXiv: 9703001 [nucl-ex]`

[17] W. Wilson et al. (DLS Collaboration), Phys. Rev. C **57**, 1865 (1998), `arXiv: 9708002 [nucl-ex]`

[18] D. Adamova et al. (CERES/NA45 Collaboration), Phys. Rev. Lett. **91**, 042301 (2003), `arXiv: 0209024 [nucl-ex]`

[19] R. Arnaldi et al. (NA60 Collaboration), Phys. Rev. Lett. **96**, 162302 (2006), `arXiv: 0605007 [nucl-ex]`

[20] H. van Hees, R. Rapp, Phys. Rev. Lett. **97**, 102301 (2006), `arXiv: 0603084 [hep-ph]`

[21] J. Ruppert, C. Gale, T. Renk, P. Lichard, J.I. Kapusta, Phys. Rev. Lett. **100**, 162301 (2008), `arXiv: 0706.1934 [hep-ph]`

[22] H. van Hees, R. Rapp, Nucl. Phys. A **806**, 339 (2008), `arXiv: 0711.3444 [hep-ph]`

[23] E. Bratkovskaya, W. Cassing, R. Rapp, J. Wambach, Nucl. Phys. A **634**, 168 (1998), `arXiv: 9710043 [nucl-th]`

[24] C. Ernst, S. Bass, M. Belkacem, H. Stoecker, W. Greiner, Phys. Rev. C **58**, 447 (1998), `arXiv: 9712069 [nucl-th]`

[25] E. Bratkovskaya, C. Ko, Phys. Lett. B **445**, 265 (1999), `arXiv: 9809056 [nucl-th]`

[26] K. Shekhter, C. Fuchs, A. Faessler, M. Krivoruchenko, B. Martemyanov, Phys. Rev. C **68**, 014904 (2003), `arXiv: 0305015 [nucl-th]`

[27] G. Agakichiev et al. (HADES Collaboration), Phys. Rev. Lett. **98**, 052302 (2007), `arXiv: 0608031 [nucl-ex]`

[28] G. Agakishiev et al. (HADES Collaboration), Phys. Lett. B **663**, 43 (2008), `arXiv: 0711.4281 [nucl-ex]`

[29] G. Agakishiev et al. (HADES Collaboration), Phys. Lett. B **690**, 118 (2010), `arXiv: 0910.5875 [nucl-ex]`

[30] G. Agakishiev et al. (HADES Collaboration), Phys. Rev. C **84**, 014902 (2011), `arXiv: 1103.0876 [nucl-ex]`

[31] G. Agakishiev et al. (HADES Collaboration), Eur. Phys. J. A **48**, 64 (2012), `arXiv: 1112.3607 [nucl-ex]`

[32] G. Agakishiev et al. (HADES Collaboration), Phys. Rev. C **85**, 054005 (2012), `arXiv: 1203.2549 [nucl-ex]`

[33] G. Agakishiev et al. (HADES Collaboration), Phys. Lett. B **715**, 304 (2012), `arXiv: 1205.1918 [nucl-ex]`

[34] D. Trnka et al. (CBELSA/TAPS Collaboration), Phys. Rev. Lett. **94**, 192303 (2005), `arXiv: 0504010 [nucl-ex]`

[35] M. Kotulla et al. (CBELSA/TAPS Collaboration), Phys. Rev. Lett. **100**, 192302 (2008), `arXiv: 0802.0989 [nucl-ex]`

[36] M. Nanova et al. (CBELSA/TAPS Collaboration), Phys. Rev. C **82**, 035209 (2010), `arXiv: 1005.5694 [nucl-ex]`

[37] M. Nanova et al. (CBELSA/TAPS), Eur. Phys. J. A **47**, 16 (2011), `arXiv: 1008.4520 [nucl-ex]`

[38] G. Wolf, G. Batko, W. Cassing, U. Mosel, K. Niita et al., Nucl. Phys. A **517**, 615 (1990)

[39] A. Titov, B. Kämpfer, E. Bratkovskaya, Phys. Rev. C **51**, 227 (1995)

[40] E. Bratkovskaya, W. Cassing, M. Effenberger, U. Mosel, Nucl. Phys. A **653**, 301 (1999), `arXiv: 9903009 [nucl-th]`

[41] A. Faessler, C. Fuchs, M. Krivoruchenko, B. Martemyanov, J. Phys. G **29**, 603 (2003), `arXiv: 0010056 [nucl-th]`

[42] M. Zetenyi, G. Wolf, Phys. Rev. C **67**, 044002 (2003), `arXiv: 0103062 [nucl-th]`

[43] R. Shyam, U. Mosel, Phys. Rev. C **67**, 065202 (2003), `arXiv: 0303035 [hep-ph]`

[44] L. Kaptari, B. Kampfer, Nucl. Phys. A **764**, 338 (2006), `arXiv: 0504072 [nucl-th]`

[45] D. Schumacher, S. Vogel, M. Bleicher, Acta Phys. Hung. A **27**, 451 (2006), `arXiv: 0608041 [nucl-th]`

[46] M. Thomere, C. Hartnack, G. Wolf, J. Aichelin, Phys. Rev. C **75**, 064902 (2007), `arXiv: 0702004 [nucl-th]`

[47] E. Bratkovskaya, W. Cassing, Nucl. Phys. A **807**, 214 (2008), `arXiv: 0712.0635 [nucl-th]`

[48] E. Santini, M. Cozma, A. Faessler, C. Fuchs, M. Krivoruchenko et al., Phys. Rev. C **78**, 034910 (2008), `arXiv: 0804.3702 [nucl-th]`

[49] K. Schmidt, E. Santini, S. Vogel, C. Sturm, M. Bleicher et al., Phys. Rev. C **79**, 064908 (2009), `arXiv: 0811.4073 [nucl-th]`

[50] H. Barz, B. Kampfer, G. Wolf, M. Zetenyi (2009), `arXiv:0910.1541[nucl-th]`

[51] R. Shyam, U. Mosel, Phys. Rev. C **82**, 062201 (2010), `arXiv: 1006.3873 [hep-ph]`

[52] B. Martemyanov, M. Krivoruchenko, A. Faessler, Phys. Rev. C **84**, 047601 (2011), `arXiv: 1108.4265 [nucl-th]`

[53] E. Bratkovskaya, J. Aichelin, M. Thomere, S. Vogel, M. Bleicher (2013), `arXiv: 1301.0786 [nucl-th]`

[54] M. Effenberger, E. Bratkovskaya, U. Mosel, Phys. Rev. C **60**, 044614 (1999), `arXiv: 9903026 [nucl-th]`

[55] M. Effenberger, E.L. Bratkovskaya, W. Cassing, U. Mosel, Phys. Rev. C **60**, 027601 (1999), `arXiv: 9901039 [nucl-th]`

[56] P. Mühlich, Ph.D. thesis, Justus-Liebig-Universität Gießen (2007), available online at `http://theorie.physik.uni-giessen.de/`

[57] J. Messchendorp, A. Sibirtsev, W. Cassing, V. Metag, S. Schadmand, Eur. Phys. J. A **11**, 95 (2001), `arXiv: 0106041 [hep-ex]`

[58] P. Mühlich, T. Falter, U. Mosel, Eur. Phys. J. A **20**, 499 (2004), `arXiv: 0310067 [nucl-th]`

[59] M. Kaskulov, E. Hernandez, E. Oset, Eur. Phys. J. A **31**, 245 (2007), `arXiv: 0610067 [nucl-th]`

[60] P. Mühlich, U. Mosel, Nucl. Phys. A **773**, 156 (2006), `arXiv: 0602054 [nucl-th]`

[61] O. Buss, T. Gaitanos, K. Gallmeister, H. van Hees, M. Kaskulov et al., Phys. Rep. **512**, 1 (2012), `arXiv: 1106.1344 [hep-ph]`

[62] *GiBUU website*, `http://gibuu.physik.uni-giessen.de`

[63] A. Lang, Ph.D. thesis, Justus-Liebig-Universität Gießen (1991), available online at `http://theorie.physik.uni-giessen.de/`

[64] S. Teis, Ph.D. thesis, Justus-Liebig-Universität Gießen (1997), available online at `http://theorie.physik.uni-giessen.de/`

[65] A. Hombach, Ph.D. thesis, Justus-Liebig-Universität Gießen (1999), available online at `http://theorie.physik.uni-giessen.de/`

[66] M. Effenberger, Ph.D. thesis, Justus-Liebig-Universität Gießen (1999), available online at `http://theorie.physik.uni-giessen.de/`

[67] T. Falter, Ph.D. thesis, Justus-Liebig-Universität Gießen (2004), available online at `http://theorie.physik.uni-giessen.de/`

[68] O. Buss, Ph.D. thesis, Justus-Liebig-Universität Gießen (2008), available online at `http://theorie.physik.uni-giessen.de/`

[69] J. Lehr, Ph.D. thesis, Justus-Liebig-Universität Gießen (2003), available online at `http://theorie.physik.uni-giessen.de/`

[70] T. Leitner, Ph.D. thesis, Justus-Liebig-Universität Gießen (2009), available online at `http://theorie.physik.uni-giessen.de/`

[71] W. Botermans, R. Malfliet, Phys. Rep. **198**, 115 (1990)

[72] L. Kadanoff, G. Baym, *Quantum Statistical Mechanics* (Addison Wesley Publishing Company, 1994)

[73] G. Welke, M. Prakash, T. Kuo, S. Das Gupta, C. Gale, Phys. Rev. C **38**, 2101 (1988)

[74] D. Manley, E. Saleski, Phys. Rev. D **45**, 4002 (1992)

[75] V. Shklyar, H. Lenske, U. Mosel, G. Penner, Phys. Rev. C **71**, 055206 (2005), `arXiv: 0412029 [nucl-th]`

[76] A. Anisovich, R. Beck, E. Klempt, V. Nikonov, A. Sarantsev et al., Eur. Phys. J. A **48**, 15 (2012), `arXiv: 1112.4937 [hep-ph]`

[77] V. Mokeev et al. (CLAS Collaboration), Phys. Rev. C **86**, 035203 (2012), `arXiv: 1205.3948 [nucl-ex]`

[78] J. Beringer et al. (Particle Data Group), Phys. Rev. D **86**, 010001 (2012)

[79] V. Dmitriev, O. Sushkov, C. Gaarde, Nucl. Phys. A **459**, 503 (1986)

[80] J. Koch, N. Ohtsuka, E. Moniz, Annals Phys. **154**, 99 (1984)

[81] B.J. VerWest, Phys. Lett. B **83**, 161 (1979)

[82] S. Bass, M. Belkacem, M. Bleicher, M. Brandstetter, L. Bravina et al., Prog. Part. Nucl. Phys. **41**, 255 (1998), `arXiv:9803035[nucl-th]`

[83] U.W. Heinz, K.S. Lee, Nucl. Phys. A **A44**, 503 (1992)

[84] G.Q. Li, C. Ko, Nucl. Phys. A **A82**, 731 (1995), `arXiv: 9407016 [nucl-th]`

[85] M. Berlowski, C. Bargholtz, M. Bashkanov, D. Bogoslawsky, A. Bondar et al., Phys. Rev. D **77**, 032004 (2008)

[86] T. Browder et al. (CLEO), Phys. Rev. D **56**, 5359 (1997), `arXiv: 9706005 [hep-ex]`

[87] L.G. Landsberg, Phys. Rep. **128**, 301 (1985)

[88] B. Spruck, Ph.D. thesis, Justus-Liebig-Universität Gießen (2008), http://geb.uni-giessen.de/geb/volltexte/2008/6667/

[89] R. Arnaldi et al. (NA60 Collaboration), Phys. Lett. B **677**, 260 (2009), `arXiv: 0902.2547 [hep-ph]`

[90] H. Berghäuser, V. Metag, A. Starostin, P. Aguar-Bartolome, L. Akasoy et al., Phys. Lett. B **701**, 562 (2011)

[91] E. Bratkovskaya, O. Teryaev, V. Toneev, Phys. Lett. B **348**, 283 (1995)

[92] G. Agakishiev et al. (HADES Collaboration), Eur. Phys. J. A **48**, 74 (2012), `arXiv: 1203.1333 [nucl-ex]`

[93] E.L. Bratkovskaya, W. Cassing, Nucl. Phys. A **619**, 413 (1997), `arXiv: 9611042 [nucl-th]`

[94] M.I. Krivoruchenko, A. Faessler, Phys. Rev. D **65**, 017502 (2002), `arXiv: 0104045 [nucl-th]`

[95] K. Nakamura et al. (Particle Data Group), J. Phys. G **37**, 075021 (2010)

[96] M. Krivoruchenko, B. Martemyanov, A. Faessler, C. Fuchs, Annals Phys. **296**, 299 (2002), `arXiv: 0110066 [nucl-th]`

[97] G. Caia, V. Pascalutsa, J. Tjon, L. Wright, Phys. Rev. C **70**, 032201 (2004), `arXiv: 0407069 [nucl-th]`

[98] Q. Wan, F. Iachello, Int. J. Mod. Phys. A **20**, 1846 (2005)

[99] G. Ramalho, M. Pena, Phys. Rev. D **85**, 113014 (2012), `arXiv: 1205.2575 [hep-ph]`

[100] M. Post, S. Leupold, U. Mosel, Nucl. Phys. A **689**, 753 (2001), `arXiv: 0008027 [nucl-th]`

[101] `http://gibuu.physik.uni-giessen.de/GiBUU/wiki/Xsections/Compton`

[102] C. Gale, J.I. Kapusta, Phys. Rev. C **40**, 2397 (1989)

[103] M. Zetenyi, G. Wolf, Phys. Rev. C **86**, 065209 (2012), `arXiv: 1208.5671 [nucl-th]`

[104] *Pythia website*, `http://projects.hepforge.org/pythia6`

[105] T. Sjostrand, S. Mrenna, P. Skands, JHEP **05**, 026 (2006), `arXiv: 0603175 [hep-ph]`

[106] K. Gallmeister, U. Mosel, Nucl. Phys. A **826**, 151 (2009), `arXiv: 0901.1770 [hep-ex]`

[107] J. Weil, K. Gallmeister, U. Mosel, PoS **BORMIO2011**, 053 (2011), `arXiv: 1105.0314 [nucl-th]`

[108] S. Teis, W. Cassing, M. Effenberger, A. Hombach, U. Mosel et al., Z. Phys. A **356**, 421 (1997), `arXiv: 9609009 [nucl-th]`

[109] R. Arndt, W. Briscoe, I. Strakovsky, R. Workman, Phys. Rev. C **74**, 045205 (2006), `arXiv: 0605082 [nucl-th]`

[110] J. Weil, H. van Hees, U. Mosel, Eur. Phys. J. A **48**, 111 (2012), `arXiv: 1203.3557 [nucl-th]`

[111] J. Cugnon, J. Vandermeulen, D. L'Hote, Nucl. Instrum. Meth. B **111**, 215 (1996)

[112] L. Montanet et al. (Particle Data Group), Phys. Rev. D **50**, 1173 (1994)

[113] H. Calen, J. Dyring, K. Fransson, L. Gustafsson, S. Haeggstroem et al., Phys. Rev. C **58**, 2667 (1998)

[114] F. Balestra, Y. Bedfer, R. Bertini, L. Bland, A. Brenschede et al., Phys. Rev. C **69**, 064003 (2004)

[115] X. Cao, B.S. Zou, H.S. Xu, Phys. Rev. C **81**, 065201 (2010), `arXiv: 1004.0140 [nucl-th]`

[116] A. Dybczak, *private communications*

[117] V. Kashevarov et al. (Crystal Ball at MAMI Collaboration, TAPS Collaboration, A2 Collaboration), Eur. Phys. J. A **42**, 141 (2009), `arXiv: 0901.3888 [hep-ex]`

[118] U. Mosel, M. Post (2001), `arXiv: 0103059 [nucl-th]`

[119] M. Post, U. Mosel, Nucl. Phys. A **699**, 169 (2002), `arXiv: 0108017 [nucl-th]`

[120] G. Penner, U. Mosel, Phys. Rev. C **66**, 055212 (2002), `arXiv: 0207069 [nucl-th]`

[121] A. Sibirtsev, Nucl. Phys. A **604**, 455 (1996)

[122] M. Abdel-Bary et al. (COSY-TOF Collaboration), Phys. Lett. B **647**, 351 (2007), `arXiv: 0702059 [nucl-ex]`

[123] E. Paryev, J. Phys. G **36**, 015103 (2009), `arXiv: 0810.1124 [nucl-th]`

[124] K. Teilab, Ph.D. thesis, Goethe-Universität Frankfurt am Main (2011), https://www.gsi.de/documents/DOC-2012-May-21-1.pdf

[125] W. Grein, P. Kroll, Nucl. Phys. A **338**, 332 (1980)

[126] R. Bhalerao, L. Liu, Phys. Rev. Lett. **54**, 865 (1985)

[127] T. Feuster, U. Mosel, Phys. Rev. C **59**, 460 (1999), `arXiv: 9803057 [nucl-th]`

[128] G. Penner, U. Mosel, Phys. Rev. C **66**, 055211 (2002), `arXiv: 0207066 [nucl-th]`

[129] A. Baldini, V. Flaminio, W. Moorhead, D. Morrison, H. Schopper, Landolt-Börnstein. New Series, 1/12B (1988)

[130] K. Tsushima, A. Sibirtsev, A.W. Thomas, Phys. Lett. B **390**, 29 (1997), `arXiv: 9608029 [nucl-th]`

[131] G. Lykasov, W. Cassing, A. Sibirtsev, M. Rzyanin, Eur. Phys. J. A **6**, 71 (1999), `arXiv: 9811019 [nucl-th]`

[132] A. Donnachie, P. Landshoff, Phys. Lett. B **348**, 213 (1995), `arXiv: 9411368 [hep-ph]`

[133] I. Horn et al. (CB-ELSA Collaboration), Eur. Phys. J. A **38**, 173 (2008), `0806.4251`

[134] J. Barth, W. Braun, J. Ernst, K.H. Glander, J. Hannappel et al., Eur. Phys. J. A **18**, 117 (2003)

[135] J. Barth, Ph.D. thesis, Friedrich-Wilhelms-Universität Bonn (2002)

[136] A. Larionov, U. Mosel, Nucl. Phys. A **728**, 135 (2003), `arXiv: 0307035 [nucl-th]`

[137] D. Barber et al. (LAMP2 GROUP), Z.Phys. **C26**, 343 (1984)

[138] A. Donnachie, P. Landshoff, Phys. Lett. B **478**, 146 (2000), `arXiv: 9912312 [hep-ph]`

[139] H. Pi, Comput.Phys.Commun. **71**, 173 (1992)

[140] C. Friberg, T. Sjostrand, JHEP **0009**, 010 (2000), `hep-ph/0007314`

[141] S. Protopopescu, M. Alston-Garnjost, A. Barbaro-Galtieri, S.M. Flatte, J. Friedman et al., Phys. Rev. D **7**, 1279 (1973)

[142] E. Alekseeva, A. Kartamyshev, V. Makarin, K. Mukhin, O. Patarakin et al., Sov. Phys. JETP **55**, 591 (1982)

[143] F. Halzen, K. Igi, M. Ishida, C. Kim, Phys. Rev. D **85**, 074020 (2012), `arXiv: 1110.1479 [hep-ph]`

[144] W. Cassing, S. Juchem, Nucl. Phys. A **665**, 377 (2000), `arXiv: 9903070 [nucl-th]`

[145] S. Leupold, Nucl. Phys. A **672**, 475 (2000), `arXiv: 9909080 [nucl-th]`

[146] M. Effenberger, U. Mosel, Phys. Rev. C **60**, 051901 (1999), `nucl-th/9906085`

[147] A.B. Larionov, U. Mosel, Phys. Rev. C **66**, 034902 (2002), `nucl-th/0202008`

[148] S. Leupold, M. Lutz, Eur. Phys. J. A **39**, 205 (2009), `arXiv: 0807.4686 [hep-ph]`

[149] E. Oset, L. Salcedo, Nucl. Phys. A **468**, 631 (1987)

[150] M. Effenberger, A. Hombach, S. Teis, U. Mosel, Nucl. Phys. A **613**, 353 (1997), `arXiv: 9607005 [nucl-th]`

[151] *HADES website*, `http://www-hades.gsi.de`

[152] T. Galatyuk, *private communications*

[153] G. Agakishiev et al. (HADES Collaboration), Eur. Phys. J. A **40**, 45 (2009), `arXiv: 0902.4377 [nucl-ex]`

[154] P. Tlusty et al. (HADES Collaboration) (2009), `arXiv: 0906.2309 [nucl-ex]`

[155] R.B. Wiringa, V. Stoks, R. Schiavilla, Phys. Rev. C **51**, 38 (1995), `arXiv: 9408016 [nucl-th]`

[156] M. Schäfer, H. Donges, A. Engel, U. Mosel, Nucl. Phys. A **575**, 429 (1994), `arXiv: 9401006 [nucl-th]`

[157] F. de Jong, U. Mosel, Phys. Lett. B **379**, 45 (1996), `arXiv: 9602016 [nucl-th]`

[158] P. Adlarson et al. (WASA-at-COSY Collaboration), Phys. Rev. Lett. **106**, 242302 (2011), `arXiv: 1104.0123 [nucl-ex]`

[159] A. Buckley, H. Hoeth, H. Lacker, H. Schulz, J.E. von Seggern, Eur. Phys. J. C **65**, 331 (2010), `arXiv: 0907.2973 [hep-ph]`

[160] L. Winckelmann, H. Sorge, H. Stoecker, W. Greiner, Phys. Rev. C **51**, 9 (1995)

[161] S. Endres, M. Bleicher, J. Phys. Conf. Ser. **426**, 012033 (2013)

[162] A. Titov, B. Kampfer, B. Reznik, Eur. Phys. J. A **7**, 543 (2000), `arXiv: 0001027 [nucl-th]`

[163] G. Agakishiev, A. Balanda, D. Belver, A. Belyaev, J. Berger-Chen et al. (2013), `arXiv: 1305.3118 [nucl-ex]`

[164] S. Barsov, I. Lehmann, R. Schleichert, C. Wilkin, M. Buescher et al., Eur. Phys. J. A **21**, 521 (2004), `arXiv:0305031[nucl-ex]`

[165] M. Lorenz et al. (HADES Collaboration), J. Phys. Conf. Ser. **426**, 012034 (2013)

[166] A. Larionov, W. Cassing, S. Leupold, U. Mosel, Nucl. Phys. A **696**, 747 (2001), `arXiv: 0103019 [nucl-th]`

[167] M. Wagner, A. Larionov, U. Mosel, Phys. Rev. C **71**, 034910 (2005), `arXiv: 0411010 [nucl-th]`

[168] R. Hagedorn, Nuovo Cim.Suppl. **3**, 147 (1965)

[169] *DLS website*, `http://macdls.lbl.gov/DLS_WWW_Files`

[170] A. Dybczak (HADES Collaboration), J. Phys. Conf. Ser. **426**, 012015 (2013)

[171] T. Weidmann, E. Bratkovskaya, W. Cassing, U. Mosel, Phys. Rev. C **59**, 919 (1999), `arXiv: 9711004 [nucl-th]`

[172] M.F. Lutz, B. Friman, M. Soyeur, Nucl. Phys. A **713**, 97 (2003), `arXiv: 0202049 [nucl-th]`

[173] S. Damjanovic et al. (NA60 Collaboration), Nucl. Phys. A **783**, 327 (2007), `nucl-ex/0701015`

[174] G. Agakichiev et al. (CERES Collaboration), Phys. Rev. Lett. **75**, 1272 (1995)

[175] G. Agakishiev et al. (CERES/NA45 Collaboration), Phys. Lett. B **422**, 405 (1998), `nucl-ex/9712008`

[176] S. Afanasiev et al. (PHENIX Collaboration) (2007), `0706.3034`

[177] A. Adare et al. (PHENIX Collaboration), Phys. Lett. B **670**, 313 (2009), `0802.0050`

[178] A. Adare et al. (PHENIX Collaboration), Phys. Rev. C **81**, 034911 (2010), `0912.0244`

[179] J. Zhao (STAR Collaboration), J. Phys. G **38**, 124134 (2011), `1106.6146`

[180] K. Aamodt et al. (ALICE Collaboration), JINST **3**, S08002 (2008)

[181] W. Cassing, E. Bratkovskaya, Phys. Rev. C **78**, 034919 (2008), `arXiv: 0808.0022 [hep-ph]`

[182] H. Petersen, J. Steinheimer, G. Burau, M. Bleicher, H. Stocker, Phys. Rev. C **78**, 044901 (2008), `arXiv: 0806.1695 [nucl-th]`

[183] J. Lehr, M. Effenberger, H. Lenske, S. Leupold, U. Mosel, Phys. Lett. B **483**, 324 (2000), `arXiv: 0002013 [nucl-th]`

[184] B. Aubert et al. (BaBar Collaboration), Phys. Rev. D **70**, 112006 (2004), `arXiv: 0407003 [hep-ex]`

[185] S. Das, Phys. Rev. C **83**, 064608 (2011), `arXiv: 1106.4376 [nucl-th]`

[186] T. Rodrigues, J. Arruda-Neto, Phys. Rev. C **84**, 021601 (2011)

[187] T.E. Rodrigues, J.D. de Toledo Arruda-Neto, Journal of Physics: Conference Series **420**(1), 012014 (2013), `http://stacks.iop.org/1742-6596/420/i=1/a=012014`

[188] M. Thiel, *private communications*

[189] M. Thiel et al., *submitted to Eur. Phys. J. A*

[190] M. Williams et al. (CLAS Collaboration), Phys. Rev. C **80**, 065209 (2009), `arXiv: 0908.2911 [nucl-ex]`

List of Figures

List of Tables

Acknowledgement